Energetics and mixing in stratified turbulent flows

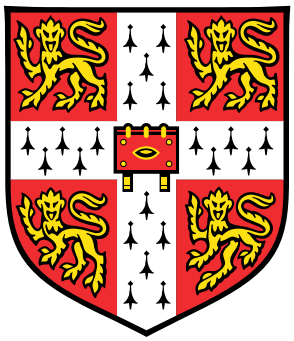

Christopher James Howland

Supervisors: Prof. C.P. Caulfield
Dr. J.R. Taylor

Department of Applied Mathematics and Theoretical Physics
University of Cambridge

This thesis is submitted for the degree of
Doctor of Philosophy

Pembroke College June 2020

Declaration

This thesis is the result of my own work and includes nothing which is the outcome of work done in collaboration except as declared in the Preface and specified in the text. It is not substantially the same as any that I have submitted, or, is being concurrently submitted for a degree or diploma or other qualification at the University of Cambridge or any other University or similar institution except as declared in the Preface and specified in the text. I further state that no substantial part of my thesis has already been submitted, or, is being concurrently submitted for any such degree, diploma or other qualification at the University of Cambridge or any other University or similar institution except as declared in the Preface and specified in the text. It does not exceed the prescribed word limit for the relevant Degree Committee.

Christopher James Howland
June 2020

Energetics and mixing in stratified turbulent flows

Christopher James Howland

Turbulent mixing has an important influence on many physical processes in the ocean. For example, the upwelling of water through the stably stratified ocean interior, needed to close the global circulation, is only possible through the enhanced vertical mixing resulting from turbulence. The transport of heat, carbon and nutrients is also affected by this mixing. Understanding its spatial and temporal intermittency is therefore vital for determining the regional distribution of these important tracers. Away from boundaries, turbulence in the ocean is commonly attributed to the breaking of internal waves. When an internal wave grows to a large amplitude, it can break due to convective instabilities or shear instabilities. A fundamental understanding of the turbulent transition arising from these instabilities is useful for both interpreting observations and predicting 'hotspots' of turbulence in the field. Focusing solely on canonical instabilities however neglects the wide range of complex flows occuring at small scales in the ocean. Interactions with mean flows or with the background internal wave field can alter the properties of turbulence and the ensuing mixing. In this thesis, we use numerical simulations to investigate three problems aimed at enhancing our understanding of mixing in such stratified flows.

We first investigate the development of Kelvin–Helmholtz instability in a stratified shear layer. We quantify the maximum energy extracted from the mean flow by the instability as a function of the Richardson number Ri. By applying forcing to the governing equations, we are able to extend our simulations up to the marginal stability threshold of $Ri = 1/4$, and show that the maximum energy decreases to a small but non-zero value as this threshold is approached. Our next study focuses on mixing in stratified turbulence that is kept in a statistically steady state through large-scale forcing. We compare flows forced by vortical modes with those forced by internal gravity waves. A higher mixing efficiency in the wave-forced simulations is attributed to a more convective-driven mixing process. Intermittency in the flows allows us to verify that the mixing efficiency is constant throughout each domain. This is despite wavelet analysis showing that regions of high and low energy dissipation have distinct scalings in their energy spectra. Finally, we consider the interaction of a large-amplitude internal gravity wave with a sinusoidal shear flow. We find both convective and shear processes to be important in the transition to turbulence. Through extending the concept of available potential energy to triply periodic domains, we show that the scalar variance dissipation rate χ is a good approximation to the 'true' rate of mixing $\mathcal{M}$, even when sizeable regions of static instability are present.

For Sarah

Acknowledgements

A PhD is often described as a solitary pursuit, but this thesis would not look as it does today without the support of a special group of people. Firstly, I must thank my supervisors Colm and John, who were a constant source of guidance and encouragement throughout my four years in Cambridge. I always left our meetings with a renewed sense of determination and a better understanding of the challenges I was facing. DAMTP has been a fantastic place to work, and I would like to thank all of the PhD students and postdocs who helped create a friendly and relaxed atmosphere in Pavilion H. I will particularly miss the somewhat endless coffee breaks, and the many entertaining conversations that they sparked. I am also thankful to the graduate community of Pembroke College for providing a welcoming space to wind down away from the department, and I am grateful for the support of my friends across Cambridge over the course of my degree.

I have also been extremely lucky to venture away from Cambridge at various points in my degree and learn from scientists across the world at a range of conferences, workshops, and schools. The Les Houches summer school on Turbulence in Climate, the 2018 GFD Program at WHOI, and the WITGAF workshop in Cargèse will live long in my memory for the special experiences they provided and the great friends I made through them. I thank all of the organisers and participants of those programs for making my time there so special. I must also acknowledge funding from Pembroke College, the Cambridge Philosophical Society, and NERC that allowed me to attend these programs.

I am of course endlessly grateful to my parents for the continuous love and care they have provided throughout my degree and indeed the rest of my life. It was wonderful to spend more time with them as I wrote up this dissertation, after they had valiantly taken me in as a pandemic swept the nation. Finally, I must thank Sarah for her endless support and encouragement during my time in Cambridge. Above all I am grateful for her patience as I completed this degree that has kept us apart for too long.

Table of contents

List of figures **xv**

List of tables **xvii**

1 Turbulent mixing in the ocean **1**
1.1 Turbulent mixing, heat transport, and the ocean 1
1.2 Oceanic fluid dynamics across multiple scales 7
1.2.1 Astrophysical forcing, internal waves, and turbulence 7
1.2.2 A spectral perspective 9
1.3 A note on 'strongly stratified turbulence' 12
1.4 Modelling small-scale mixing in the ocean 15
1.5 Problems in turbulent stratified mixing addressed by this thesis 20

2 Nonlinear 2-D saturation of Kelvin–Helmholtz billows **23**
2.1 Stratified shear instabilities and 'marginal stability' 23
2.2 Simulation Setup 27
2.3 Results 29
2.3.1 Class D: Diffusing shear layers 29
2.3.2 Class S: Steady shear layers 30
2.3.3 Class A: Accelerating shear layers 32
2.4 Discussion and Conclusions 35
2.5 Recent developments 37

3 Mixing in forced stratified turbulence **39**
3.1 Stratified turbulence maintained by large-scale forcing 39
3.2 Mixing and energetics in a triply-periodic domain 43
3.3 Forced numerical simulations 49
3.4 Results 51
3.4.1 Flow structure 51

3.4.2 Volume-averaged quantities . . . 53
3.4.3 Spatial variation . . . 55
3.4.4 Energy spectra . . . 60
3.5 Discussion and conclusions . . . 63

4 Shear-induced breaking of internal gravity waves 71
4.1 Observations of internal waves in the thermocline . . . 71
4.2 Internal wave breaking . . . 74
4.3 Numerical simulations . . . 78
4.3.1 Nonlinear 3D simulations: domain and initial conditions . . . 78
4.3.2 Wave propagation using ray theory . . . 82
4.4 Results . . . 88
4.4.1 Flow phenomenology and wave breakdown . . . 88
4.4.2 Energetics . . . 93
4.4.3 Turbulence and mixing . . . 95
4.4.4 Mean flow interactions . . . 99
4.5 Discussion and conclusions . . . 101

5 Quantifying mixing and APE in simulations of stratified flows 107
5.1 Mixing and available potential energy . . . 107
5.2 Quantifying mixing in triply-periodic domains . . . 110
5.2.1 Local APE density . . . 113
5.2.2 Potential energy between isopycnal boundaries . . . 115
5.2.3 APE and BPE between isopycnal boundaries . . . 117
5.3 Numerical simulations . . . 119
5.4 Results . . . 121
5.4.1 Energy budgets . . . 121
5.4.2 Visualising mixing with local APE . . . 122
5.4.3 Estimating mixing with χ . . . 125
5.4.4 The effect of mean flow dissipation . . . 127
5.5 Discussion and conclusions . . . 129

6 A perspective on stratified mixing 135
6.1 Thesis summary . . . 135
6.2 An outlook on the future . . . 140

References 143

Appendix A Further details on mixing and APE **153**
A.1 Considering a more general boundary isopycnal 153
A.2 Derivation of the potential energy equations 155
A.2.1 Total potential energy 155
A.2.2 Background potential energy 157
A.3 Equivalence of various local APE definitions 159

List of figures

1.1 Overturning circulation schematic 3
1.2 Oceanic internal wave schematic 9
1.3 A model spectrum for vertical shear in the ocean 13

2.1 Energy and saturation time: diffusive shear layers 30
2.2 Vorticity snapshots: steady shear layers 31
2.3 Energy and saturation time: steady shear layers 32
2.4 Richardson number and growth rate time series: accelerating shear layers 33

3.1 Energy pathway schematic 46
3.2 Buoyancy snapshots: forced periodic simulations 52
3.3 Energy time series 53
3.4 Time series of energy budget terms 54
3.5 Dissipation rate and mixing coefficient time series 55
3.6 Plane snapshot, space-time plot, and mean vertical profile of ε 56
3.7 2D pdf of ε and χ from horizontal averages 57
3.8 2D pdf of Γ and Fr from horizontal averages 57
3.9 2D pdf of χ and ε from pointwise calculations 59
3.10 2D pdf of Γ and Fr from pointwise calculations 59
3.11 Conditionally averaged energy spectra 61
3.12 2D pdf of Γ and L_E/L_O 65

4.1 Observations of overturning events in the thermocline 73
4.2 Shear and internal wave initial condition 81
4.3 Ray tracing paths in a shear flow 85
4.4 Wave steepness time series 87
4.5 Buoyancy snapshots of wave breaking 90
4.6 Vorticity snapshots of wave breaking 91
4.7 Comparison of initial and final mean profiles 92

4.8 Energy time series for wave breaking simulations 93
4.9 Space-time diagram of mean buoyancy flux 95
4.10 Dissipation rate time series 97
4.11 Vorticity snapshots at time of maximum ε 98
4.12 Shear production 99

5.1 Aperiodic buoyancy field example 112
5.2 Periodic domain tiling schematic 114
5.3 Buoyancy field sketch with moving boundaries 117
5.4 Initial condition of unforced simulation 120
5.5 Energy budgets for unforced simulation 121
5.6 Energy budgets for forced simulation 122
5.7 Snapshots of local APE 123
5.8 Time series comparison of $\mathcal{M}$ and χ 126
5.9 Time series of mixing efficiency with and without mean dissipation . . 128
5.10 Time series comparison of diapycnal diffusivity and Osborn-Cox 131

List of tables

2.1 Parameters for shear layer simulations 28

3.1 Input parameters: forced periodic simulations 50
3.2 Statistics: Forced periodic simulations 52

4.1 Sheared wave simulation parameters 82

5.1 Simulation parameter overview 119

Chapter 1

Turbulent mixing in the ocean

1.1 Turbulent mixing, heat transport, and the ocean

Turbulence, characterised by highly disordered motions across a wide range of scales, is pervasive throughout the ocean. We see disorder on large scales in the eddying surface currents of the Gulf Stream and the Antarctic Circumpolar Current, but on a far smaller scale turbulence plays an important role in the vertical transport of heat, salt, and nutrients. By stirring these non-uniform scalar fields such that their local gradients become sharpened, turbulent flows can irreversibly mix scalars by enhancing their diffusion.

Across the vast majority of its breadth and depth, the ocean is stably stratified, that is its density increases with depth. This stable stratification is primarily due to changes in temperature, salinity or in some cases a combination of the two. For simplicity, let us consider the case of a thermally stratified fluid where cool water underlies warm water. We shall also assume that the water is far enough from the fresh water density maximum of 4 °C that density changes scale linearly with temperature. In this case surfaces of constant density, known as *isopycnals*, are equivalent to surfaces of constant temperature. In much of the ocean, the presence of salt means that seawater monotonically increases in density as temperature decreases, and the density maximum seen in fresh water does not occur. Nonlinearities in the relationship between density, temperature and salinity can still affect mixing in peculiar ways, as discussed by McDougall (1987).

If salinity is uniform throughout the fluid, diffusion will act in the direction of temperature gradients, and mixing of the temperature field will be inherently *diapycnal*, that is perpendicular to the isopycnal surfaces. Passive tracers such as dissolved CFCs and dye can be spread along isopycnal surfaces by advection of the flow, but can only be transported across isopycnals through such diapycnal diffusive processes. When a turbulent flow stirs up the stably stratified fluid, the warm, light water is mixed down-

wards and the cold, dense water is mixed upwards. The downward diffusion of heat is matched by the upwelling of dense water.

It has long been known that this upwelling and the associated diapycnal mixing is important in the ocean. In a seminal paper Munk (1966) proposed that uniform upwelling of dense water balanced the heat transfer associated with the sinking of the dense water as it is formed in polar regions. Assuming that the upwelling velocity w and turbulent diffusivity K_T are related through a steady advection-diffusion balance

$$w\frac{dT}{dz} = \frac{d}{dz}\left(K_T\frac{dT}{dz}\right), \tag{1.1}$$

and that the temperature profile $T(z)$ is exponential, Munk (1966) estimated that the mean turbulent diffusivity was $K_T \approx 1\times10^{-4}\,\mathrm{m^2\,s^{-1}}$. Since the molecular diffusivity of heat is only $1.4\times10^{-7}\,\mathrm{m^2\,s^{-1}}$, it can be inferred that turbulent processes are vital in enhancing this diffusion by a factor of 700 to close the global overturning circulation.

Munk and Wunsch (1998) later revisited this problem after a range of observational studies inferred lower values of the turbulent diffusivity from small-scale turbulence measurements and tracer release experiments. This study highlighted the importance of distinguishing a 'bulk' measure of mixing from such localised measures. Munk and Wunsch (1998) argued that $K_T \approx 1\times10^{-4}\,\mathrm{m^2\,s^{-1}}$ remained an appropriate bulk measure to describe how much diapycnal mixing is required to maintain the abyssal stratification. However they also acknowledged that such mixing can be achieved in various ways. For example, a bulk value of $K_T \approx 1\times10^{-4}\,\mathrm{m^2\,s^{-1}}$ could be achieved primarily through highly localised 'hotspots' where diapycnal fluxes, and the corresponding local measures of K_T, are very large.

Indeed modern descriptions of the overturning circulation, as reviewed by Talley (2013) and Cessi (2019), present a more complex picture of the return circulation than uniform upwelling. For example it was highlighted by Marshall and Speer (2012) that wind-driven upwelling can be responsible for significant mass transport along isopycnals in the Southern Ocean. This provides an alternative *advective* pathway for returning dense waters to the surface that does not rely on diapycnal mixing. Nevertheless diapycnal mixing remains integral to the ocean circulation through the upwelling of dense water as shown in the textbook schematic of figure 1.1. Talley (2013) argues that the wind-driven upwelling in the Southern Ocean primarily affects the upper cell of the overturning circulation (the purple loop in figure 1.1), and a bulk diapycnal diffusivity of $1\times10^{-4}\,\mathrm{m^2\,s^{-1}}$ is still therefore required in the deep ocean. Diapycnal mixing is of further importance in the strongly stratified thermocline since it affects fluxes of trac-

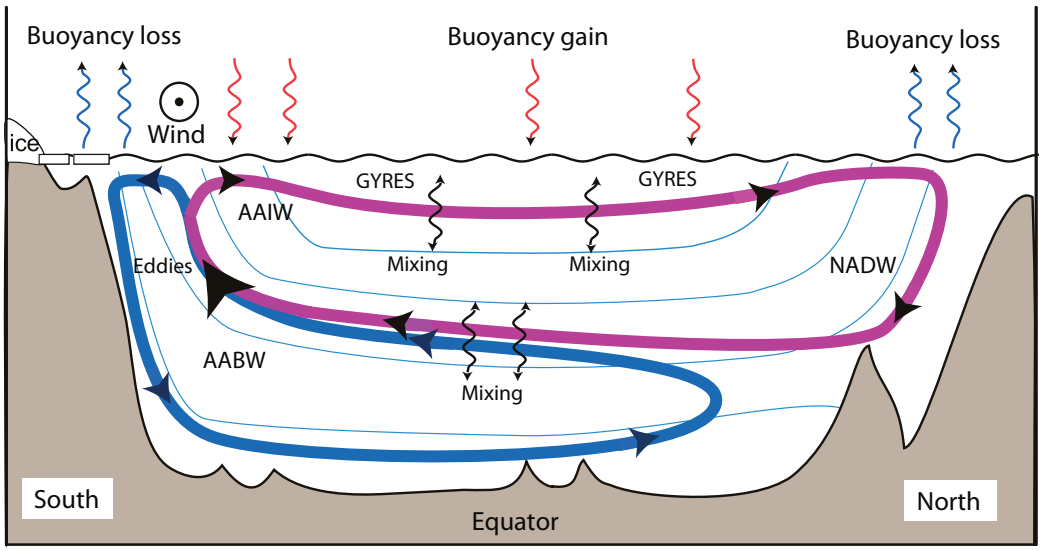

Fig. 1.1 A simplified schematic overview of the ocean's meridional overturning circulation from Vallis (2017). The key role of diapycnal mixing in upwelling dense water is highlighted by the wavy, black arrows. © Geoffrey K. Vallis. Used with permission.

ers between the surface mixed layer and the ocean interior. Rippeth et al. (2014) for instance find that diapycnal fluxes of dissolved carbon in the thermocline can have an impact on the vital air-sea exchange of CO_2.

In terms of *local* measures of mixing, an extensive compilation of observational estimates from Waterhouse et al. (2014) show that mixing is far from uniform in the ocean. As well as showing strong regional variability, their estimates of diapycnal diffusivity highlight increased mixing towards the bottom of the ocean in locations where the seafloor topography is rough. This increase is not limited to turbulent boundary layers, but remains significant even 1 km above the ocean floor. Such "knowledge" of the topography signifies the strong presence of internal waves that transport information through the water column. The key role of these internal waves in transferring energy to turbulence will be discussed further in §1.2.

The dataset analysed by Waterhouse et al. (2014) does not come from direct measurements of diapycnal fluxes, and indeed such measurements would be practically impossible in the field. The most precise estimates come from 'microstructure' measurements of temperature fluctuations or velocity shear. For the case of small scale temperature measurements, the method of Osborn and Cox (1972) is used to estimate the turbulent diffusivity of heat. This method assumes that a balance exists between the production

and dissipation of temperature variance:

$$-\overline{w'T'}\frac{\partial\overline{T}}{\partial z} = \kappa\overline{|\boldsymbol{\nabla}T'|^2}. \tag{1.2}$$

Here κ is the molecular diffusivity of heat, an overbar denotes some appropriate average, and primes are used for perturbations from this average. The above balance is then substituted into the definition of the turbulent diffusivity to produce

$$K_T \equiv -\frac{\overline{w'T'}}{\partial\overline{T}/\partial z} = \kappa\frac{\overline{|\boldsymbol{\nabla}T'|^2}}{\left(\partial\overline{T}/\partial z\right)^2}. \tag{1.3}$$

If we assume as earlier that density changes are solely dependent on temperature, then we can rewrite the turbulent diffusivity as

$$K_T = \kappa\frac{\overline{|\boldsymbol{\nabla}\rho'|^2}}{\left(\partial\overline{\rho}/\partial z\right)^2} \equiv \frac{\chi}{N^2}, \tag{1.4}$$

where N is the buoyancy frequency, defined through $N^2 \equiv -\frac{g}{\rho_0}\frac{\partial\overline{\rho}}{\partial z}$ and ρ_0 is the constant, global mean density. N is the frequency at which a parcel of fluid will naturally oscillate in a stably stratified fluid with vertical density gradient $\partial\overline{\rho}/\partial z$. The symbol χ is used to denote various quantities related to the dissipation of scalar variance in the literature. Throughout this thesis we shall use χ, defined through (1.4) to denote the destruction rate of $(g\rho'/\rho_0)^2/2N^2$, a quantity that estimates available potential energy.

Available potential energy is the difference between the potential energy of a system and the minimum potential energy that can be obtained through rearranging the density field. For a fluid stratified by a single scalar, Winters and D'Asaro (1996) derive an exact expression for the diapycnal flux through an isopycnal surface, and show that the diapycnal diffusivity is directly related to the destruction rate of available potential energy. Furthermore, their exact expression for K_T takes a very similar form to the Osborn and Cox (1972) estimate of (1.4). If one can obtain suitably accurate measurements of T', it therefore seems that the Osborn and Cox (1972) method can provide a reliable estimate of diapycnal mixing in thermally stratified regions of the ocean. We return to test this hypothesis in chapter 5.

Due to technological limitations, however, accurate estimation of χ in observational oceanography has only been made possible relatively recently (e.g. Moum and Nash 2009; Bluteau et al. 2013). The microstructure data in Waterhouse et al. (2014) therefore

rely on measurements of small-scale velocity gradients. Under assumptions of homogeneity and isotropy, a measure of the turbulent kinetic energy (TKE) dissipation rate ε can be inferred from such measurements. The dissipation rate ε is linked to a diapycnal diffusivity through the model of Osborn (1980) that is commonly applied throughout the oceanographic literature. To derive the model diffusivity, we assume a steady state balance between the production S_p of turbulence by a mean shear, the dissipation rate ε of TKE, and the turbulent buoyancy flux $\mathcal{J}$:

$$-S_p \equiv \overline{u_i{}' u_j{}'} \frac{\partial \overline{u_i}}{\partial x_j} = -2\nu \overline{s_{ij}{}' s_{ij}{}'} - \frac{g\overline{w'\rho'}}{\rho_0} \equiv -\varepsilon + \mathcal{J}, \tag{1.5}$$

where $s_{ij}{}' = \frac{1}{2}\left(\partial u_i/\partial x_j + \partial u_j/\partial x_i\right)$ is the symmetric strain-rate tensor. We then define the flux Richardson number as $R_f \equiv -\mathcal{J}/S_p$, and note that in a statistically steady state this is equivalent to the mixing efficiency η, the proportion of energy supplied to turbulence that is used to mix the fluid. Osborn (1980) uses this ratio to eliminate the shear production S_p from the above equation, and express the turbulent diffusivity in terms of ε and the buoyancy frequency N:

$$K_T \equiv -\frac{\mathcal{J}}{N^2} = \frac{\eta}{1-\eta}\frac{\varepsilon}{N^2}. \tag{1.6}$$

Based on earlier experimental and theoretical predictions, Osborn (1980) proposes that the prefactor $\Gamma = \eta/(1-\eta)$ should have an upper bound of 0.2 in a steady state. Osborn (1980) argues that turbulence would decay too quickly when $\Gamma > 0.2$, making a steady state impossible to sustain.

Although Γ is now frequently taken to be *equal* to 0.2 in observational estimates of mixing, both experimental and numerical studies have shown that Γ can vary depending on the nature of the stratified turbulent flow (see for example the reviews of Linden 1979; Ivey et al. 2008; Gregg et al. 2018). Identifying the key dimensionless parameters on which Γ depends remains a topic of controversy. For the case of statistically steady turbulence driven by a mean shear, as considered by Osborn (1980), the numerical results of Shih et al. (2005) are often cited to motivate dependence on the buoyancy Reynolds number $Re_b = \varepsilon/\nu N^2$. However recent simulations from Portwood et al. (2019) suggest that the flows in Shih et al. (2005) had not reached a steady state, and that $\Gamma \approx 0.2$ holds as Re_b varies in this case.

Furthermore there remain significant questions over whether such a setup is representative of turbulent mixing in the ocean. When different flows appear to exhibit different dependence for Γ, it is imperative to identify which flows are most relevant

for ocean mixing. For example, Maffioli et al. (2016) find that statistically steady turbulent flows arising from large scale vortical forcing (rather than a mean shear) exhibit dependence of Γ on the turbulent Froude number $Fr = \varepsilon/N\mathcal{K}$ where $\mathcal{K} = \overline{\boldsymbol{u}' \cdot \boldsymbol{u}'}/2$ is the turbulent kinetic energy. Moving away from steady states, Garanaik and Venayagamoorthy (2019) observe the same $\Gamma(Fr)$ dependence in simulations of the decay of an initially isotropic turbulent velocity field.

This contrasts with a large body of literature on mixing from stratified shear layers (Caulfield and Peltier 2000; Peltier and Caulfield 2003; Mashayek et al. 2013; Salehipour and Peltier 2015). In this classical example of an unsteady, shear-driven, turbulent flow, the mixing efficiency (and hence Γ) varies over the lifecycle of the transient event. The gradient Richardson number $Ri_g = N^2/S^2$ (where $S = |\partial\overline{\boldsymbol{u}}/\partial z|$ is the magnitude of the vertical shear), buoyancy Reynolds number Re_b, and Prandtl number $Pr = \nu/\kappa$ have all been proposed as relevant parameters for mixing in this flow. For example Mashayek et al. (2017) propose a parameterization for $\Gamma(Re_b)$ based on a combination of shear layer simulations and microstructure observations of turbulent patches. This parameterization takes yet a different functional form to *both* of the trends seen in the steady shear flows mentioned above.

Mater and Venayagamoorthy (2014) argue that understanding the multi-parameter dependence of Γ is important for developing accurate mixing models. Indeed, many of the parameters listed above can be interconnected. Considering the balance of (1.5), we see that if the turbulence is sustained by a mean shear $\partial\overline{u_i}/\partial x_j$, then

$$\mathcal{K}S \sim \overline{u_i{}' u_j{}'}\frac{\partial \overline{u_i}}{\partial x_j} \sim \varepsilon. \tag{1.7}$$

Therefore in shear-driven flows, Froude and Richardson numbers are essentially interchangeable through $Ri = N^2/S^2 \sim (N\mathcal{K}/\varepsilon)^2 = Fr^{-2}$. The parameters Re_b and Fr are also linked by $Re_b = Fr^2 Re_t$, where $Re_t = \mathcal{K}^2/\varepsilon\nu$ is a dimensionless parameter independent of the stratification and is sometimes referred to as a 'turbulent Reynolds number'. Both Re_b and Re_t can be obtained from the classical form of the Reynolds number $Re = LU/\nu$ when appropriate length and velocity scales are chosen:

$$L = \left(\frac{\varepsilon}{N^3}\right)^{1/2}, \qquad U = \left(\frac{\varepsilon}{N}\right)^{1/2}, \qquad \Rightarrow Re = \frac{LU}{\nu} = \frac{\varepsilon}{\nu N^2}, \tag{1.8}$$

$$L = \frac{\mathcal{K}^{3/2}}{\varepsilon}, \qquad U = \mathcal{K}^{1/2}, \qquad \Rightarrow Re = \frac{LU}{\nu} = \frac{\mathcal{K}^2}{\varepsilon\nu}. \tag{1.9}$$

This further highlights the difficulty in choosing appropriate dimensionless parameters to describe a system with many varying and potentially interconnected quantities.

The debate surrounding variations in mixing efficiency is not merely a fluid dynamical curiosity, but has significant implications for the accurate parameterization of mixing in large-scale ocean models. Not only does mixing efficiency affect the observations used to verify parameterizations in global models, but recent studies have also moved towards directly using mixing efficiency in new versions of these parameterizations. For example Klymak and Legg (2010) use the Osborn (1980) form of diffusivity in (1.6) to model the mixing due to breaking waves near topography in a regional ocean model. On a larger scale, de Lavergne et al. (2015) and Cimoli et al. (2019) have shown that using a parameterization where Γ depends on Re_b strongly affects the spatial distribution of mixing, and this in turn affects large-scale exchanges of water masses and the deep overturning circulation.

Despite such intense focus on the mixing efficiency and its parameterization, there remain significant uncertainties associated with other aspects of observational methods such as Osborn (1980). In regions close to boundaries, Arthur et al. (2017) highlight how difficulties in obtaining an appropriate measure of the buoyancy frequency N can significantly impact local estimates of mixing. An even greater challenge is that of sufficiently sampling the ocean, as hinted at by the observational analysis of Ijichi et al. (2020). By comparing temperature and velocity microstructure measurements, they found that bulk estimates of mixing efficiency are dominated by a small number of extreme turbulence events. Understanding how such turbulence is generated may therefore be vital for interpreting potentially under-sampled mixing measurements.

1.2 Oceanic fluid dynamics across multiple scales

1.2.1 Astrophysical forcing, internal waves, and turbulence

Wunsch and Ferrari (2004) provide an overview of the energetics associated with the global ocean circulation. Although there remains some controversy regarding the importance of heating and cooling at the upper surface of the ocean as a source of potential energy (see Hughes et al. 2009), it is generally accepted that the primary sources of kinetic energy are tides and atmospheric winds (Ferrari and Wunsch 2009). Some of this energy is dissipated immediately as turbulence in thin boundary layers at the sea floor (as tidal currents flow over it) and at the sea surface. A large fraction of wind energy con-

tributes to the maintenance of the surface mixed layer of the ocean and the production of surface waves.

The vast majority of the ocean's kinetic energy is contained in so-called 'balanced' motions, where a large scale balance exists at leading order between horizontal pressure gradients and the Coriolis force due to the Earth's rotation. These motions, typically appearing on planetary scales of $O(100\,\mathrm{km})$ and larger, have been effectively modelled using simplified fluid models such as quasi-geostrophy (Vallis 2017). However such models do not allow for the generation of small scale turbulence that is required to dissipate the excess energy being added to the ocean system. A key reason for this is that balanced models filter out the smaller scale, faster motions of internal waves.

Any stably stratified fluid has the potential to support internal waves, and the ocean is no exception. Linearising the inviscid equations of motion for a rotating, stratified fluid gives the equation

$$\partial_t^2(\nabla^2 w) + f^2\partial_z^2 w + N^2(\partial_x^2 + \partial_y^2)w = 0, \tag{1.10}$$

where $N(z)$ is the buoyancy frequency and $f = 2\Omega\sin\psi$ is the Coriolis frequency with Ω the rotation rate of the Earth and ψ latitude. If we assume N is constant (or at least varies on a larger scale than the wave), substituting in a plane wave solution of the form $w \propto \exp[i(kx + ly + mz - \omega t)]$ provides the dispersion relation

$$\omega^2 = \frac{N^2(k^2 + l^2) + f^2m^2}{k^2 + l^2 + m^2} = N^2\cos^2\varphi + f^2\sin^2\varphi. \tag{1.11}$$

Here φ is the angle that the wave vector makes with the horizontal plane in wavenumber space. Since $f < N$ throughout the ocean, this relation implies that any internal wave must satisfy $f \leq \omega \leq N$. Importantly these waves are not only solutions to the linearised equation, but are also exact solutions to the full nonlinear equations of motion.

Energy from the wind and tides that is not dissipated in turbulent boundary layers (or supplied to larger-scale currents) propagates away in the form of internal waves. In the case of tidal generation, internal waves are produced at tidal frequencies as water is pulled across topographic features on the ocean floor (Garrett and Kunze 2007). The dispersion relation (1.11) shows that the frequency of an internal wave only determines its propagation angle. This means that waves can be generated over a wide range of wavenumbers, depending on the shape of the topographic features, at the same tidal frequency. Similar behaviour occurs with internal waves generated due to wind stress at the ocean surface, although such waves are usually produced at frequencies close to $\omega \approx f$, and are referred to as near-inertial waves (Alford et al. 2016). Internal waves are

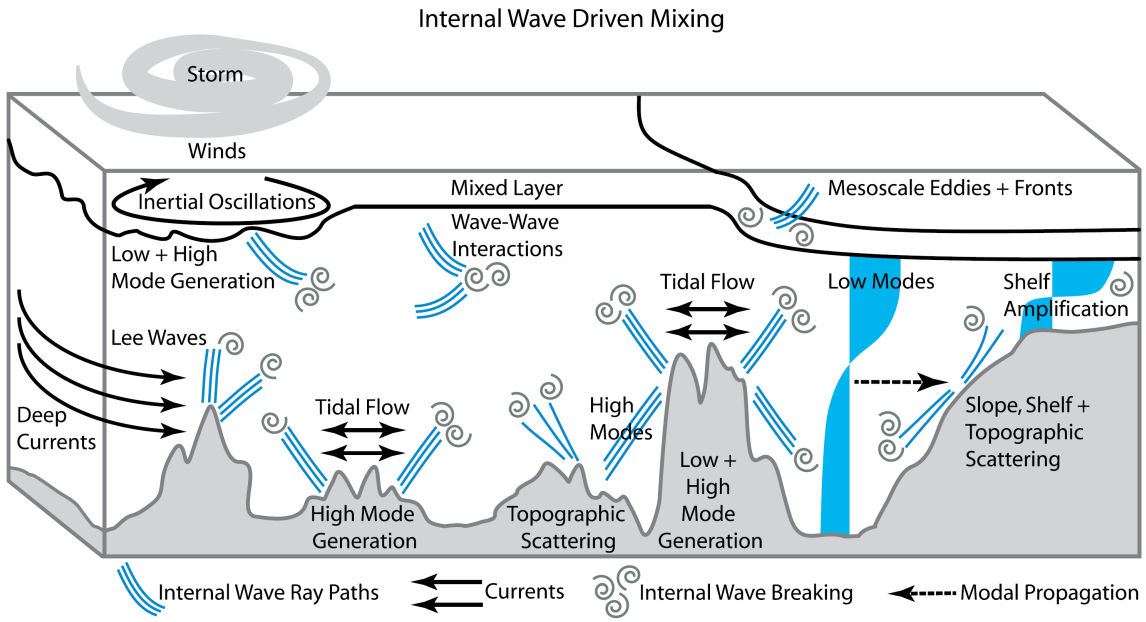

Fig. 1.2 A schematic overview of various ways in which internal waves can form, interact and dissipate in the ocean from MacKinnon et al. (2017). © American Meteorological Society. Used with permission.

not only observed at the frequencies mentioned above. Nonlinear interactions between waves can produce waves at new frequencies, and in the ocean this leads to a continuous spectrum of waves at frequencies between f and N that we will discuss next in §1.2.2.

Patches of turbulence are often associated with the 'breaking' of internal waves on scales of $O(10\,\mathrm{m})$ (e.g. Moum 1996). If waves grow to large amplitude, perhaps through focusing by topography or nonlinear interactions with other waves, they can introduce strong shears in the flow and large changes in the local density gradient. These flow features will then be susceptible to instabilities that cause disturbances to grow, triggering a transition to turbulence. An overview of how internal waves may interact to generate turbulence and mixing in the ocean is presented in figure 1.2. Internal waves at low wavenumbers (associated with large length scales) contain the most energy, but are unlikely to produce strong enough gradients to drive turbulence. To identify the nature of irreversible mixing generated by internal waves it is therefore vital to understand the downscale energy transfer through internal waves and turbulence to dissipation scales.

1.2.2 A spectral perspective

To quantify how the energy of internal waves in the ocean is distributed throughout a range of spatial and temporal scales, we use the concept of a spectrum (or more precisely

a spectral density). An energy spectrum expresses the distribution of energy as a function of wavenumbers $\boldsymbol{k} = (k, l, m)$ and frequency ω, instead of the physical variables of space $\boldsymbol{x}$ and time t. If the Fourier transform of the velocity field $\boldsymbol{u}(\boldsymbol{x}, t)$ is defined to be $\widehat{\boldsymbol{u}}(\boldsymbol{k}, \omega) = \int \boldsymbol{u}(\boldsymbol{x}, t) e^{2\pi i(\boldsymbol{k}\cdot\boldsymbol{x} - \omega t)} \, \mathrm{d}\boldsymbol{x}$, then the kinetic energy spectrum takes the form

$$E(\boldsymbol{k}, \omega) = \frac{1}{2} |\widehat{\boldsymbol{u}}(\boldsymbol{k}, \omega)|^2. \tag{1.12}$$

In the case of internal waves, we can assume the spectrum to be horizontally isotropic since both gravity and the Coriolis vector are aligned with the vertical. The wavenumbers k and l can then be replaced with a horizontal wavenumber $k_h = \sqrt{k^2 + l^2}$ so the spectrum only depends on k_h, m, and ω. Applying the dispersion relation (1.11) allows us to eliminate one more of these variables, and the full internal wave spectrum can then be expressed as a function of just two variables.

Armed with this knowledge, Garrett and Munk (1972) constructed an empirical energy spectrum based on one-dimensional spectra obtained from observations. The distribution of energy associated with internal waves in the open ocean is generally well described by this 'GM spectrum'. The empirical spectrum was subsequently refined by (among others) Munk (1981), and has proved remarkably universal for regions away from ocean boundaries. Although the shape of the spectrum is often the same, its magnitude can vary regionally depending on the total energy contained by the internal wave field. Since energy transfer acts downscale on average within the internal wave field, knowledge of the spectrum can also inform the mean small-scale properties of turbulence and dissipation.

For example, Gregg (1989) compares observed spectra of vertical shear with the GM spectrum to determine regional variation in internal wave energy and then infer regional changes in the mean turbulent dissipation rate ε. This parameterization of ε, as an energy transfer *out of* the wave field, is consistent with the transfer rates of energy *within* the internal wave field outlined by Müller et al. (1986). In their review Müller et al. (1986) propose that, away from scales associated with forcing or dissipation, energy transfers can be well described through resonant wave-wave interactions. Such interactions require at least three waves to be involved, and the waves' frequencies ω_i and wave vectors $\boldsymbol{k}_i$ must satisfy

$$\omega_1 \pm \omega_2 \pm \omega_3 \pm \ldots = 0, \qquad \boldsymbol{k}_1 \pm \boldsymbol{k}_2 \pm \boldsymbol{k}_3 \pm \ldots = 0, \tag{1.13}$$

for resonance to occur. If the waves are resonant then they can exchange energy through the nonlinear advective term in the equations of motion. These interactions are typically

modelled in a weakly nonlinear framework, meaning that only the leading-order nonlinear effects are captured. Waves are considered to be small amplitude in this framework, but not infinitesimal as in the linear case.

Three particular mechanisms are singled out by Müller et al. (1986) as being responsible for wave-wave energy transfers in the ocean's internal wave field: elastic scattering, induced diffusion, and parametric subharmonic instability. Each of these mechanisms are examples of triadic resonance instability, where three waves are involved in the resonant interaction. Elastic scattering describes the reflection of a high frequency internal wave as it interacts with a near-inertial wave of low frequency. Induced diffusion refers to the almost continuous interactions that a high wavenumber wave experiences as it propagates through a larger scale wave field. These interactions lead to behaviour similar to a random walk between nearby values of $\boldsymbol{k}$, and so high wavenumber waves are thought of as 'diffusing' across wavenumber space. Parametric subharmonic instability describes the decay of an internal wave into two waves of approximately half the original wave's frequency. Successive occurences of this resonant interaction leads to an energy transfer towards waves with near-inertial frequencies, and provides a possible pathway for the generation of significant vertical shear (Alford et al. 2016).

More recent work by Polzin and Lvov (2011) approaches the energy transfer problem more generally, by applying the weakly nonlinear 'wave turbulence' framework to the internal wave spectrum. Wave turbulence allows for generic resonant interactions between waves through a statistical mechanics formalism, without prescribing individual mechanisms to model the system as in Müller et al. (1986). A comprehensive overview of this framework can be found in Nazarenko (2011). Polzin and Lvov (2011) also present observations that highlight variability from the GM spectrum depending on geographical location, and call into question some of the assumptions underlying the simpler models of e.g. induced diffusion. The aim of deriving an appropriate internal wave spectrum from 'first principles' remains elusive, but there appears to be a general consensus that at moderate to large scales, energy transfers between internal waves in the ocean can be attributed to weakly nonlinear resonant interactions. The relative importance of wave-vortex interactions (such as those considered by Bühler and McIntyre 2005) at these scales however remains an open question and an active area of research.

At sufficiently small scales, resonant interactions are no longer the dominant mechanism by which energy is transferred and strongly nonlinear interactions between waves, vortices, and mean currents can be important. This coincides with a distinct change in the vertical shear spectrum at a scale of $O(10\,\mathrm{m})$, as seen in the observations of Gargett et al. (1981). We define the vertical shear spectrum similarly to the energy spectrum

(1.12) as

$$\Phi(m) = \left| \widehat{\frac{\partial \boldsymbol{u}}{\partial z}}(m) \right|^2 , \tag{1.14}$$

and if we assume energy is primarily in the horizontal motions, we can link the shear and energy spectra through $\Phi(m) \sim m^2 E(m)$. The spectral shape $\Phi \sim m^{-1}$ at scales smaller than $O(10\,\mathrm{m})$ is commonly attributed to breaking internal waves or 'stratified turbulence'. We can more generally associate energy at these scales with strongly nonlinear motions that remain constrained by buoyancy effects. By taking N^{-1} to be the dominant time scale, and assuming that the vertical length scales of motion scale inversely with m, dimensional analysis suggests that the shear spectrum must take the form $\Phi(m) \sim LT^{-2} \sim N^2 m^{-1}$.

Although the vertical shear spectra are consistent across measurements (see also Gregg et al. 1993), and collapse when appropriately scaled with the buoyancy frequency, they sample flow fields that are highly intermittent, as highlighted for example by Baker and Gibson (1987). In this sense, the concept of breaking internal waves is appealing to describe the generation of this intermittent turbulence from the larger scale wave field. Historically, this interpretation was a subject of intense disagreement between Gregg and Gibson. Whereas Gregg attributed turbulence to breaking internal waves, Gibson favoured the interpretation of Armi (1978) that suggests that patches of turbulence in the ocean interior simply arise through the lateral advection of boundary-driven turbulence.

However the universality of the small scale shear spectrum has led to an alternative interpretation, where the flow at these scales takes the form of a continuously decaying state of "strongly stratified turbulence", sustained by energy transfer from the internal wave field. This regime has recently been highlighted in the oceanographic literature by Kunze (2018), and has long been the subject of intense interest in the wider fluid dynamical community.

1.3 A note on 'strongly stratified turbulence'

In a stably stratified fluid, the act of raising a fluid parcel does work against gravity and requires a supply of energy that is converted to potential energy. Indeed, the exchange between kinetic energy and potential energy is exactly the mechanism behind an internal gravity wave. In the context of turbulence, this energy penalty leads to a fast decay of any eddies with large vertical scales, and explains the anisotropic development of turbulent flows subject to strong stratification. Experimental and numerical work has shown

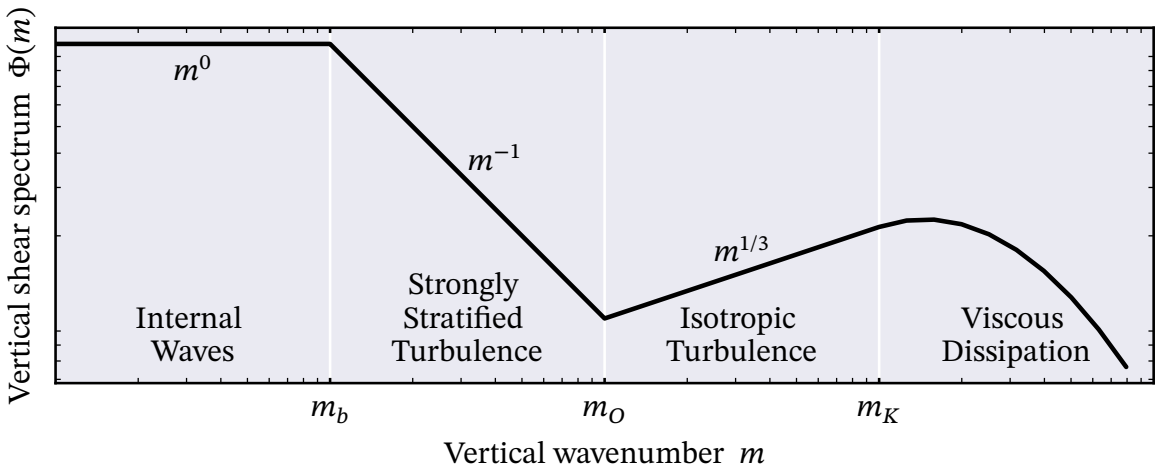

Fig. 1.3 A model spectrum for vertical shear in the ocean. Transitions between regimes are predicted to occur at the buoyancy wavenumber $m_b = N/U_h$, the Ozmidov wavenumber $m_O = (N^3/\varepsilon)^{1/2}$, and the Kolmogorov wavenumber $m_K = (\varepsilon/\nu^3)^{1/4}$.

quasi-horizontal 'pancake eddies' to emerge after a few buoyancy periods in the decay of a turbulent cloud (e.g. Riley and de Bruyn Kops 2003; Maffioli and Davidson 2016).

Riley et al. (1981) performed an early scaling analysis to investigate the dynamics of these anisotropic motions. By separately scaling horizontal length scales with L_h and vertical scales with L_v, they find that the effects of stratification on the flow are determined by two dimensionless flow parameters, the horizontal and vertical Froude numbers:

$$Fr_h = \frac{U_h}{N_0 L_h}, \qquad Fr_v = \frac{U_h}{N_0 L_v}, \tag{1.15}$$

where N_0 is the (constant) buoyancy frequency and U_h is the velocity scale of horizontal motions. In the 'strongly stratified' limit of $Fr_h \ll 1$, Riley et al. (1981) find that the equations become purely two-dimensional at leading order, with vertical velocity and density perturbations fully determined by the horizontal velocity field. Vertical variations in the solutions are possible, but are undetermined in this limit.

Significant progress in understanding the development of vertical scales in strongly stratified flows was made in the work of Billant and Chomaz (2001). Whereas Riley et al. (1981) assumed that $Fr_v \to 0$ as $Fr_h \to 0$, Billant and Chomaz (2001) performed a scaling analysis where the vertical Froude number Fr_v is left as a free parameter. Remarkably the resulting (three-dimensional) equations exhibit self-similarity for the choice of $Fr_v = 1$. This suggests that in a strongly stratified flow where no vertical length scale is externally imposed, say by an obstacle, then vertical variations will emerge on a length

scale of $L_v = U_h/N_0$. The aforementioned experimental and numerical evidence appears to support this hypothesis. Furthermore, this self-similar regime naturally permits an energy spectrum of the form $E(m) \sim N^2 m^{-3}$, consistent with the observed vertical shear spectra of Gargett et al. (1981) mentioned in the previous section.

Billant and Chomaz (2001) only considered their scaling analysis in the inviscid limit, and did not elaborate on the energy transfers one might expect in the strongly stratified regime. With the aid of numerical simulations and further scaling analysis Lindborg (2006) and Brethouwer et al. (2007) confirmed that the energy cascade is downscale in this regime, which is valid on vertical scales larger than the Ozmidov scale $L_O = (\varepsilon/N^3)^{1/2}$. At smaller scales, the turbulent velocity field becomes close to isotropic since the stratification is relatively weak. The range of scales in this isotropic regime is determined by the buoyancy Reynolds number, since $Re_b = \varepsilon/\nu N^2 = (L_O/L_K)^{4/3}$ where $L_K = (\nu^3/\varepsilon)^{1/4}$ is the Kolmogorov scale at which viscous effects dissipate turbulence.

Gregg et al. (2018) state that a wide range of buoyancy Reynolds numbers can be appropriate in the ocean ($20 \lesssim Re_b \lesssim 10^5$), with typical 'background' levels associated with a GM spectrum of internal waves being $Re_b \lesssim 200$. High values of Re_b, even intermittently, can however produce large contributions to mixing. This can be seen by rewriting (1.6) as

$$K_T = \Gamma Pr Re_b \kappa, \tag{1.16}$$

where, as above, κ is the molecular diffusivity of heat. With Pr and κ constant, high values of Re_b therefore lead to high values of the turbulent diffusivity. Accurately capturing the mixing associated with intermittent high Re_b patches in large-scale models is therefore vital, and requires a physical understanding of how such patches may occur.

It remains a significant challenge to connect the typical observed energy or vertical shear spectrum, shown in figure 1.3, with physical mechanisms driving the energy transfer. Kunze (2018) hypothesises that energy cascades downscale through the 'strongly stratified' regime, and that this regime is sustained through the anisotropic instability of near-inertial waves. An alternative hypothesis comes from the 'fossil turbulence' approach of Gibson (1986). In that framework the $\Phi \sim m^{-1}$ scaling is indicative of the anisotropic motions formed during the decay of a previously energetic turbulent event. It remains unclear how best to interpret the transition between internal waves and strongly nonlinear motions in the ocean, which makes applying results from laboratory experiments and turbulence simulations to the field particularly challenging.

1.4 Modelling small-scale mixing in the ocean: the appropriate equations of motion

Regardless of the physical mechanisms at play, it is clear that a large dynamical range of scales is important between the breakdown of internal waves and the viscous dissipation of turbulence. In this thesis, we are primarily interested in how the motions on these scales affect mixing and other significant energy transfers. Direct numerical simulation (DNS) is best suited to tackling this problem. Since DNS involves accurately resolving the flow down to dissipative scales, it can provide a detailed picture of small-scale motion. It is computationally expensive, however the ongoing development of efficient algorithms to take advantage of recent progress in parallel computing means that problems with a wide range of scales, such as turbulent mixing, are now tractable.

Of course, we cannot resolve the smallest scales of motion while simulating an entire ocean basin. For example simulating the volume of the Atlantic Ocean (from Eakins and Sharman 2010) with a grid spacing of 1 cm would require a computational domain of approximately 3×10^{23} grid points! By restricting the size of our domain and solely focusing on the small scales associated with turbulence and mixing, we do not need to account for all types of motion found in the ocean, and we can make some simplifying assumptions.

Since the Coriolis frequency f is smaller than the buoyancy frequency N throughout the ocean, effects due to the Earth's rotation become important on longer time scales than buoyancy effects. Rotation plays an important role in the generation and propagation of phenomena such as near-inertial waves that can lead to turbulence. However this turbulence is triggered through the development of strong vertical shears, which themselves have a far shorter time scale than rotation. This is equivalent to saying that the Rossby number $Ro \equiv U/fL$ associated with such small-scale motions is large, and that inertial terms dominate those associated with rotation. We shall therefore neglect the effect of rotation in our simulations.

We now outline the appropriate system of equations for investigating turbulent mixing relevant to the stratified ocean interior. As well as excluding background rotation from the system, we justify a number of further assumptions relating to the Boussinesq approximation in the following derivation. We then nondimensionalise the equations and discuss the most appropriate values of the resulting dimenisonless parameters in the context of small-scale ocean dynamics.

The Boussinesq approximation

We start with the classical Navier–Stokes equations, representing conservation of mass and momentum for a fluid of density ρ and dynamic viscosity μ

$$\frac{\partial \rho}{\partial t} + \boldsymbol{\nabla} \cdot (\rho \boldsymbol{u}) = 0, \tag{1.17}$$

$$\rho \left(\frac{\partial \boldsymbol{u}}{\partial t} + (\boldsymbol{u} \cdot \boldsymbol{\nabla}) \boldsymbol{u} \right) = -\boldsymbol{\nabla} p + \mu \nabla^2 \boldsymbol{u} - \rho g \hat{\boldsymbol{z}}, \tag{1.18}$$

where $\boldsymbol{u}$ is the flow velocity and p is the pressure. We can rewrite the mass conservation equation as

$$\frac{\partial \rho}{\partial t} + (\boldsymbol{u} \cdot \boldsymbol{\nabla}) \rho = -\rho \, (\boldsymbol{\nabla} \cdot \boldsymbol{u}) \, . \tag{1.19}$$

Assuming that changes in density are small compared with the mean density of the fluid, we can write the density as $\rho = \rho_0 + \rho'$ where $\rho' \ll \rho_0$. This is known as the Boussinesq approximation and leads to the following form for the mass conservation equation

$$\frac{\partial \rho'}{\partial t} + (\boldsymbol{u} \cdot \boldsymbol{\nabla}) \rho' = - (\rho_0 + \rho') (\boldsymbol{\nabla} \cdot \boldsymbol{u}) \approx -\rho_0 (\boldsymbol{\nabla} \cdot \boldsymbol{u}) \, , \tag{1.20}$$

$$\Rightarrow \boldsymbol{\nabla} \cdot \boldsymbol{u} = 0, \tag{1.21}$$

at leading order in ρ'. Applying the same density decomposition to the momentum equation gives

$$\rho_0 \left(\frac{\partial \boldsymbol{u}}{\partial t} + (\boldsymbol{u} \cdot \boldsymbol{\nabla}) \boldsymbol{u} \right) = -\boldsymbol{\nabla} p^* + \mu \nabla^2 \boldsymbol{u} - g \rho' \hat{\boldsymbol{z}}, \tag{1.22}$$

where the hydrostatic part of the gravitational term has been absorbed into the new pressure variable $p^* = p + \rho_0 g z$, and we have neglected any effect of the density perturbation on the inertia. The equations of motion (1.21) and (1.22) consist of four equations for five unknowns, namely the three components of velocity $\boldsymbol{u} = (u, v, w)$, the density perturbation ρ', and the pressure p^*. We therefore need another equation to close the system. This comes from assuming a linear equation of state for the density, and assuming that the density only depends on a single scalar, e.g. temperature or salinity.

In the ocean the density of seawater is determined by both temperature and salinity, and these two scalars have molecular diffusion rates that differ by two orders of magnitude. The difference in diffusivities can lead to peculiar dynamics through what are known as 'double diffusive' processes, as thoroughly reviewed by Radko (2013) and Garaud (2018). Although these processes are known to be important for mixing in polar regions (see for example Shibley et al. 2017), their role in open ocean dynamics more

generally is less well constrained. In many locations, the ocean is primarily stratified by only one of temperature or salinity and our single scalar approximation is likely to be appropriate. McDougall (1987) highlights further complexity arising in the case of a nonlinear equation of state, although the resulting processes are again most consequential where the density changes are related to variations in multiple scalar fields.

Assuming our single scalar to be temperature, we take $\rho' = -\alpha T'$ where α is a constant thermal expansion coefficient, and assume that the temperature perturbation T' satisfies an advection-diffusion equation

$$\frac{\partial T'}{\partial t} + (\boldsymbol{u} \cdot \boldsymbol{\nabla})\, T' = \kappa \nabla^2 T', \tag{1.23}$$

where κ is the molecular diffusivity of heat. The linear equation of state then allows us to rewrite this as an equation for the density perturbation:

$$\frac{\partial \rho'}{\partial t} + (\boldsymbol{u} \cdot \boldsymbol{\nabla})\, \rho' = \kappa \nabla^2 \rho'. \tag{1.24}$$

At first, it is unclear how the diffusive term in this equation relates to the original form of the mass conservation equation in (1.20). Spiegel and Veronis (1960) show that despite this discrepancy, given our previous assumptions, it is thermodynamically consistent to solve the advection-diffusion equation in conjunction with the incompressible form of mass conservation given in (1.21). Importantly, we must assume that any density fluctuations due to local variations in pressure are negligible for (1.24) to be valid. Indeed under the Boussinesq approximation, the pressure is entirely determined by the velocity field, and acts as a Lagrange multiplier to enforce (1.21).

It is common to replace the density perturbation in the above equations with the buoyancy $b = -g\rho'/\rho_0$, that is the force per unit mass associated with the gravitational effect on the fluid. Dividing (1.22) through by ρ_0, we arrive at the Boussinesq equations:

$$\boldsymbol{\nabla} \cdot \boldsymbol{u} = 0, \tag{1.25}$$

$$\frac{\partial \boldsymbol{u}}{\partial t} + (\boldsymbol{u} \cdot \boldsymbol{\nabla})\, \boldsymbol{u} = -\frac{1}{\rho_0} \boldsymbol{\nabla} p^* + \nu \nabla^2 \boldsymbol{u} + b\hat{\boldsymbol{z}}, \tag{1.26}$$

$$\frac{\partial b}{\partial t} + (\boldsymbol{u} \cdot \boldsymbol{\nabla})\, b = \kappa \nabla^2 b, \tag{1.27}$$

where $\nu = \mu/\rho_0$ is the kinematic viscosity.

Nondimensionalising the Navier–Stokes equations

It is useful to nondimensionalise the equations and identify the key parameters that determine the dynamics in this system. We therefore introduce the dimensionless variables

$$\widehat{\boldsymbol{x}} = \frac{\boldsymbol{x}}{L_0}, \qquad \widehat{\boldsymbol{u}} = \frac{\boldsymbol{u}}{U_0}, \qquad \hat{b} = \frac{b}{B_0} = \frac{b\rho_0}{g\Delta\rho}, \tag{1.28}$$

where L_0, U_0 and $\Delta\rho$ are typical scales of length, velocity, and density variations respectively. We scale time with the advective time scale, and choose a pressure scale to balance the scaling of the inertial terms such that

$$\hat{t} = \frac{t}{T_0} = \frac{tU_0}{L_0}, \qquad \widehat{p} = \frac{p^*}{P_0} = \frac{p^*}{\rho_0 {U_0}^2}. \tag{1.29}$$

Substituting these variables into the dimensional system gives the Boussinesq equations in dimensionless form

$$\widehat{\boldsymbol{\nabla}} \cdot \widehat{\boldsymbol{u}} = 0, \tag{1.30}$$

$$\frac{\partial \widehat{\boldsymbol{u}}}{\partial \hat{t}} + \left(\widehat{\boldsymbol{u}} \cdot \widehat{\boldsymbol{\nabla}}\right)\widehat{\boldsymbol{u}} = -\widehat{\boldsymbol{\nabla}}\widehat{p} + \frac{1}{Re}\widehat{\nabla}^2\widehat{\boldsymbol{u}} + Ri_0\hat{b}\hat{\boldsymbol{z}}, \tag{1.31}$$

$$\frac{\partial \hat{b}}{\partial \hat{t}} + \left(\widehat{\boldsymbol{u}} \cdot \widehat{\boldsymbol{\nabla}}\right)\hat{b} = \frac{1}{RePr}\widehat{\nabla}^2\hat{b}. \tag{1.32}$$

It is now apparent that the system only depends on three dimensionless parameters: the Reynolds number, Prandtl number, and bulk Richardson number

$$Re = \frac{L_0U_0}{\nu}, \qquad Pr = \frac{\nu}{\kappa}, \qquad Ri_0 = \frac{g\Delta\rho L_0}{{U_0}^2}. \tag{1.33}$$

A scale for the typical buoyancy frequency can be obtained by combining the length and buoyancy scales from (1.28) such that $N_0^2 = g\Delta\rho/\rho_0 L_0$. This reveals that the bulk Richardson number can be expressed in terms of a bulk Froude number $Fr_0 = U_0/N_0L_0$ (defined similarly to those discussed in §1.3) as $Ri_0 = Fr_0^{-2}$. We are primarily interested in flows where $Ri_0 = O(1)$, such that the inertia and buoyancy are both important in determining the dynamics of the flow.

Implications for numerical simulation of oceanographically relevant flows

Since the kinematic viscosity of water is $1 \times 10^{-6}\,\mathrm{m^2\,s^{-1}}$, flows on metre-scales and larger in the ocean can be considered as large Re. Viscosity is important for dissipating energy at very small scales, but does not directly affect the larger scale flow when Re is large. High Re flows are computationally expensive for DNS since they require the resolution of a wide range of length scales. Pope (2000) suggests that accurate simulation of a turbulent flow is possible if the grid spacing is within a factor of two of the Kolmogorov length scale L_K. When also calculating a diffusive scalar, such as our buoyancy field from (1.32), a similar rule can be applied for the Batchelor scale L_B. In our dimensionless system, the Kolmogorov and Batchelor scales are given by

$$\frac{L_K}{L_0} = \left(Re^3\hat{\varepsilon}\right)^{-1/4}, \qquad \frac{L_B}{L_0} = \left(Re^3Pr^2\hat{\varepsilon}\right)^{-1/4}, \tag{1.34}$$

where $\hat{\varepsilon}$ is the TKE dissipation rate (divided by the inertial scaling U_0^3/L_0).

These expressions suggest that an accurate three-dimensional simulation of a turbulent flow requires a volume containing $O(Re^{9/4}Pr^{3/2})$ grid points for the scalar field. We wish to keep Re as large as possible so that we can observe the interplay between stratification and turbulence over a wide range of scales. In light of limited computational resources, we therefore restrict all our simulations to $Pr = 1$. This is smaller than the true values for heat in water ($Pr \approx 7$) or for salt in water ($Pr \approx 700$). Recent numerical studies have highlighted varying impacts on mixing from increases in the Prandtl number, either in decreasing mixing efficiency associated with Kelvin–Helmholtz instability (Salehipour et al. 2015), or in subtle changes to the near-wall structure of buoyancy in stratified plane Couette flow (Zhou et al. 2017). Throughout this thesis, we shall discuss how the restriction of $Pr = 1$ may affect the results of our simulations, and whether this leaves open questions for future research.

All of the simulations performed as part of this thesis use DIABLO, originally developed by Taylor (2008) and Bewley (2010). The software is MPI parallelised, and uses highly efficient pseudospectral methods and fast Fourier transforms to compute spatial derivatives. Time stepping is achieved through the combination of an explicit third-order Runge–Kutta scheme and a Crank–Nicolson scheme. As part of this thesis, the implementation of the HDF5 data format for I/O in the code has been significantly extended, resulting in more effective data storage for easier post-processing.

1.5 Problems in turbulent stratified mixing addressed by this thesis

The remainder of this thesis consists of a set of investigations into various stratified flows. As discussed above, a wide range of possible mechanisms exist for the generation of turbulence in the ocean, and we therefore choose not to focus continuously on a single 'model' of ocean turbulence. Indeed a key theme of this thesis is investigating how different dynamics associated with vertical shear and internal waves may affect the small-scale properties of turbulence and mixing. We now provide a brief outline of the problems considered in the forthcoming chapters, and how they connect to the more general discussion of ocean mixing presented above.

Kelvin–Helmholtz instability and marginal stability

As mentioned above in §1.1, stratified shear layers have frequently been used as a relatively simple setup that is still representative of wave breaking at small scales in the ocean. Smyth and Moum (2012) provide a readable overview of the linear Kelvin–Helmholtz instability that arises in such flows and its relevance to ocean mixing. In this system, where the maximum vertical shear coincides with the largest buoyancy gradient, the linear stability of the flow is determined by the gradient Richardson number Ri_g. The theorem of Miles (1961) and Howard (1961) tells us that the flow must be linearly stable if $Ri_g > 1/4$.

Observational studies of strongly sheared ocean flows by Thorpe and Liu (2009) and Smyth and Moum (2013) have invoked the linear stability boundary as a threshold for determining the growth or decay of naturally occuring, fully nonlinear turbulent flows. In chapter 2, we perform two-dimensional DNS of a stratified shear layer for various values of Ri_g. By simulating the nonlinear saturation of the linear instability as $Ri_g \to 1/4$, we investigate the connection between linear stability theory and the nonlinear dynamics required to push the flow towards a state of 'marginal stability' at $Ri_g = 1/4$.

Turbulent stratified flows sustained by large-scale forcing

The regime of 'strongly stratified turbulence' discussed in §1.3 has been difficult to observe consistently in laboratory experiments and numerical simulations since the decay of turbulence in a stratified fluid is an inherently transient process. To obtain greater insight into the energy transfers in stratified turbulent flows, it has become common practice to add large-scale forcing to the equations of motion as in, e.g., Smith and Wal-

effe (2002), Laval et al. (2003), and Waite and Bartello (2004). This supplies energy at large scales that can sustain the flow in a statistically steady state, feeding the dissipative scales through a downscale cascade.

However such forcing is rarely motivated by the picture described by figure 1.3, where energy is supplied downscale from the internal wave field to the scales relevant for stratified turbulence. Random forcing of vortical modes is often applied, with the aim of not introducing large-scale coherent structures into the flow. Although this is useful for drawing general conclusions about the interplay of turbulence and stable stratification, the observational energy spectra suggest that internal waves play an important role at the largest scales of stratified turbulence in the ocean.

In chapter 3 we perform high resolution, three-dimensional simulations of forced turbulence in a triply-periodic domain subject to a constant mean stratification. We compare the random vortical forcing of Maffioli (2017) with two novel large-scale forcing methods that provide energy through resonant internal gravity waves. The initial condition of the simulations is motivated by the Garrett–Munk internal wave spectrum to provide a background state somewhat representative of the ocean interior. We focus on how changing the large scale forcing affects the small-scale mixing properties. By identifying local correlations between various quantities, we investigate how the mixing efficiency varies both locally and between the simulations. We also apply wavelets to extract local energy spectra that showcase multiple regimes, even when scale separation is small on average.

Breaking mechanisms of a sheared internal gravity wave

Although turbulence continuously forced by internal gravity waves at large scales provides comprehensive statistics of mixing, the continuous transfer of energy across multiple scales makes identifying important physical mechanisms difficult. We therefore return to a conceptually simpler setup in chapter 4 by considering the flow arising from the superposition of a sinusoidal shear flow and a plane internal gravity wave.

We are motivated to study this flow not just due to its simplicity, but also by the detailed thermocline observations of Alford and Pinkel (2000). On scales of $O(10\,\mathrm{m})$, they find wave breaking events in regions where varying vertical shear (most likely due to a near-inertial wave) and large amplitude internal gravity waves coexist. The interaction of small-amplitude internal waves and vertical shear has been studied since the early work of Bretherton (1966) and Booker and Bretherton (1967) that predicted the development of critical levels where the mean flow matches the horizontal phase velocity of the waves, leading to a focusing of internal wave energy. We compare the linear the-

ory developed in those studies to simulations of large amplitude waves, and investigate whether the physical intuition of wave refraction remains relevant in the nonlinear case. As an internal gravity wave is focused by a shear flow, it steepens and becomes susceptible to both shear and convective instabilities. We determine the relative importance of these instabilities for the breakdown of the wave and for the ensuing turbulent mixing. The end state of the simulation arises from a complex three-way interaction of the mean shear flow, the internal gravity wave, and the turbulence produced. By analysing the energetics of the wave breaking event, we determine the respective roles of the buoyancy flux, turbulent shear production, and the wave-mean flow interaction in modifying the flow field.

Accurate quantification of diapycnal mixing in numerical simulations

The use of triply-periodic domains in the simulations of chapters 3 and 4 permits the use of efficient numerical methods and allows for the continuous propagation of waves. However, consistently quantifying potential energy in a vertically periodic domain with a mean, imposed stratification is not straightforward. This has significant consequences for accurately quantifying diapycnal mixing in these simulations.

Winters et al. (1995) provide a rigorous method for calculating diapycnal mixing in a stratified fluid through the destruction of available potential energy (APE). In chapter 5 we highlight how ambiguity can arise in applying this method to stratified flows in a triply-periodic domain. We propose a new technique that ensures the consistent definition of a background buoyancy profile in such a system, and is consistent with the definition of a local APE density by Scotti and White (2014). We reanalyse the simulations of chapters 3 and 4, quantifying the true rates of diapycnal mixing and diapycnal diffusivity. The mixing estimates made in the previous chapters (and in many previous studies that use similar domains) are analogous to applying the method of Osborn and Cox (1972), used to infer mixing from small-scale temperature probes. We determine the accuracy of this estimate for the flows we have considered, and discuss possible implications for ocean microstructure measurements.

The findings of this thesis are finally summarised in chapter 6, where a personal outlook is also presented on the future of research into stratified turbulence and diapycnal mixing in the ocean.

Chapter 2

Nonlinear 2-D saturation of Kelvin–Helmholtz billows

In this chapter, we investigate the energetics associated with the nonlinear development of Kelvin–Helmholtz instability in a stratified shear layer. Motivated by studies applying the linear concept of marginal stability to nonlinear flows, we investigate how the 'billow' state of maximum energy changes with the minimum Richardson number in the flow Ri_m. We focus particularly on how growth to this state is modified as Ri_m tends to the 'marginal' value of 1/4.

This chapter covers work that was published in Howland, C. J. et al. (2018), "Testing linear marginal stability in stratified shear layers", *J. Fluid Mech.* 839: R4. We briefly outline relevant recent developments since the publication of this work at the end of the chapter.

2.1 Stratified shear instabilities, transition to turbulence, and 'marginal stability'

As discussed in chapter 1, parameterizing small-scale turbulent quantities in global circulation models is necessary to provide an accurate description of the physical processes driving the circulation (Ivey et al. 2008). Since turbulence in the atmosphere and oceans is intermittent in time and inhomogeneous in space (Baker and Gibson 1987), this is an intensely challenging task. One conventional avenue of research has been the consideration of flow instabilities, as they naturally are mechanisms by which disordered motions can arise from a laminar flow. A very commonly considered instability-mediated route to turbulence is via the so-called Kelvin–Helmholtz instability (KHI) (or perhaps

more appropriately 'stratified Rayleigh instability'). This normal-mode instability develops in stably stratified shear flows with inflectional background profiles of velocity and density (or equivalently buoyancy) when the destabilising effect of the shear is sufficiently strong to overcome the stabilising effect of the stratification for infinitesimal perturbations. The finite amplitude manifestation of the KHI takes the form of elliptical vortices or 'billows', which have been observed in multiple oceanic circumstances (Smyth and Moum 2012), including in the thermocline (Woods 1968), the abyssal ocean (van Haren and Gostiaux 2010), and above continental shelves (Moum et al. 2003). Many laboratory experiments and numerical simulations have been performed to investigate the initiation, development and breakdown of KHI (Thorpe 1973; Fernando 1991; Klaassen and Peltier 1985; Peltier and Caulfield 2003), which are known to be prone, particularly for sufficiently large Reynolds numbers, to a large 'zoo' of secondary instabilities (Mashayek and Peltier 2012*a*).

From consideration of the Taylor–Goldstein equation (Taylor 1931; Goldstein 1931), it is possible to derive the influential 'Miles–Howard' criterion (Miles 1961; Howard 1961), which states that a sufficient condition for linear stability of an inviscid, incompressible, stably stratified shear flow defined by a (laminar) steady parallel velocity profile $\overline{U}(z)$, and buoyancy frequency $N(z) = \sqrt{-\frac{g}{\overline{\rho}}\frac{d\overline{\rho}}{dz}}$ is that the gradient Richardson number $Ri_g(z) \geq 1/4$ *everywhere* in the flow, where

$$Ri_g(z) = \frac{N^2}{\left(d\overline{U}/dz\right)^2}. \tag{2.1}$$

Thorpe and Liu (2009) applied this criterion to develop the concept of 'marginal instability' to interpret and predict the existence of a range of naturally occurring stably stratified *turbulent* flows. In this particular context, the marginal instability of a flow is quantified by a parameter Φ, which is the fractional change in flow speed required to ensure linear stability of the flow. By applying the critical value of $Ri_c = 1/4$ to this idea, Φ satisfies

$$(1 + \Phi)^2 = 4Ri, \tag{2.2}$$

where Ri is some characteristic value of the gradient Richardson number Ri_g, typically its minimum Ri_m. A flow is then said to be marginally unstable if it is in a linearly unstable state (so $Ri < 1/4$ and hence $\Phi < 0$) and the fractional change is small compared to unity ($|\Phi| \ll 1$).

It is important to distinguish between this particular meaning of 'marginal stability', based around the concept of *linear* normal-mode instabilities growing and ulti-

mately *triggering* turbulence, and an alternative meaning based around the concept of inherently *nonlinear* processes *maintaining* turbulence for sufficiently low values of a Richardson number defined in terms of the mean profiles of velocity and density. Smyth and Moum (2013) discuss applying the 'linear' marginal instability concept as proposed by Thorpe and Liu (2009) to turbulent flows, but also provide an alternative to the latter's linear stability arguments, to explain observations of deep cycle turbulence with a Richardson number close to 1/4. They use the results of Rohr et al. (1988) which show growth and decay of stratified turbulence below and above $Ri = 1/4$ respectively, effectively thus applying the 'nonlinear' marginal stability concept to the maintenance of turbulence. In a distinct (although somewhat related) approach, Thorpe et al. (2013) add an eddy viscosity and eddy diffusivity to the Taylor–Goldstein equation to modify the critical Richardson number in the Miles–Howard criterion. These added diffusive effects model a key property of a weakly turbulent background flow, but this approach is still based around appealing to linear instability processes with (an appropriate) Ri close to the Miles–Howard criterion as the mechanism by which perturbations can grow to sufficiently large amplitude to maintain the turbulence. Indeed, since any small perturbation will be modified by small-scale turbulence in such a flow, the validity of performing linear stability analysis in this regime is at least formally questionable, especially if the predicted growth rate is small. Despite this, they claim that applying the concept of marginal instability to such flows may explain the behaviour of shear layers after KHI breakdown.

For inviscid flows susceptible to KHI, as Ri_m approaches 1/4 from below, the exponential growth rate of the linear instabilities is predicted to drop to zero (Hazel 1972). However, this prediction does not in itself preclude the possibility that the finite amplitude 'billow' can still have significant amplitude for flows with such 'marginal' Richardson numbers, particularly in light of the results of Kaminski et al. (2017). Using a direct-adjoint-looping method, they demonstrated that billow-like structures with nontrivial amplitude can still be triggered by 'linear optimal' perturbations of small initial perturbation energy (i.e. non-normal perturbations with a structure which exhibits maximum transient perturbation energy growth over a finite time interval) in flows where $Ri_g > 1/4$ everywhere initially. However, the classical Miles–Howard criterion cited in the linear marginal stability arguments does not apply to these non-normal perturbations, and so we focus our study on normal-mode perturbations. Despite all these caveats, it is still at least conceivable that a billow could reach large amplitude at very late times for a marginally unstable flow.

Our principal aim here is to investigate whether marginal instability, in the above-discussed sense of being based around linear stability arguments for the triggering of, rather than the maintenance of pre-existing turbulence, is useful in describing transitional flows, with finite, yet large Reynolds number $U_0 d_0/\nu$, where ν is the kinematic viscosity, d_0 is the shear-layer half-depth, and U_0 is half the velocity difference across the shear layer. For simplicity, we restrict attention to flows with $Pr = \nu/\kappa = 1$, where κ is the density diffusivity. We are particularly focused on determining whether saturated billows of nontrivial amplitude can develop in such flows perturbed by normal-mode perturbations associated with the classical KHI in flows where $Ri_m \simeq 1/4$. Since the growth rate of such instabilities gets very small as Ri_m approaches 1/4 from below, we consider three classes of flows: class 'D' where the background distributions of velocity and density diffuse naturally (thus modifying and increasing $Ri_g(z)$ with time); class 'S' with imposed body forces designed to maintain 'steady' background distributions (and hence Ri_g remains close to constant in time); and class 'A' where U_0 increases exponentially with time so that Ri_m can decrease through 1/4. In particular, this last class allows us to test the viability of 'marginally unstable' flows to develop perturbation billows of significant amplitude. We are principally interested in the viability of the marginal instability/stability concepts as mechanisms to drive or trigger self-limiting turbulent flows, and so we are only interested in identifying the maximum amplitude (and the time at which this occurs) of the billows. Therefore, we restrict our numerical calculations to two dimensions, precluding any consideration of subsequent secondary instabilities, or indeed the ensuing turbulent break down and associated irreversible mixing. (As we discuss below, our observed initial maximum amplitudes of inherently two-dimensional KHI billows are consistent with the three-dimensional simulation results of Mashayek et al. (2013), giving us confidence that our two-dimensional calculations yield useful estimates for the amount of energy which can be transiently stored in a billow, and thus be ultimately available to drive turbulent motions.) The rest of the paper is organised as follows. In section 2.2, we describe our numerical model, the choice of domain and initial conditions. In section 2.3, we describe the particular characteristics of the three qualitatively different classes of flows we consider, and analyse the results of the simulations of each of these three different classes, identifying the key parameters controlling perturbation growth. Finally, we discuss the implications of our findings in section 2.4, particularly regarding the viability of the linear marginal (in)stability concepts as predictors of energetic turbulence and mixing in stratified shear flows.

2.2 Simulation Setup

We are interested in flows susceptible to primary instabilities of Kelvin-Helmholtz type, and so we consider dimensional (marked with an asterisk) background velocity $\overline{U}^*(z^*)$ and buoyancy $\overline{B}^*(z^*) = g^*(\rho_a^* - \overline{\rho}^*)/\rho_a^*$ distributions

$$\overline{U}^*(z^*) = U_0^* \tanh(z^*/d_0), \quad \overline{B}^*(z^*) = (g^*\rho_0^*/\rho_a^*)\tanh(z^*/d_0^*) = B_0^* \tanh(z^*/d_0^*), \quad (2.3)$$

where g^* is the acceleration due to gravity, ρ_a^* is a reference density, and the Boussinesq approximation applies so that $\rho_0^* \ll \rho_a^*$. We perform two-dimensional direct numerical simulations using the DIABLO software (Taylor 2008), which implements a combination of explicit third-order Runge–Kutta and implicit Crank–Nicholson schemes. The code solves the two-dimensional Boussinesq equations for the non-dimensional velocity, buoyancy and pressure fields $\boldsymbol{u} = (u, w)$, b and p:

$$\boldsymbol{\nabla} \cdot \boldsymbol{u} = 0, \quad (2.4a)$$

$$\frac{\partial \boldsymbol{u}}{\partial t} + (\boldsymbol{u} \cdot \boldsymbol{\nabla})\,\boldsymbol{u} = -\boldsymbol{\nabla} p + \frac{1}{Re}\nabla^2 \boldsymbol{u} + Ri_0 b\hat{\boldsymbol{z}}, \quad (2.4b)$$

$$\frac{\partial b}{\partial t} + (\boldsymbol{u} \cdot \boldsymbol{\nabla})\, b = \frac{1}{RePr}\nabla^2 b. \quad (2.4c)$$

Nondimensional variables are defined as $\boldsymbol{u} = \boldsymbol{u}^*/U_0^*$, $b = b^*/B_0^*$, $\boldsymbol{x} = \boldsymbol{x}^*/d_0^*$, and $t = t^*/(d_0^*/U_0^*)$. The key parameters are the Reynolds number $Re = U_0^* d_0^*/\nu^*$, the Prandtl number $Pr = \nu^*/\kappa^*$ (here $Pr = 1$), and the bulk Richardson number $Ri_0 = B_0^* d_0^*/{U_0^*}^2$.

The computational domain is 20 non-dimensional units in the vertical (z) direction and free-slip, no flux boundary conditions are imposed at $z = \pm 10$. This prevents boundary effects from interfering with the shear layer in the centre of the domain. Periodicity is imposed in the streamwise (x) direction and we choose the length of the domain to be the wavelength of the most unstable normal mode for each simulation. The initial nondimensional background profiles are hence $U(z) = B(z) = \tanh(z)$, which ensures that the gradient Richardson number

$$Ri_g(z) = Ri_0 \frac{dB/dz}{(dU/dz)^2} = Ri_0 \cosh^2 z \rightarrow Ri_m = Ri_g(0) = Ri_0, \quad (2.5)$$

where Ri_m is the minimum, occurring at the midpoint of the shear layer $z = 0$. These background profiles are perturbed by the fastest growing normal-mode perturbations $\boldsymbol{u}'$

Table 2.1 Parameters for numerical simulations. The number of grid points in each direction are N_x and N_z, which are varied with Re and Ri_0 to ensure accurate flow simulation.

Group	Class	Re	Ri_0	N_x	N_z	E_0
D1	D: diffusive	1000	0, 0.05, 0.1, 0.15, 0.2	215 - 230	321	10^{-6}
D2	D: diffusive	2000	0, 0.05, 0.1, 0.15, 0.2	322 - 342	481	10^{-6}
D3	D: diffusive	4000	0, 0.05, 0.1, 0.15, 0.2	429 - 456	641	10^{-6}
D4	D: diffusive	6000	0, 0.05, 0.1, 0.15, 0.2	644 - 683	961	10^{-6}
S	S: steady	4000	0 - 0.245	609 - 683	961	10^{-5}
A	A: accelerating	4000	0.26	609	961	10^{-6}

and b', giving the following initial conditions:

$$\boldsymbol{u}|_{t=0} = U(z)\widehat{\boldsymbol{x}} + \epsilon\boldsymbol{u}', \qquad b|_{t=0} = B(z) + \epsilon b'. \tag{2.6}$$

We calculate the normal modes using a matrix method code originally developed by Smyth and Peltier (1990), which implements a finite Re/Pr generalisation of the Taylor–Goldstein equation (or equivalently a stratified generalisation of the Orr–Sommerfeld equation). The amplitude of the normal-mode perturbation is chosen such that an appropriate measure of the initial perturbation 'energy', defined in Kaminski et al. (2014) as

$$E = \frac{1}{2}\langle \boldsymbol{u}', \boldsymbol{u}' \rangle + \frac{Ri_0}{2}\langle b', b' \rangle = K + P, \tag{2.7}$$

is equal to a prescribed value E_0. (As our background buoyancy distribution has non-uniform gradient, this does not correspond precisely to the sum of the perturbation kinetic energy and perturbation potential energy, but we use this measure for computational convenience and consistency with the previous study of Kaminski et al. 2014.) We use the inner product $\langle \boldsymbol{u}, \boldsymbol{v} \rangle = 1/A \int_A \boldsymbol{u} \cdot \boldsymbol{v}\, \mathrm{d}x\, \mathrm{d}z$, where A is the area of the domain. Table 2.1 lists the range of parameters used.

By taking $\boldsymbol{u}'$ and b' to be the perturbations to the initial background hyperbolic tangent profiles, we can measure the perturbation energy defined in (2.7) throughout the development of the shear layer. At early times, the perturbation energy grows exponentially as predicted by linear stability analysis. Growth of the normal mode causes redistribution of vorticity in the shear layer, which leads to a roll-up of the shear layer (Corcos and Sherman 1976). This produces vortex-like 'core' or 'billow' regions joined by thin 'braid' structures. Fluid is entrained into the core from both sides of the shear layer, with baroclinic torques intensifying the vorticity in the braid (and elsewhere) when the

flow is stratified. Soon after the roll-up, perturbation energy peaks as the primary KHI reaches its 'saturation point', which we characterise both by the maximum value of the perturbation energy, $E_{\max}$ and the time at which this occurs, $t_{\max}$.

This is the first step in the turbulent transition of a stratified shear layer (Caulfield and Peltier 2000). In the ocean such a shear layer may develop through the instability of a larger-scale structure such as an internal wave, but for this simplified setup we treat KHI as the primary instability. Mashayek and Peltier (2012*a*) showed that a large range of secondary instabilities can develop once the saturation point has been reached, and indeed, depending on the initial perturbation structure, various merging instabilities, where one billow engulfs or drains its neighbour, can occur before saturation. Such merging events however, are suppressed at high Re by the other secondary instabilities, justifying our choice of one wavelength for the length of the domain (Mashayek and Peltier 2013). These secondary instabilities are typically three-dimensional in nature, and the subsequent energy cascade cannot be realistically modelled by two-dimensional simulations. We therefore restrict our investigation to the growth of the primary instability, and the variation in the saturation point. As noted in the introduction, we are interested in the amount of energy 'stored' in the primary billow, which would then be available to secondary instabilities and turbulent transition in a three-dimensional flow.

2.3 Results

2.3.1 Class D: Diffusing shear layers

As mentioned in the introduction, we consider three distinct classes of flow. In the first class D (runs D1 to D4 in table 2.1), we consider $Re \in [1000, 6000]$ and $Ri_m \in [0, 0.2]$. We refer to this class as class D since no body forcing is added to the equations of motion and the shear layer is allowed to diffuse freely. Figure 2.1 shows the variation in $E_{\max}$ and $t_{\max}$ at the saturation point for these simulations. For all these simulations, we choose the initial amplitude of the perturbation to be $E_0 = 10^{-6}$ so that the perturbations exhibit an initial period of exponential growth, consistent with our linear stability calculations. At all Re, increasing Ri_0 (and Ri_m) produces a monotonic decrease in $E_{\max}$ as well as a monotonic increase in $t_{\max}$. The saturation point is weakly dependent on Re at low values of Ri_0, with a 4% decrease in $E_{\max}$ between $Re = 1000$ and 6000 at $Ri_0 = 0.05$. The peak energy, $E_{\max}$, decreases towards zero at higher Ri_0, although there is clearly nontrivial Re-dependence. When the perturbation amplitude is still relatively close to E_0, diffusion of the background profiles leads to an increase in Ri_m over time.

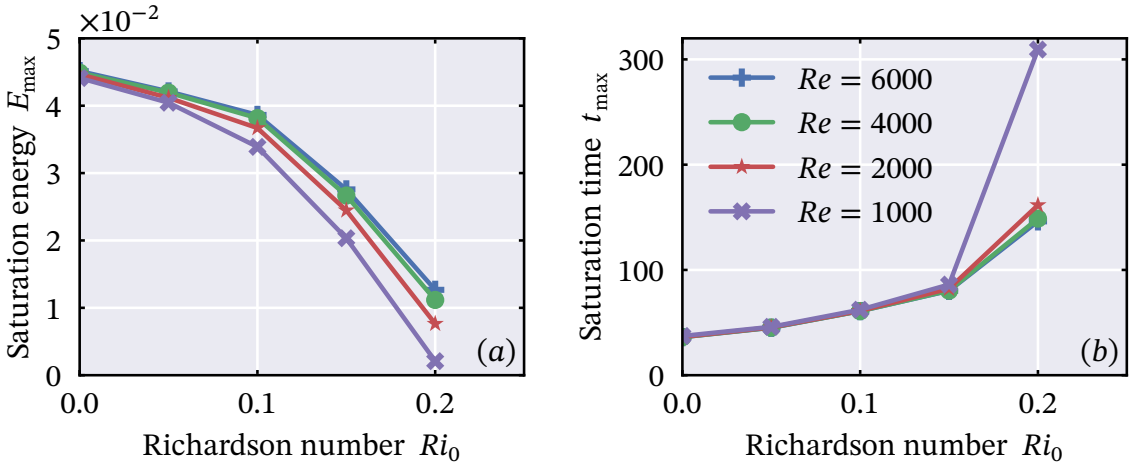

Fig. 2.1 For class D simulations, variation with Re and Ri_0 of (a) peak energy $E_{\max}$ and (b) time to saturation $t_{\max}$.

The primary effect of decreasing Re is to speed up this process. As a consequence, at $Ri_0 = 0.2$, decreasing Re monotonically decreases $E_{\max}$ and monotonically increases $t_{\max}$. Furthermore, since we define the perturbation energy as the difference from the initial velocity and buoyancy profiles defined by $U(z) = B(z) = \tanh(z)$, diffusion contributes to perturbation growth. This contribution is small compared to $E_{\max}$ except in the simulation $Re = 1000$, $Ri = 0.2$, for which no clear billow structure develops. In fact, the 'saturation point' plotted in figure 2.1 corresponds to this simulation's end when the mean profiles have most diffused.

2.3.2 Class S: Steady shear layers

It is apparent that diffusion influences the 'saturation point' by altering the mean velocity and density profiles, particularly for $Ri_0 \simeq 1/4$. To investigate the behaviour at higher Richardson numbers, we introduce body forces F_U and F_b to the equations of motion to prevent diffusion of the background profiles. The governing equations become

$$\frac{\partial \boldsymbol{u}}{\partial t} + (\boldsymbol{u}\cdot\boldsymbol{\nabla})\,\boldsymbol{u} = -\boldsymbol{\nabla} p + \frac{1}{Re}\nabla^2\boldsymbol{u} + Ri_0\, b\,\hat{\boldsymbol{z}} + F_U\hat{\boldsymbol{x}}, \tag{2.8a}$$

$$\frac{\partial b}{\partial t} + (\boldsymbol{u}\cdot\boldsymbol{\nabla})\, b = \frac{1}{RePr}\nabla^2 b + F_b, \tag{2.8b}$$

where setting $F_U = F_b = 2\tanh(z)\,\mathrm{sech}^2(z)/Re$ ensures that the initial background profiles $\overline{U} = \overline{B} = \tanh(z)$ are steady solutions. Crucially, Ri_m of the background flow is then equal to Ri_0 throughout the initial development of the primary instability. We re-

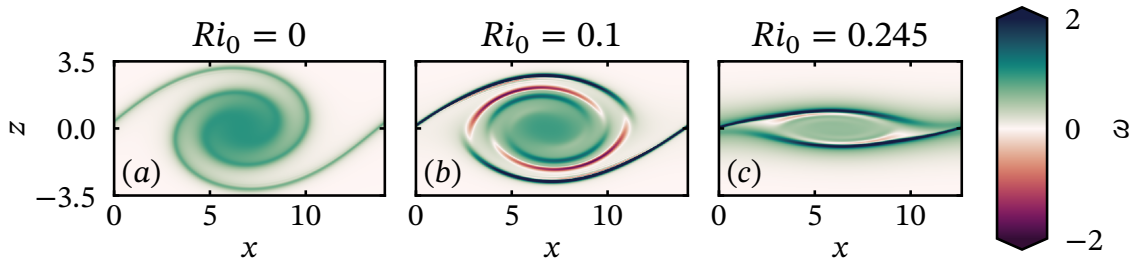

Fig. 2.2 Snapshots of spanwise vorticity $\omega = \partial_z u - \partial_x w$ at times $t = t_{\max}$ for class S simulations with: (a) $Ri_0 = 0$; (b) $Ri_0 = 0.1$; and (c) $Ri_0 = 0.245$.

fer to these simulations, whose properties are listed in table 2.1, with $0 \leq Ri_0 \leq 0.245$ as being in class S. Since variations in Re have little effect on the subsequent evolution of the flow, we fix $Re = 4000$. For this class, it is natural to consider the proportion of the background kinetic energy converted to perturbation (both kinetic and potential) energy in the primary billow. At the saturation point, we therefore consider the perturbation energy density in the centre of the domain E_c and the kinetic energy of the background flow K_B, and calculate the ratios

$$R_T = \frac{E_c}{K_B} = R_K + R_P = \frac{E_K + E_P}{K_B} = \frac{\frac{1}{2}\int_{-3.5}^{3.5}\int_0^{L_x} \boldsymbol{u}' \cdot \boldsymbol{u}' + Ri_0 b'^2 \,\mathrm{d}x\,\mathrm{d}z}{\frac{L_x}{2}\int_{-3.5}^{3.5} \tanh^2(z)\,\mathrm{d}z}, \tag{2.9}$$

where the vertical range is chosen so that it contains all saturated billows, as is demonstrated in figure 2.2 for three characteristic choices of $Ri_0 = 0, 0.1$ and 0.245. As is well-known, at higher Ri_0, baroclinic effects cause vorticity to become concentrated in the braid and the height of the billow to decrease (Caulfield and Peltier 2000)

Figure 2.3a demonstrates a decreasing monotonic relationship between the total perturbation energy ratio R_T at the saturation point and Ri_0. The kinetic energy component R_K decreases approximately linearly with increasing Ri_0, whereas the potential energy component R_P varies nonmonotonically, explaining the 'kink' in the variation of R_T with Ri_0 at $Ri_0 \approx 0.1$. Although we suppress diffusion of the background flows, some mixing still occurs within the billow as it rolls up, altering the mean velocity and buoyancy profiles, contributing approximately 30% of the maximum perturbation energy. Interestingly, despite the lack of linear perturbation growth at $Ri_0 = 1/4$, the various scaled perturbation energy ratios R_T, R_K and R_P do not approach zero as $Ri_0 \to 1/4$. Figure 2.3b displays the time $t_{\max}$ to the saturation point for this class, which appears to diverge as $Ri_0 \to 1/4$. Performing linear regression on the logarithmic values of this plot provides the divergent scaling $t_{\max} \sim (0.25 - Ri_0)^{-5/8}$. A logarithm-scaled plot of

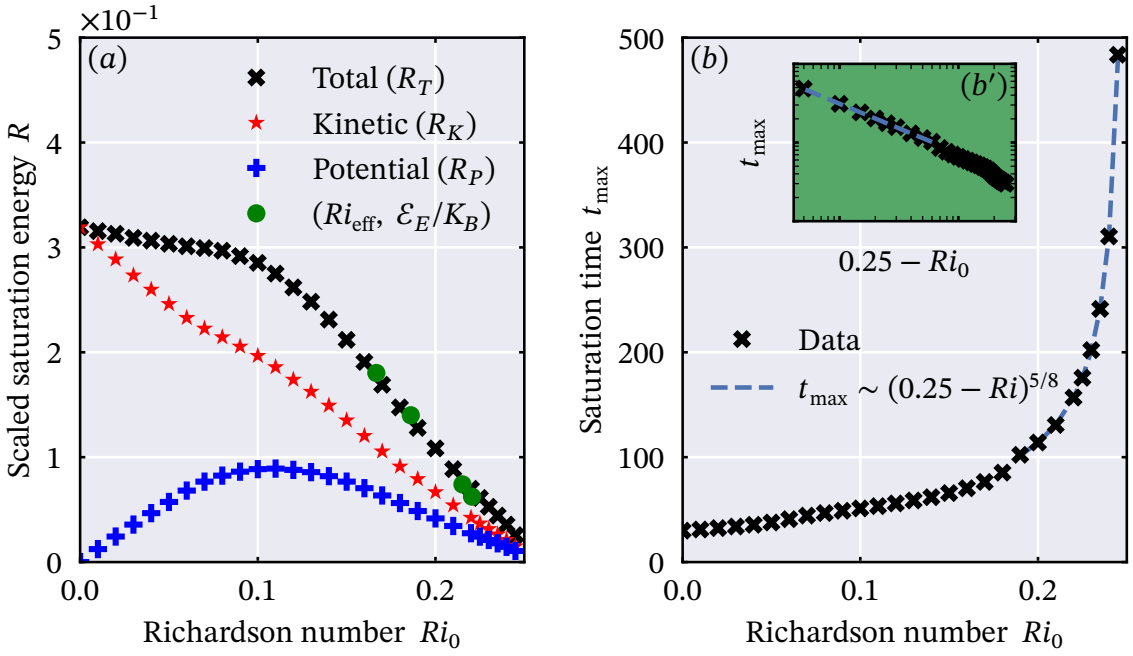

Fig. 2.3 For class S simulations, variation with Ri_0 of: (a) scaled maxima of total perturbation energy R_T (crosses), perturbation kinetic energy R_K (stars) and perturbation potential energy R_P (pluses) as defined in (2.9); (b) $t_{\max}$. (b') displays the same data as (b) but on a logarithmic scale. In (a) circles mark Ri_{eff} and the maximum value of $\mathcal{E}_E/K_B$ for class A simulations as discussed in section 2.3.3.

the data is plotted on the inset axes of figure 2.3b′, highlighting this scaling. Crucially, it appears impossible to 'store' significant energy in a primary saturated billow from KHI when $Ri_m \lesssim 1/4$, thus calling into question the applicability of the linear marginal stability concept to the triggering of turbulence in flows with $Ri_m \simeq 1/4$.

2.3.3 Class A: Accelerating shear layers

Although steady flows with $Ri_m \simeq 1/4$ appear not to be able to generate substantial saturated perturbation energy, to test the marginal stability/instability concepts it is also necessary to investigate whether time-dependent flows with decreasing Richardson numbers can lead to energetic billows as Ri_m drops (slightly) below 1/4. To investigate this issue, we consider the final class A of simulations, which start in a linearly stable state with $Ri_0 = 0.26$, and are then accelerated by body forcing which lowers Ri_m below 1/4. Precisely, we solve (2.8) by specifying $F_b = 0$ (so that buoyancy freely diffuses) and

$$F_U = \left(\frac{2}{Re}\tanh(z)\mathrm{sech}^2(z) + \gamma\tanh(z)\right)e^{\gamma t}, \tag{2.10}$$

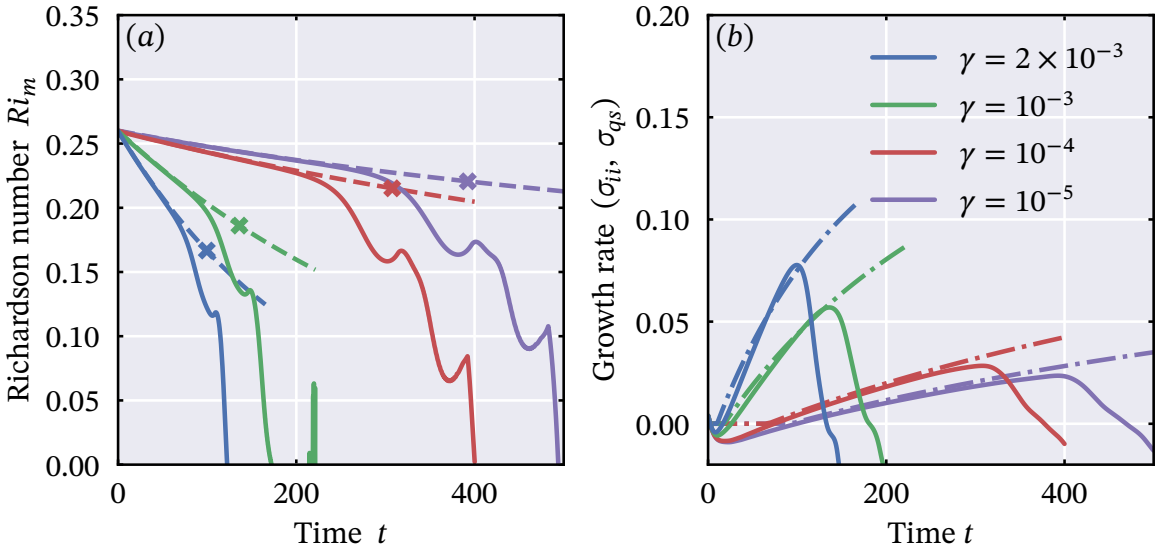

Fig. 2.4 (a) Time series of minimum measured Richardson number $\langle Ri_m \rangle$ from unperturbed (dashed lines) and growing (solid lines) simulations in the accelerating regime. The crosses indicate the value of Ri_{eff} for each simulation, at the time t_p. (b) Time series of predicted growth rate σ_{qs} from quasi-steady linear analysis (dash-dot lines) and inferred instantaneous growth rate σ_{ii} as defined in (2.13) (solid lines) for various forcing rates γ. The time t_p is defined as the instant when σ_{ii} is maximum.

which thus has an accelerating background velocity solution $\overline{U} = \tanh(z)e^{\gamma t}$. Here, γ is a forcing rate, which we prescribe as a constant between 10^{-5} and 2×10^{-3}. Such an accelerating background flow increases the effective Reynolds number of the flow, limiting our choice of γ to ensure that all simulations are well-resolved up to the saturation point.

Figure 2.4a shows the effect of the forcing on the minimum mean gradient Richardson number $\langle Ri_m \rangle$, defined by

$$\langle Ri_m \rangle(t) = \min_z \langle Ri_g \rangle_x(z,t) \; = Ri_0 \min_z \left\{ \frac{\langle \partial b/\partial z \rangle_x}{\langle (\partial u/\partial z)^2 \rangle_x} \right\}, \tag{2.11}$$

where $\langle \cdot \rangle_x$ denotes a streamwise average. Since no growing normal-mode perturbation exists for $Ri_0 = 0.26$, the initial profiles are perturbed with the most unstable mode for $Ri_0 = 0.245$ and the length of the domain is set to the corresponding wavelength for that Richardson number. We also conduct unperturbed simulations for each forcing rate to track $\langle Ri_m \rangle$ of the purely accelerating background flow in the absence of billow formation, which is plotted with dashed lines on figure 2.4a.

For comparison we perform a linear stability analysis for a quasi-steady background flow with $\overline{U} = \overline{B} = \tanh(z)$ and midplane Richardson number $Ri_0 = \langle Ri_m \rangle(t)$. The analysis provides a predicted quasi-steady growth rate σ_{qs} at each time t and forcing rate γ, as shown in figure 2.4b. Energy is added to the system by the body forcing, so the appropriate effective perturbation energy is

$$\mathcal{E}_E = E_c[\boldsymbol{u}, b] - E_c[\widehat{\boldsymbol{u}}, \hat{b}], \tag{2.12}$$

i.e. the difference between E_c for the perturbed $(\boldsymbol{u}, b)$ and unperturbed $(\widehat{\boldsymbol{u}}, \hat{b})$ simulations, where E_c is defined in (2.9).

If the flow is linearly unstable $\boldsymbol{u}', b' \sim e^{\sigma t}$, or equivalently $\mathcal{E}_E \sim e^{2\sigma t}$. We can therefore test the accuracy of the linear stability analysis by calculating an inferred instantaneous growth rate from the perturbed nonlinear simulations

$$\frac{1}{2\mathcal{E}_E}\frac{d\mathcal{E}_E}{dt} = \sigma_{ii}. \tag{2.13}$$

The solid lines on figure 2.4b show this inferred instantaneous growth rate σ_{ii}. Once the predicted quasi-steady growth rate σ_{qs} becomes non-zero, the inferred instantaneous growth rate σ_{ii} matches the quasi-steady linear prediction σ_{qs} well for a certain period of time. For each choice of forcing rate γ, σ_{ii} reaches a peak at some time t_p where nonlinear effects start to become significant, before falling through zero at the saturation point, when the effective perturbation energy $\mathcal{E}_E$ is maximum. Interestingly, for this class of flows, the effective perturbation energy $\mathcal{E}_E$ at the instant when the growth rate peaks is approximately 0.75% of the initial background energy K_B, independent of the forcing rate. Simulations in class S also appear to deviate from purely 'linear' exponential-in-time perturbation growth for a similar ratio of perturbation energy to background energy K_B. The remaining perturbation growth depends on the effective Richardson number Ri_{eff}, i.e. the value of $\langle Ri_m \rangle$ in the unperturbed flow at the time instant t_p when σ_{ii} reaches its peak value in the (perturbed) simulations, marked with crosses in figure 2.4a. The maximum value of the appropriately scaled perturbation energy $\mathcal{E}_E/K_B$ at the saturation points is plotted (with circles) against Ri_{eff} on figure 2.3a, showing striking agreement with the simulations in the steady class S. It appears that the maximum amplitude of the nonlinear billow state is controlled by the minimum value of Ri_g of the background flow relatively early in the development of the instability (specifically when nonlinear effects start to reduce the inferred instantaneous growth rate), and that such maximum amplitude is very small when the relevant $Ri_0 \simeq 1/4$, even in accelerating flows.

2.4 Discussion and Conclusions

We have performed three classes of two-dimensional direct numerical simulations of stratified shear layers susceptible to KHI: class D where the background flow profiles are free to diffuse; class S where body forcings allow the initial background flow profiles to be steady solutions of the governing equations; and class A where the background velocity profile accelerates. In each class, the saturated amplitude of the nonlinear billow state decreases as the initial minimum gradient Richardson number, Ri_m, increases. In class D, Re becomes important as $Ri_m \to 1/4$ since diffusion of the background flow increases the Richardson number to a linearly stable value. For class S, where body forcing keeps Ri_m constant, a clear monotonic relationship arises between Ri_m and the saturated amplitude of the nonlinear state. The time at which this saturated amplitude occurs diverges as $Ri_m \to 1/4$, while the saturated amplitude of the billow decreases to a small but non-zero value. This limit yields flattened billows, as shown in figure 2.2c. It is important to appreciate that these results are not direct consequences of the Miles–Howard criterion, which only considers the exponential growth of infinitesimal perturbations on steady, inviscid flows, and not the properties of potentially ensuing nonlinear states.

We find that the instabilities which develop in the accelerating shear layers of class A are still, at early times, well-described by quasi-steady linear stability analyses using an instantaneous Richardson number. The saturated energy of these billows is still consistent with the relationship shown in figure 2.3a, reaffirming that the saturated amplitude is restricted by Ri_m. We find that nonlinear effects become important when a perturbation reaches an amplitude corresponding to 0.75% of the initial background kinetic energy. This particular percentage is a result of the particular integral limits chosen in (2.9), but the fact that the value is consistent across the simulations is still significant.

The above results seem inconsistent with the connection between marginally unstable flow states and the generation or 'triggering' of turbulence through unstable linear normal-mode disturbances. In particular, the application of the Miles–Howard criterion to provide a stability boundary for naturally occurring turbulent shear flows appears inconsistent with the demonstrated nonlinear development of KHI in laminar states at high Re. Indeed, our results are broadly consistent with studies of internal solitary waves, which have similarly suggested that wave breaking requires the minimum Richardson number in the pycnocline to be below approximately 0.1 (Lamb 2014). We hypothesise that vigorous energy injection to finite amplitude structures which have the

potential to trigger turbulent transition requires minimum Richardson numbers within the flow to be substantially below 1/4.

This hypothesis is not inconsistent with the observations discussed by Thorpe and Liu (2009) and Smyth and Moum (2013), since we are concerned with the laminar states required for turbulent transition rather than the ensuing turbulent flow itself. However, the use of linear stability analysis by Thorpe and Liu (2009) and Thorpe et al. (2013) to determine the stability of turbulent shear flows by the Miles–Howard criterion does not appear valid given our results. Since the nonlinear structures that develop in our marginally unstable laminar flows are very small and take a long time to saturate, any linear perturbation in a similarly marginal turbulent flow is likely to be strongly influenced by the surrounding turbulence. This introduces uncertainty to both the development of a linear perturbation and the nature of its finite amplitude manifestation as a nonlinear billow structure. We conclude that the application of marginal stability to naturally occurring turbulent flows should be based on results concerning the growth and decay of stratified turbulence around certain Richardson numbers (e.g. Rohr et al. 1988; Zhou et al. 2017), rather than linear stability arguments.

Although we have only performed simulations in a two-dimensional domain, we remain confident that our results have relevance to fully three-dimensional realisations of these flows. By computing the turbulent kinetic energy of the class S simulations, we obtain comparable values at saturation to those found in figure 3b of the three-dimensional study of Mashayek et al. (2013). The peak energy we get takes slightly higher values than Mashayek et al. (2013) because of the reduced diffusion keeping the minimum Richardson number at a lower value in our case. For our highest Ri_0 values no three-dimensional studies have been performed, but Mashayek and Peltier (2012*b*) found that the growth rates of all secondary instabilities decrease as Ri_0 is increased past 0.12. We therefore believe that the behaviour of the two-dimensional roll-up is still important at higher Ri_0.

It is important to remember that we have only considered the nonlinear development of a linear normal-mode perturbation. As noted in the introduction, Kaminski et al. (2017) have shown that sufficiently large amplitude perturbations with the structure of a linear optimal perturbation can still develop into a 'KH-like' billow state for flows with Ri_m as high as 0.4, which may perhaps explain why the maximum energy in figure 2.3a does not tend to zero as $Ri_m \to 1/4$. Indeed, with a specific type of large forcing, a saturated nonlinear overturning billow structure may possibly develop at $Ri_m = 1/4$ through a different (and inherently transient, non-normal) mechanism, distinct from perturbation by a classical normal-mode linear instability.

Although flows in the atmosphere or oceans are far more complex than those considered here, our results from time-dependent shear layers (class A) suggest that minimum values of Ri_g directly control the saturated amplitude of Kelvin–Helmholtz billows. In particular, we have shown that the time for the perturbation energy to saturate becomes very long as $Ri_m \to 1/4$ and the billow amplitude is small in this limit, implying that a laminar flow in this state is unlikely to become turbulent. For example, using the typical value 1m for a shear layer half-depth, and velocity difference $2U_0^* = 7.5 \times 10^{-2}\mathrm{ms}^{-1}$ from measurements by van Haren and Gostiaux (2010) to calculate an advective time scale gives $t_{\max}$ greater than 22 minutes for $Ri_0 \geq 0.2$. At $Ri_0 = 0.24$, the appropriately scaled saturation time becomes longer than an hour. Further work to examine the effect of ambient turbulence or internal waves on the saturated billow amplitudes would be invaluable for quantifying the potential for enhanced mixing and turbulence of shear-driven overturning structures in the ocean.

2.5 Recent developments

Since the publication of this work in Howland et al. (2018), a number of new publications have explored the behaviour of shear instabilities close to the threshold of $Ri_g = 1/4$, and re-evaluated the concept of 'marginal stability'. We now discuss how the results presented above connect to these new developments.

Kaminski and Smyth (2019) perform three-dimensional DNS of a stratified shear layer where the initial condition is perturbed by a field of pre-existing stratified turbulence. The study follows a similar motivation to the stability analysis of Thorpe et al. (2013), in that stratified shear layers in geophysical scenarios rarely occur in the laminar environment studied here. In their DNS, Kaminski and Smyth (2019) observe significant changes in the billow development as the amplitude of the pre-existing turbulence is increased, and these changes are most significant at higher values of Ri_m. Consistent with our results, the normal mode instability grows too slowly at $Ri_m \lesssim 1/4$ to overcome the effect of the pre-existing turbulence, and the ensuing lack of a coherent vortex leads to a smaller value of mixing efficiency.

Such vortices, as seen in figure 2.2c, are in fact linked to steady solutions of the equations of motion. This is shown by Parker et al. (2019) who use branch continuation to investigate a system analogous to that used for our class 'S' simulations. They find that this (linearly unstable) branch of solutions even extends slightly beyond the critical value of $Ri_m = 1/4$, consistent with our result of figure 2.3 showing that the saturation energy decreases to a small but non-zero value as $Ri_0 \to 1/4$. The solution branch undergoes

a Hopf bifurcation at $Ri_0 \approx 0.250127$, so the potential for accessing such a state when $Ri > 1/4$ is limited. However Parker et al. (2019) note that supercritical behaviour may become more important for $Pr > 1$, and work is ongoing to investigate the behaviour of the solution branch at more oceanographically relevant values of Pr.

The more general concept of 'marginal stability' for a system continuously forced towards an unstable state has recently been reframed in the framework of self-organized criticality (SOC) by Smyth et al. (2019). Indeed the classical example of SOC in an avalanching sandpile provides a useful analogy for describing the cycle of growth and decay in a stratified flow subject to an externally forced shear. Smyth et al. (2019) also present a remarkable power law scaling in the distribution of overturn length scales from the observations of Smyth and Moum (2013) to support this interpretation. Their justification for using $Ri_g = 1/4$ as a critical value, however, remains empirical.

SOC rears its head again in the study of turbulence induced by Holmboe instability (named after Holmboe 1962) at a relatively sharp density interface. Salehipour et al. (2018) perform high resolution 3-D DNS of such a stratified shear layer, where the minimum Richardson number occurs above and below the density interface, not coincident with it. Holmboe instability manifests itself through vortices that propagate horizontally along these regions of low Ri_g, and the ensuing turbulence is long-lived and mixes by 'scouring' the interface. The simulations show that the value of Ri_g at the interface adjusts to 1/4 in such flows, regardless of its initial value, and that the mixing efficiency in the long-lived turbulence tends to the upper bound of 1/6 used by Osborn (1980). The distribution of 'energy containing' length scales in the flow also exhibits a power law scaling indicative of SOC behaviour. Although both Salehipour et al. (2018) and Smyth et al. (2019) describe a self-organisation towards $Ri_g = 1/4$, the mechanisms they propose are slightly different. It is not clear whether such a 'critical' state should be best interpreted as a cycle of Kelvin–Helmholtz-style breaking events or the steady 'scouring' of a stratified environment akin to Holmboe instability.

Portwood et al. (2019) approach the problem in a different way, by directly simulating the equilibrium state for a flow subject to a constant mean shear. By allowing the strength of gravity to vary freely through a control system, Ri_g is not prescribed, but naturally emerges as a constant required to maintain a stationary state. Portwood et al. (2019) find this constant to be approximately 0.16 for all values of the buoyancy Reynolds number $Re_b = \varepsilon/\nu N^2$ simulated. This result may relate to our finding that significant energy growth is difficult to achieve through linear instabilities when Ri_m is close to (but still less than) 1/4. The possible self-organized criticality of sheared stratified turbulence around a state of $Ri \approx 0.16$ warrants further investigation.

Chapter 3

Mixing in forced stratified turbulence

In this chapter, we investigate the effect that different large-scale forcing methods can have on mixing in a stratified turbulent flow. As discussed in chapter 1, there are a range of possible mechanisms by which turbulence can be generated or sustained through a downscale energy cascade in the ocean. We are interested in whether the nature of the energy transfer from larger scales affects the small-scale properties associated with turbulent dissipation and mixing. We perform high-resolution three-dimensional simulations in a triply-periodic cube, and represent the downscale transfer of energy from scales larger than we can resolve through forcing terms added to the equations of motion. We compare the flows arising from three different forcing methods that take the form of vortical modes or internal gravity waves. In these flows, we quantify local correlations between turbulent quantities to investigate appropriate scalings for the mixing efficiency, and we use wavelets to obtain local energy spectra for dynamically distinct regions of the domain.

This chapter has recently been published in the Journal of Fluid Mechanics as Howland, C. J. et al. (2020), "Mixing in forced stratified turbulence and its dependence on large-scale forcing", *J. Fluid Mech.* 898: A7

3.1 Turbulence maintained by large-scale forcing in a stably stratified fluid

We begin with a further discussion of energy transfers in the ocean, introduced in §1.2, relevant to this chapter. As discussed earlier, the vast majority of energy input to the

ocean comes from the tides and large-scale surface forcing by winds (Wunsch and Ferrari 2004). The closure of the global ocean energy budget however requires dissipation by viscosity at millimetre scales. A significant fraction of the energy input to the ocean is dissipated in turbulent boundary layers near the top and bottom of the ocean. Energy that is not dissipated close to these boundaries typically propagates away into the interior of the ocean as internal gravity waves. For example Waterhouse et al. (2014) estimate that 69% of the energy input into the internal wave field is not dissipated locally but is instead dissipated in the interior of the ocean. Away from the boundaries the empirical Garrett–Munk (GM) spectrum (Munk 1981) describes the distribution of energy in internal waves well in a surprisingly wide range of oceanic environments. Energy transfer within the large-scale part of the GM spectrum is explained by Müller et al. (1986) as weakly nonlinear resonant wave-wave interactions.

At high wavenumbers energy in the GM spectrum scales as $E \sim m^{-2}$ with vertical wavenumber m. This scaling is observed up to a 'cutoff wavenumber', beyond which a vertical energy spectrum of m^{-3} is measured (Gargett et al. 1981). At yet smaller scales an inertial range scaling as $m^{-5/3}$ associated with isotropic turbulence can be observed with sufficiently high resolution measurements. The intermediate range of scales for which $E \sim m^{-3}$ is sometimes associated with the breaking of internal waves; in particular that of high-frequency (in the sense of having frequency close to the buoyancy frequency N) internal gravity waves (see e.g. Eckermann 1999). Although the fundamental breaking mechanisms of internal gravity waves by shear and convective instabilities can be described as in Thorpe (2018), the strongly nonlinear interactions that transfer energy to and between these small scale waves are less well understood. The m^{-3} scaling is readily obtained from dimensional analysis if one assumes that N^{-1} is the dominant time scale, leading to $E(m) \sim L^3T^{-2} \sim N^2m^{-3}$. This suggests that buoyancy does indeed have a dominant effect on the dynamics at these scales.

The strongly nonlinear motions at small scales can also be considered as a state of 'stratified turbulence', although there is by no means consensus in the oceanographic and fluid dynamical literature as to what precisely is meant by this term. Often (see for example Gregg et al. 2018) 'stratified turbulence' in an oceanographic context is used to describe any turbulent flow affected by stratification. In a fluid dynamical context on the other hand, Riley and Lindborg (2008) use it to describe the particular distinguished limit of $Fr_h = U_h/NL_h \ll 1$, $Re_h = U_hL_h/\nu \gg 1$ and $Re_hFr_h^2 \gg 1$ (where U_h and L_h are horizontal velocity and length scales and ν is the kinematic viscosity of the fluid). This particular regime is also referred to as "strongly stratified turbulence" (Brethouwer et

al. 2007; Maffioli 2017; Zhou and Diamessis 2019) or alternatively "layered anisotropic stratified turbulence" (Falder et al. 2016).

Furthermore turbulence in the stratified ocean interior is strongly intermittent in both space and time. Baker and Gibson (1987) show that turbulent dissipation rates are often lognormally distributed, which leads to regions of high stratification such as the thermocline exhibiting the highest intermittency. This presents a great challenge in sampling the ocean to determine the nature of turbulent flows relevant to mixing in the stratified ocean.

If turbulence is generated in a stratified fluid without a source of sustaining energy, the energetics of its decay inevitably become affected by the stratification at leading order. The energy cost associated with raising dense fluid up leads to an anisotropic decay of the vertical velocity (Riley and Lelong 2000). Billant and Chomaz (2001) exploit such inevitable anisotropy in the flow velocity to identify a self-similar inviscid regime in the strongly stratified limit of $Fr_h = U_h/NL_h \to 0$. This self-similar scaling suggests that vertical scales adjust so that $L_v \sim U_h/N$ and the flow becomes dominated by horizontal motion that varies vertically on this scale. Increasingly high resolution numerical simulations have been used to study the decay of an initially isotropic and homogeneous turbulent state subject to a background stratification (Maffioli and Davidson 2016; de Bruyn Kops and Riley 2019). After approximately one buoyancy period these flows do indeed become anisotropic and adjust to this vertical length scale predicted by Billant and Chomaz (2001). Although the $E \sim N^2 m^{-3}$ vertical spectrum is consistent with the self-similar regime, the numerical studies of decaying stratified turbulence have thus far been unable to replicate it clearly.

To investigate the properties of stratified turbulence in a statistically steady state, it seems sensible to apply body forcing to the governing equations with the aim of removing the transient dynamics of turbulent decay. It also seems natural to force flows at the large scale and then hope to rely on the net downscale cascade to transfer energy to small dissipative scales such that the total dissipation matches the energy input from the forcing. Stochastic forcing of large-scale vortical modes has often been implemented to study anisotropic stratified turbulence dominated by horizontal motion (e.g. Waite and Bartello 2004; Brethouwer et al. 2007; Maffioli et al. 2016). This approach has the advantage of not imposing a vertical length scale on the flow, allowing the predicted length scale U_h/N to emerge spontaneously. Furthermore, a recent study implementing this forcing by Maffioli (2017) replicates the predicted $N^2 m^{-3}$ energy spectrum by considering only large horizontal scales of the flow. The forcing does not force vertical shear directly but is thought to enhance small existing vertical gradients through the so

called 'zigzag' instability, first identified by Billant and Chomaz (2000*a*,*b*). It is unclear how relevant these vortically-dominated flows are for small-scale mixing in the ocean. In particular, the lack of significant vertical motion is inconsistent with the breaking of high-frequency internal gravity waves. A recent study by Kunze (2018) however suggests a new interpretation of oceanic spectra, where strongly anisotropic patches of stratified turbulence may be generated from finescale near-inertial waves. It is therefore of interest to compare flows forced by vortical modes with flows forced by internal gravity waves. Waite and Bartello (2006) implement such forcing in hyperdiffusive simulations at moderate numerical resolution, but do not reach their aim of reproducing the N^2m^{-3} energy spectrum. It is important to recognise that although the forcing of vortical modes or internal waves is applied at the large scale in these turbulence studies, the forced scale is in fact very small in the context of a geophysical energy spectrum.

For determining mean transport of relevant oceanic tracers we are primarily concerned with irreversible mixing, related to changes in background potential energy by Winters et al. (1995) and Peltier and Caulfield (2003). Investigating such irreversible mixing in stratified turbulence requires accurate resolution of dissipation scales through direct numerical simulation (DNS). Many of the forced studies mentioned above rely on large eddy simulation or hyperdiffusion to prevent energy building up at small scales, and it is only recent studies that have used DNS to investigate these flows (e.g. Almalkie and de Bruyn Kops 2012; Portwood et al. 2016; Maffioli et al. 2016; Maffioli 2017).

The small-scale nature of irreversible turbulent mixing inevitably requires the development and use of relatively simple parameterization models to estimate mixing from both observations and large-scale circulation models. As outlined in Gregg et al. (2018) an appropriate definition of a mixing efficiency η is required for inferring and parameterizing mixing in such scenarios, but there is disagreement between numerical studies, laboratory experiments and observational estimates regarding both the precise definition of η and also its functional dependence on other flow parameters. In shear-driven flows susceptible to Kelvin–Helmholtz instability, a mixing efficiency defined in terms of volume-averaged irreversible rates of increase of potential energy and turbulent viscous dissipation rate ε has been shown to depend non-monotonically on the gradient Richardson number $Ri_g = N^2/S^2$, the ratio of the local buoyancy frequency N to the local vertical shear S, defined formally below (Mashayek et al. 2013). However a recent study by Portwood et al. (2019) shows that homogeneously sheared stratified turbulence equilibrates to a constant value of Ri_g, with the mixing efficiency also appearing to be independent of the buoyancy Reynolds number $Re_b = \varepsilon/\nu N^2$, where ν is the kinematic viscosity of the fluid. In the absence of a dominant mean shear, Maffioli et al. (2016)

and Garanaik and Venayagamoorthy (2019) instead construct theoretical scalings for the mixing efficiency in terms of a turbulent Froude number $Fr = \varepsilon/(N\mathcal{K}')$, where $\mathcal{K}'$ is the turbulent kinetic energy (density). Indeed, the equilibrated flows considered by Portwood et al. (2019) converged to a constant value of Fr, and it is still an open question why flows forced in this manner tune to constant values of Ri_g, Fr and Γ. This plethora of potential dimensionless parameters highlights the challenge in parameterizing mixing and the need to test how generically these parameterizations apply in different flows.

In this study we aim to determine the effects on irreversible mixing (quantified by an appropriately defined efficiency) of changing the large-scale forcing applied to a stratified fluid. We are particularly interested in how the 'breaking' of internal gravity waves modulates mixing in stratified turbulence compared to the mixing occuring in flows forced by vortical modes. We investigate the mechanisms by which mixing occurs through probing the energetics of our numerical simulations. We then relate the differences in these mechanisms to changes in the 'mixing efficiency' defined both locally and globally through appropriate averaging in space and time. The rest of this paper is organised as follows. In §3.2 the energetics of the governing equations are discussed in the context of mixing and its parameterization. §3.3 outlines our numerical model and the setup of our simulations, providing details of the initial condition and body forcing used. §3.4 presents analysis of the simulation results, focusing on key properties of the statistically quasi-steady states that arise in each case. Finally we conclude and discuss the implications of our results for the parameterization of irreversible mixing in the ocean in §3.5.

3.2 Mixing and energetics in a triply-periodic domain

We consider an incompressible fluid with a velocity field $\boldsymbol{u}(\boldsymbol{x}, t)$ and a buoyancy field determined by a perturbation $\theta(\boldsymbol{x}, t)$ to a constant background linear stratification. We apply the Boussinesq approximation that density changes are negligible compared to the mean density and furthermore assume that the associated buoyancy field has a linear equation of state and hence satisfies an advection-diffusion equation. The flow is thus governed by the Navier–Stokes equations in the form

$$\boldsymbol{\nabla} \cdot \boldsymbol{u} = 0, \tag{3.1}$$

$$\frac{\partial \boldsymbol{u}}{\partial t} + (\boldsymbol{u} \cdot \boldsymbol{\nabla})\, \boldsymbol{u} = -\boldsymbol{\nabla} p + \frac{1}{Re} \nabla^2 \boldsymbol{u} + Ri_0 \theta \hat{\boldsymbol{z}} + \boldsymbol{F_u}, \tag{3.2}$$

$$\frac{\partial \theta}{\partial t} + (\boldsymbol{u} \cdot \boldsymbol{\nabla})\, \theta = \frac{1}{RePr} \nabla^2 \theta - w + F_\theta, \tag{3.3}$$

where we have non-dimensionalised the equations using length and velocity scales L_0 and U_0, and $\hat{\boldsymbol{z}}$ is the unit vector in the vertical direction. The buoyancy perturbation has also been non-dimensionalised by $g\Delta\rho/\rho_0$ where $\Delta\rho$ is the scale of density perturbations. External forcing acting on the velocity and buoyancy fields are denoted by $\boldsymbol{F_u}$ and F_θ, the precise forms of which are detailed in the next section. The three dimensionless parameters in the equations are the Reynolds number, Prandtl number and bulk Richardson number

$$Re = \frac{L_0 U_0}{\nu}, \qquad Pr = \frac{\nu}{\kappa}, \qquad Ri_0 = \frac{g\Delta\rho L_0}{\rho_0 {U_0}^2} = \frac{{N_0}^2 {L_0}^2}{{U_0}^2}, \tag{3.4}$$

where ν is the kinematic viscosity, κ is the density diffusivity, and ρ_0 is the mean density. The constant background buoyancy gradient is $g\Delta\rho/\rho_0 L_0$, which can be used to define $N_0 = \sqrt{g\Delta\rho/\rho_0 L_0}$ as a background buoyancy frequency. Since $\Delta\rho$ also acts as the dimensional scale for density perturbations, the Boussinesq approximation requires that $\Delta\rho \ll \rho_0$. For clarity, the full *dimensional* density field will be written as

$$\rho^* = \rho_0 - \Delta\rho\,[z + \theta(\boldsymbol{x}, t)] \tag{3.5}$$

in this formalism, where $z = z^*/L_0$ and z^* are respectively the dimensionless and dimensional vertical coordinates.

Stably stratified flows are commonly anisotropic, with horizontal length scales much larger than vertical length scales. When analysing these flows, it is therefore natural to consider the decomposition of the velocity and buoyancy fields into horizontally-averaged mean quantities and perturbations from them. We will use the following notation, denoting mean quantities with an overbar and perturbations with a prime, i.e.

$$f(\boldsymbol{x}, t) = \overline{f}(z, t) + f'(\boldsymbol{x}, t), \qquad \overline{f}(z, t) = \frac{1}{L_x L_y} \int_0^{L_x} \int_0^{L_y} f(\boldsymbol{x}, t)\,\mathrm{d}x\,\mathrm{d}y. \tag{3.6}$$

Taking a horizontal mean of the incompressibility condition (3.1) gives $\partial\overline{w}/\partial z = 0$, so if $\overline{w} = 0$ initially then it remains zero for all time. From now on, we will assume that this is the case and hence that the mean velocity $\overline{\boldsymbol{u}}(z, t) = (u, v, 0)$ is purely horizontal.

In this paper we consider flow in a triply-periodic domain, which allows us to construct simple equations for the energy of the system from (3.2) and (3.3). Implementing the decomposition (3.6) yields four energy quantities of interest: the kinetic and potential energies (per unit mass) associated with both the mean and perturbation fields,

namely

$$\overline{\mathcal{K}} = \frac{1}{2}\left\langle |\overline{\boldsymbol{u}}|^2 \right\rangle, \qquad \mathcal{K}' = \frac{1}{2}\left\langle |\boldsymbol{u}'|^2 \right\rangle, \tag{3.7}$$

$$\overline{\mathcal{P}} = \frac{Ri_0}{2}\left\langle \overline{\theta}^2 \right\rangle, \qquad \mathcal{P}' = \frac{Ri_0}{2}\left\langle \theta'^2 \right\rangle, \tag{3.8}$$

where $\langle\cdot\rangle$ denotes a volume average. This positive semi-definite form of potential energy is valid since θ is a departure from a linear background profile. Motivated by the 'pancake vortices' description of stratified turbulence, we refer to $\mathcal{K}'$ as the turbulent kinetic energy and to $\mathcal{P}'$ as the turbulent potential energy. Since $\overline{w} = 0$ and $\langle \boldsymbol{u} \rangle = 0$, the mean kinetic energy $\overline{\mathcal{K}}$ is often associated with what are conventionally referred to as "shear modes", and there is a body of literature investigating its development in stratified turbulence (e.g. Smith and Waleffe 2002; Augier et al. 2015).

Multiplying (3.2) and (3.3) by the velocity and buoyancy fields respectively leads to the following evolution equations for the energy:

$$\frac{d\overline{\mathcal{K}}}{dt} = -S_p - \overline{\varepsilon}, \qquad \frac{d\mathcal{K}'}{dt} = S_p - \varepsilon' + \mathcal{J} + P_K, \tag{3.9}$$

$$\frac{d\overline{\mathcal{P}}}{dt} = -N_p - \overline{\chi}, \qquad \frac{d\mathcal{P}'}{dt} = N_p - \chi' - \mathcal{J} + P_P. \tag{3.10}$$

The terms on the right hand side of these equations act as inputs, exchanges and outputs of energy for the system as sketched in figure 3.1 and detailed below.

The rate at which energy is dissipated by the flow is quantified by the expressions

$$\overline{\varepsilon} = \frac{1}{Re}\left\langle \left| \frac{\partial \overline{\boldsymbol{u}}}{\partial z} \right|^2 \right\rangle \qquad \varepsilon = \frac{1}{Re}\left\langle \frac{\partial u_i'}{\partial x_j}\frac{\partial u_i'}{\partial x_j} \right\rangle, \tag{3.11}$$

$$\overline{\chi} = \frac{Ri_0}{RePr}\left\langle \left| \frac{\partial \overline{\theta}}{\partial z} \right|^2 \right\rangle \qquad \chi = \frac{Ri_0}{RePr}\left\langle \frac{\partial \theta'}{\partial x_j}\frac{\partial \theta'}{\partial x_j} \right\rangle, \tag{3.12}$$

where ε is commonly known as the turbulent kinetic energy (TKE) dissipation rate. It is important to appreciate that these various rates are defined in terms of volume averages over the whole computational domain.

Energy can be exchanged between kinetic and potential energy through the buoyancy flux $\mathcal{J}$. Since we have assumed that the mean flow is purely horizontal, this exchange can only take place between the turbulent energies $\mathcal{K}'$ and $\mathcal{P}'$. The small-scale turbulence instead interacts with the mean flow via the turbulent shear production S_p, and by an analogous term that appears in the potential energy equations which we refer

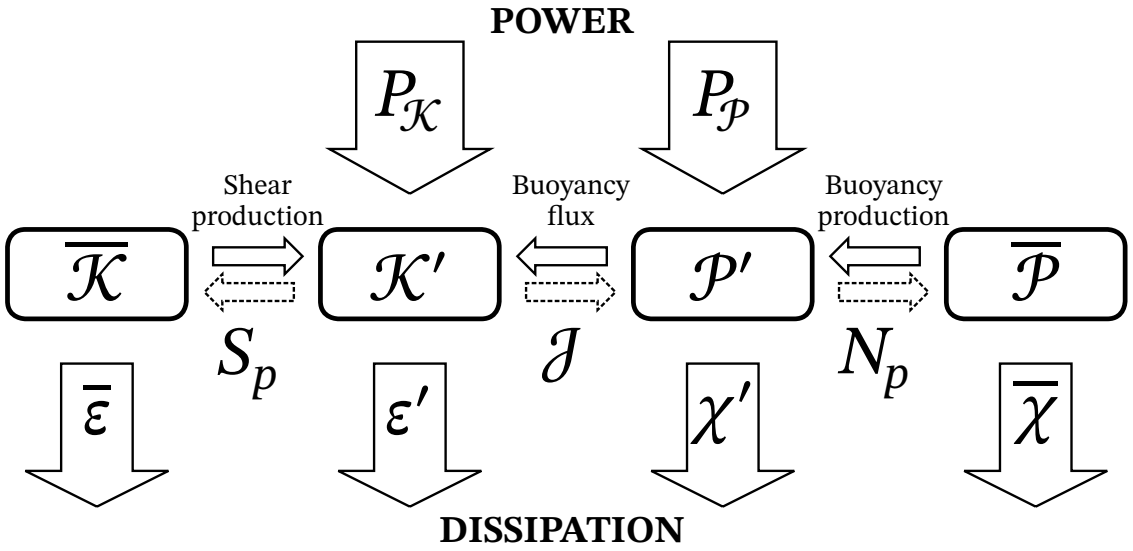

Fig. 3.1 Schematic detailing the energy pathways

to as buoyancy production N_p. The three energy exchange terms are defined

$$\mathcal{J} = Ri_0 \langle w'\theta' \rangle, \qquad S_p = -\left\langle \overline{w'\boldsymbol{u}'} \cdot \frac{\partial \overline{\boldsymbol{u}}}{\partial z} \right\rangle, \qquad N_p = -Ri_0 \left\langle \overline{w'\theta'} \, \frac{\partial \overline{\theta}}{\partial z} \right\rangle. \tag{3.13}$$

The energy input provided by the forcing is prescribed to *not* act directly on the mean flow, so the energy input rates only appear in the perturbation energy equations and are defined as

$$P_K = \langle \boldsymbol{u}' \cdot \boldsymbol{F}_{\boldsymbol{u}} \rangle, \qquad P_P = Ri_0 \langle \theta' F_\theta \rangle. \tag{3.14}$$

This is consistent with the forcing terms used in our numerical simulations.

In the formulation, we have chosen to retain flexibility to force both the velocity and buoyancy fields. In particular, whether or not the buoyancy field has explicit forcing has important implications for the energy budget of a quasi-steady turbulent state when $d\mathcal{P}'/dt \approx 0$. It is worth noting that in the flows considered by this study the buoyancy production N_p is typically much smaller than the other terms on the right hand side of (3.10), so if there is no buoyancy forcing then the turbulent potential energy budget reads

$$0 \approx -\chi' - \mathcal{J}, \tag{3.15}$$

in a steady state. Since χ' is positive semi-definite this implies that $\mathcal{J} \leq 0$ and so the buoyancy flux acts to transfer energy from kinetic to potential. When $F_\rho \neq 0$ this restriction is not enforced, and we will investigate the effect of introducing buoyancy forcing on the energy pathways later on. This flexibility is also physically motivated since nonlinear interactions between internal gravity waves can transfer kinetic and potential energy across spatial scales.

As noted in the introduction, we are interested in defining an appropriate measure of the 'efficiency' of mixing. We would wish to define an instantaneous mixing efficiency η as the proportion of energy lost by turbulence that leads to irreversible mixing. In our triply-periodic domain it is difficult to unambiguously define a background potential energy quantity as is used to quantify irreversible mixing in, for example, Peltier and Caulfield (2003). We therefore treat $\mathcal{P}'$ as a proxy for available potential energy and use χ' (as defined in (3.12)) to quantify the irreversible loss of $\mathcal{P}'$ that leads to mixing, yielding

$$\eta \coloneqq \frac{\chi'}{\chi' + \varepsilon'}, \tag{3.16}$$

as the expression for mixing efficiency. We shall revisit how well χ' approximates irreversible mixing in these flows in chapter 5, where we develop a self-consistent method for quantifying available potential energy and diapycnal mixing in triply-periodic systems. For now we assure the reader that this extended analysis leaves the conclusions presented in the current chapter essentially unchanged.

The denominator $\chi' + \varepsilon'$ of (3.16) represents the total instantaneous energy lost due to turbulence, and specifically excludes any laminar diffusion of the mean flow through $\overline{\chi}$ or $\bar{\varepsilon}$. We focus on mixing by turbulence because geophysical flows will typically occur at much larger Reynolds numbers than we can accurately simulate, leading to negligible laminar diffusion. Even at our modest *Re* the results are qualitatively unchanged by including the dissipation of the mean flow, with the average mixing efficiency only decreasing by between 4% and 8% across the simulations.

The mixing efficiency η is closely related to Γ, the turbulent flux coefficient commonly used in oceanography to infer measures of mixing from observations. The original definition of Osborn (1980) postulates a linear relationship between the buoyancy flux and the turbulent dissipation rate in a quasi-steady state of fully-developed turbulent flow, with Γ as the constant of proportionality. However, since we are considering flows where the buoyancy flux may well have a significant reversible component associated with internal waves, we believe it is more appropriate to define Γ in terms of the

ratio between χ' and ε', so that

$$\Gamma \coloneqq \frac{\chi'}{\varepsilon'} = \frac{\eta}{1-\eta}. \tag{3.17}$$

Recent stratified turbulence studies by Maffioli et al. (2016) and Garanaik and Venayagamoorthy (2019) have derived scalings for such a defined Γ in terms of the turbulent Froude number

$$Fr \coloneqq \frac{\varepsilon'}{{Ri_0}^{1/2}\mathcal{K}'}. \tag{3.18}$$

In the strongly stratified regime associated with $Fr \ll O(1)$ the scalings and associated simulations suggest that Γ is independent of Fr. Although this might be thought to provide some justification for the use of a constant Γ to infer mixing in geophysical flows, there is most definitely no consensus in the fluid dynamical community as to what value Γ takes in this regime, the region of validity of the regime, or indeed the variability of Γ outside of this regime.

In particular, there is an alternative approach to parameterizaion based around the argument that the appropriate parameter to use is the buoyancy Reynolds number

$$Re_b \coloneqq \frac{\varepsilon' Re}{Ri_0}, \tag{3.19}$$

(see for example Monismith et al. 2018), which can be considered to quantify how 'energetic' the turbulence is. Monismith et al. (2018) present data from numerical simulations and energetic nearshore flow observations that suggest the mixing efficiency scales as $\eta \sim Re_b^{-1/2}$ when the flow is 'energetic', which may also loosely be thought of as being weakly stratified, defined as $Re_b > O(100)$.

Monismith et al. (2018) still support the hypothesis that Γ is constant in strongly stratified flows with $Re_b < O(100)$, taking an approximate value of 0.2, although we caution associating smaller values of Re_b with 'strong' stratification, as smaller values of Re_b should really be considered to be associated with flows which are viscously dominated, or at least viscously affected. Gregg et al. (2018) also argue in favour of using the estimate $\Gamma \simeq 0.2$ which dates back to the early parameterization of Osborn (1980). They however caution the use of Re_b as a sole parameter for the functional dependence of Γ, and note that the turbulence produced by internal waves typically has $Re_b \lesssim 200$, where Γ is thought to be constant. Indeed, it is not at all clear at the moment whether the independence of Γ with respect to Fr when $Fr \ll 1$ is in any way associated with the classic empirically useful estimate that $\Gamma \simeq 0.2$, not least because it is exceptionally computationally challenging to consider flows with $Fr \ll 1$ and larger values of Re_b.

Since we are primarily concerned with internal wave-driven mixing in the open ocean, we choose to focus on 'strongly stratified' flows associated with $Fr \ll O(1)$, rather than classifying flows in terms of Re_b. Even in this regime, there are still discrepancies in the value of Γ between observations and numerical simulations. Maffioli et al. (2016) find a trend towards the constant value of $\Gamma = 0.33$ from their simulations of forced stratified turbulence, and simulations of decaying stratified turbulence by de Bruyn Kops and Riley (2019) have shown sustained values of Γ as large as 0.54. Understanding how these discrepancies may arise is vital if we hope to relate these numerical studies to observed mixing in the ocean.

One issue in comparing observations with these scaling arguments is that Fr is rarely recorded and requires simultaneous measurement of multiple turbulent quantities. Observationally it is easier to obtain the fundamental length scales named after Ellison and Ozmidov, defined as

$$L_E \coloneqq \frac{{\rho^*}_{\text{rms}}}{\left|\partial\overline{\rho^*}/\partial z\right|}, \qquad L_O \coloneqq \left(\frac{\varepsilon}{N^3}\right)^{1/2}. \tag{3.20}$$

For example Ivey et al. (2018) use a mixing length model to infer diapycnal diffusivity from L_E and the mean shear measured by moorings. They find good agreement with microstructure measurements, but it is unclear whether this estimate would work well in regions where the background state is dominated by the internal wave spectrum rather than a mean shear. Ivey and Imberger (1991) use L_E/L_O more generally to infer Fr, and therefore determine whether a flow is strongly turbulent or significantly affected by stratification. Many observational studies however assume that these length scales are approximately equal, as originally postulated by Dillon (1982), based on limited experimental data and due to restrictions in measurement equipment. A detailed comparison of these length scales in the thermocline can be found in Moum (1996).

3.3 Forced numerical simulations

We use the DIABLO software (Taylor 2008) to perform three-dimensional numerical simulations of equations (3.1)-(3.3). The software implements pseudo-spectral methods to calculate spatial derivatives and a third-order Runge–Kutta scheme for time stepping. The equations are solved in a cubic domain of length 2π represented by a uniformly-spaced grid of 1024^3 points. A 2/3 rule is applied for dealiasing the calculation of non-linear terms. Periodic boundary conditions are applied in every direction to the velocity and buoyancy fields $\boldsymbol{u}$ and θ. Recall that θ represents the buoyancy perturbation so

Table 3.1 Input parameters for the numerical simulations.

Re	Ri_0	Pr	L_x, L_y, L_z	N_x, N_y, N_z	$P_K + P_P$
10^4	1	1	2π	1024	10^{-3}

periodicity in the vertical does not contradict our use of a stable background buoyancy gradient. Table 3.1 summarises the input parameters used across all simulations.

Motivated by the existence of a background internal wave field in the ocean, we construct the initial condition for the simulations as follows. Computational constraints mean that we cannot resolve the range of scales required to represent a full Garrett–Munk (GM) spectrum in our domain. We therefore take an approach similar to that of Furue (2003) to construct an initial state where the large scales of the flow field are representative of the small-scale portion of the GM spectrum as defined by Munk (1981). To obtain the desired vertical energy spectrum of $E \sim m^{-2}$ we need to account for waves with horizontal wavelengths larger than the domain. Furue (2003) achieves this by integrating the GM spectrum over small horizontal wavenumbers to obtain a shear flow containing all of the 'missed' energy. We simply define the initial shear as a sum of shear modes $\boldsymbol{u}_0 \sim \frac{A}{m} e^{imz}$ that give an energy spectrum of m^{-2}. The shear modes are large-scale in the domain and are thus limited to $m \leq m_c = 7$. Each shear mode is randomly phased, and the total energy in this component is normalised such that the mean gradient Richardson number $Ri_g = Ri_0/\langle S^2 \rangle$ is equal to Ri_0. Here $S^2 = (\partial u/\partial z)^2 + (\partial v/\partial z)^2$ is the dimensionless squared shear, and $\langle \cdot \rangle$ denotes a volume average (simply equivalent to a vertical average in this case). The shear component is complemented by a collection of randomly-phased internal waves that satisfy the three-dimensional GM energy spectrum $E(\boldsymbol{k})$ defined in Furue (2003). These waves contribute 10% of the initial energy and are non-zero for $|\boldsymbol{k}| \leq 7$.

We numerically integrate the system for approximately 20 time units without body forcing to allow initial transient dynamics to dissipate, and for the associated dissipation rate to reach its maximum value. From this state we perform three simulations, each with a different form of body forcing applied. All three types of forcing can be expressed as

$$\boldsymbol{F_u} = \sum_{\substack{2.5 \leq |\boldsymbol{k}| \leq 3.5 \\ \kappa \neq 0}} \widetilde{\boldsymbol{F_u}}(\boldsymbol{k}) e^{i\boldsymbol{k}\cdot\boldsymbol{x}}, \qquad F_\theta = \sum_{\substack{2.5 \leq |\boldsymbol{k}| \leq 3.5 \\ \kappa \neq 0}} \widetilde{F_\theta}(\boldsymbol{k}) e^{i\boldsymbol{k}\cdot\boldsymbol{x}}, \tag{3.21}$$

where $\boldsymbol{k} = (k, l, m)$ is the wave vector and $\kappa = \sqrt{k^2 + l^2}$ is the horizontal wavenumber.

The first type of forcing we consider is that used by Maffioli (2017). We refer to this forcing as case H since the forcing acts purely on the *horizontal* components of velocity and therefore $F_w = F_\theta = 0$. Forcing H is representative of vertically-uniform 'vortical modes' with $(\widetilde{F_u}, \widetilde{F_v}) \propto (l, -k)$ and the modes being non-zero only when $m = 0$. Each mode is randomly phased at every time step.

The other two types of forcing are intended to be representative of flows induced by internal gravity waves, with the forcing components satisfying the internal wave polarisation relations

$$(\widetilde{F_u}, \widetilde{F_v}) = \mathcal{A}\frac{(k,l)m}{\kappa|\boldsymbol{k}|}, \qquad \widetilde{F_w} = -\mathcal{A}\frac{\kappa}{|\boldsymbol{k}|}, \qquad \widetilde{F_\theta} = \mathcal{A}\frac{i}{Ri_0{}^{1/2}}. \tag{3.22}$$

We denote one variant of this forcing as case R where the phase of the complex amplitude $\mathcal{A}$ for each mode is chosen *randomly* at every time step. The final type of forcing represents energy input from a *propagating* wave field and we refer to it as case P. In this case the phase of each $\mathcal{A}$ is shifted at time t by $-\omega t$ where the frequency ω is determined by the linear internal gravity wave dispersion relation, which in our nondimensionalisation is given by

$$\omega = \frac{Ri_0^{1/2}\kappa}{|\boldsymbol{k}|}. \tag{3.23}$$

To ensure that the dissipation rates are comparable across the simulations, we enforce the total energy input rate $P_K + P_P$ to be constant. We normalise the amplitude of the forcing at each time step to achieve the constant energy input rate shown in table 3.1. We also use the 'constant power minimal forcing' method from Maffioli (2017) to avoid large artificial energy inputs arising from discrete time-stepping. Each simulation is run for a total of 150 time units.

3.4 Results

3.4.1 Flow structure

After the initial transient dynamics and a further adjustment period in each case that lasts until $t \approx 50$, the turbulence characterised by $\mathcal{K}'$ and $\mathcal{P}'$ reaches a quasi-steady state. Table 3.2 details turbulent quantities calculated for these quasi-steady regimes. The values highlight a key difference between the horizontally-forced simulation (case H) and the wave-forced simulations (case R and case P). The turbulent potential energy $\mathcal{P}'$ is much larger in the wave-forced cases than in case H, and this coincides with a

Table 3.2 Volume-averaged quantities as defined in section 3.2 further averaged in time for $t > 50$ for each numerical simulation. Note that the volume-averaged buoyancy Reynolds number is given by $Re_b = \varepsilon' \times 10^4$ when using the chosen non-dimensionalisation.

Simulation	$\mathcal{K}'$	$\mathcal{P}'$	ε'	χ'	Γ	Fr
H (vortical)	1.17×10^{-2}	2.11×10^{-3}	7.48×10^{-4}	2.77×10^{-4}	0.370	6.40×10^{-2}
R (waves)	1.45×10^{-2}	1.02×10^{-2}	4.64×10^{-4}	2.40×10^{-4}	0.518	3.19×10^{-2}
P (waves)	1.18×10^{-2}	7.56×10^{-3}	5.14×10^{-4}	2.55×10^{-4}	0.496	4.36×10^{-2}

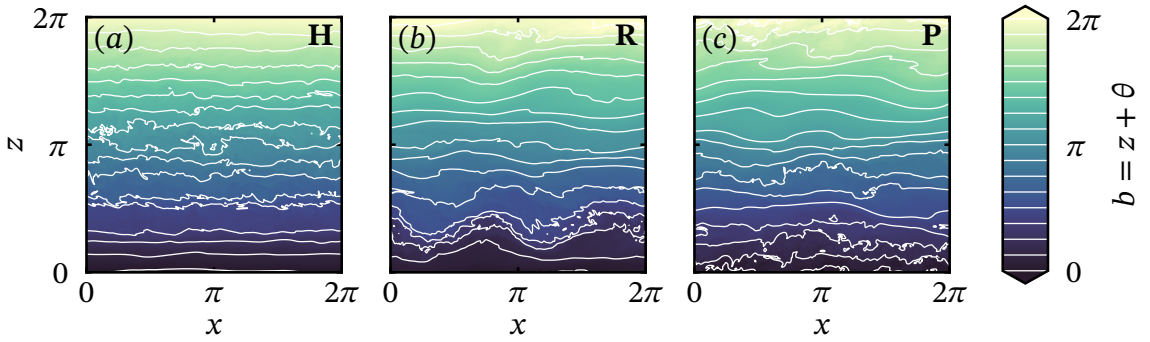

Fig. 3.2 Snapshots in the x-z plane at the midpoint of the computational domain of the total buoyancy field $b = z + \theta$ at $t = 150$ for flows forced by: (a) horizontal motions (case H); (b) internal waves with random phases (case R); (c) propagating internal waves (case P).

reduction in the TKE dissipation rate ε'. The value of χ' is remarkably consistent across the simulations, resulting in a larger value of Γ that is associated with more efficient mixing in cases R and P. All simulations exhibit values of the turbulent Froude number Fr that suggest the flow is in a stratification-dominated regime, i.e. $Fr \ll 1$.

Figure 3.2 shows contours of the buoyancy field in the vertical plane $y = 0$ at the final time of each simulation. These provide visual evidence of the qualitative difference between the wave-forced and horizontally-forced flows. In case H we observe mostly flat isopycnals except where there are small-scale overturns in the centre of the domain, suggestive of mixing driven by local shear instabilities. This contrasts with the wave-forced cases where we observe large vertical displacement of the isopycnals throughout the domain. Regions of statically unstable stratification typically occur through larger-scale overturnings than in case H, suggesting (perhaps unsurprisingly) that convective mechanisms may be more important for mixing in the wave-forced regime.

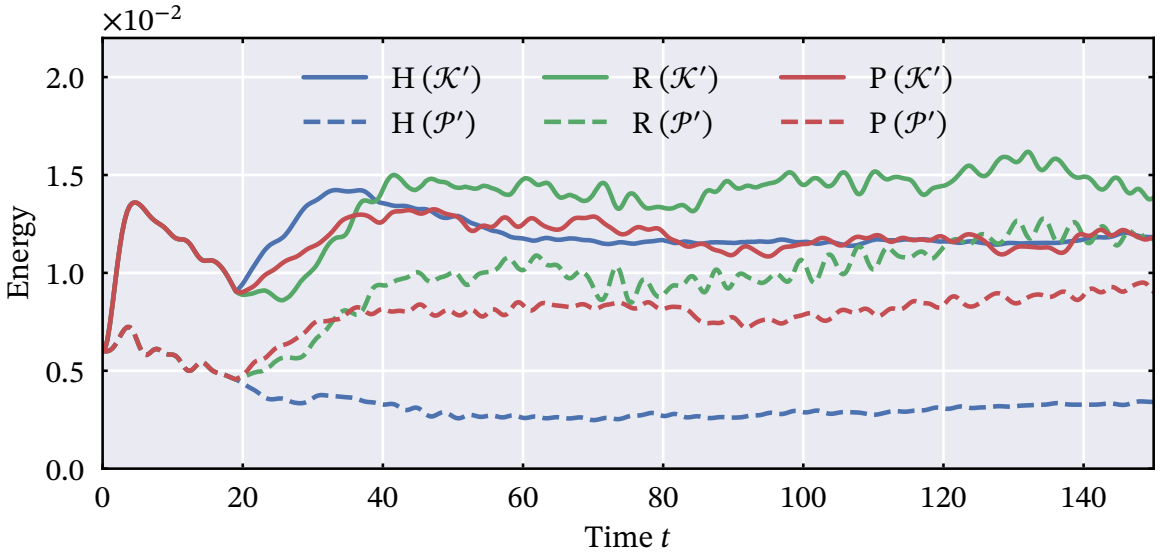

Fig. 3.3 Evolution with time of the volume-averaged kinetic energy $\mathcal{K}'$ (solid line) and potential energy $\mathcal{P}'$ (dashed line) for the simulations with: case H forcing (blue lines); case R forcing (green lines); and case P forcing (red lines).

3.4.2 Volume-averaged quantities

Figure 3.3 shows time series of the turbulent energy quantities $\mathcal{K}'$ and $\mathcal{P}'$ from each simulation. The energy time series for cases R and P (green and red lines) exhibit prominent oscillations that are absent in case H (blue lines). These oscillations can be attributed to internal waves exchanging energy between the kinetic and potential reservoirs. Since this oscillating buoyancy flux dominates the turbulent energy budgets (3.9) and (3.10), we consider the cumulative effect of each term in the energy budget rather than their instantaneous values. Figure 3.4 plots these cumulative (i.e. time-integrated) contributions over the period $t > 20$, when forcing is active in each simulation. This figure reveals another key difference between case H and the wave-forced cases R and P. The buoyancy flux $\mathcal{J}$ in case H is negative and acts to transfer energy from kinetic energy to potential energy. This is in some sense inevitable as the buoyancy flux must balance the dissipation χ' in the potential energy budget. In contrast, cases R and P have a positive mean buoyancy flux acting to transfer energy from the potential energy to the kinetic energy. This different energy pathway is consistent with the significant influence of the convective overturning apparent in figures 3.2b and 3.2c. Locally these large overturns contain excess potential energy that is transferred to kinetic energy as the locally unstable buoyancy gradient drives a flow.

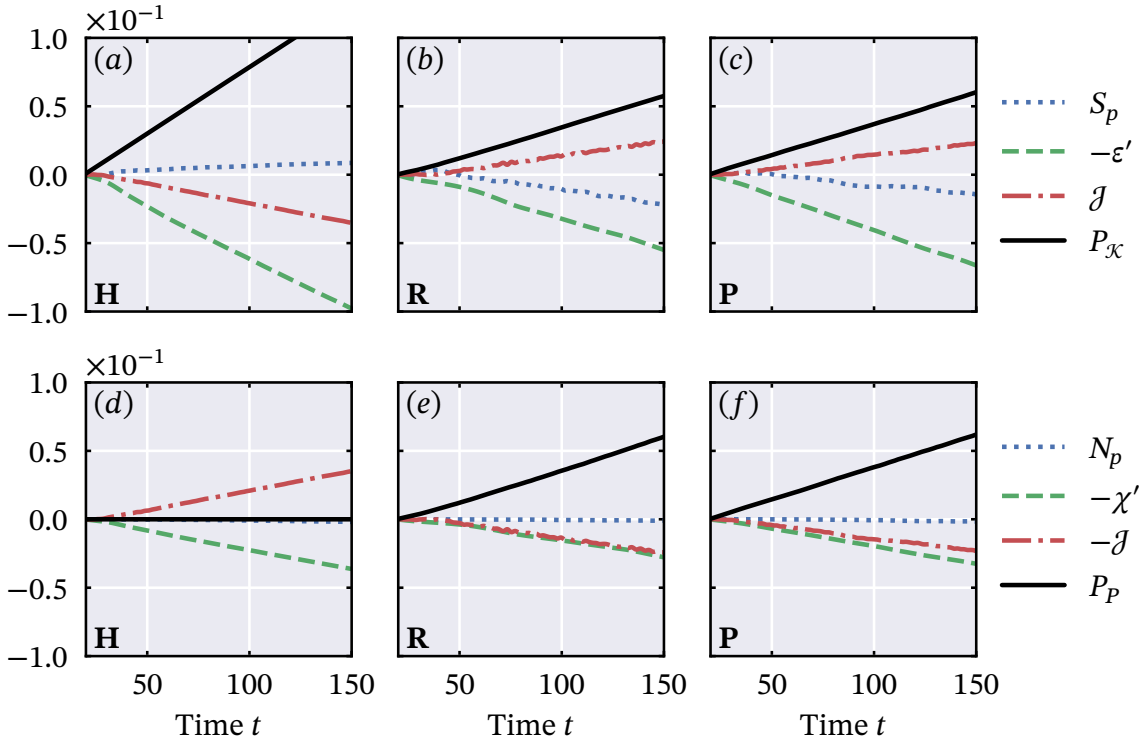

Fig. 3.4 Variation with time (after $t = 20$ when the forcing is switched on) of cumulative (time-integrated) budget terms from the kinetic energy budget (top row) and the potential energy budget (bottom row) as defined in (3.11)-(3.14) for the simulations associated with: (a), (d) case H; (b), (e) case R; and (c), (f) case P.

Figure 3.5a shows time series for the dissipation rates of kinetic energy (i.e. ε') and potential energy (i.e. χ') for the various simulations. As noted before, the late-time value of χ' is similar for all three simulations, whereas the value of ε' is lower in the wave-forced cases R and P than in the horizontally-forced case H. This leads to a higher mixing efficiency η and mixing coefficient Γ in the simulations R and P, as shown by the time series in figure 3.5b.

We recall that the total energy input rate due to the forcing is set to $P_K + P_P = 10^{-3}$, and so in a steady state we expect the total turbulent dissipation $\varepsilon' + \chi'$ to equal this value as well. The differing values of ε' between the wave-forced cases and case H actually mean that the total dissipation is greater than the total energy input for simulation H, whereas the opposite is true for simulations R and P. This difference is related to how the waves and turbulence interact with the horizontally-averaged mean flow. By inspecting the time series of the cumulative shear production S_p in figures 3.4a-c, we find that energy is extracted from the mean flow in case H. Conversely in the wave-forced flows, the mean flow extracts energy *from* the perturbation fields. Therefore, despite

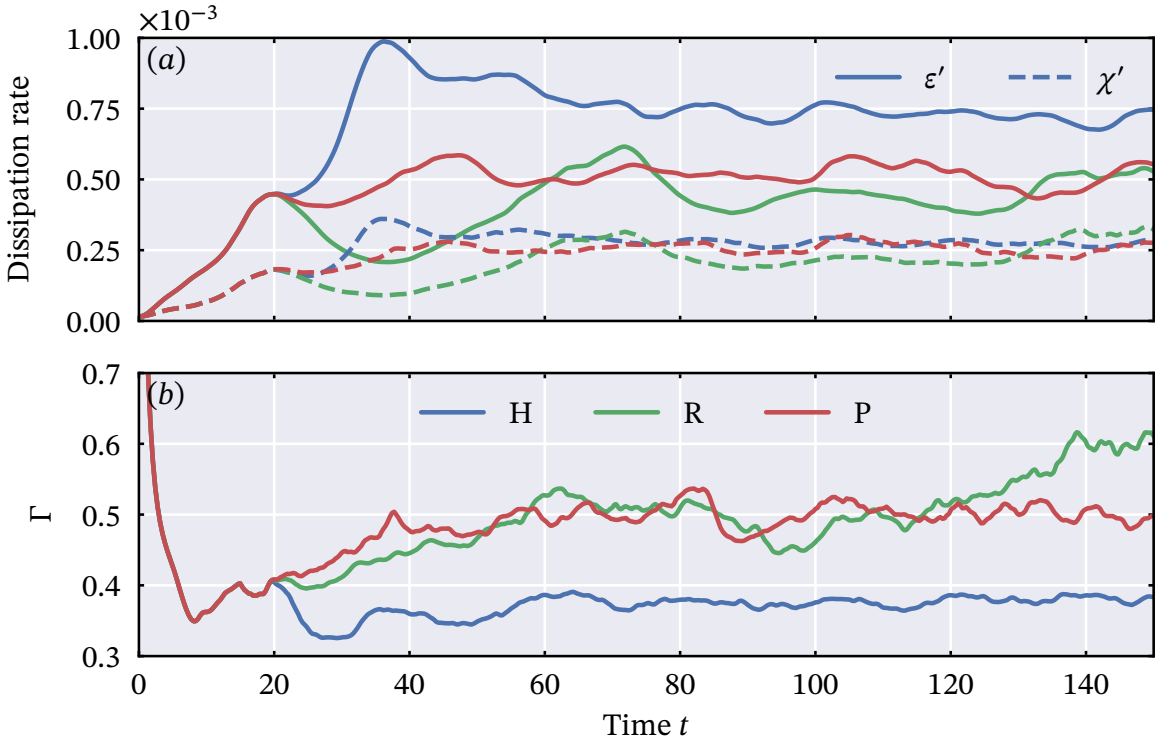

Fig. 3.5 Variation with time of: (*a*) the turbulent dissipation rates ε' (solid lines) and χ' (dashed lines); (*b*) instantaneous mixing coefficient $\Gamma = \chi'/\varepsilon'$ for: case H (blue lines); case R (green lines); case P (red lines).

the turbulence characterised by $\mathcal{K}'$ and $\mathcal{P}'$ being in a quasi-steady state, the mean flow is not. The kinetic energy of the mean flow $\overline{\mathcal{K}}$ changes by approximately 10% in each simulation, but remains at least 5 times greater than the energy in the perturbation field.

3.4.3 Spatial variation

Thus far we have relied on volume-averaged quantities to describe the flows that develop in our simulations. To investigate how localised processes may lead to the different pathways in the energy budget, we now consider how mixing properties vary throughout our domain. We can define local and horizontally-averaged measures of the TKE dissipation rate as

$$\varepsilon_L(\boldsymbol{x},t) = \frac{1}{Re}\frac{\partial u_i'}{\partial x_j}\frac{\partial u_i'}{\partial x_j}, \qquad \varepsilon_H(z,t) = \overline{\varepsilon_L} = \frac{1}{L_x L_y}\int_0^{L_x}\int_0^{L_y} \varepsilon_L \,\mathrm{d}x\,\mathrm{d}y. \tag{3.24}$$

The dissipation rate ε' as defined in (3.11) is simply the volume average of ε_L. Figure 3.6a shows a vertical plane snapshot of the local dissipation rate ε_L for the flow with

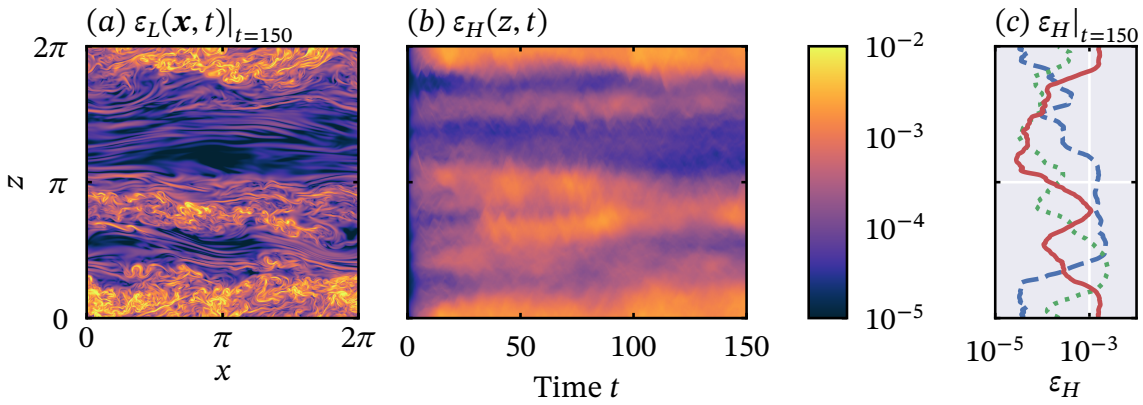

Fig. 3.6 (*a*) Snapshot in the x-z plane at the midpoint of the computational domain at final time $t = 150$ of the local TKE dissipation rate $\varepsilon_L(\mathbf{x},t)$. (*b*) Time variation of the horizontally averaged $\varepsilon_H(z,t)$ for simulation P. (*c*) Vertical variation of $\varepsilon_H(z,t)$ at final time $t = 150$ for the simulations associated with: case H (dashed blue line); case R (dotted green line); and case P (solid red line).

case P forcing at $t \approx 150$. Throughout the domain ε_L varies by three orders of magnitude, with strongest variation in the vertical direction. Highly turbulent layers with significant small-scale structure lie between more quiescent regions where ε_L drops below 10^{-4}. Figure 3.6b shows the spatio-temporal evolution of the horizontally-averaged dissipation rate $\varepsilon_H(z,t)$ and shows that these turbulent layers persist throughout the quasi-steady forced regime. The vertical profiles of $\varepsilon_H(z,t)$ also differ significantly between the simulations with different forcings as shown by figure 3.6c. This highlights how important the particular *type* of large-scale forcing is in modifying how turbulence arises and is sustained in the flow.

The large range of ε_H allows us to investigate correlations between quantities related to mixing across several orders of magnitude. We are particularly interested in spatio-temporal correlations between the dissipation rates of kinetic energy and buoyancy variance, and how these correlations may explain the high volume-averaged efficiency observed in the wave-forced simulations. Figure 3.7 shows the two-dimensional probability density function (pdf) of $\varepsilon_H(z,t)$ and the analogous term $\chi_H(z,t)$, the horizontally averaged potential energy dissipation rate, for the quasi-steady states of each simulation. Each pdf is constructed from a 2D histogram of $\log_{10}\varepsilon_H$ and $\log_{10}\chi_H$ with bins of size 1/64. Strikingly these plots show that Γ calculated from volume averages accurately describes the relationship between ε_H and χ_H over at least two orders of magnitude. All three simulations in fact have a Pearson correlation coefficient greater than $r = 0.9$ for ε_H and χ_H. Although the dissipation rates in more turbulent regions (in the

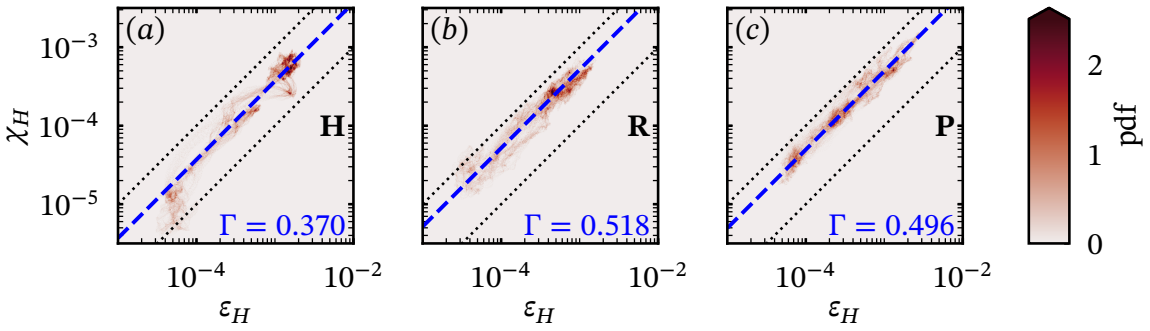

Fig. 3.7 Two-dimensional pdf of horizontally averaged dissipation rates ε_H and χ_H calculated at each output time for $t > 50$. The two dotted lines on each panel mark values of $\Gamma = 0.1$ and $\Gamma = 1$, and the blue dashed lines show the volume-averaged value of Γ for each simulation from table 3.2. (a) shows data from the case H simulation, (b) shows data from the case R simulation, and (c) shows data from the case P simulation.

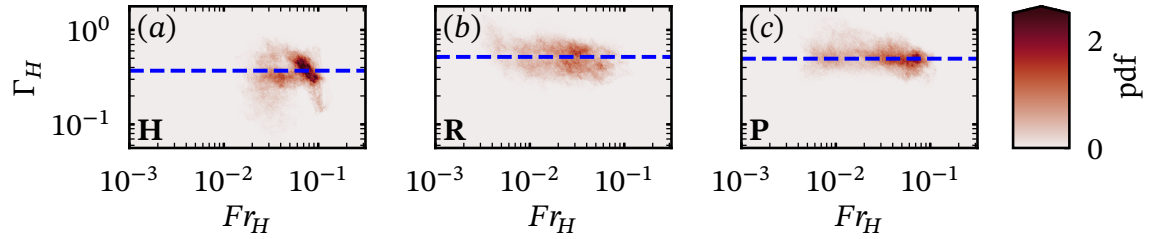

Fig. 3.8 Two-dimensional pdf of Fr_H and Γ_H calculated from horizontally-averaged quantities for $t > 50$. (a) shows data from the case H simulation, (b) shows data from the case R simulation, and (c) shows data from the case P simulation.

sense of being associated with larger values of ε_H) are the dominant contribution to Γ, these results show that the difference in Γ across the simulations is not solely due to changes in these (more turbulent) regions. The pdfs in figure 3.7 instead show that the wave-forced cases also exhibit higher values of $\Gamma_H \coloneqq \chi_H/\varepsilon_H$ in the less energetic (and hence lower local dissipation rate) regions of the flow.

Figure 3.8 further highlights this distinction by showing the analogous 2D pdf of the turbulent Froude number and appropriately horizontally-averaged flux coefficient Γ_H. As we are considering horizontally-averaged quantities, the definition of the Froude number is modified from (3.18) to account for the (in practice) small changes in the mean buoyancy profile to yield

$$Fr_H(z,t) = \frac{2\varepsilon_H}{{Ri_0}^{1/2}\left(1+\frac{\partial\bar{\theta}}{\partial z}\right)^{1/2}\overline{\boldsymbol{u}'\cdot\boldsymbol{u}'}}. \tag{3.25}$$

Figure 3.8 shows that all three flows can be considered as low Fr at all heights in the domain, with each simulation having a maximum Fr_H of approximately 0.1. We therefore expect no dependence of Γ_H on Fr_H based on the scaling arguments of Maffioli et al. (2016). Figures 3.8b and 3.8c show this behaviour clearly for the two wave-forced cases R and P, where the pdf spreads evenly around the mean value. The limited range of Fr_H in case H makes it difficult to draw conclusions about Γ-Fr scaling from figure 3.8a. The tilted, intense cluster of points near $Fr = 10^{-1}$ is however suggestive of a negative correlation between Γ and Fr_H in the more turbulent parts of the domain.

We can extend our approach of investigating localised correlations by considering relationships between quantities calculated locally at each grid point. A single-time snapshot provides more than 10^9 data points for each variable in this approach, so we use the full 3D flow fields at the final time $t = 150$ as an example to investigate local correlations in each simulation. Figure 3.9 shows the 2D pdf of ε_L (as defined in (3.24)) and the analogous term χ_L calculated from the final-time snapshots associated with each simulation. The pdf is constructed by the same method as for figure 3.7, using a histogram of the logarithms of each quantity. The positive correlation between ε_L and χ_L is still evident in these plots, although all three cases have larger departures from the volume average than in figure 3.7. In the horizontally-forced (case H) simulation, with data plotted in figure 3.9a, there is a relatively uniform spread in the pdf along lines of constant Γ. When compared to figure 3.7a where the pdf clusters at higher values of ε_H and χ_H, this indicates that the horizontally-averaged quantities are dominated by contributions from highly-turbulent locations (associated with larger values of ε_L and χ_L) within each horizontal plane. The wave-forced cases R and P also exhibit this behaviour, with figures 3.9b and 3.9c highlighting a peak at low dissipation rates that is absent from the horizontal averages.

We also investigate how local correlations between Γ and Fr lead to the scalings observed in figure 3.8. Since the turbulent Froude number is not well-defined in the case of statically unstable stratification, we choose to keep the mean buoyancy gradient in our local definition of a turbulent Froude number:

$$Fr_L(\boldsymbol{x}, t) = \frac{2\varepsilon_L}{{Ri_0}^{1/2}\left(1 + \frac{\partial\overline{\theta}}{\partial z}\right)^{1/2}\boldsymbol{u}' \cdot \boldsymbol{u}'}. \tag{3.26}$$

This is also appropriate on physical grounds, when the Froude number is interpreted as a ratio of time scales associated with the turbulence, which can conceivably vary substantially locally, and the time scale associated with the density stratification, which

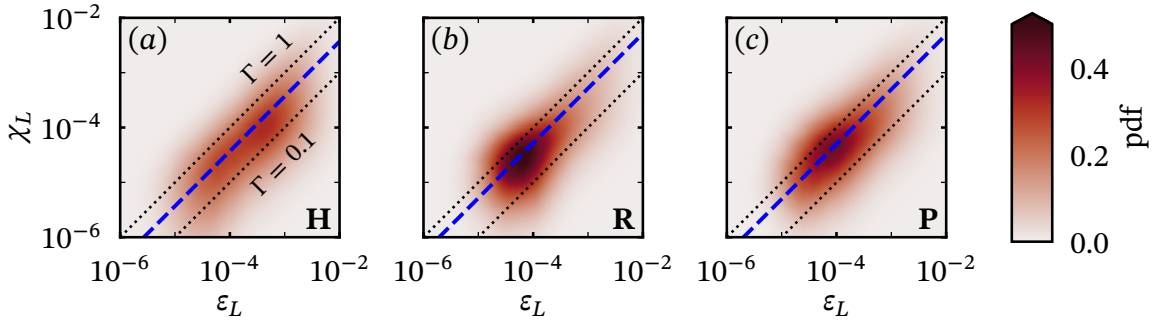

Fig. 3.9 Two-dimensional pdf of χ_L and ε_L calculated locally at every grid point of a final-time $t = 150$ snapshot for each simulation: (*a*) Case H; (*b*) Case R, (*c*) Case P. Dotted lines highlight values of $\Gamma = 0.1$ and $\Gamma = 1$, and blue dashed lines show the mean value of Γ as in figure 3.7.

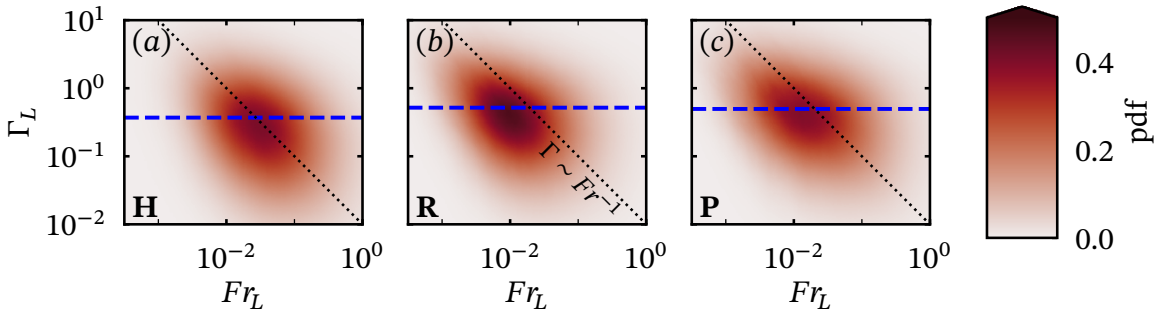

Fig. 3.10 Two-dimensional pdf of Γ_L and Fr_L calculated locally from the same final-time $t = 150$ snapshots as figure 3.9 for each simulation: (*a*) Case H; (*b*) Case R, (*c*) Case P. Blue dashed lines are as in figure 3.8, and the black dotted lines show the scaling $\Gamma \sim Fr^{-1}$.

should be determined by a global measure of the 'background' buoyancy frequency. Figure 3.10 plots the 2D pdf of Fr_L defined in this way and the local value of the mixing coefficient $\Gamma_L := \chi_L/\varepsilon_L$ for each simulation, once again at the final time $t = 150$. The difference compared to figure 3.8 is striking, with a much larger spread in values of Γ. Specifically, in every simulation there is no indication that the scaling argument $\Gamma \sim Fr^0$ holds locally. All three panels of figure 3.10 are in fact suggestive of an inverse correlation between Γ and Fr, similar to the scalings suggested by Maffioli et al. (2016) and Garanaik and Venayagamoorthy (2019) for *high* or at least moderate Fr. The statistical nature of the scaling theories involving Fr means that the lack of a clear correlation is not too surprising. Even if the local value of Γ was related to some local measure of the Froude number, our use of the mean stratification in the definition of Fr_L hinders our ability to capture local correlations in regions with variable buoyancy gradients.

3.4.4 Energy spectra

Even though figures 3.7 and 3.8 suggest that intermittency in each simulation does not affect the mixing efficiency, at least to leading order, the spatially inhomogeneous dissipation causes issues when considering energy spectra. In all of the simulations, the existence of relatively quiescent layers (as is particularly apparent in figure 3.6a) leads to an (at best) moderate volume-averaged buoyancy Reynolds number, in that when using volume-averaged dissipation rate ε', $Re_b < 10$ for all three cases. The buoyancy Reynolds number may be interpreted as a measure of the size of the inertial range expected between the Ozmidov wavenumber $m_O := (N^3/\varepsilon')^{1/2}$ and the Kolmogorov wavenumber $m_K := (\varepsilon'/\nu^3)^{1/4}$, since $Re_b \equiv (m_K/m_O)^{4/3}$. This leads to a lack of information in the vertical wavenumber energy spectrum. For example, energy associated with a particular wavenumber may represent energy at dissipation scales in one part of the domain, but energy in turbulent eddies elsewhere. Figures 3.11a and 3.11b plot the compensated energy spectra of every simulation for horizontal wavenumber κ and vertical wavenumber m respectively. Both energy spectra show a roll-off above wavenumber 50 consistent with the 'small-scale spectra' classified in Maffioli (2017). Before this roll-off, the horizontal spectrum in figure 3.11a shows a $E \sim \kappa^{-5/3}$ scaling for every energy component of each simulation, consistent with, for example, Brethouwer et al. (2007). As expected there is a local energy peak at the forcing wavenumber $\kappa = 3$ in every component except the vertical velocity and buoyancy components in case H. The vertical wavenumber spectra in figure 3.11b are compensated with m^2, although the agreement with this scaling is not clear. In particular the modest value of Re_b (and corresponding small dynamic range of scales) combined with significant variability at low wavenumbers make it hard to draw definitive conclusions about the nature of the energy distribution.

We implement continuous wavelet transforms to overcome this challenge, in an attempt to capture the spectral properties of the actively turbulent 'patches' within such spatio-temporally intermittent flows. Following Torrence and Compo (1998), we use the Morlet wavelet to construct an energy spectrum $E(m, z)$ of both vertical wavenumber and vertical position. A single 'high dissipation' spectrum is obtained by averaging the energy spectrum over heights z for which $Re_{b,H}(z) > 10$, where

$$Re_{b,H} = \frac{\varepsilon_H Re}{Ri_0\left(1 + \frac{\partial\bar{\theta}}{\partial z}\right)}, \tag{3.27}$$

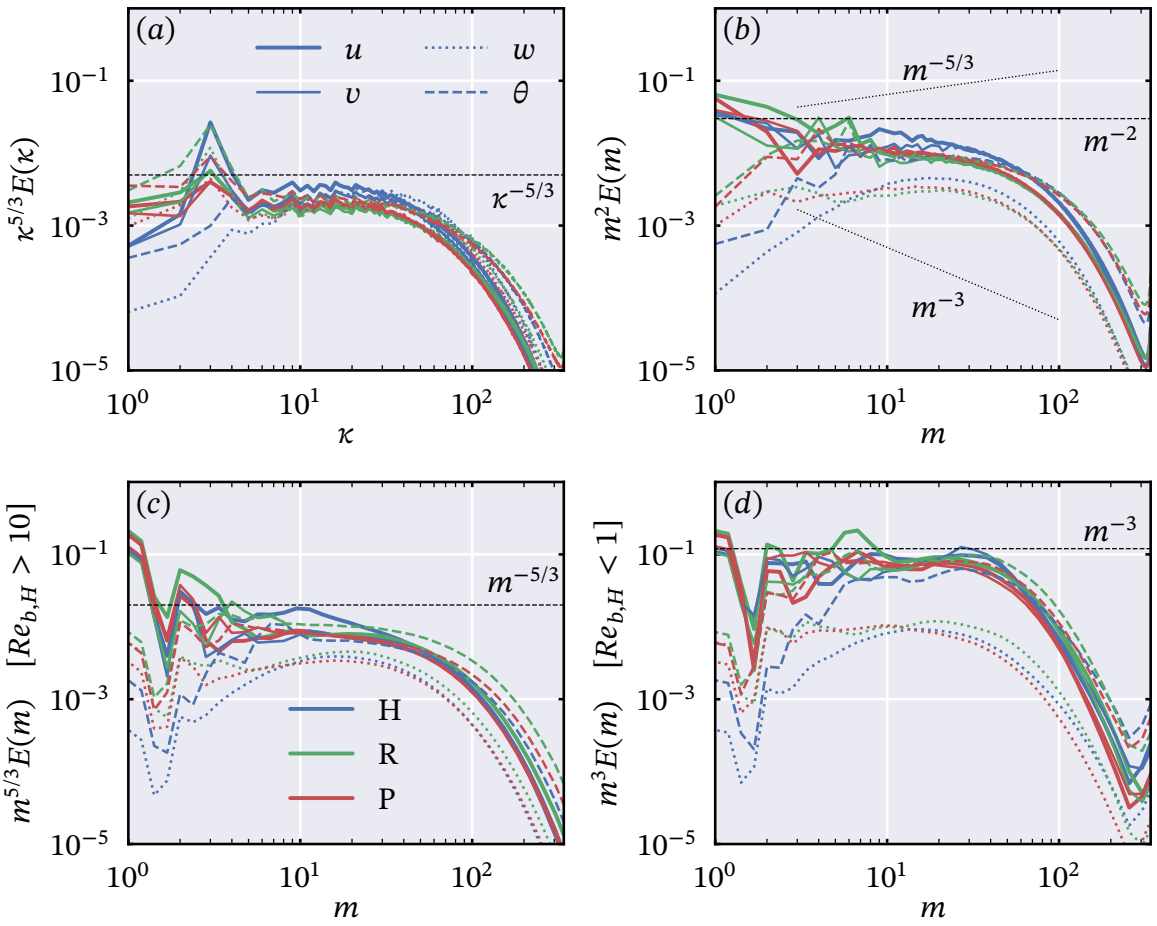

Fig. 3.11 One-dimensional compensated energy spectra of the final time $t = 150$ snapshot of each simulation. Energy components associated with different components are plotted with different line types: u (thick solid lines); v (thin solid lines); w (dotted lines); ρ (dashed lines), while the data from different simulations are plotted with different colours: case H (red); case R (green); case P (blue). (a) shows the horizontal wavenumber Fourier spectrum and (b) the vertical wavenumber Fourier spectrum for the entire datasets. (c) shows the vertical wavenumber 'high dissipation' wavelet spectra averaged over heights where $Re_{b,H}(z) > 10$ as defined in (3.27) and (d) shows the analogous 'low dissipation' spectra for $Re_{b,H}(z) < 1$.

is the buoyancy Reynolds number computed from horizontal averages in an analogous fashion to Fr_H in (3.25). A corresponding 'low dissipation' spectrum is obtained by averaging over heights where $Re_{b,H} < 1$. Figures 3.11c and 3.11d plot these spectra for each energy component and each simulation. The high Re_b spectra show a scaling similar to $m^{-5/3}$ in the wavenumber range of $O(10)$. Combined with the horizontal wavenumber spectrum in figure 3.11a, this result is at least consistent with the existence of a local inertial subrange. In every simulation, the energy spectra associated with $Re_b < 1$ are noticeably steeper than those from regions where $Re_b > 10$. The steeper 'low dissipation' spectra for each simulation all exhibit an approximate m^{-3} scaling in the same $O(10)$ wavenumber range. This scaling is dimensionally consistent with buoyancy-dominated motion where N^{-1} is the dominant time scale.

The different scalings associated with regions of high and low $Re_{b,H}$ suggest that the stratified turbulence in our simulations may be thought of as spatio-temporally intermittent regions or 'patches' of near-isotropic turbulence spaced throughout a more quiescent flow whose dynamics are buoyancy-dominated, analogously to the 'strongly stratified' flow considered by Portwood et al. (2016). The appearance of an m^{-3} scaling in the low Re_b spectrum is consistent with the m^{-3} scaling obtained by Maffioli (2017) when considering only large horizontal scales. Furthermore, high values of Re_b can naturally be associated with smaller scale motion, as evident in the snapshot of figure 3.6a, so the two results appear closely related.

We must however be careful when interpreting these spectra, particularly at lower wavenumbers. The continuous wavelet transform discretises wavenumber space as

$$k_j = 2^{j/4}, \qquad j \in \mathbb{N}. \tag{3.28}$$

Since we use a pseudospectral method in our simulations, the flow field we resolve is composed entirely of modes at integer wavenumbers. This means that the wavelet spectra are in some sense over-resolved at low wavenumbers, with multiple wavenumbers between the integer values. The scalings at moderate wavenumbers discussed above are in some sense also inconsistent with theoretical predictions. Calculating the Ozmidov wavenumber associated with the (locally) high $Re_{b,H}$ regions gives a value of $m_O \approx 20$, and a corresponding Kolmogorov wavenumber is $m_K \approx 200$. However it is common in experiments of turbulence to observe roll-off associated with dissipation before the Kolmogorov scale (e.g. Pope 2000), and even in the 'high Re_b' regions, we expect the limited range of dynamical scales to affect the spectra.

3.5 Discussion and conclusions

We have performed direct numerical simulations of stratified turbulence sustained by different forms of large-scale body forcing. The simulation of case H implements the horizontal vortical mode forcing prescribed by Maffioli (2017) that injects horizontal kinetic energy into randomly phased columnar vortex modes. The other two simulations force a field of resonant internal gravity waves at large scales of our computational domain as motivated by Furue (2003). The simulation of case R randomly phases each wave at every time step, whereas the simulation of case P shifts the phase of each wave according to the dispersion relation for linear internal gravity waves. Each simulation is initialised with a flow dominated by vertically-sheared horizontal modes that is motivated by ambient internal waves with large horizontal wavelengths. The forcing is activated after some initial transient behaviour, and after a further adjustment time the turbulence characterised by the perturbations from the horizontal mean reaches a statistically quasi-steady state.

We find that the quasi-steady states in the wave-forced simulations (cases R and P) have significantly more potential energy than the state achieved by the vortical mode forcing in the simulation of case H. This increased potential energy is provided by the direct forcing of the buoyancy field in cases R and P. We measure irreversible mixing as the dissipation of buoyancy variance χ that, as we later show in chapter 5, provides an excellent approximation to the 'true' rate of diapycnal mixing for the flows considered here. In the simulation of case H, this mixing must come via a transfer of energy from the TKE to the potential energy through the buoyancy flux. The buoyancy forcing in cases R and P allows this energy transfer to reverse, with mixing made possible without a mean transfer from kinetic to potential energy. This reversal in buoyancy flux can be associated with larger overturning, as seen in figure 3.2, and thus more convective mixing. The wave-forced simulations also exhibit a higher mixing efficiency than the horizontally forced simulation (case H), which is consistent for flows where mixing occurs through convective mechanisms. The vortical mode forcing used in the simulation of case H forces neither the vertical velocity nor the buoyancy field, and therefore cannot produce such large-scale convective overturns.

The qualitatively different energy pathways for mixing in each case also coincide with a change in the interaction between the mean shear flow and the perturbations. Whereas the turbulence extracts energy from the mean flow in the simulation for case H, the wave-forced simulations (cases R and P) show a small transfer in energy from the

perturbations *to* the mean flow on average. This small change partially contributes to the reduced value of the TKE dissipation rate ε' in the wave-forced cases.

The kinetic energy associated with the mean shear is not constant in each case, but varies slowly over time due to the exchange with the perturbation field. In our simulations, the mean shear modes are intended to represent waves at horizontal scales larger than our computational domain. Since the perturbation energy and dissipation rates are statistically quasi-steady, we believe that the small-scale turbulence is still representative of the geophysical flows which motivate us to conduct these idealized simulations. Background shear modes appear in many studies of forced stratified turbulence (Smith and Waleffe 2002; Waite and Bartello 2006; Lindborg 2006; Brethouwer et al. 2007) and are shown not to impact the turbulent dynamics significantly. Furthermore a recent study by Fitzgerald and Farrell (2018) shows that the emergence of vertically sheared horizontal flows also occurs in a forced 2D Boussinesq system. This result suggests that energy increase in the shear modes is due to a wave-mean flow interaction, which may explain why we observe the energy increase in the wave-forced cases but not from the horizontal vortical mode forcing utilized in case H.

In every simulation, the turbulent dissipation organises into quasi-horizontal layers. The vertical location of these layers varies depending on the forcing type, but it is currently unclear what determines the change in vertical structure between the simulations. Initial analysis shows that regions of high dissipation do not simply correlate with local changes in the background shear and stratification, and thus further research is needed to investigate the mechanisms by which these layers form and are sustained. This predominantly vertical variation in the dissipation rate allows us to investigate correlations between the turbulent dissipation rate and the buoyancy variance destruction rate over orders of magnitude. Intriguingly, we find that the ratio between the two, a local measure of the coefficient Γ, remains close to the volume-averaged ratio in both regions of high and low dissipation. We deduce that the local mixing efficiency is independent of turbulent intermittency below the scale of the forcing, and instead depends predominantly on the type of large-scale forcing implemented. This further supports the notion that the larger overturnings in the wave-forced cases correspond to a fundamentally different (and in some sense 'convective') mixing mechanism from that observed in the simulation of case H.

In the wave-forced simulations the dissipation rate ε is not correlated with the background stratification, so we also obtain a wide range of values for the horizontally-averaged turbulent Froude number Fr_H defined in (3.25). This confirms the lack of dependence of Γ on Fr in the low-Fr regime for these quasi-steady states. The vortical

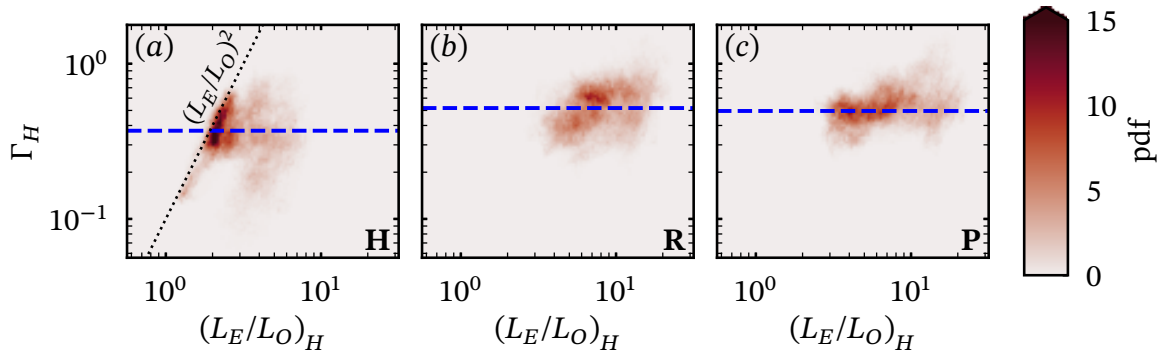

Fig. 3.12 Two-dimensional pdf of Γ and L_E/L_O calculated from horizontally-averaged quantities. Blue dashed lines show the mean value of Γ in each case and the black dotted line in (a) plots the $(L_E/L_O)^2$ scaling found in (3.33). As before, (a) plots data from case H, (b) plots data from case R, (c) plots data from case P.

mode-forced simulation (case H) does not however produce such a wide range in Fr_H. This may be a consequence of the purely horizontal forcing allowing vertical scales to adjust locally, as in the scalings of Billant and Chomaz (2001) where the vertical Froude number F_v adjusts to a constant of $O(1)$. Despite the reduced Fr range in case H, there is still at least a hint of Fr-dependence for Γ in figure 3.8a at the largest values of $Fr_H \approx 0.1$. Previous studies (e.g. Lindborg 2006) have shown that the strongly stratified limit of low Fr requires $Fr \leq O(10^{-2})$, suggesting that the observed dependence in case H is outside this regime. The variation in Γ is more clearly displayed in figure 3.12 where, following Garanaik and Venayagamoorthy (2019) henceforth denoted GV19, we plot Γ against the length scale ratio L_E/L_O. In particular, we plot these quantities defined in terms of horizontal averages as $\Gamma_H = \chi_H/\varepsilon_H$ and

$$\left(\frac{L_E}{L_O}\right)_H = \frac{{Ri_0}^{3/4}\overline{\theta'^2}^{1/2}}{{\varepsilon_H}^{1/2}\left(1+\partial\bar{\theta}/\partial z\right)^{1/4}}. \tag{3.29}$$

At first the results shown in figure 3.12a for case H appear inconsistent with any of the scalings proposed by GV19, with $\Gamma \sim (L_E/L_O)^2$ for values of L_E/L_O being $O(1)$. However this scaling can be reproduced by combining various self-consistent assumptions used in that paper, as follows.

Firstly, taking $Fr = O(1)$, we assume that the turbulent kinetic energy $\mathcal{K}' \sim {w'}^2$ and that its dissipation rate is governed by the turbulent time scale $T_L = \mathcal{K}'/\varepsilon'$, such that $\varepsilon' \sim {w'}^2/T_L$. We then scale the density field by taking $g{\rho'}_{\text{rms}}/\rho_0$ to be a 'reduced gravity' acceleration with velocity scale w' and time scale N^{-1}. Typical vertical displacements

are taken to be $z \sim w'/N$ so that the potential energy density $E_P = g\rho' z/\rho_0 \sim {w'}^2$, and its dissipation rate is governed by the buoyancy time scale N^{-1}, giving $\chi' \sim \mathcal{P}'/T \sim {w'}^2 N$. These results provide the scalings

$$\Gamma = \frac{\chi'}{\varepsilon'} \sim \frac{{w'}^2 N}{{w'}^2/T_L} = NT_L, \tag{3.30}$$

$$\frac{L_E}{L_O} = \left(\frac{g\rho'_{\text{rms}}}{\rho_0}\right) \varepsilon'^{-1/2} N^{-1/2} \sim (w'N)\left(\frac{{w'}^2}{T_L}\right)^{-1/2} N^{-1/2} = (NT_L)^{1/2}. \tag{3.31}$$

Recalling that $NT_L = Fr^{-1}$, these scalings become

$$\Gamma \sim Fr^{-1}, \qquad\qquad Fr \sim \left(\frac{L_E}{L_O}\right)^{-2}, \tag{3.32}$$

and hence at $Fr = O(1)$, we have

$$\Gamma \sim \left(\frac{L_E}{L_O}\right)^2. \tag{3.33}$$

We therefore recover the behaviour shown in figure 3.12a. GV19 instead find that $\Gamma \sim Fr^{-1}$ for $Fr = O(1)$, but $Fr \sim (L_E/L_O)^{-2}$ for $Fr < O(1)$. Indeed, the derivation of (3.31) relies only on assumptions that are also applicable in the low Fr regime. We do not believe that combining these scalings is inconsistent, since both rely on the assumptions that the dominant time scale for density-related terms is N^{-1} and the dominant time scale for kinetic energy dissipation is $T_L = \mathcal{K}'/\varepsilon'$, and at $Fr = O(1)$ both of these time scales may affect the dynamics. On the other hand in a flow dominated by internal gravity waves, it is likely that N^{-1} is the dominant time scale for both the velocity and density fields. This is evident in figures 3.12b and 3.12c, where the wave-forced cases show Γ_H to be less dependent on $(L_E/L_O)_H$, consistent with the low Fr and high L_E/L_O regime, and at least conceivably consistent with a flow dominated by internal waves, thus still strongly affected by stratification. The larger mean value of L_E/L_O in cases R and P can be associated with larger buoyancy excursions, providing further evidence that the wave-forced cases exhibit more convective behaviour. It appears that forcing with vortical modes at the same rate of energy input produces turbulence that can (at least locally) access a higher Froude number regime than the internal wave forcing. The fact that this $Fr = O(1)$ regime does not show the same L_E/L_O scaling as in GV19 may hinder the ability to infer Froude numbers from observations in this intermediate

range. The frequent appearance of $O(1)$ values of L_E/L_O in observations (e.g. Moum 1996) motivates the need for further research into mixing for flows in which $Fr = O(1)$.

The appearance of a $Fr = O(1)$ scaling in case H could suggest that the difference in volume-averaged Γ between the simulations is purely related to a difference in the average Froude number. However, figure 3.8a also shows a region at low values of Fr_H where Γ_H appears independent of Fr_H and importantly takes a much lower value than in the wave-forced cases R and P. The results of Maffioli et al. (2016) also show $\Gamma \approx 0.35$ for values of Fr similar to cases R and P but using a forcing scheme with a greater similarity to the forcing scheme used in case H. We are therefore confident that the difference in the large-scale forcing is the primary contributor to the changes in Γ between the simulations, rather than a simple dependence on Fr. Although all the simulations here exhibit Γ_H-Fr_H scalings consistent with the regimes predicted by Maffioli et al. (2016) and GV19, we believe that it is important to understand how different flows lead to scatter around these regimes. To that end, a better understanding of how the local correlations in figures 3.9 and 3.10 are distributed would be invaluable. It is not currently clear how the Fr_L dependence of Γ_L shown in figure 3.10 leads to a global Γ that is independent of Fr for $Fr \ll 1$.

Despite the significant differences in the mixing properties between the vortical mode and wave-forced simulations, spectral analysis reveals remarkable similarity between the energy spectra associated with each flow. At moderate wavenumbers of $O(10)$, each component of the energy spectra appears to follow universal scalings, with wavelet analysis revealing distinct vertical wavenumber scalings between the turbulent and quiescent regions. The emergence of an m^{-3} scaling in the low-Re_b portions of the domain is particularly of note, since it is consistent with the energy spectra being determined exclusively by the buoyancy frequency (as discussed for example in section 14.3 of Davidson 2013). Differences in the energy spectra between the three simulations are only noticeable at low wavenumbers associated with the large-scale flow, despite the contrasting mixing efficiencies for each simulation persisting throughout the domains. This emphasises the importance of understanding the larger scale flow dynamics when inferring small-scale mixing from spectra. With regions of the flows producing an m^{-3} scaling consistent with Billant and Chomaz (2001), but variations in Γ associated with the various larger scale forcing strategies, it appears that the particular form of the larger-scale forcing retains a fundamental imprint on the properties of the small-scale mixing. Therefore, it is at least plausible that mixing events in the ocean could be sensitive to the particular form of the large-scale energy injection, suggesting that generic, 'unified' arguments such as those presented by Kunze (2018) should be treated with caution.

Our results highlight a significant challenge in the measurement and parameterization of turbulent mixing in the ocean. The turbulent flux coefficient Γ, commonly used to infer mixing rates from the TKE dissipation rate, varies by over 30% depending on the nature of the larger scale flow, although local estimates of Γ can of course vary by much more. Mixing generated by internal gravity waves results in $\Gamma \approx 0.5$, consistent with recent studies of decaying stratified turbulence (de Bruyn Kops and Riley 2019) but above results from numerical studies forcing turbulence through purely horizontal motion (Maffioli et al. 2016). This is also far higher than the value 0.2 from Osborn (1980) typically used in observational studies, and also observed in simulations of statistically steady forced linearly sheared stratified turbulence with high dynamic range (Portwood et al. 2019). We conjecture that this difference may be associated with the mixing being more appropriately characterised as being 'convectively-driven' rather than 'shear instability-driven'. We can distinguish between these two characterisations by relating 'convectively-driven' mixing to turbulence arising from a source of available potential energy, compared to flows where energy is primarily supplied to the turbulence by a shear flow and the mixing is 'shear-driven'.

This is consistent with previous studies (e.g. Davies Wykes et al. 2015) that show purely buoyancy-driven flows with non-monotonic stratification can achieve very high values of mixing efficiency. Mixing via shear instabilities often also occurs through a secondary convective instability arising due to the roll-up of the density field in a Kelvin–Helmholtz billow. The larger values of L_E/L_O in our wave-forced simulations suggest the overturns are larger than from such shear-driven flows, consistent with the idea that the flow is 'convectively-driven' by 'breaking' waves.

When interpreting our results in the context of ocean mixing, some caveats must be addressed. As mentioned in the Introduction, a significant fraction of mixing in the ocean occurs in surface and bottom boundary layers. The physics determining mixing efficiency in these regions is rather different from the ocean interior, where wind-driven shear and tidal flows act as important drivers of turbulence and mixing (Thorpe 2005).

Furthermore, our simulations are performed with a molecular Prandtl number of 1 for computational efficiency, rather than a typical oceanic value of 7 for a thermally stratified region. Numerical studies of shear instabilities (Smyth et al. 2001; Salehipour et al. 2015) have shown that higher Prandtl numbers can lead to a significant decrease in the mixing efficiency. This factor may bring our results closer to the value used in oceanographic estimates, but it is unclear how the differences in mixing efficiency between the simulations would change at higher Pr.

Another issue which needs to be considered is the potential 'patchiness' of mixing, with the turbulent mixing in the ocean exhibiting significant spatio-temporal variability. Observational studies that focus on small-scale mixing frequently isolate patches of turbulence for their measurements in intermittent oceanic flows (e.g. Moum 1996). Both Smyth et al. (2001) and Ijichi and Hibiya (2018) produce a $\Gamma \sim (L_T/L_O)^{4/3}$ scaling from such patches, where L_T is the Thorpe scale. The construction of this scaling (see Ijichi and Hibiya (2018) for further details) is fundamentally associated with two assumptions consistent with high Fr dynamics, in particular that the characteristic time and length scales are determined from the turbulence properties alone, largely unaffected by the ambient stratification. The first assumption is that the turbulence is largely unaffected by stratification, and using a classical mixing length argument then leads to

$$L \sim \frac{\mathcal{K}'^{3/2}}{\varepsilon'}; \qquad \kappa_T \equiv \frac{\Gamma\varepsilon'}{N^2} \sim \mathcal{K}'^{1/2}L. \tag{3.34}$$

Here, κ_T is the turbulent 'eddy' diffusivity of density, defined in terms of the 'mixing length' L and the characteristic turbulent velocity scale $\mathcal{K}'^{1/2}$. The second assumption is that this mixing length $L \sim L_T$, leading to $\Gamma \propto (L_T/L_O)^{4/3}$ in patches where the ambient stratification has little effect on the turbulent mixing properties, although it is of course possible that this scaling can be observed in situations where the underlying assumptions are no longer completely justified.

Indeed, the results presented here pose an interesting question of how best to model mixing in a spatio-temporally intermittent flow. The combination of our wavelet analysis and the work of Maffioli (2017) suggests that the m^{-3} portion of the energy spectrum may be associated with larger scales and regions with smaller turbulent dissipation rates. The associated nonlinear buoyancy-dominated flow could be thought to act as a background from which the turbulent patches develop intermittently. Since high Fr flows are associated with lower values of mixing efficiency, it is therefore important to quantify the relative contributions to mixing of these highly energetic isolated patches compared to the total background.

The main differences between our simulations, coinciding with the change in Γ, are an increase in the energy component of the vertical velocity and the available potential energy in our simulations. Despite these changes being most significant at large scales in our domain, validation of our results in the field would be difficult. Scales we refer to as large require high resolution equipment to resolve in the ocean: for example if we take a velocity scale of $U_0 = 10^{-2}\mathrm{ms}^{-1}$ and a buoyancy frequency $N_0 = 10^{-2}\mathrm{s}^{-1}$, then our domain length will be less than 10m given the Re, Ri_0 values we have chosen. An

investigation of high-resolution measurements of vertical velocity and density fluctuations that coincide with the appearance of an $E \sim m^{-3}$ vertical wavenumber spectrum would be invaluable for determining the nature of flows at these scales. A better understanding of which flows are dominated by convective wave breaking and which mix through primarily horizontal motion or even shear instabilities, would then allow us to constrain mixing estimates better and improve our predictions of spatial patterns in diapycnal transport.

Chapter 4

Shear-induced breaking of internal gravity waves

In this chapter, we investigate the flow arising from superposing a large-amplitude plane internal gravity wave and a sinusoidal shear flow. This setup is motivated by the observations of Alford and Pinkel (2000), where wave breaking events are seen in the presence of both vertical shear and large-amplitude internal gravity waves. Given the results of chapter 3, where convective mechanisms associated with internal gravity waves lead to higher mixing efficiency, we are also interested in the mixing properties of this flow, since a combination of shear and convective processes are involved in its development. We use the linear theory of ray tracing to gain physical insight on the wave-shear interaction, although the large amplitude of the internal wave means that the interaction is strongly nonlinear. By analysing the energetics of this flow, we gain a better understanding of the complex three-way interaction between internal waves, mean shear, and turbulence.

4.1 Observations of internal waves in the thermocline

As we discussed earlier in §1.2, internal waves are thought to be the primary pathway through which energy is transferred from the large scales associated with geophysical forcing to small scales and turbulence in the ocean interior. On vertical scales larger than $O(10\,\mathrm{m})$, the distribution of energy in internal waves is well described by the empirical spectrum of Garrett and Munk (1972), and energy transfers occur through weakly nonlinear wave-wave interactions (Müller et al. 1986; Polzin and Lvov 2011). At smaller scales, the flow becomes highly nonlinear and the form of the energy spectrum changes

to the power law scaling $E(m) \sim N^2 m^{-3}$ (as observed e.g. by Gargett et al. 1981). In the previous chapter, we explored how this scaling naturally emerges at scales where nonlinear motions are constrained by buoyancy effects. Furthermore, the local dissipation rates in the simulations of chapter 3 (shown in figure 3.9) varied over at least two orders of magnitude, highlighting strong spatial intermittency. This is reminiscent of the oceanographic study of Baker and Gibson (1987) that highlights strong intermittency in turbulent dissipation rates from observations of stratified oceanic layers. Away from boundaries such intermittency suggests that the turbulence may be sustained by a collection of localised, transient 'wave breaking' events that transfer energy downscale from the internal wave field.

Further evidence of turbulence arising from wave breaking processes can be found in the thermocline observations of Alford and Pinkel (2000). Intermittent metre-scale overturns, where the vertical profile of density becomes statically unstable, are used to indicate the presence of turbulence. In the observations, these overturns favourably sample regions with high 'vertical strain'. Strain in this context refers to local changes in $(N^2(z))^{-1}$ due to vertical convergence or divergence of the flow, and regions with low local stratification relative to the mean are associated with high strain. Significant fluctuations in local stratification (and therefore strain) are suggestive of large amplitude internal waves. There are however a range of possible mechanisms by which the waves can overturn and break, and it is unclear how different types of wave breaking may affect the mean rates of diapycnal mixing. Larger scale vertical shear in the observations of Alford and Pinkel (2000) is often colocated with the internal wave field, and is likely to play an important role in the breaking process.

Figure 4.1, taken from Alford and Pinkel (2000), presents a selection of 'overturning events' with seemingly different characteristics in terms of the roles of internal waves and shear. Figure 4.1a shows overturns emerging in a region where the Richardson number persistently takes low values, suggesting that overturning and turbulence here is primarily triggered through shear instabilities. By contrast, the overturns in figure 4.1b are not always associated with low Ri. A key feature in the location of the overturns is the strong heaving of isopycnals as internal waves pass through the profile. Indeed Alford and Pinkel (2000) find the majority of overturns to be associated with regions of high strain, where isopycnals move apart and the local stratification is reduced. Figure 4.1c presents in some senses a hybrid of the previous breaking events, with both high strain and low Richardson number colocated with the overturns.

We must note that the resolution of the velocity measurements used to estimate the shear in these observations is only 6.4m, so it is possible that low local values of the

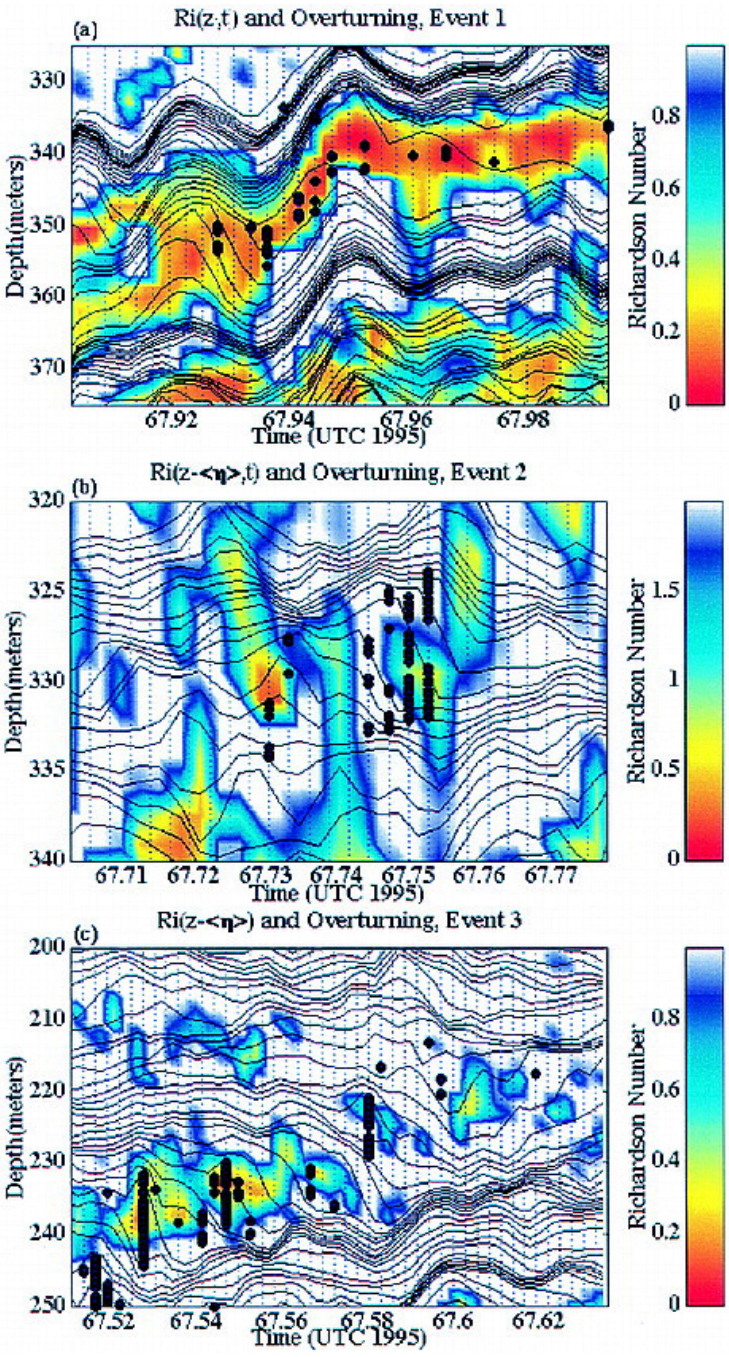

Fig. 4.1 Depth-time plots of individual overturning events in the thermocline. 6.4-m Richardson number is plotted with colour, with red colours indicating low Ri. Note the change in colour scale for panel (b). Isopycnals with a mean spacing of 1m are also plotted, with black dots marking the locations of overturns whose maximum Thorpe displacement $L_{\max} \geq 2$m. Faint blue, dotted, vertical lines show the times of individual CTD profiles used to measure the buoyancy frequency N. Figure taken from Alford and Pinkel (2000). © American Meteorological Society. Used with permission.

gradient Richardson number $Ri_g = N^2/S^2$ can drive shear instabilties at smaller scales in event (b). The brief appearance of low Ri_g should not however be associated too closely with wave breaking due to shear instabilities. Density overturns are indeed themselves associated with negative values of Ri_g, and so any smooth transition to this state involves passing through small, positive values of Ri_g. 'Billows' arising from shear instabilities can also break down through secondary, convective instabilities making a distinction between shear and convective processes even more challenging.

In this case however, the vertical extent of the overturns in figures 4.1b and 4.1c is comparable to the vertical scale of the strain features. This suggests that the overturns here may be associated with the breakdown of large amplitude internal waves. Identifying the mechanisms by which this may happen is therefore important for understanding the distribution of internal wave-driven mixing in the ocean.

4.2 Internal wave breaking

Since the time scales associated with the overturns in figure 4.1 are short relative to the inertial period $2\pi/f$, and the waves appear to be of relatively high frequency, we restrict the following discussion to the breakdown of internal *gravity* waves and neglect any effects due to the rotation of the Earth. In our earlier discussion of energy transfers between internal waves in the ocean, we focused on resonant interactions that rely on nonlinearities being weak. Waves in this framework, as originally considered by Phillips (1966), must necessarily have relatively small amplitude in contrast with the high strain conditions seen in the observations of figure 4.1.

The existence of parametric instabilities in the small amplitude case proved useful as a starting point for the early work by Mied (1976) and Drazin (1977) on the stability of finite amplitude internal gravity waves. Through linear stability analysis in a 2D plane, they independently found that the finite amplitude waves were generally unstable to small perturbations. Unlike for parallel shear flows, there is importantly no critical Richardson number above which internal waves are linearly stable. In the limited number of calculations they performed the instabilities take the form of parametric instabilities, mimicking the wave resonance behaviour of the small amplitude case. Klostermeyer (1991) extended this analysis to include three-dimensional perturbations, and found that the fastest growing modes are three-dimensional for waves that produce regions of statically unstable density. He however cautioned against the separate consideration of 'static instability' and other resonant or non-resonant interactions, de-

ducing that the presence of statically unstable density profiles in itself is not sufficient to determine the nature of the dominant instability of a particular wave.

Lombard and Riley (1996) expanded upon this work with a comprehensive study of linear stability analysis that varies the amplitude of the wave, the angle of wave propagation, and the wave vector of the perturbation. Their results are consistent with the previous studies while also revealing new insights into the problem. By considering waves at steepness (i.e. dimensionless amplitude) $s = 0.9$ and $s = 1.1$ for a propagation angle of $\varphi = 45°$, Lombard and Riley (1996) found no qualitative change in the distribution of the fastest growing modes across the static instability threshold of $s = 1$. Unlike in Klostermeyer (1991), they found that the fastest growing modes remain two-dimensional, even as the wave steepness increases and the growth rates of 3D perturbations increases. This is due to the difference in the wave propagation angle, which was set to $\varphi = 72°$ by Klostermeyer (1991). Indeed Lombard and Riley (1996) found significant changes to the fastest growing modes as the propagation angle increases. At higher values of φ the growth rate of two-dimensional perturbations decrease, and the associated parametric instabilities become insignificant. This is important in the context of the above thermocline observations, where Alford and Pinkel (2000) estimated a propagation angle of $\varphi \approx 85°$ for the waves associated with high strain values.

Few studies have researched the fully nonlinear breakdown of internal gravity waves through direct numerical simulation (DNS). Koudella and Staquet (2006) performed two-dimensional DNS of a plane internal gravity wave in a periodic domain, propagating at 45°. Their results are consistent with the analysis of Lombard and Riley (1996), with resonant interactions primarily driving the breakdown of the wave. The study is however limited by the restriction to two dimensions, and therefore excludes potentially interesting subsequent dynamics.

A later numerical study by Fritts et al. (2009*a*,*b*) used high resolution 3D DNS to resolve more details of the breakdown at high *Re*. Their triply-periodic computational domain is aligned with the phase of the wave and contains only one wavelength to allow for the resolution of small-scale turbulence. Fritts et al. (2009*a*,*b*) considered a wave propagating at $\varphi = 72°$ for the steepness values $s = 0.9$ and $s = 1.1$. In agreement with Klostermeyer (1991) and Lombard and Riley (1996) the simulations show that the wave breaks down through three-dimensional non-resonant processes in both cases. Initial static instability of the wave does not appear to significantly impact its breakdown, characterised by the emergence of streamwise-aligned counter-rotating vortices in both simulations. Although $s > 1$ is typically associated with wave breaking through convective instability (e.g. Thorpe 2018), the above studies cautioned using such a threshold to de-

note qualitatively different events. High steepness waves are more likely to break down through three-dimensional instabilities, but it seems that these do not necessarily have to be convective in nature.

We have so far only discussed the breakdown of a finite amplitude internal gravity wave triggered by initially small perturbations. As we have seen in section 4.1, internal waves in the ocean cannot be considered in isolation and interact with numerous flow features including other internal waves and mean currents. The observations of Alford and Pinkel (2000) particularly highlight the presence of mean vertical shear that varies on a larger scale than the internal waves. An important feature in the interaction of an internal gravity wave and a shear flow was first outlined in the work of Bretherton (1966) and Booker and Bretherton (1967). These studies revealed the possible emergence of critical levels, where the horizontal phase speed of the waves matches the velocity of the shear flow. As vertical propagation of the waves is halted at these critical levels, local wave amplitudes can increase and cause the waves to break. This phenomenon was subsequently confirmed by the experiments of Koop and McGee (1986).

As a wave approaches a critical level, its propagation angle approaches 90° (such that propagation is purely horizontal) and the associated velocity field produces that of a sinusoidal shear flow. Since velocity and density perturbations are out of phase for internal gravity waves, the maximum shear in this configuration occurs where the local density gradient is equal to the mean. Indeed, at $\varphi = 90°$ the minimum gradient Richardson number only decreases below the Miles–Howard criterion of 1/4 when the wave amplitude is large enough for regions of static instability to appear. Due to the phase differences, statically unstable density profiles become centred on regions where there is *zero* shear induced by the wave.

Winters and Riley (1992) investigated the linear stability of such an one-dimensional shear flow to elucidate the breaking mechanisms of an internal wave approaching a critical level. They found similar growth rates for perturbations associated with shear instabilities and convective instabilities, suggesting that the breaking process may involve a combination of these mechanisms. The eigenfunctions associated with the shear instability appear unaffected by the presence of nearby unstable stratification, whereas convective instabilities are suppressed in the plane of the shear flow. The fastest growing modes associated with the statically unstable regions are aligned perpendicular to the plane of the wave shear, making the breakdown inherently three-dimensional.

Motivated by these stability calculations, Winters and D'Asaro (1994) performed 3-D hyper-diffusive simulations of internal wave packets approaching a critical level in a shear flow. Consistent with their previous study, they observed the emergence of con-

vective rolls in the spanwise plane as the waves approach the critical level. The rolls are in turn strongly affected by the enhanced shear of the refracted wave. The low-resolution hyperdiffusive simulations are able to capture the initial breakdown of the wave, but cannot capture the subsequent details of turbulence and mixing in the flow.

Higher resolution studies of internal gravity waves with shear were performed by Fritts et al. (2013) and Fritts and Wang (2013), although their approach is quite different. Rather than focusing on waves propagating through a larger scale mean shear flow, they considered the effect of 'finescale' shear on a single, large scale internal wave of steepness $s = 0.5$. Motivated by atmospheric flows, they superimposed high wavenumber vertical shear onto the single-wave, periodic domain setup of Fritts et al. (2009*a*,*b*). The superposition of the shear and the internal wave produces regions susceptible to shear instability in the initial condition, and advection of the density perturbations by the shear also leads to the emergence of convective rolls in the spanwise plane. Fritts et al. (2013) also considered the case where the shear is not aligned with the internal wave, but found that wave-shear interactions in such cases are weak and do not lead to a breakdown of the wave.

We shall consider a similar problem to that of Fritts et al. (2013) in this chapter, using DNS to investigate the flow arising from a superposition of a plane internal gravity wave and a sinusoidal shear flow in a triply periodic domain. Motivated by the observations of Alford and Pinkel (2000), we prescribe the shear flow to vary on a larger vertical scale than the wavelength of the internal wave. We are primarily interested in understanding the key mechanisms involved in the interaction of the wave and the shear, as well as the properties of the turbulence generated from the breakdown of the wave. In this idealised study, we do not specify the source of the internal gravity wave, but simply choose appropriate parameters to remain consistent with the observations. We acknowledge that for many oceanographic applications, it is useful to quantify mixing associated with specific generation mechanisms, such as oceanic lee waves (Legg 2021).

The remainder of the chapter is organised as follows. Section 4.3 describes the setup of the numerical simulations, and also presents the results of some basic ray tracing calculations to provide a link between our nonlinear flow and linear predictions of critical levels from wave-mean flow analysis. Section 4.4 presents the results of our DNS, focusing on the nature of the wave breaking, the mixing achieved by turbulence, and the effect of the breaking wave on the mean flow. Our findings are summarised in section 4.5, and their implications are then discussed in the context of internal wave driven mixing in the ocean.

4.3 Numerical simulations

4.3.1 Nonlinear 3D simulations: domain and initial conditions

As in the previous chapter, we use DIABLO to perform direct numerical simulations of the Navier–Stokes equations subject to the Boussinesq approximation and an imposed, constant mean stratification, namely

$$\boldsymbol{\nabla} \cdot \boldsymbol{u} = 0, \tag{4.1}$$

$$\frac{\partial \boldsymbol{u}}{\partial t} + (\boldsymbol{u} \cdot \boldsymbol{\nabla})\, \boldsymbol{u} = -\boldsymbol{\nabla} p + \frac{1}{Re} \nabla^2 \boldsymbol{u} + Ri_0 \theta \hat{\boldsymbol{z}}, \tag{4.2}$$

$$\frac{\partial \theta}{\partial t} + (\boldsymbol{u} \cdot \boldsymbol{\nabla})\, \theta = \frac{1}{RePr} \nabla^2 \theta - w. \tag{4.3}$$

Here θ is the dimensionless buoyancy perturbation to a uniform background stratification. The total dimensionless buoyancy is therefore given by

$$b = z + \theta, \tag{4.4}$$

which is related to the full, *dimensional* density profile by

$$\rho = \rho_0 - b\Delta\rho, \tag{4.5}$$

where ρ_0 is a typical scale for the mean density and $\Delta\rho$ is a typical scale for the density fluctuations. The dimensionless parameters in (4.1)-(4.3) are

$$Re = \frac{L_0 U_0}{\nu}, \qquad Pr = \frac{\nu}{\kappa}, \qquad Ri_0 = \frac{g\Delta\rho L_0}{\rho U_0^2} = \frac{N_0^2 L_0^2}{U_0^2}, \tag{4.6}$$

where N_0 is the buoyancy frequency of the uniform background stratification. In all of our simulations, the bulk Richardson number Ri_0 is set equal to one so that the inertial time scale L_0/U_0 is equal to the buoyancy time scale ${N_0}^{-1}$. The Prandtl number Pr is also set to one in every simulation to enable, subject to the constraint of the computational resources available to us, adequate resolution of small-scale dynamics at (what we believe to be) sufficiently high Reynolds number.

Motivated by observations of wave breaking in the thermocline, we consider the flow developing from the superposition of a plane internal gravity wave and a sinusoidal shear flow. Alford and Pinkel (2000) estimated the vertical wavenumber of large amplitude internal waves associated with overturning events to be about $m \approx 1/(12\text{m})$. By inspecting vertical profiles of the effective strain rate $\partial w/\partial z$ and accounting for Doppler

shifts by horizontal currents, they also estimated a typical horizontal wavenumber of the waves as $\kappa \approx 1/(180\text{m})$. These estimates coincide with measurements of vertical shear that vary on a length scale of $O(30\text{m})$. It is not possible to resolve centimetre-scale dissipation adequately using direct numerical simulations (DNS) while also resolving the dynamics associated with lengths $O(100\text{m})$. We therefore perform a 'miniaturised' simulation of the shear and internal wave interaction by reducing the Reynolds number to a computationally tractable value.

In a periodic domain of dimensionless height 2π, the base shear flow is given by $\overline{u}(z) = \sin z$. The minimum gradient Richardson number of this flow $Ri_m = \min(Ri_g)$ is equal to the bulk Richardson number $Ri_0 = 1$, with Ri_g taking this value at the edge of the domain ($z = 0,\ 2\pi$) as well as at the mid-height $z = \pi$. This ensures that the background shear profile is linearly stable, as shown by Balmforth and Young (2002). We superimpose this shear flow and a plane internal gravity wave with dimensionless wave vector $\boldsymbol{k} = (k, l, m) = (1/4, 0, 3)$. Compared to the observational estimates of Alford and Pinkel (2000) the wave has a similar propagation angle, and the ratio between the vertical wavenumber of the shear ($m = 1$) and the vertical wavenumber of the wave ($m = 3$) also provides a good match to the observations. Preliminary simulations showed that waves oriented perpendicular to the shear flow (with $k = 0,\ l \neq 0$) produce insignificant interactions even at large amplitude, consistent with the findings of Fritts et al. (2013). We therefore focus only on the case where the planes of the wave and shear are aligned.

We perform simulations at Reynolds numbers of 5000 and 8000. The dimensionless domain size is chosen to fit one horizontal wavelength of the internal wave and one wavelength of the shear. Preliminary runs showed that the scale of spanwise motion that develops is small, so we choose a narrow domain of size $8\pi \times \pi/2 \times 2\pi$. Setting the kinematic viscosity to $\nu = 10^{-6}\text{m}^2\,\text{s}^{-1}$, typical of water, and choosing a typical buoyancy frequency of $N_0 = 5 \times 10^{-3}\text{s}^{-1}$, we can deduce typical velocity and length scales from our choices of Re and Ri_0. For the highest value of $Re = 8000$ this gives $L_0 = 1.26\text{m}$ and $U_0 = 6.3\text{mm}\,\text{s}^{-1}$, and hence an effective domain size of approximately $32\text{m} \times 2\text{m} \times 8\text{m}$.

In the dimensionless Boussinesq system (4.1)-(4.3), internal gravity waves in the x-z plane are given by the real parts of the polarisation relations

$$\theta = \frac{s}{m} e^{i(\boldsymbol{k}\cdot\boldsymbol{x} - \omega t + \phi)}, \qquad u = \frac{-is\omega}{k} e^{i(\boldsymbol{k}\cdot\boldsymbol{x} - \omega t + \phi)}, \qquad w = \frac{is\omega}{m} e^{i(\boldsymbol{k}\cdot\boldsymbol{x} - \omega t + \phi)}, \tag{4.7}$$

where ϕ is an arbitrary constant phase and $s > 0$ is the wave steepness, representing a dimensionless amplitude that satisfies $s = 1$ when buoyancy contours first become vertical somewhere in the domain. The dimensionless wave frequency ω satisfies the

dispersion relation

$$\omega^2 = \frac{\widetilde{N}^2 k^2}{k^2 + m^2}, \tag{4.8}$$

where we have written $Ri_0 = \widetilde{N}^2$ for consistency with the standard notation of dimensional internal gravity waves. $\widetilde{N} = N_0 L_0 / U_0$ can be interpreted as the dimensionless buoyancy frequency. To construct the initial condition for our simulations, we take the positive root of (4.8), set $k = 1/4$ and $m = 3$, and (without loss of generality) choose $\phi = 0$. Superposed with the shear flow, this gives the initial condition

$$u(\boldsymbol{x}, 0) = \sin z + \frac{4\widetilde{N}s}{\sqrt{145}} \sin\left(\frac{x}{4} + 3z\right), \qquad w(\boldsymbol{x}, 0) = -\frac{\widetilde{N}s}{3\sqrt{145}} \sin\left(\frac{x}{4} + 3z\right), \tag{4.9}$$

$$\theta(\boldsymbol{x}, 0) = \frac{s}{3} \cos\left(\frac{x}{4} + 3z\right). \tag{4.10}$$

As mentioned above, all simulations are run with $Ri_0 = 1$ and hence also $\widetilde{N} = 1$. The values of wave steepness s used in the simulations are outlined with all other relevant parameters in table 4.1.

The initial conditions for the buoyancy and velocity fields are displayed in figure 4.2 for two values of s used in the simulations. Small-amplitude, three-dimensional noise is added to the velocity field to allow the development of spanwise motion from the two-dimensional initial condition of (4.9). All simulations begin on a uniformly-spaced grid at the 'initial resolution' specified in table 4.1. This resolution corresponds to a grid spacing of $\Delta x = \pi/256 \approx 1.2 \times 10^{-2}$. As the simulations develop, this spacing is compared to the minimum Kolmogorov length scale calculated from the horizontally averaged turbulent dissipation rate

$$L_K(t) = \min_z \left(\varepsilon_H(z,t) Re^3\right)^{-1/4}, \qquad \varepsilon_H(z,t) = \frac{1}{Re} \overline{\frac{\partial u_i'}{\partial x_j} \frac{\partial u_i'}{\partial x_j}}. \tag{4.11}$$

Here an overbar denotes a horizontal average, and a prime denotes the deviation from that horizontal average. Once L_K becomes smaller than the initial Δx, the flow is upscaled to a higher resolution grid with a grid spacing of $\Delta x = \pi/512 \approx 6.1 \times 10^{-3}$. The upscaling is achieved through performing an inverse fast Fourier transform onto the higher resolution grid to preserve the spectral form of the flow fields. At late times in the simulations, L_K once again rises above the initial grid resolution as the turbulence decays. Once this happens, the extra Fourier modes associated with the higher resolution are truncated and we return to simulating the flow on the initial grid.

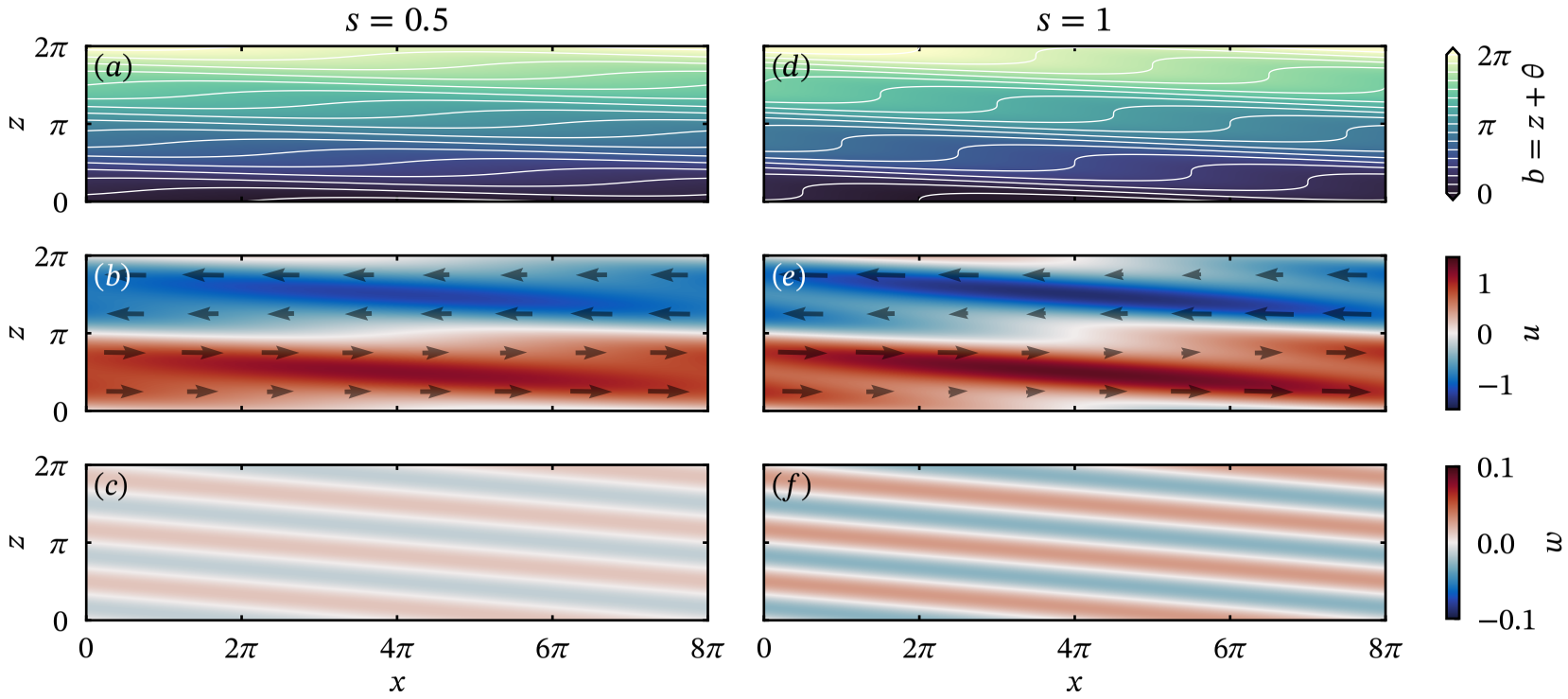

Fig. 4.2 Initial condition as defined in (4.9)-(4.10) for (a)-(c) $s = 0.5$; (d)-(f) $s = 1$. (a) and (d) plot contours of the total buoyancy field $b = z + \theta$; (b) and (e) plot the streamwise velocity u along with a quiver plot of the *total* velocity field; (c) and (f) plot the vertical velocity field w.

Table 4.1 Parameters used in the simulations.

Simulation	R8s1	R8s0	R5s1	R5s0
Reynolds number (Re)	8000	8000	5000	5000
Wave steepness (s)	1	0.5	1	0.75
Richardson number ($Ri_0 = \widetilde{N}^2$)	1			
Prandtl number (Pr)	1			
Domain size ($L_x \times L_y \times L_z$)	$8\pi \times \pi/2 \times 2\pi$			
Initial resolution	$2048 \times 128 \times 512$			
Maximum resolution	$4096 \times 256 \times 1024$			

4.3.2 Wave propagation using ray theory

In the absence of any mean flow, the internal gravity wave (4.7) propagates (in terms of its energy) at the group velocity

$$\boldsymbol{c_g} = \left(\frac{\partial\omega}{\partial k}, \frac{\partial\omega}{\partial m}\right) = \frac{m\widetilde{N}}{(k^2+m^2)^{3/2}}\,(m,-k)\,, \tag{4.12}$$

where we have taken the positive root of the dispersion relation (4.8) to match the initial condition. For $k, m > 0$ the wave therefore propagates down and to the right. In a constant mean flow $\boldsymbol{U}$, the frequency of the internal gravity wave appears to change as the wave is Doppler shifted. The frequency seen by a stationary observer, which we shall refer to as the *extrinsic* frequency, is given by

$$\omega = \boldsymbol{U}\cdot\boldsymbol{k} + \widehat{\omega}, \tag{4.13}$$

where $\widehat{\omega}$ is the frequency arising from the dispersion relation (4.8), which we shall refer to as the *intrinsic* frequency. This intrinsic frequency may equivalently be defined as the frequency observed when travelling with the mean flow. The terminology regarding Doppler shifts can often be unclear from the literature, with Sutherland (2010) and Bühler (2014) disagreeing on the extrinsic/intrinsic distinction. In defining the extrinsic frequency ω as that seen by a stationary observer, we follow the notation and terminology of Bühler (2014).

We now consider how an internal gravity wave is modified as it propagates through a (mean) shear flow. One key assumption in this analysis is that the mean flow varies on a much larger scale than the wave. In our setup of (4.9)-(4.10) the vertical wavelength of the mean shear is only three times that of the internal wave, so the following analysis cannot be expected to describe the dynamics quantitatively. Furthermore the large val-

ues of wave steepness we consider ($s \geq 0.5$) break the underlying linear assumption at the heart of the theory. Nevertheless considerable insight about the nature of the wave breaking *can* surprisingly be gained from a linear ray tracing analysis.

We consider the propagation of an internal wave through the one-dimensional mean shear flow $\overline{u}(z)$. Assuming that this shear flow varies 'slowly' in z, the extrinsic frequency defined in (4.13) becomes

$$\omega(k, m, z) = \overline{u}(z)k + \frac{\widetilde{N}k}{\sqrt{k^2 + m^2}}. \tag{4.14}$$

The wave will then propagate along a 'ray' in the direction of the *extrinsic* group velocity

$$\frac{dx}{dt} = \frac{\partial \omega}{\partial k} = \overline{u} + \hat{c}_{g,x}, \qquad \frac{dz}{dt} = \frac{\partial \omega}{\partial m} = \hat{c}_{g,z}, \tag{4.15}$$

where $\hat{\boldsymbol{c}}_{\boldsymbol{g}}$ is the intrinsic group velocity detailed in (4.12). Since the mean shear flow is independent of time, the extrinsic frequency will be conserved along the ray, that is $d\omega/dt = 0$. The wave vector $\boldsymbol{k} = (k, m)$ must therefore vary along the ray such that

$$\frac{dk}{dt} = -\frac{\partial \omega}{\partial x} = 0, \qquad \frac{dm}{dt} = -\frac{\partial \omega}{\partial z} = -k\frac{d\overline{u}}{dz}. \tag{4.16}$$

The horizontal wavenumber $k = k_0$ is conserved along the ray, whereas the vertical wavenumber m will change according to the mean shear.

In the simple case of a constant mean shear $\partial\overline{u}/\partial z = S_0$, the vertical wavenumber satisfies $dm/dt = -kS_0$. For positive k, the vertical wavenumber therefore decreases in the presence of positive shear, and increases in the presence of negative shear. As m increases, with k kept constant, the intrinsic frequency $\widehat{\omega}$ decreases and the group velocity vector becomes closer to horizontal (as can be inferred from (4.12) for large m). In fact, conservation of $\omega = \omega_0$ combined with the form of (4.14) can predict the existence of a *critical level* where the intrinsic frequency $\widehat{\omega}$ drops to zero and m becomes infinite. Setting $\widehat{\omega} = 0$ in (4.14) implicitly defines the height of a critical level as

$$\omega_0 = \overline{u}(z_c)k_0. \tag{4.17}$$

As waves propagate towards a critical level, they typically grow in amplitude until they 'break' through instabilities. This growth can (at least initially) be described by considering the conservation of wave action.

Except in special circumstances, internal waves do *not* conserve energy as they propagate along a ray. In the linear framework considered above, another quantity known

as wave action instead satisfies a conservation equation. We define wave action as

$$\mathcal{A} = \frac{\overline{E}}{\widehat{\omega}}, \qquad E = \frac{1}{2}|\boldsymbol{u}'|^2 + \frac{Ri_0}{2}|\theta|^2, \tag{4.18}$$

where $\overline{E}$ is the horizontally-averaged energy of the wave. The conservation equation for wave action can be derived from the linearised momentum equation (e.g. Bühler (2014)) and takes the form

$$\frac{\partial \mathcal{A}}{\partial t} + \frac{\partial(\mathcal{A} c_{g,z})}{\partial z} = 0. \tag{4.19}$$

We can now combine this conservation equation with the ray equations of (4.15) to give a system of three ODEs that describe the evolution of the path and amplitude of the internal wave. Recall that in (4.15), the time derivative is defined as $d/dt = \partial/\partial t + \boldsymbol{c_g} \cdot \boldsymbol{\nabla}$, so we can rewrite (4.19) as

$$\frac{dx}{dt} = \overline{u}(z) + \frac{\widetilde{N} m(z)^2}{\left({k_0}^2 + m(z)^2\right)^{3/2}}, \quad \frac{dz}{dt} = \frac{-\widetilde{N} k_0 m(z)}{\left({k_0}^2 + m(z)^2\right)^{3/2}}, \quad \frac{d\mathcal{A}}{dt} = -\mathcal{A}\frac{\partial c_{g,z}}{\partial z}. \tag{4.20}$$

Here $m(z)$ can be inferred from the dispersion relation (4.14) as

$$m(z) = k_0 \sqrt{\frac{\widetilde{N}^2}{\left(\omega_0 - \overline{u}(z) k_0\right)^2} - 1}. \tag{4.21}$$

An analytic expression for the group velocity gradient can also be obtained by expressing $c_{g,z}$ as a function of m and using the chain rule, namely

$$\frac{\partial c_{g,z}}{\partial z} = \frac{dm}{dz}\left[\frac{\widetilde{N} k_0 \left(2m(z)^2 - {k_0}^2\right)}{\left({k_0}^2 + m(z)^2\right)^{5/2}}\right]. \tag{4.22}$$

We now have a closed system to solve numerically for initial values of x, z, k, m, and $\mathcal{A}$.

These ray tracing calculations are commonly used to investigate the propagation of a localised wavepacket through a large-scale (i.e. slowly varying compared to characteristic length scales of the wavepacket) mean flow. Our setup of a relatively large amplitude plane wave superposed on a shear flow throughout the entirety of our computational domain is quite different. We attempt to model this system by considering the paths of wavepackets, (traced using this inherently linear ray equations) with the same properties as the plane wave, from different initial positions. All wavepackets have the initial wave vector (1/4, 3), and hence also have the same initial *intrinsic* frequency. However

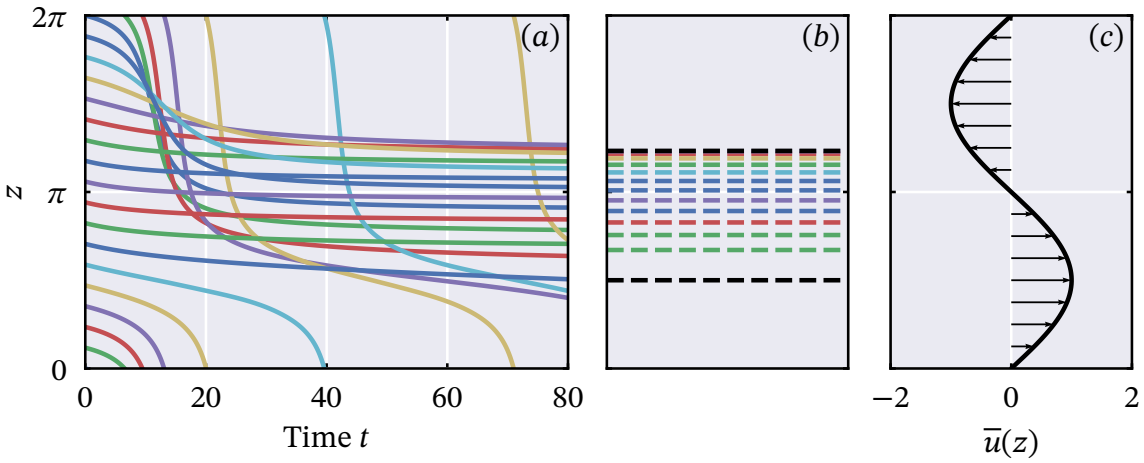

Fig. 4.3 (*a*) The vertical position of wavepackets over time $z(t)$ from the solution of (4.20) from various initial heights. (*b*) Critical levels z_c predicted from (4.17) for each of the inital positions of (*a*). Black lines represent the maximum and minmum critical levels that can arise from any initial height. (*c*) The mean shear flow $\overline{u} = \sin z$.

the *extrinsic* frequencies, that are conserved along each ray, depend on the initial height z_0.

Figure 4.3 displays the results of numerically solving (4.20) for the mean shear flow $\overline{u} = \sin z$. The vertical propagation of 17 wavepackets, equally spaced out at time 0, is shown in figure 4.3a. The majority of the rays end up in the centre of the domain where the background shear is negative, and their vertical propagation decreases. This is consistent with our earlier discussion of wave propagation through a uniform shear. Since each initial wavepacket height has a different extrinsic frequency ω_0, (4.17) can predict critical levels at multiple heights. For the flow considered, (4.17) gives the predicted critical levels through

$$\sin z_c = \sin z_0 + \frac{\widetilde{N}}{\sqrt{k^2 + m^2}} = \sin z_0 + \frac{4}{\sqrt{145}}. \tag{4.23}$$

Figure 4.3b plots the critical levels (if they exist) associated with each of the rays in figure 4.3a. The above equation predicts critical levels for approximately 75% of possible initial heights z_0. The upper and lower bounds on critical levels are also shown in figure 4.3b.

The paths of the rays in figure 4.3 are independent of the wave action $\mathscr{A}$ and can be calculated solely from the middle equation of (4.20). To investigate how the waves behave as they are refracted towards the middle of the domain, we now also consider the evolution of the wave action along the rays. As described previously, the vertical wavenumber m increases as a wave approach a critical level. This means that molecular

diffusion, thus far neglected in the analysis, may become important, particularly for the Reynolds numbers of our direct numerical simulations. We therefore propose a simple modification to the ray tracing equations that incorporates diffusive effects below.

Consistent with the assumption that m is larger than the vertical wavenumber of the shear, we only consider diffusion associated with the internal wave, and assume that the mean shear flow $\overline{u}(z)$ is constant in time. Defining the wave energy density E as in (4.18), diffusive effects will appear in the energy evolution equation as a dissipation rate $\mathscr{D}$:

$$\frac{\partial E}{\partial t} + \cdots = -\mathscr{D} = -\frac{1}{Re}\left(\frac{\partial u_i}{\partial x_j}\frac{\partial u_i}{\partial x_j} + \frac{Ri_0}{Pr}\frac{\partial \theta}{\partial x_j}\frac{\partial \theta}{\partial x_j}\right). \tag{4.24}$$

For $Pr = 1$, if we substitute the internal gravity form of (4.7) (where ω in the velocity pre-factors should be replaced with the intrinsic frequency $\widehat{\omega}$) then the dissipation term simplifies to $\mathscr{D} = 2(k^2 + m^2)E/Re$. Dividing this by $\widehat{\omega}$ then gives the corresponding dissipation rate to add to the wave action equation, which becomes

$$\frac{d\mathscr{A}}{dt} = -\mathscr{A}\frac{\partial c_{g,z}}{\partial z} - \frac{2\left({k_0}^2 + m(z)^2\right)}{Re}\mathscr{A}. \tag{4.25}$$

This equation can be solved in conjunction with the first two equations of (4.20) to provide an estimate of the energy buildup in the centre of the domain.

Although now easy to calculate, wave action can be difficult to interpret intuitively. In particular, it is not clear what a specific value of $\mathscr{A}$ can tell us about how susceptible a wave is to different instabilities. Stability analyses of finite amplitude internal waves have shown that the local wave steepness s is a key parameter in determining the nature of wave breakdown (e.g. Lombard and Riley 1996). We therefore convert wave action to wave steepness by assuming the wave locally maintains the form given in (4.7). In this form, the energy density of the wave is simply given by $E = \widetilde{N}^2 s^2/2m$. Wave steepness and wave action can then be exchanged through the equations

$$\mathscr{A} = \frac{\widetilde{N}s^2\sqrt{k^2+m^2}}{2km^2}, \qquad s = \sqrt{\frac{2\mathscr{A}km^2}{\widetilde{N}\sqrt{k^2+m^2}}}. \tag{4.26}$$

Figure 4.4 presents the results of solving (4.25) in terms of the wave steepness obtained through (4.26) for a range of initial wavepacket heights z_0. The initial wave steepness is set at $s = 0.5$, and we compare the results for the inviscid limit in figure 4.4a with the results for $Re = 5000$ in figure 4.4b. In the inviscid case, s increases consistently over time for those rays that approach a critical level. The high values of s seen in figure 4.4a predict the development of highly unstable convective regions in the centre of

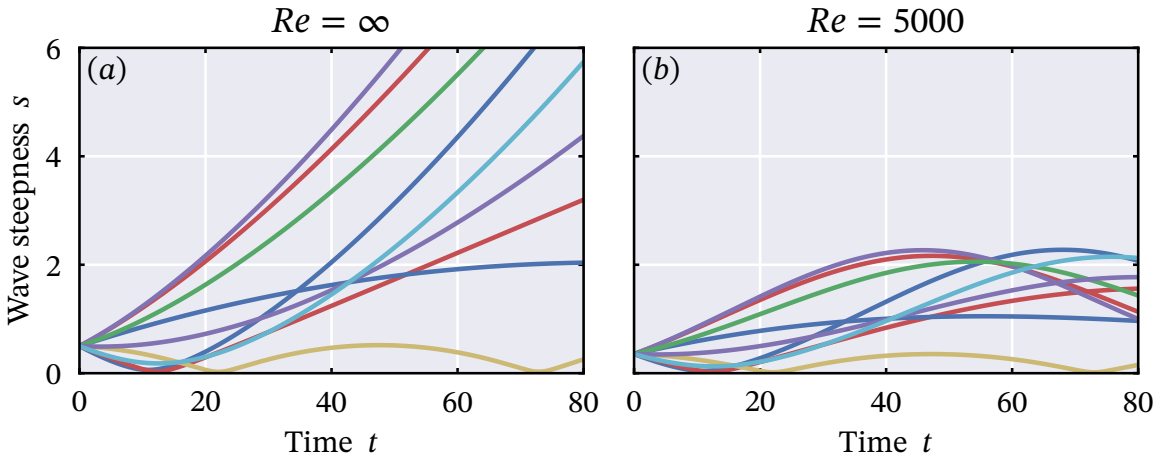

Fig. 4.4 Comparison of wave steepness evolution with and without diffusive effects. The evolution of wave action is calculated from (4.25) and then inverted to give wave steepness by (4.26).

the domain. However once diffusion is taken into account, wave steepness is shown to peak on a timescale of $O(50)$ and then decrease as the critical levels are approached. For $Re = 5000$ the peak wave steepness is less than 4 times that of the initial wave steepness. Note that since (4.25) is linear in $\mathcal{A}$, this factor will remain the same for any initial value of wave steepness. As Re increases, the peak will occur later and allow the steepness to reach higher values. Although convectively unstable regions associated with $s > 1$ are still predicted in the finite-Re case, their development is likely to be strongly impacted by diffusion.

Before moving on to analyse the results of the direct numerical simulations, we must emphasise that we do not expect the above linear analysis to describe the development of the flow quantitatively. We instead believe that the analysis nicely illustrates qualitatively some key phenomena that occur in the flow and provides some physical insight into its behaviour. In particular, we expect energy to build up in the region of negative shear due to wave refraction and the appearance of critical levels. A subsequent breakdown to turbulence is then likely through small-scale instabilities and nonlinearities, although this may be affected by diffusion if the instabilities develop on a sufficiently slow time scale.

4.4 Results

4.4.1 Flow phenomenology and wave breakdown

We now describe the results of the (inherently nonlinear) 3D direct numerical simulations outlined in §4.3.1. We begin by outlining key features of the flow arising from the initial condition with wave steepness $s = 1$, and later compare these results to those with less energetic initial conditions. Figure 4.5 presents vertical plane snapshots of the total buoyancy field $b = z + \theta$ at various times of simulation R8s1 up to $t = 32$. Figure 4.6 shows the vorticity field associated with the same vertical planes, with the streamwise vorticity $\zeta_x = \partial_y w - \partial_z v$ plotted in the yz-planes and the spanwise vorticity $\zeta_y = \partial_z u - \partial_x w$ in the xz-planes.

By time $t = 8$, shown in panel (d), the tilted structure of the internal gravity wave has been distorted by the shear flow. As predicted by the ray tracing calculations in §4.3.2, vertical length scales associated with the wave decrease where the mean shear is negative, at mid-heights in the domain. The effect of this wave refraction on the buoyancy field can be seen in figure 4.5d. In the centre of the domain, regions with statically unstable buoyancy profiles emerge, flanked by 'sheets' of strong stratification where buoyancy contours are pushed close together. This is consistent with the predictions of figure 4.4 for the local wave steepness to increase near $z = \pi$, and points to a local buildup of available potential energy. In contrast, the buoyancy contours closer to the top and bottom of the domain flatten and relax towards the mean uniform stratification.

Panel (e) is the first to highlight three-dimensional motion in the flow at time $t = 16$. Coherent normal mode-like disturbances emerge in the streamwise vorticity of figure 4.6e with a spanwise wavenumber of $l \approx 20$. These vorticity structures are generated in the regions where the buoyancy field is statically unstable, which suggests that they are generated through a convective instability. Indeed, the mushroom-like plumes in figure 4.5e further suggest that the structures can be classified as convective rolls aligned on the streamwise axis. Preliminary simulations at lower resolution showed that the wavenumber l associated with the rolls is independent of the depth (in y) of the domain. We are therefore confident that the narrow domain still captures sufficient three-dimensionality in the flow, particularly since the rolls subsequently break down into smaller scale turbulence as they are advected by the flow.

At the same time as the appearance of the convective rolls, spanwise vorticity intensifies locally in the xz-plane. The dark green regions in figure 4.6f highlight strong negative vertical shears that emerge in the centre of the domain. In a canonical stratified shear layer, the stability of such a region would be determined by the gradient

Richardson number, but in this case such a number is difficult to quantify. Firstly, the shear layer depth Δz, shown on figure 4.6f, varies in both space and time. Secondly, the maximum shear is offset compared to the peak in stratification. In fact the shear layer spans regions where the buoyancy field transitions between static instability and strong stratification. The strong local shears nevertheless present a potential route for further instabilities to develop.

By time $t = 24$, shown in panels (g) and (h), the small-scale convective disturbances have interacted with the strong shears in the centre of the domain, generating a turbulent flow characterised by relatively intense small-scale vortices. Comparing the vorticity field in figure 4.6h with the buoyancy field in figure 4.5h, we find that the turbulence emerges in a region of highly variable local stratification. This can have a significant impact on local irreversible mixing of the buoyancy field, as we investigate further in chapter 5.

The final snapshots presented in figures 4.5 and 4.6 highlight a striking organisation of the turbulence into large, elliptical structures. These are reminiscent of the 'billows' that arise from the development of Kelvin–Helmholtz instability (KHI). Through calculations performed in chapter 2, similar to those of Hazel (1972), we know that the fastest growing mode of KHI has a wavelength approximately seven times the depth of the (initial) shear layer. By comparing the shear layer depth estimate from figure 4.6f with the streamwise length of the billows in figure 4.6j, it appears that the average size of the turbulent structures is not inconsistent with the linear prediction. It is therefore plausible that these billows are essentially finite-amplitude manifestations of a linear shear instability, although we must add a number of caveats to this interpretation. As mentioned above, the shear layer that develops is not steady and its depth and velocity jump both vary in space and time. Kaminski et al. (2017) and Kaminski and Smyth (2019) have also shown that finite amplitude perturbations and pre-existing turbulence can significantly impact the development of shear-driven billows in a stratified shear layer. The disturbances introduced by the convective rolls therefore make it difficult to estimate the size of the billows from the initial wave setup. An alternative hypothesis is that small-scale vortices, formed through shearing of the convective disturbances, undergo a form of inverse cascade in the presence of the mean shear. Why this should saturate at a length scale coincidentally consistent with linear normal mode analysis is however unclear.

By the time $t = 32$ of the final snapshots, the turbulent dissipation rate ε' has already peaked and the subsequent flow is that of a turbulent decay. Figure 4.7 highlights the change in various horizontally-averaged quantities between the initial condition and

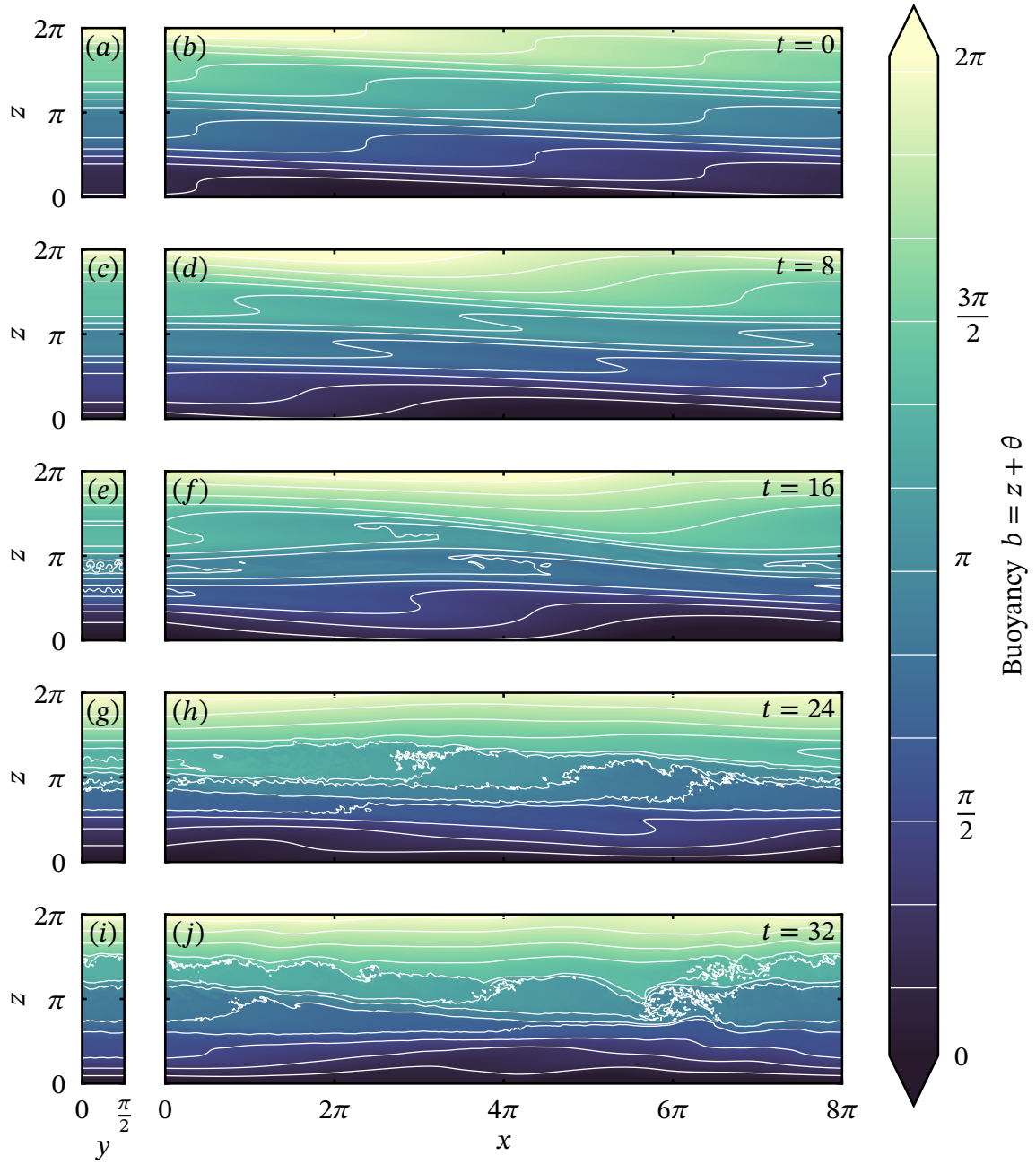

Fig. 4.5 Vertical plane snapshots of buoyancy $b = z + \theta$ in the planes $x = 0$ (left column) and $y = 0$ (right column) from simulation R8s1, where $Re = 8000$ and $s = 1$. Evenly spaced contours are overlaid on the colour plot to highlight structures.

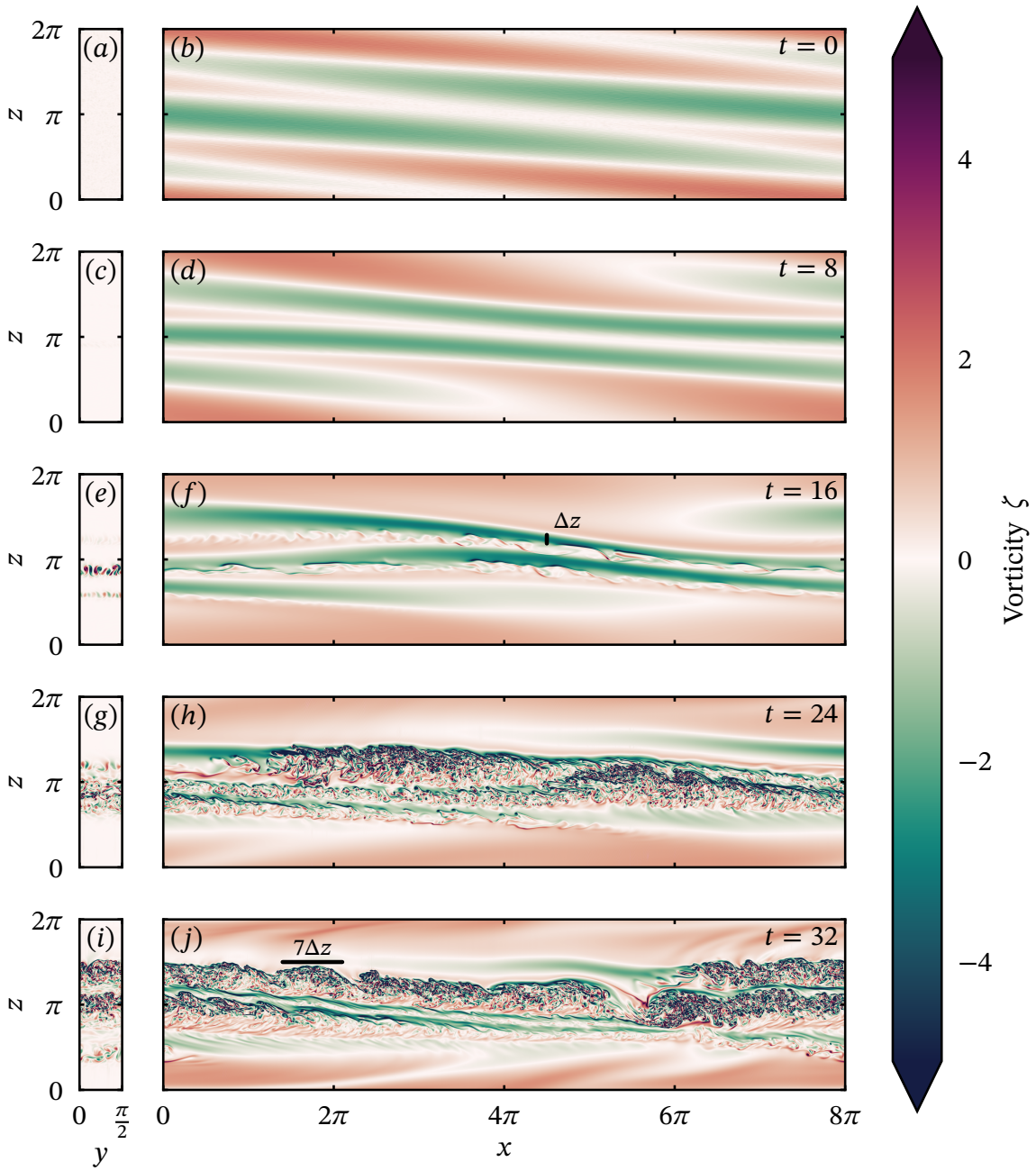

Fig. 4.6 Vertical plane snapshots of streamwise vorticity $\zeta_x = \partial_y w - \partial_z v$ in the plane $x = 0$, and snapshots of spanwise vorticity $\zeta_y = \partial_z u - \partial_x w$ in the plane $y = 0$ from simulation R8s1. Panels (f) and (j) are annotated with length scale estimates for a shear layer.

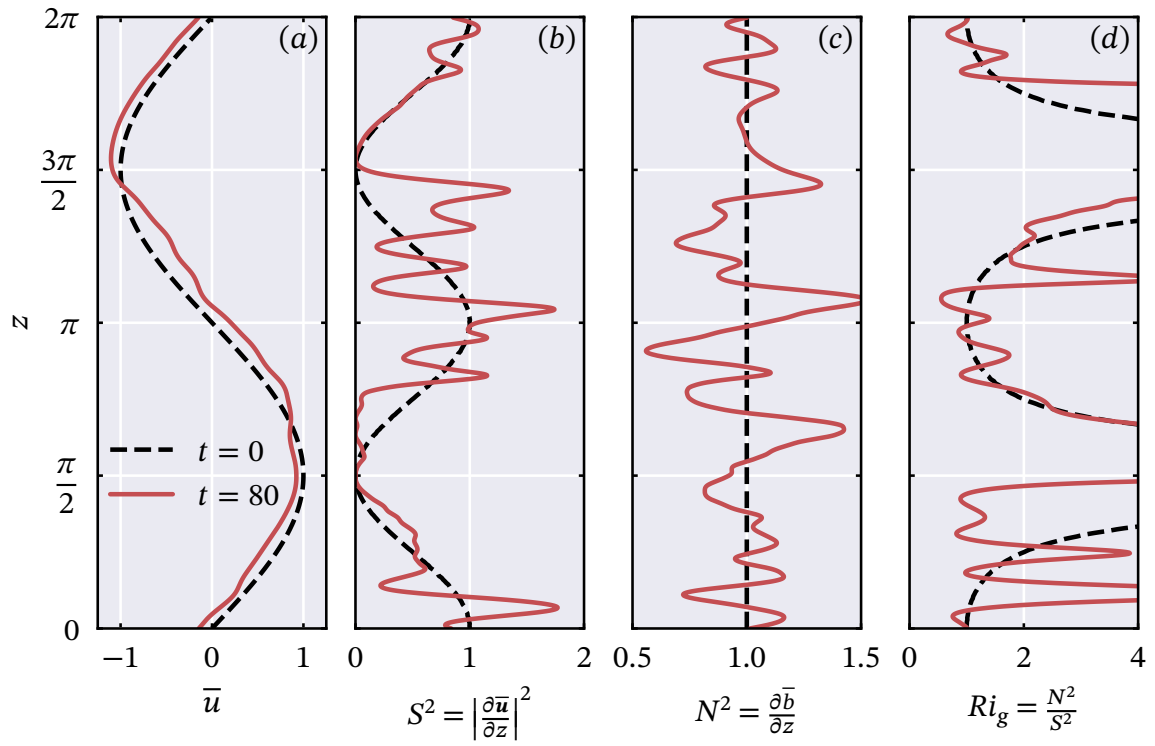

Fig. 4.7 Comparison between times $t = 0$ and $t = 80$ of vertical profiles of: (a) mean streamwise velocity; (b) squared mean shear; (c) mean buoyancy gradient; (d) gradient Richardson number, where 'mean' refers to a horizontal average.

the flow state at the late time $t = 80$. As the turbulence decays, the buoyancy contours flatten in the middle of the domain and leave alternating regions of relatively weak and strong stratification. This variation is clear in the mean vertical profiles of N^2 shown in figure 4.7c, with three strong peaks in the middle of the domain associated with a 30-50% increase in the local buoyancy gradient. The mean shear shows similar vertical variation in figure 4.7. At mid-heights in the domain, local extrema in S^2 appear offset from local extrema in N^2, akin to the form of an internal wave. Despite the intense turbulent mixing that has occurred before this time, there appears to be a signature of the wave remaining imprinted in the late-time mean profiles. Despite this offset, regions with significant shear exhibit a gradient Richardson number of $Ri_g \approx 1$, similar to the initial profile. The most intense mean shears lead to a minimum Richardson number of $Ri_m \approx 1/2$, significantly above the value of 1/4 that ensures linear stability. The simulations are continued up until $t \approx 150$, although the remaining dynamics after $t = 80$ in case R8s1 could primarily be characterized as relaminarization, with the smaller-scale variations seen in figure 4.7 being smeared out by diffusion.

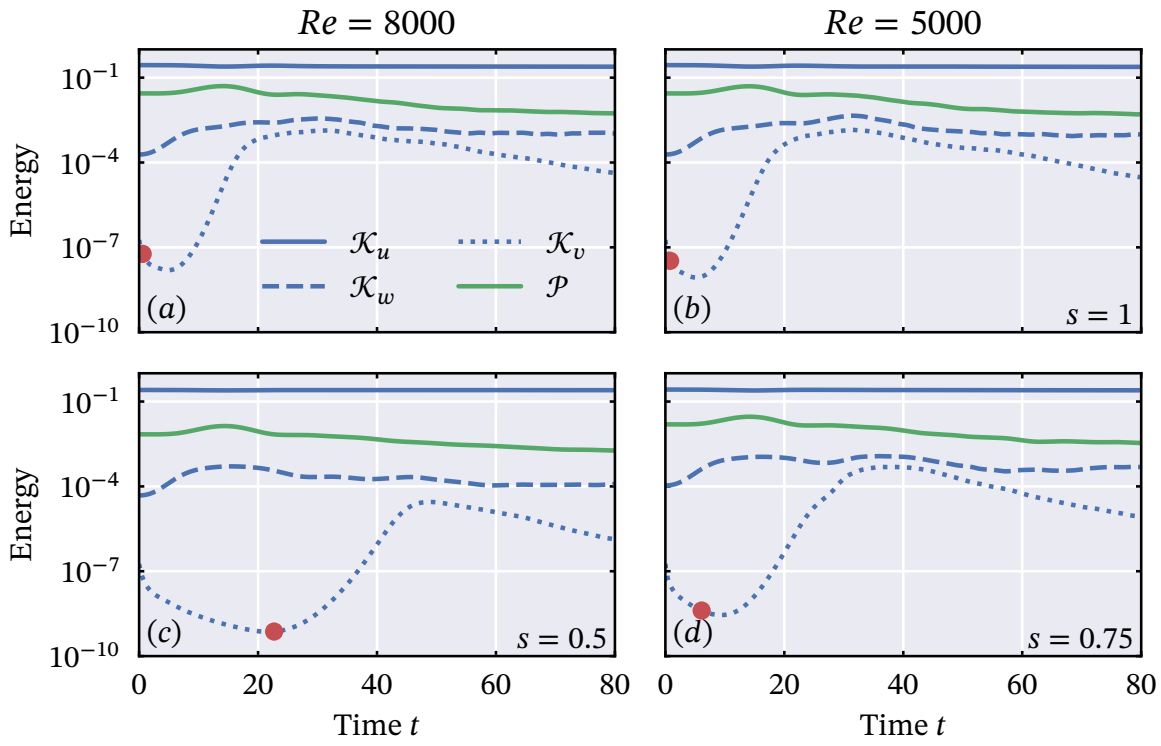

Fig. 4.8 Energy time series for each simulation, separated into individual components of velocity and buoyancy. A logarithmic scale is used on the y-axis. Red dots denote the time at which the maximum local Rayleigh number in the domain exceeds 2000.

4.4.2 Energetics

With a basic understanding of how the flow develops in simulation R8s1, we now investigate how the Reynolds number Re and initial wave steepness s modify the dynamics. We begin by further investigating the emergence of three-dimensional motion associated with the convective rolls in figures 4.5e and 4.6e. Time series for individual components of the kinetic energy

$$\mathcal{K} = \mathcal{K}_u + \mathcal{K}_v + \mathcal{K}_w = \frac{\langle u^2 \rangle}{2} + \frac{\langle v^2 \rangle}{2} + \frac{\langle w^2 \rangle}{2}, \tag{4.27}$$

and the potential energy $\mathcal{P} = Ri_0 \langle \theta^2 \rangle / 2$ are plotted in figure 4.8, where $\langle \cdot \rangle$ denotes a volume average. The time series are plotted on a logarithmic scale, and in every simulation we see a period where the energy of the spanwise velocity $\mathcal{K}_v$ increases with an approximately linear slope, thereby indicating exponential growth. This growth in $\mathcal{K}_v$ is less steep for the two cases with initial wave steepness, and occurs significantly later for simulation R8s0, where $s = 0.5$.

To confirm that the mechanism driving this growth is convective in all cases, we calculate a Rayleigh number, defined in our dimensionless framework as

$$Ra = Ri_0 Re^2 Pr \Delta b (\Delta z)^3. \tag{4.28}$$

where Δb and Δz are calculated as follows. For every horizontal position (x, y), we consider the vertical profile of buoyancy $b(z)$. In this profile we identify the largest continuous region with $\partial b/\partial z < 0$ and denote its size by Δz. We then take Δb as the buoyancy difference across this region to compute the Rayleigh number through (4.28). Taking the maximum Rayleigh number across all horizontal positions then provides us with some information on whether convection is likely to be occurring *somewhere* in the domain. Classical linear stability results predict the onset of convection above a Rayleigh number of $O(1000)$, with the critical value varying depending on the boundary conditions considered (see, for example, Drazin and Reid 2004). In figure 4.8 we additionally plot the time at which the maximum value of Ra in the domain first exceeds 2000 for each simulation. Every case shows that the growth in $\mathcal{K}_v$ only occurs after statically unstable regions form and the Rayleigh number gets sufficiently large. This, together with the quasi-exponential energy growth, provides strong evidence that three-dimensional motion is brought about through a convective linear instability. To be clear, this result only informs us of the *first* source of small-scale disturbances in the flow, and it cannot be used to determine how energy is supplied to turbulence for mixing at later times.

For simulation R8s0, with the smallest initial wave steepness $s = 0.5$, the peak in the energy of the spanwise velocity $\mathcal{K}_v$ is significantly lower than in any of the other cases. The fact that the energy growth occurs later and more slowly than in other cases may allow diffusive effects to impact the saturation of the convective instability. Indeed in figure 4.4 it was predicted that diffusion would significantly impact the local wave steepness on a time scale of $O(50)$. Convective instabilities grow on a timescale of $T_c \sim (\Delta z/\Delta b)^{1/2}$, and so a lower local wave steepness would in turn lead to a slower growth rate. The low growth rate and weak saturation in case R8s0 are therefore both consistent with the ray tracing analysis with diffusive effects.

The ray theory analysis of section 4.3.2 of course relies on a number of bold assumptions that are not even well satisfied by the initial conditions. It is therefore remarkable how well it can describe certain aspects of the flow, such as in figure 4.9, where we plot the horizontally-averaged buoyancy flux $\mathcal{J} = Ri_0 \overline{w\theta}$ for each simulation. Recall that positive values of $\mathcal{J}$ describe a transfer of potential energy to kinetic energy. The net buoyancy flux associated with the plane wave initial condition is zero, but as the wave is distorted by the mean flow, large and reversible exchanges between the kinetic and

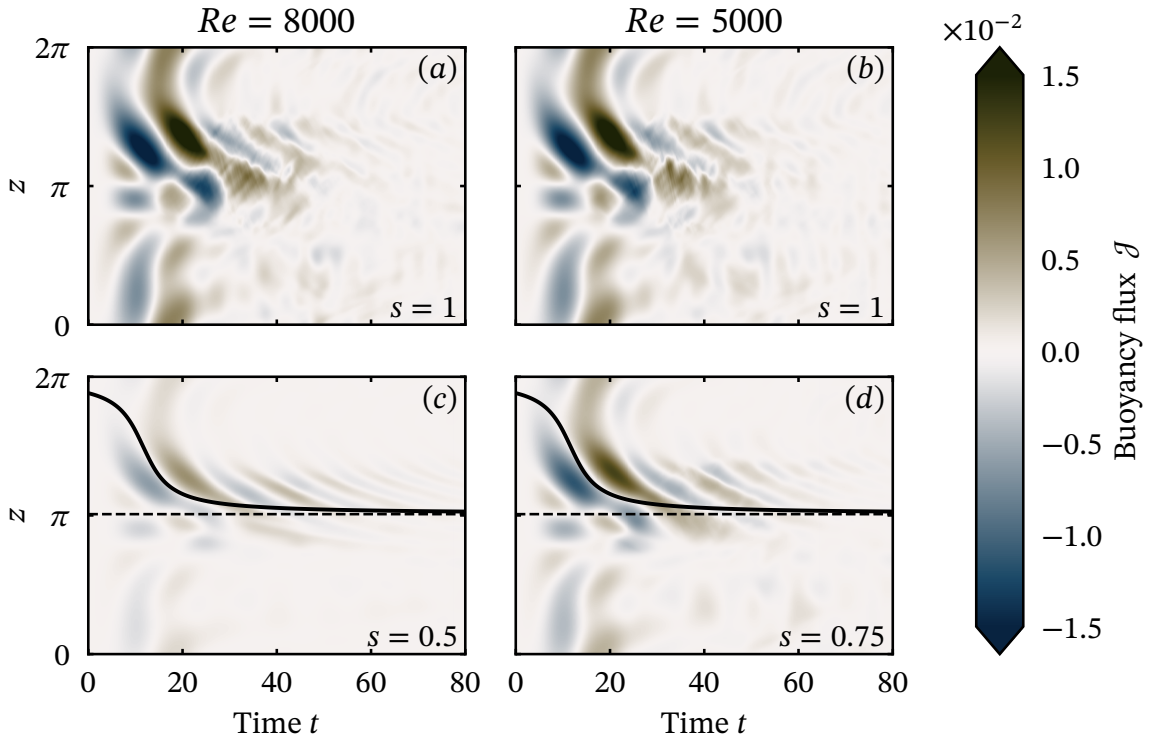

Fig. 4.9 Space-time plots of horizontally-averaged buoyancy flux. One ray path from figure 4.3 is additionally plotted on panels (*c*) and (*d*) as well as the corresponding critical level prediction.

potential energies occur. Figure 4.9 highlights that these exchanges are qualitatively similar at early times for all of the simulations. In the top half of the domain, alternating patches of high and low buoyancy flux appear to propagate downwards over time. For the cases with lower initial wave steepness, shown in panels (*c*) and (*d*), this propagation proves a reasonable match to some of the ray tracing results. One ray from figure 4.3 is re-plotted on figures 4.9c and 4.9d, along with its predicted critical level. In both cases, the ray path closely matches the zero contour of buoyancy flux, suggesting that the early-time dynamics are somewhat well described by the concept of wave refraction. At late times in panel (*c*), significant wave activity, inferred from the buoyancy flux, is only present at heights reminiscent of the critical level locations specified in figure 4.3b.

4.4.3 Turbulence and mixing

For the simulations with higher initial wave steepness, the turbulent wave breaking event leads to high-frequency, small-scale features in figure 4.9. However the large-scale pattern in the buoyancy flux $\mathcal{J}$ remains present during the burst of turbulent activity for

times $20 < t < 40$, with patches of alternating sign overlaying the small-scale details associated with turbulence. This is significant in the context of irreversible mixing, where $\mathcal{J}$ is often used to infer a diapycnal mixing rate when appropriately averaged. Recall the energetic framework of chapter 3:

$$\frac{d\mathcal{K}'}{dt} = S_p + \mathcal{J} - \varepsilon', \qquad \frac{d\mathcal{P}}{dt} = -\mathcal{J} - \chi, \tag{4.29}$$

In a statistically steady state where energy is supplied from the mean flow through the shear production S_p, we expect the buoyancy variance destruction rate χ to balance $-\mathcal{J}$. This in turn implies that $\mathcal{J} < 0$ and the buoyancy flux represents a mean transfer of kinetic energy to potential energy. In our simulations however, turbulence can be most intense in regions where the larger scale wave-mean flow interaction leads to a positive buoyancy flux (for example, see $z \approx \pi$ in panel (a) for $20 < t < 40$). In fact the total mean buoyancy flux (integrated over the domain and in time) is positive in all of the simulations, indicating a net transfer of potential energy to kinetic energy. The classic shear-driven steady state assumption, as used by Osborn (1980), clearly does not apply to our flows. Indeed as discussed in chapter 1, this assumption does not even apply to the canonical evolution of a stratified shear layer (Mashayek and Peltier 2013).

Since the buoyancy flux is not a reliable measure of mixing in the flows, we now focus on the volume-averaged dissipation rates

$$\varepsilon = \frac{1}{Re}\left\langle \frac{\partial u_i}{\partial x_j}\frac{\partial u_i}{\partial x_j}\right\rangle, \qquad \chi = \frac{Ri_0}{RePr}\left\langle \frac{\partial \theta}{\partial x_j}\frac{\partial \theta}{\partial x_j}\right\rangle, \tag{4.30}$$

to investigate mixing properties and the evolution of turbulence in the simulations. As in chapter 3, we decompose the dissipation rates into contribution from the horizontally-averaged fields $\overline{\boldsymbol{u}}$, $\overline{\theta}$, and their perturbations $\boldsymbol{u}'$, θ'. We continue to assume that the available potential energy of the system can be approximated by $\mathcal{P} = Ri_0\left\langle\theta^2\right\rangle/2$, and therefore that χ is an appropriate measure of irreversible diapycnal mixing. The validity of this approximation is revisited in chapter 5, where we find only small discrepancies between χ and the 'true' rate of diapycnal mixing $\mathcal{M}$ for the flows considered here.

Time series of the decomposed dissipation rates are plotted for each simulation in figure 4.10. Comparing the time series with the vorticity snapshots in figure 4.6, we unsurprisingly see that the dissipation rates peak when intense small-scale turbulence spans the domain at mid-heights. In figures 4.10a and 4.10b, the fact that χ' peaks at the same time as ε' suggests that although the convective rolls seen in figures 4.5e and 4.6e are the first small-scale structures to emerge, their contribution to mixing is small.

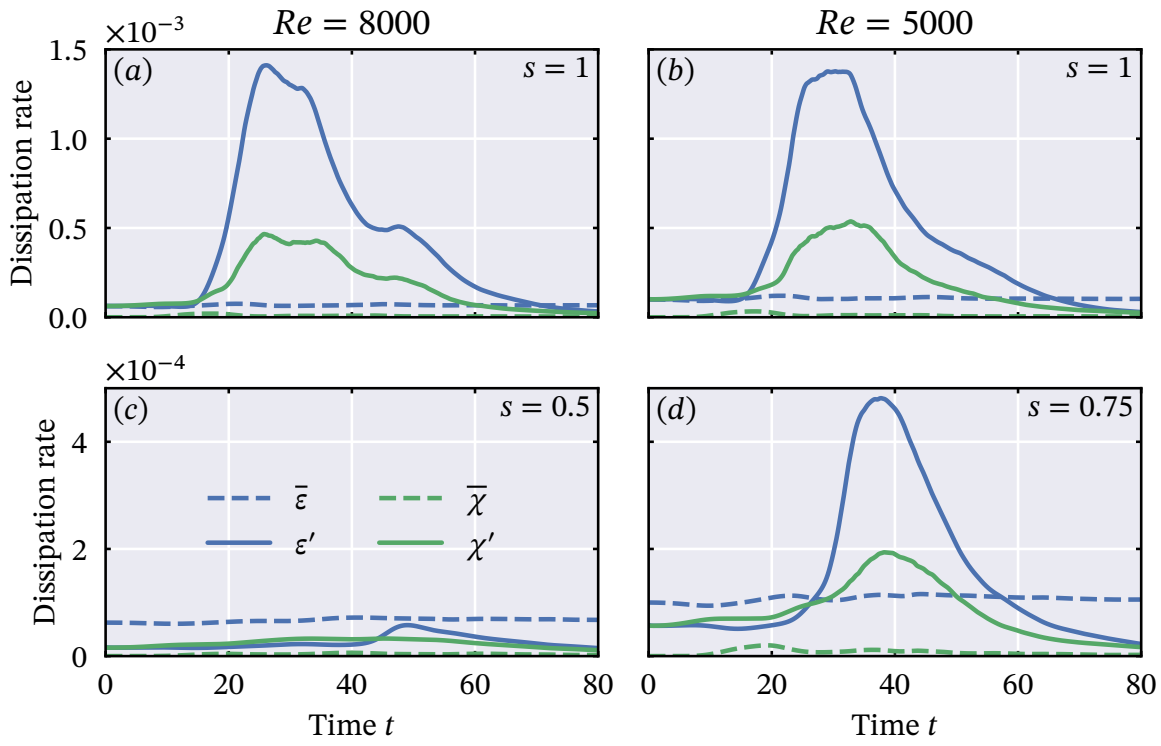

Fig. 4.10 Time series of dissipation rates for each simulation.

Indeed the overall shape of the time series curves for $s = 1$ in figure 4.10 are reminiscent of those for the development of Kelvin–Helmholtz instability (KHI) in a stratified shear layer (see e.g. Salehipour et al. 2015). Particular features that stand out include a sharp, early rise in ε', a short-lived 'fully turbulent' stage where the dissipation rates are approximately constant, and a fast decay from this regime. This is in contrast to some other canonical flows, such as the development of Holmboe instability, which lead to more long-lived turbulent activity (Salehipour et al. 2016).

In the simulations with $s = 1$, the dominant contribution to mixing (quantified by the time integral of χ) comes from the 'fully turbulent' period $25 \lesssim t \lesssim 35$. The instantaneous mixing efficiency during this period is $\eta = \chi/(\chi+\varepsilon) \approx 0.24$, which matches the KHI simulations of Salehipour et al. (2015) for $Pr = 1$. Together with the temporal evolution of ε' and the development of 'billow' structures in figure 4.6j, this makes a strong argument that mixing in these flows is primarily the result of turbulence driven by local shear instabilities, despite the presence of localised convection. Indeed the similarity in mixing efficiency is remarkable given the highly irregular buoyancy field on which the billows develop in our simulations.

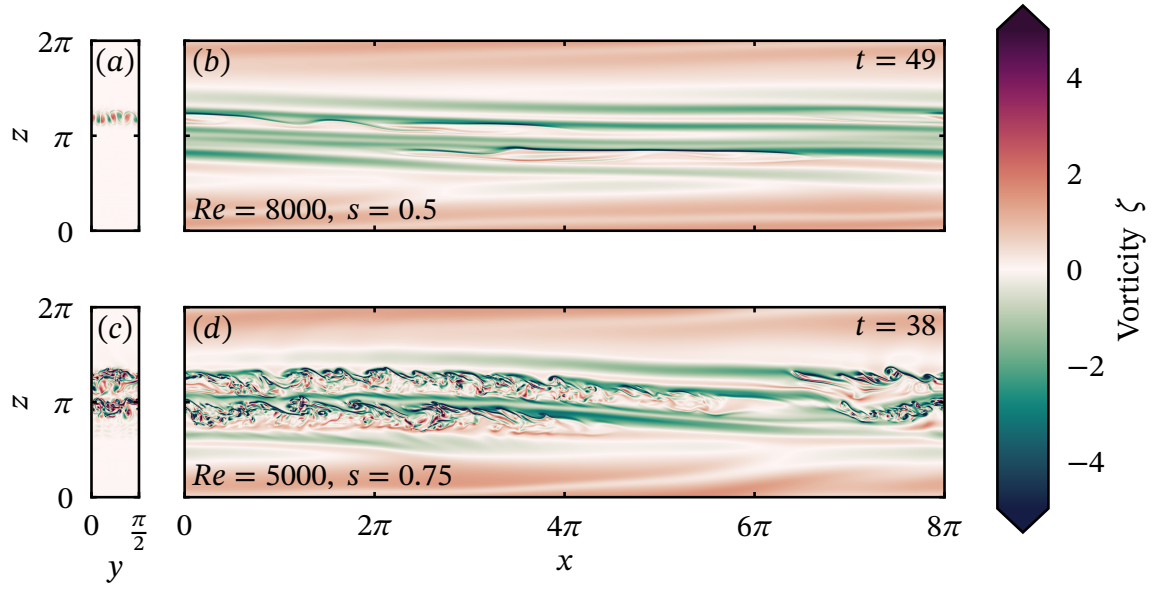

Fig. 4.11 Plane snapshots of vorticity at times of maximum turbulent dissipation rate ε' for simulations R8s0 and R5s0. Planes and vorticity components match those shown in figure 4.6.

In both of the simulations with lower initial wave steepness, the peaks in dissipation rates are far smaller than for the more energetic initial conditions. For simulation R8s0, where $s = 0.5$, the maximum value of ε' never even exceeds the dissipation rate associated with laminar diffusion of the mean flow $\bar{\varepsilon}$. To visualise how these flows differ from the higher dissipation cases, vorticity snapshots are plotted in figure 4.11 for the times at which ε' is at its maximum. Panels (a) and (b) show that no large billow structures develop in case R8s0, and the maximum TKE dissipation rate is instead achieved when the convective rolls saturate in the spanwise plane. Although the buoyancy field is sufficiently distorted by the shear to drive local convection, the local amplification of shear in the xz-plane is reduced compared figure 4.6. Treating the dynamics as that of a refracted wave, we can think of the wave only achieving high values of steepness once its vertical wavenumber m has also increased significantly. The smaller scales associated with high values of m are more susceptible to viscous effects, and it is possible that locally intense shear is smeared out by diffusion before instabilities can grow significantly. As seen in figures 4.11c and 4.11d, turbulent structures emerge from regions of high shear at slightly higher initial wave steepness ($s = 0.75$). The local shear layers are not as thin as for $s = 0.5$, consistent with the idea that instabilities are more likely to develop when viscous effects are reduced. At larger values of Re, it may be possible for turbulent billows to grow from $s = 0.5$ and lead to significant local dissipation and

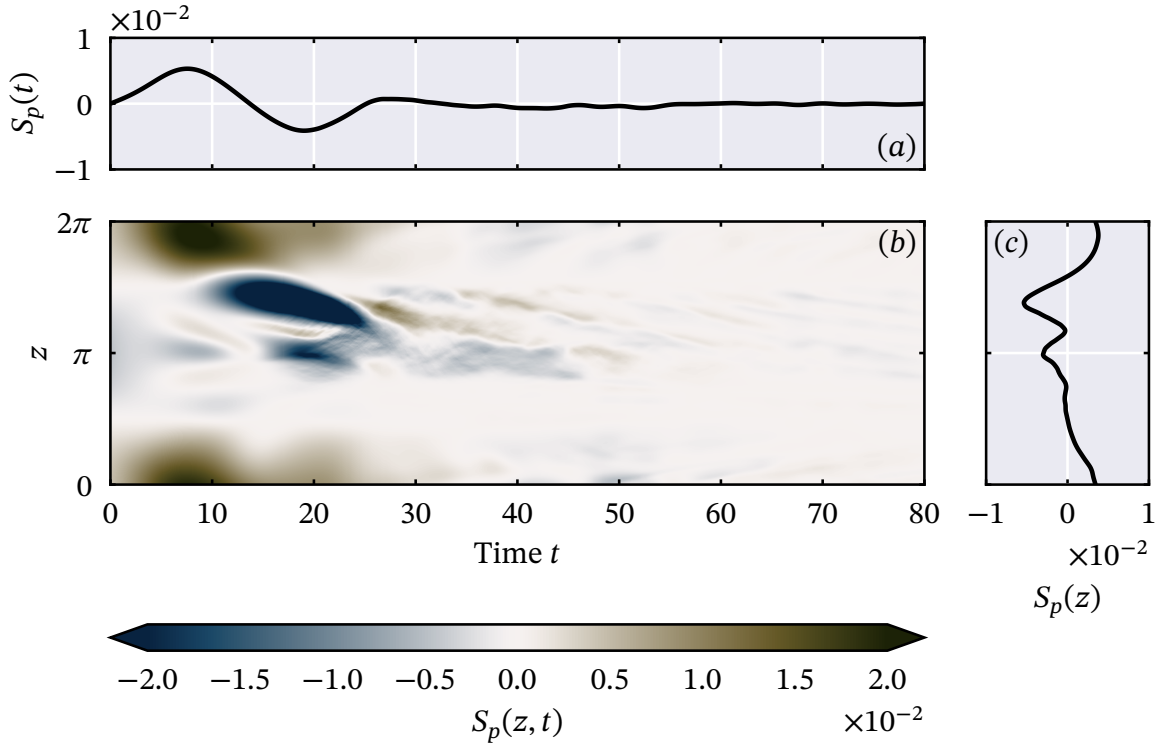

Fig. 4.12 Spatio-temporal evolution of shear production S_p, defined in (4.31), for simulation R8s1. (*a*) Time series of volume-averaged S_p; (*b*) Pseudo-colour plot of $S_p(z,t)$; (*c*) Vertical profile of time-averaged S_p.

mixing. The turbulence would remain far more localised due to the thinner shear layers, but it is possible that the combination of convective and shear mechanisms seen in the cases where $s = 1$ would remain relevant.

4.4.4 Mean flow interactions

For the simulations with largest wave steepness, we have deduced that the majority of turbulent dissipation and mixing can be associated with turbulence arising from shear instabilties. As mentioned above, turbulent shear flows are often associated with a transfer of energy from the mean flow to the turbulence through the shear production

$$S_p = -\overline{w'\boldsymbol{u}'} \cdot \frac{\partial \overline{\boldsymbol{u}}}{\partial z}. \tag{4.31}$$

Positive values of S_p represent an extraction of energy from the mean flow, as highlighted by the TKE evolution equation in (4.29).

From another perspective, internal waves breaking at a critical level typically provide momentum to the mean flow as shown in the classical experiments of Koop and McGee (1986). This momentum transfer is a vital part of the mechanism discussed by Plumb (1977) to describe the atmospheric Quasi-Biennial Oscillation. In our simulations, we appear to observe shear instabilities developing near critical levels, and therefore expect the development of the mean flow to rely on a combination of these effects.

To investigate how the wave breaking affects the mean flow, we plot the shear production S_p from simulation R8s1 as a function of z and t in figure 4.12. The time series of volume-averaged shear production, shown in figure 4.12a, is dominated by large, reversible changes at early stages of the simulation. Indeed the mean value of S_p, averaged over both space and time for 80 time units, is only $O(10^{-5})$, indicating a negligible net transfer of energy between the mean flow and its perturbation. This contrasts with the evolution of Kelvin–Helmholtz instability in a stratified shear layer (Salehipour and Peltier 2015). Although large, reversible changes are also seen at early times in that setup, the lack of initial perturbation energy requires a significant net transfer of energy from the mean flow over the course of a turbulent event.

The negligible net energy transfer does not however mean that the mean flow is unaffected by its interaction with the breaking wave. Figure 4.12c plots the time-averaged shear production as a function of height, showing that $S_p < 0$ in the centre of the domain, whereas $S_p > 0$ near the edges. This suggests that although the turbulence produced at mid-heights in the domain is reminiscent of that triggered by shear instabilities, any extraction of energy from the mean flow in this region is dominated by the earlier wave-mean flow interaction. This is emphasised in the space-time plot of figure 4.12b, where a strong patch of negative shear production persists at mid-heights even as the turbulence develops at $t \approx 25$. As hinted at earlier in figure 4.6, we can therefore interpret the billows as arising from instabilities of the wave's shear rather than the mean flow. The evolution of the mean flow appears primarily governed by its interaction with the coherent internal wave, and is only slightly modified by the subsequent turbulence.

This interpretation of a wave-mean flow interaction is also consistent with the shift in mean streamwise velocity shown earlier in figure 4.7a. Since the wavenumbers of the internal wave k and m are both positive, we expect the wave to propagate to the right and downwards (in the positive x and negative z directions) even as it is refracted by the shear flow. If the wave then deposits its momentum as it approaches the predicted critical levels, we would expect a positive shift in the streamwise velocity in that region, since the wave is propagating to the right. This is precisely what we see in figure 4.7a, where $\overline{u}$ increases over the region $3\pi/4 \lesssim z \lesssim 3\pi/2$.

4.5 Discussion and conclusions

We have investigated the flow arising from the superposition of a large amplitude plane internal gravity wave and a mean shear flow. This initial condition is motivated by observations of high internal wave strain in the presence of variable shear in regions of the thermocline by Alford and Pinkel (2000). In our simulations, some aspects of the dynamics at early times can be reasonably described by ray tracing analysis, despite a lack of the necessary, assumed scale separation between the base flow and the wave field. The propagation of wave energy quantities towards the centre of the domain is well predicted, as seen in figure 4.9. This inherently linear analysis suggests that critical levels, whose locations are highlighted in figure 4.3, exist in this region where the mean shear is negative. Combined with wave action conservation, ray tracing predicts an increase in the vertical wavenumber m and the local wave steepness s as waves approach the critical levels. The increase in local wave steepness far above $s = 1$ shown in figure 4.4a, together with the near-horizontal ray propagation close to the critical levels, suggests that the flow field can subsequently be susceptible to instabilities, as analysed by Winters and Riley (1992).

The fully nonlinear DNS is consistent with this picture, (even though the underlying assumptions of the ray theory are clearly not satisfied) as seen in the snapshots of figures 4.5 and 4.6. Vertical length scales are reduced in the centre of the domain, and regions of statically unstable buoyancy emerge as the wave field is distorted by the shear. Streamwise-aligned convective rolls, best highlighted by figures 4.5e and 4.6e, emerge from the regions of static instability in all of the simulations, regardless of their initial wave steepness. Quasi-exponential growth in the energy of the spanwise velocity is observed in figure 4.8 once the maximum local Rayleigh number in the domain becomes large. We deduce that the roll structures in the spanwise plane are simply driven by a linear convective instability.

The accumulation of wave energy in the centre of the domain also leads to an intensification of local shear in the xz-plane. Flows arising from the more energetic initial condition (where $s = 1$) subsequently become turbulent and exhibit large-scale organisation in the form of elliptical billow structures. These billows, visualized in figure 4.6j, are reminiscent of those arising due to Kelvin–Helmholtz instability (KHI) in a stratified shear layer. Indeed, relative to the width of the shear layers produced by the refracted wave, the length of each billow is consistent with the fastest growing mode arising from linear stability analysis of a shear layer (see e.g. Drazin and Reid 2004).

Furthermore the time series of dissipation rates in figure 4.10 show that wave breaking is characterised by a 'burst' or 'flare' of turbulence, rather than a sustained event. This bursting nature is again reminiscent of turbulence initiated through KHI. When turbulence persists throughout the domain at mid-heights, the mixing efficiency is also largely similar to that found in previous studies of KHI at $Pr = 1$. The buoyancy field surrounding the local shear layers in our simulations is complex, with regions of strong, stable stratification, and static instability present either side of the shear layer. It is therefore somewhat surprising that the mixing results are consistent with a typical stratified shear layer, particularly given the results of Mashayek et al. (2013) highlighting strong Richardson number dependence within that simple setup. A future study of shear-induced mixing for a wider range of background buoyancy profiles would be useful in pinpointing the key parameters governing variations in mixing efficiency. Nevertheless in the simulations with larger initial wave steepness, mixing appears predominantly shear-driven despite the prior emergence of convective rolls in the breakdown of the wave. To be clear, by 'shear-driven' we mean that energy is supplied to turbulence primarily through shear instabilities, and in this case the unstable shear is that in the velocity field of the refracted internal wave.

As seen in figure 4.11, the less energetic initial conditions do not lead to as much turbulent activity. The waves are still refracted towards the centre of the domain and reach sufficient steepness to drive local convection, but we do not observe as intense shear amplification in the xz-plane in these cases. We suggest that viscous effects are damping the wave before strong shears can be generated. Although high wave steepness values occur at later times, high local wavenumbers are still produced earlier by the wave refraction, and as time progresses these gradients will be smeared out by diffusion. We can model these diffusive effects by adding a simple dissipative term to the conservation of wave action (4.25). Consistent with the simulations, we find in figure 4.4 that this wave damping limits the growth of the wave steepness on a time scale similar to the time taken to reach peak dissipation.

Even at the high resolution of our simulations, we cannot consider Reynolds numbers that match our motivating oceanographic observations, suggesting that viscous effects are overemphasised in our flows. It is therefore possible that the mechanisms driving turbulence and mixing in our more energetic simulations may be relevant for flows arising from smaller initial wave steepness. In these cases unstable shear layers would be produced at higher wavenumbers, potentially limiting the size of the billows and the extent of the turbulence. Nevertheless this wave breaking may be representative of a process leading to intense mixing from internal waves in the ocean.

Shear-driven turbulence is commonly associated with an extraction of energy from the mean shear flow, characterised by positive values of shear production $S_p > 0$. However even in our most energetic simulations, we find on average that $S_p < 0$ in the region of most intense turbulence, as shown in figure 4.12. This instead suggests that the primary effect on the mean flow comes from a wave-mean flow interaction, where the wave transfers its momentum into the mean flow as it breaks. The change in the mean streamwise velocity shown in figure 4.7a supports this interpretation. Indeed, since the strong local shears are associated with the wave rather than the mean flow, it may be expected that simple energetics arguments regarding the interaction of turbulence and a mean flow do not apply here.

Although this counterexample to the traditional picture of shear-driven turbulence is specific to our setup, it highlights a generic difficulty in analysing turbulent stratified flows. The effects of internal gravity waves and turbulence are often considered in isolation, although their interplay is vital at the scales associated with wave breaking that are of interest to us. Waves break to produce turbulence, turbulence itself can emit internal waves, and the evolution of a turbulent patch in a stratified fluid is affected at leading order by the presence of internal waves (as reviewed e.g. by Davidson 2013). Continuous energy transfer between waves and turbulence can lead to great difficulties in interpreting their respective roles in the dynamics.

In our simulations, the internal wave appears to drive both the generation of turbulence and the modification of the mean flow. However our setup of an initial value problem superimposing a wave and shear is not typical of how such an interaction would arise in the ocean. Internal waves in the ocean continuously propagate away from generation sites such as topographic features where waves are generated through tidal flows (Sarkar and Scotti 2017). It is unclear what behaviour could be expected over a longer time scale as more waves propagate towards the breaking event through the shear. If a critical level were responsible for the breakdown, one might expect a continuous supply of energy to maintain the turbulence as waves propagate towards it.

Our simulation of an isolated 'burst' of turbulence arising from a large amplitude internal wave is however more consistent with the time scales of overturning events observed by Alford and Pinkel (2000), henceforth AP. Taking the dimensionless duration of the wave breaking event in simulation R8s1 as $N_0 t = 50$ and the background buoyancy frequency as $N_0 = 5 \times 10^{-3}\,\mathrm{s}^{-1}$, we deduce a duration of $T = 1 \times 10^4\,\mathrm{s} \approx 0.116\,\mathrm{d}$, consistent with the time scales of figure 4.1. Of course the observations of AP rely on individual vertical profiles, and it is possible for longer lasting turbulent patches to simply be advected away from the profiler.

In the context of these observations in the thermocline, we have neglected the effect of the Earth's rotation in our simulations. For the field site of AP, buoyancy effects are important on much faster time scales than rotation, as evidenced by the typical ratio $f/N = 1.6 \times 10^{-3}$. The slowly varying shear may however be intrinsically related to the effects of rotation, and it is most likely associated with a slowly-propagating near-inertial wave. Although the observations of AP tell us the strength of the vertical shear, they do not report on the orientation of the mean flow or how it changes. This orientation may have significant consequences on the nature of the wave breakdown. For example Fritts et al. (2013) find that a spiralling finescale shear flow weakens the spanwise convective instability relative to the case of a shear flow aligned with the internal wave. Broutman et al. (1997) also add the time-dependent nature of propagating near-inertial shear to their ray tracing analysis and find that this can reduce the proportion of short internal waves that end up dissipated in critical layers. Determining whether these types of interaction could impact our results on mixing and mean flow acceleration would be useful in understanding how specific the results are to our setup.

In regions away from the thermocline, f/N typically takes larger values and rotation can be expected to play more of an important role, although similar wave breaking mechanisms may still be relevant. For example the deep ocean measurements of Waterman et al. (2012) highlight a local peak in turbulent dissipation and internal wave energy approximately 1 km above the ocean floor, where stratification remains relatively weak. From corresponding measurements of the mean shear flow, they attribute this peak to waves breaking at critical levels. Waterman et al. (2012) also find a mismatch in this region between dissipation rates measured from microstructure and those inferred from the internal wave energy. One explanation for this is that, like in our simulations, wave energy is split between the mean flow and turbulence as the waves break. Investigating how incoming wave energy is distributed between mean flow acceleration, turbulent dissipation, and mixing in a fully turbulent critical layer would be useful for improving parameterizations for such scenarios. Such parameterizations could depend strongly on the properties of the incoming waves, and therefore require a fundamental understanding of the various sources of internal waves in the ocean. A key open question remains of how much mixing can be attributed to each of these sources, such as tidal beams (Dauxois et al. 2018), lee waves (Legg 2021), and near-inertial waves (Alford et al. 2016).

The energetic simulations presented in this chapter have highlighted a flow where, although convective instabilities emerge first in the transition to turbulence, mixing is primarily associated with shear-driven turbulence. We quantify mixing here by the buoyancy variance destruction rate χ. Through this definition, mixing relates to the

evolution of the system towards a state where the buoyancy perturbation θ is uniform throughout the domain (Villermaux 2019). However in oceanographic models we are primarily concerned with *diapycnal* mixing related to the diffusive flux across a surface of constant buoyancy. Accurate quantification of this diapycnal mixing is vital when applying DNS results to improve parameterizations of mixing efficiency or diapycnal diffusivity. Furthermore, large variations in the mean buoyancy gradient, as observed in this chapter's simulations, may cause χ and the diapycnal mixing rate to differ significantly. To explore diapycnal mixing more carefully in our simulations, the following chapter focuses on the development of an extended framework for available potential energy that is applicable to stratified, triply periodic domains. We apply this framework to both the simulations of the current chapter and those of chapter 3, and discuss how diapycnal mixing can best be estimated or parameterized for such flows.

Chapter 5

Quantifying mixing and APE in simulations of stratified flows

In this chapter, we propose a new technique for the calculation of available potential energy (APE) in triply-periodic domains where a mean stratification is imposed. We highlight how the aperiodicity of the buoyancy b in the vertical leads to ambiguities when applying the APE framework of Winters et al. (1995), widely used for bounded domains. By overcoming this problem, we are now able to calculate diapycnal mixing in periodic systems directly, and we subsequently apply the new technique to the simulations of chapters 3 and 4. In those chapters, mixing had been approximated by χ, similar to the model of Osborn and Cox (1972). We investigate how well this assumption performs and discuss the implications of using the Osborn and Cox (1972) model to estimate a diapycnal diffusivity in such flows.

This chapter is based on a manuscript that is currently under review for the Batchelor Centenary Commemorative Volume of the *Journal of Fluid Mechanics*.

5.1 Mixing and available potential energy

The transport of heat and salt across surfaces of constant density (isopycnals) in the ocean provides a vital contribution to the closure of the ocean's energy budget (Wunsch and Ferrari 2004; Hughes et al. 2009). As discussed in §1.1, such a diapycnal flux arising from molecular diffusion alone is insufficient to balance the generation of dense water in polar regions and close the global circulation. Turbulence therefore plays an important role in enhancing mixing through the stirring of tracer fields (such as temperature or salinity) and the subsequent generation of small-scale gradients. In the ocean interior,

turbulence is often associated with breaking internal waves (MacKinnon et al. 2017), which in turn lead to mixing that is strongly intermittent in both space and time.

Here we define mixing as the irreversible diffusive flux across isopycnals that arises due to macroscopic fluid motions, as in Peltier and Caulfield (2003). This flux is sometimes expressed as the mean vertical flux of buoyancy $b = -g(\rho - \rho_0)/\rho_0$. The flux $\langle w'b' \rangle$ can however include significant contributions from entirely reversible processes such as internal waves. Indeed equating buoyancy flux and irreversible mixing is only appropriate when both are averaged over time and applied to a statistically stationary state. Winters et al. (1995) show that the true rate of irreversible mixing in a Boussinesq fluid is equal to the conversion rate of available potential energy (APE) to background potential energy (BPE). As introduced by Lorenz (1955), APE refers to the change in energy resulting from adiabatically sorting the buoyancy field of a fluid to its state of minimum potential energy. By extending the APE framework to compressible flows Tailleux (2009) argues that mixing should in fact be described as the dissipation of APE into internal energy, which is balanced exactly by an enhancement in the generation of BPE in the Boussinesq limit. In this study, we focus on the dynamics of a single-component Boussinesq fluid with a linear equation of state, and refer the reader to Tailleux (2013*a*) for a discussion of mixing and APE in more complex scenarios.

Although the Winters et al. (1995) framework provides an exact expression with which to calculate diapycnal mixing, it is not practical for use in oceanographic observations. The most precise observational estimates of mixing come from vertical microstructure profilers that record small-scale gradients of velocity or temperature in isolated vertical profiles. The methods of Osborn and Cox (1972) and Osborn (1980), which are derived from mean balances in the buoyancy variance and turbulent kinetic energy equations respectively, can then be used to estimate an effective diapycnal diffusivity K_d. This diffusivity is related to the mixing rate through $\mathcal{M} = K_d N^2$ where N is some appropriate measure of the buoyancy frequency. Note that N may not be straightforward to identify if there is significant spatio-temporal variability in the flow. Both estimation methods are derived on the assumption that the flow is statistically steady and thus that the mixing is well described by some average of the buoyancy flux. The diffusivity K_d obtained from these microstructure measurements can then be checked against estimates of diffusivity from tracer release experiments (Ledwell et al. 2000). Understanding how K_d varies throughout the ocean is also vital for improving the accuracy of global circulation models, where diapycnal turbulent fluxes are only captured through a prescribed parameterization of K_d, such as that of Klymak and Legg (2010).

Accurately quantifying mixing in computational fluid dynamics requires the use of direct numerical simulations (DNS) that resolve down to the dissipative scales of motion. These simulations can then be used to test the assumptions used to derive the above models (as in Taylor et al. 2019), or to quantify the differences in inferred diffusivity arising from the models (Salehipour and Peltier 2015). The need to resolve the smallest scales of motion restricts the Reynolds numbers *Re* it is possible to attain through DNS, and so massive computational grids are needed to push *Re* up towards geophysical values. Since the earliest days of simulating turbulence through DNS, triply periodic domains have been used to reduce computational cost (Orszag and Patterson 1972). The lack of fixed boundaries in this setup means that higher values of *Re* can be obtained. Thin boundary layers do not need to be resolved and highly efficient pseudospectral methods, exploiting the imposed periodicity, can be implemented.

Riley et al. (1981) were the first to include a mean density stratification in such a triply periodic setup by decomposing the buoyancy field into a linear profile $N_0^2 z$ and a periodic perturbation θ. This system has since proved popular for studying the dynamics of high *Re* stratified turbulence (e.g. Staquet and Godeferd 1998; Riley and de Bruyn Kops 2003; Brethouwer et al. 2007). Investigations of mixing in periodic domains, recent examples of which can be found in Maffioli et al. (2016) and Garanaik and Venayagamoorthy (2019), do not however implement the rigorous Winters et al. (1995) framework for quantifying APE, thus identifying explicitly irreversible mixing. It is common instead to describe mixing in terms of the destruction rate of buoyancy variance χ. This approximation is closely related to the methodology underlying the diffusivity estimate of Osborn and Cox (1972).

As we later explore in §5.4.3, approximating mixing with χ can result in an over- or under-estimate depending on whether the most intense turbulence in the flow preferentially samples regions of locally high/low stratification (and thus is associated with different characteristic *local* values of the buoyancy frequency). It is therefore important to be able to quantify mixing accurately in the periodic system and identify whether such discrepancies can be significant. Since the buoyancy in the system is only defined through its periodic perturbation θ, ambiguity arises in how to construct the background state of minimum potential energy. In §5.2 we use a simple example to highlight this issue and then provide an extension to the framework of Winters et al. (1995) that resolves the ambiguity in the case of triply periodic domains. §5.3 gives a brief overview of the numerical simulations we shall use to test the new framework, including the numerical method used. §5.4 uses the new framework to analyse the simulations, and compares the exact mixing rates to commonly used estimates. Finally, we conclude and discuss

these results in §5.5, with a particular focus on how our findings impact the estimation and parameterization of mixing in the ocean.

5.2 Quantifying mixing in triply-periodic domains

We consider the problem of quantifying irreversible mixing in a system governed by the dimensionless Boussinesq equations subject to an imposed, constant, mean stratification. We decompose the buoyancy field as $b = z + \theta$, where $b = z$ represents the buoyancy profile of the imposed mean stratification. Note that b has been non-dimensionalized by $L_0 N_0^2$, where L_0 is a typical length scale and N_0 is the mean dimensional buoyancy frequency, so the mean buoyancy gradient in the dimensionless system is always equal to one.

$$\boldsymbol{\nabla} \cdot \boldsymbol{u} = 0, \tag{5.1}$$

$$\frac{\partial \boldsymbol{u}}{\partial t} + (\boldsymbol{u} \cdot \boldsymbol{\nabla})\, \boldsymbol{u} = -\boldsymbol{\nabla} p + \frac{1}{Re} \nabla^2 \boldsymbol{u} + Ri_0 \theta \hat{\boldsymbol{z}}, \tag{5.2}$$

$$\frac{\partial \theta}{\partial t} + (\boldsymbol{u} \cdot \boldsymbol{\nabla})\, \theta = \frac{1}{RePr} \nabla^2 \theta - w. \tag{5.3}$$

We apply periodic boundary conditions in all three directions to the flow velocity $\boldsymbol{u}$, pressure p and buoyancy perturbation θ. The (dimensionless) domain sizes in the x, y, and z directions are L_x, L_y, and L_z, respectively. The dimensionless parameters in the system are the Reynolds number, Prandtl number and bulk Richardson number, given by

$$Re = \frac{L_0 U_0}{\nu}, \qquad Pr = \frac{\nu}{\kappa}, \qquad Ri_0 = \frac{{N_0}^2 {L_0}^2}{{U_0}^2}, \tag{5.4}$$

where U_0 is a velocity scale, ν is the kinematic viscosity, and κ is the diffusivity of buoyancy. As mentioned in the introduction, these equations are frequently used in studies of stratified turbulence where the periodicity allows for the use of efficient spectral methods and removes the effect of solid boundaries.

Although the buoyancy perturbation θ is periodic in the vertical, the total buoyancy $b = z + \theta$ is not. We are instead left with a jump condition for b at the upper and lower boundaries that has consequences for the calculation of irreversible mixing and potential energy. The mean potential energy in the domain is defined as

$$\mathcal{P}(t) = \langle -Ri_0 bz \rangle, \tag{5.5}$$

where $\langle f \rangle = \frac{1}{V}\int_V f\, dV$ denotes an average over the domain volume V. Substituting $\theta = b - z$ into (5.3) and multiplying by $-Ri_0 z$ provides an evolution equation for the potential energy in the form

$$\frac{d\mathcal{P}}{dt} = -Ri_0 \langle wb \rangle + \frac{Ri_0}{V}\int_{\partial V} zb\boldsymbol{u}\cdot\boldsymbol{n}\,\mathrm{d}S + \frac{Ri_0}{RePr}\left\langle \frac{\partial b}{\partial z}\right\rangle - \frac{Ri_0}{VRePr}\int_{\partial V} z\boldsymbol{\nabla} b\cdot\boldsymbol{n}\,\mathrm{d}S. \quad (5.6)$$

Taking the top and bottom boundaries to be at $z = L_z$ and $z = 0$ respectively, and applying the periodic boundary conditions simplifies the equation to

$$\frac{d\mathcal{P}}{dt} = -Ri_0\langle w\theta\rangle + Ri_0\,\overline{w\theta}\Big|_{z=0} - \frac{Ri_0}{RePr}\,\frac{\partial\overline{\theta}}{\partial z}\Big|_{z=0}, \quad (5.7)$$

where an overbar denotes a horizontal average. The conversion rate of internal energy to potential energy, given by the third term on the right hand side of (5.6), has been cancelled out by the main contribution of the diffusive flux through the boundary - the final term in (5.6). The evolution equation (5.7) highlights how sensitive the evolution of the potential energy can be to the choice of the boundary.

The accurate quantification of irreversible mixing requires partitioning the potential energy into background and available components. The background potential energy (BPE) is defined as the minimum value of potential energy that can be achieved through adiabatic rearrangement of the fluid in the domain. In this minimum state, the buoyancy profile is given by a monotonically increasing one-dimensional function $b_*(z,t)$, so the mean BPE is given by $\mathcal{P}_B = \langle -Ri_0 b_* z\rangle$. Winters et al. (1995) show that BPE can also be expressed as

$$\mathcal{P}_B(t) = \langle -Ri_0\, b(\boldsymbol{x},t)\, z_*(\boldsymbol{x},t)\rangle\,, \quad (5.8)$$

where z_* is the height a parcel of fluid with buoyancy $b(\boldsymbol{x},t)$ is moved to under the adiabatic rearrangement. Following Lorenz (1955), the available potential energy (APE) is defined as the surplus potential energy

$$\mathcal{P}_A(t) = \langle -Ri_0 b\,(z - z_*)\rangle\,. \quad (5.9)$$

The rate of irreversible mixing associated with fluid motion is then given by the energy transfer rate from APE to BPE, which takes the form

$$\mathcal{M} = \frac{Ri_0}{RePr}\left\langle \frac{\partial Z_*}{\partial b}\Big|_{b(\boldsymbol{x},t)} |\boldsymbol{\nabla} b|^2 - \frac{\partial b}{\partial z}\right\rangle = \frac{Ri_0}{RePr}\left(\left\langle \frac{\partial Z_*}{\partial b}\Big|_{b(\boldsymbol{x},t)} |\boldsymbol{\nabla} b|^2\right\rangle - 1\right), \quad (5.10)$$

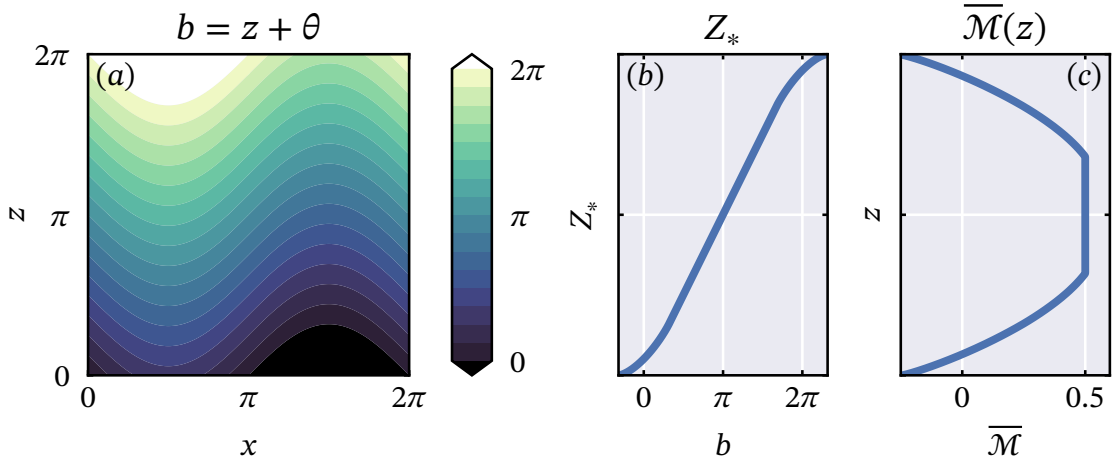

Fig. 5.1 (a) displays contours of the total buoyancy field given by $\theta = \sin x$; (b) shows the sorted profile $Z_*(b)$ associated with this buoyancy field; (c) shows the horizontally averaged irreversible mixing rate $\overline{\mathcal{M}}(z) = \overline{\frac{\partial Z_*}{\partial b}|\boldsymbol{\nabla} b|^2} - \frac{\partial \bar{b}}{\partial z}$. Note that an overbar here denotes an average over x, and $\partial Z_*/\partial b$ is evaluated at $b(x, z)$.

where $Z_*(b, t)$ is the inverse function associated with the sorted buoyancy profile b_* which satisfies $z_*(\boldsymbol{x}, t) = Z_*(b(\boldsymbol{x}, t), t)$. It is important to appreciate that the term scaling $|\boldsymbol{\nabla} b|^2$ in (5.10) is effectively the inverse square of the buoyancy frequency of the sorted variables, and so accentuates the contributions where the sorted buoyancy gradient is relatively weak. As discussed below in §5.4.3, this is a potential source of difference between $\mathcal{M}$ and the buoyancy variance destruction rate χ.

We now present a simple example to highlight how the aperiodicity of b can cause issues for calculating the mixing rate $\mathcal{M}$. We consider the buoyancy field given by $\theta = \sin x$ in a domain of length 2π. This might be thought of as a representation of the buoyancy field associated with a standing internal gravity wave, at an instant when half the columns of fluid in the domain are raised up and half are pushed down relative to their equilibrium location.

The total buoyancy field $b = z + \sin x$ and its corresponding sorted profile $Z_*(b)$ are shown in figures 5.1a and 5.1b respectively. In an unbounded domain, we would expect a linear profile for Z_* since the wave is simply a rearrangement of the initial linear stratification. However by taking the boundaries at $z = 0$ and $z = 2\pi$, we produce a profile with deviations from a uniform slope close to these values. Since θ is independent of z, we would also expect the mixing rate $\mathcal{M}$ to be constant regardless of the vertical extent that we average over. Figure 5.1c instead shows that the variations in $\partial Z_*/\partial b$ change the value of $\mathcal{M}$ across much of the domain, with the horizontally-averaged mixing rate even taking negative values close to the boundary.

5.2.1 Local APE density

The simplest way of tackling the issue highlighted above would appear to be the use of a localised measure of APE. This concept has been used as an alternative framework for quantifying available potential energy in situations where fluxes through a boundary are important. Originally devised by Holliday and McIntyre (1981) and Andrews (1981), local APE has seen renewed interest recently in its application to numerical simulations. We follow Scotti and White (2014) in defining the local APE density E_{APE} as a function of space and time by

$$E_{APE}(\boldsymbol{x}, t) = -Ri_0 \int_{b_*(z,t)}^{b(\boldsymbol{x},t)} z - Z_*(s,t)\,\mathrm{d}s, \tag{5.11}$$

We use this form primarily for its ease of notation, although as we show in appendix A.3, for the setup we consider it is equivalent to various other expressions proposed for local APE density. Although this quantity varies in space and time, its dependence on the globally sorted profiles b_* and Z_* means that it cannot be calculated solely from local fields. In particular, the issue for quantifying mixing highlighted by figure 5.1 remains unresolved unless we can obtain the appropriate background profile b_*.

We propose the use of a control volume bounded by surfaces of constant buoyancy (isopycnals) to construct a reliable background profile b_*. Consider tiling the computational domain by stacking several computational domains vertically, as in figure 5.2. The velocity and buoyancy perturbation repeat in each domain, but the vertical coordinate, z, is continuous such that the total buoyancy in one tile is L_z larger than the total buoyancy at the same relative position in the tile immediately below it. In this system it is particularly useful to consider two isopycnals separated by the vertical periodic length, i.e. L_z. These isopycnals will have the same shape due to the periodicity of θ, and the volume enclosed by these two isopycnals will therefore be constant. The buoyancy profile can then be sorted into a *background* state $b_*(z)$, where the parcels are sorted into the one-dimensional domain $0 \leq z - \overline{z_1}(t) < L_z$ and $\overline{z_1}$ is the mean height of the lower isopycnal. Essentially we are restricting b to lie in a range $[b_0, b_0 + L_z)$, and then sorting the values of b to obtain b_*. Given θ at each point, b (and therefore also z) can be uniquely determined from such a range. Although this background profile must have a mean vertical gradient equal to the imposed mean stratification, its local gradients $\partial b_*/\partial z$ can vary more generally. In the simple example considered in figure 5.1, this technique recovers the linear profile $Z_*(b) = b$ expected from the column displacement argument mentioned above.

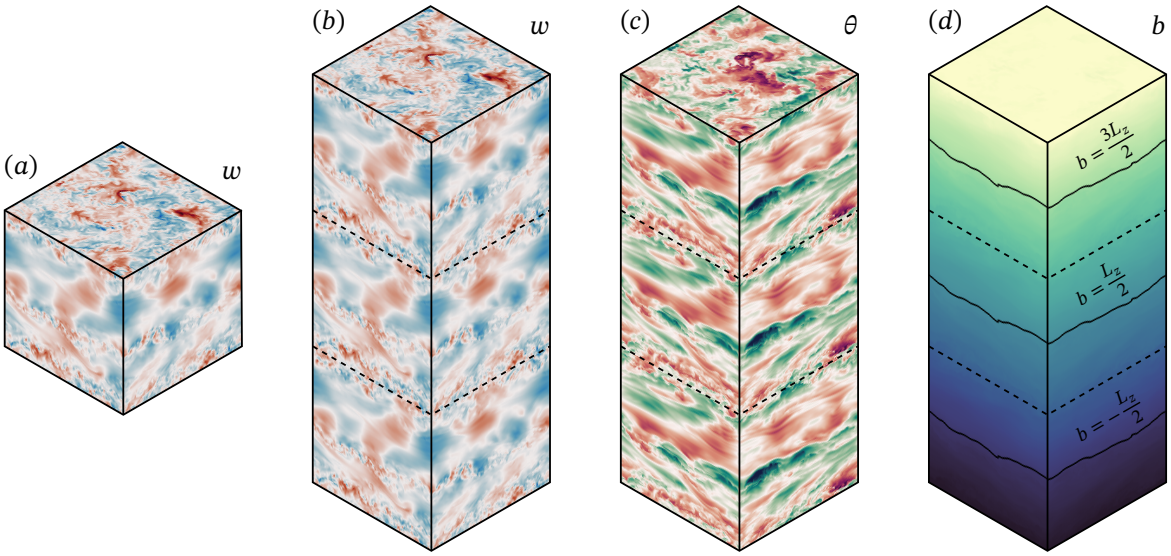

Fig. 5.2 Example schematic of tiling the periodic computational domain vertically. The vertical velocity w, shown in (a) and (b), and buoyancy perturbation θ, shown in (c), simply repeat thanks to their periodic boundary conditions. The total buoyancy $b = z + \theta$, shown in (d), is not periodic in the vertical, although isopycnal surfaces separated by the vertical period L_z are of identical shape.

By using such a method to obtain the background profile b_*, local APE as defined in (5.11) becomes a useful tool for investigating the mechanisms that lead to mixing in the domain. We are also able to accurately calculate the rate of irreversible mixing defined in (5.10), and by volume-averaging (5.11) we can obtain a global measure of the APE in the system. The mean local APE defined in this way can also be written in the form

$$E_A \equiv \langle E_{APE} \rangle = -Ri_0 \langle b\,(z - z_*) \rangle - Ri_0 \left\langle \int_z^{z_*(\boldsymbol{x},t)} b_*(s,t)\,\mathrm{d}s \right\rangle. \tag{5.12}$$

recovering the Winters et al. (1995) form of APE from (5.9) and an extra term. Winters and Barkan (2013) explain that this term accounts for the energy changes arising from the requirement of incompressibility, leading to displacement of some fluid elements to make room for the rearrangement of a fluid parcel in the sorting process. They also showed through considering fluid parcel exchanges that this term vanishes in the case of fixed horizontal boundaries.

We now consider a simple example to show how this term can change with the new definition of the background profiles. We prescribe $\theta = -z_1(x, y, t)$ as the buoyancy perturbation field, so the domain represents that of a uniform stratification where each fluid column has been shifted so that the $b = 0$ isopycnal is at z_1, analogously to the

situation shown in figure 5.1a. We enforce that b lies in the range $[0, L_z)$, so in this case the reference profiles simply take the form $b_*(s,t) = s - \overline{z_1}(t)$, and $Z_*(s,t) = s + \overline{z_1}(t)$. This is equivalent to considering our domain to be the volume bounded by the isopycnals $b = 0$ and $b = L_z$. We can therefore analytically compute

$$E_{APE}(\boldsymbol{x}, t) = \frac{Ri_0}{2}\left(z_1(x,y,t) - \overline{z_1}(t)\right)^2. \tag{5.13}$$

Recall that $z \equiv b - \theta$ now depends on the range we have specified b to take, so considering each of the terms in (5.12) separately, we also find that

$$-Ri_0 \left\langle b\,(z - z_*)\right\rangle = 0, \qquad -Ri_0 \left\langle \int_z^{z_*(\boldsymbol{x},t)} b_*(s,t)\,\mathrm{d}s \right\rangle = \frac{Ri_0}{2}\left(\overline{{z_1}^2} - \overline{z_1}^2\right). \tag{5.14}$$

The integral term, which is zero in the case of a fixed, bounded domain, accounts for all of the available potential energy in this scenario of raised and lowered fluid columns. The expression also only requires knowledge of the isopycnal shape, which acts as a moving boundary for our domain of sorting. We can envision that a global measure of APE can be split into a contribution from 'interior' APE of the form in (5.9), and a 'boundary' APE associated with the integral term.

In the following subsections, we further explore this concept by associating global quantities with a moving periodic domain that is bounded by two isopycnal surfaces. We shall show that the integral term above arises from the 'surface' potential energy associated with the deformation of the boundaries. We also obtain evolution equations for the global available and background potential energies $\mathcal{A}$ and $\mathcal{B}$. This global framework relies on computing surface integrals along the moving boundaries, which can become difficult if the isopycnals overturn or split into multiple surfaces. For calculating APE, it will often be simplest to compute the local APE as in (5.11) and then volume average.

5.2.2 Potential energy between isopycnal boundaries

We now describe more precisely the details of implementing isopycnal boundaries for quantifying available potential energy and mixing. We first choose a buoyancy value b_0 that defines the lower boundary surface $z_1(x,y,t)$ implicitly through

$$b(x, y, z_1(x,y,t), t) = b_0. \tag{5.15}$$

Vertical periodicity of θ then requires that the upper boundary surface $b = b_0 + L_z$ is defined by $z_2 = L_z + z_1$. It is important to appreciate that (5.15) defines z_1 (and hence

also z_2) as a single surface that spans the horizontal cross-section of the domain. This ensures that the volume enclosed by the isopycnals is clearly defined. To aid the calculation of volume integrals, we also require (essentially for clarity of exposition) z_1 to be a single-valued function of x and y, or equivalently that the boundary isopycnal cannot exhibit overturning. Such an isopycnal may be difficult to find in homogeneous turbulence, although stratified flows are often strongly spatially inhomogeneous. A discussion of how this approach could be generalised for an overturning isopycnal surface can be found in appendix A.1.

Constructing evolution equations for mean energy quantities requires us to take time derivatives of volume integrals. Since the boundaries of our domain now depend on time, we must apply the Leibniz rule to any such integral, that is

$$\frac{d}{dt}\left(\int_V f \,\mathrm{d}V\right) = \int_V \frac{\partial f}{\partial t}\,\mathrm{d}V + \int_A \left(f|_{z=z_2} - f|_{z=z_1}\right)\frac{\partial z_1}{\partial t}\,\mathrm{d}A, \tag{5.16}$$

where A is the horizontal cross-sectional area of the domain and $\mathrm{d}A = \mathrm{d}x\mathrm{d}y$ is the area element.

The mean kinetic energy of the system $\mathcal{K} = \langle|\boldsymbol{u}|^2\rangle/2$ is unaffected by the change of boundaries, since its integrand is periodic in the vertical direction. The evolution of $\mathcal{K}$ can therefore be derived straightforwardly from (5.2) and takes the simple form

$$\frac{d\mathcal{K}}{dt} = \mathcal{J} - \varepsilon, \tag{5.17}$$

where the buoyancy flux and kinetic energy dissipation rate are respectively given by

$$\mathcal{J} = Ri_0\langle w\theta\rangle, \qquad \varepsilon = \frac{1}{Re}\left\langle\frac{\partial u_i}{\partial x_j}\frac{\partial u_i}{\partial x_j}\right\rangle. \tag{5.18}$$

Note that from this definition, positive values of buoyancy flux correspond to a conversion of potential energy to kinetic energy.

However, extra terms do arise compared to (5.6) when deriving the potential energy evolution equation. These new terms provide a secondary reservoir of potential energy for the system, as is explained below. The advective flux across the boundary, given by the second term on the right of (5.6), is now zero since the bounding isopycnals have the same shape and the same gradients due to periodicity. Applying the Leibniz result (5.16) to the potential energy $\mathcal{P}$ and imposing the boundary conditions therefore produces the evolution equation

$$\frac{d\mathcal{P}}{dt} + \frac{d\mathcal{S}}{dt} = -\mathcal{J} + \mathcal{D}_p - \mathcal{F}_d. \tag{5.19}$$

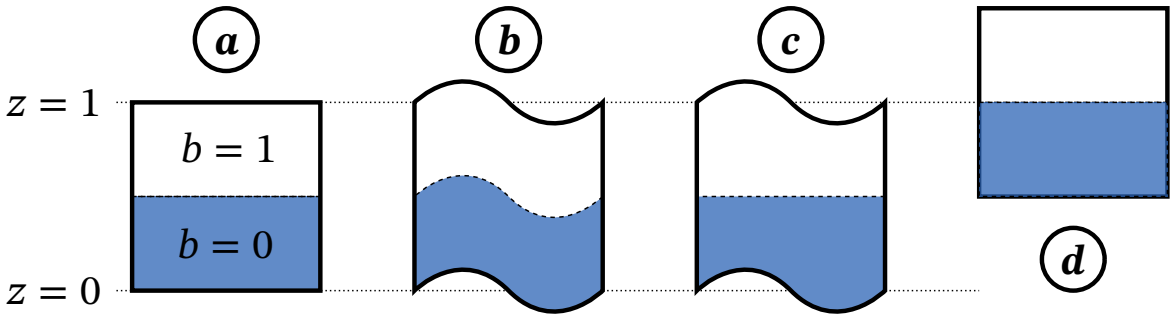

Fig. 5.3 A sketch of two-layer buoyancy fields with varying vertical boundaries.

A more detailed derivation of this equation can be found in appendix A.2.1. The term $\mathcal{D}_p = Ri_0/RePr$ is the conversion rate of internal energy to potential energy, and $\mathcal{F}_d$ is the diffusive boundary term given by

$$\mathcal{F}_d = \frac{Ri_0}{ARePr}\int_A \left[\frac{|\boldsymbol{\nabla} b|^2}{\partial b/\partial z}\right]_{z=z_1} \mathrm{d}A = \frac{Ri_0}{RePr}\overline{\left(\frac{|\boldsymbol{\nabla} b|^2}{\partial b/\partial z}\right)_{z=z_1}}, \tag{5.20}$$

where the overbar denotes a cross-sectional average over x and y, importantly taken after the quantity in brackets is evaluated at $z = z_1(x, y, t)$. We refer to the quantity $\mathcal{S}$ as the *surface potential energy*, where $\mathcal{S}$ is defined as

$$\mathcal{S} = Ri_0\left(\langle b_0 z\rangle + \frac{\overline{z_2^2}}{2}\right). \tag{5.21}$$

We can arbitrarily set $b_0 = 0$ in all of the above by shifting our vertical coordinate to $z - b_0$. $\mathcal{S}$ then takes the form of potential energy associated with an interface at z_2, motivating our choice for its name.

5.2.3 APE and BPE between isopycnal boundaries

Using the Winters et al. (1995) form of APE defined in (5.9) is not appropriate for the time-varying domains considered here. This can be understood by considering the simple two-layer system shown in figure 5.3. Panel (a) shows the background state obtained through constructing the one-dimensional buoyancy profile b_* for the buoyancy fields in panels (b) and (c). Since the buoyancy field in figure 5.3b can be obtained from the background state through shifting the same number of fluid columns up as down, $\mathcal{P}$ does not change between states (a) and (b). $\mathcal{P} = \mathcal{P}_B$ therefore holds for state (b), and hence $\mathcal{P}_A = 0$. It is simple however to construct a state (c) with lower potential energy

than state (b). The Winters et al. (1995) definition would then in fact give $\mathcal{P}_A < 0$ for the buoyancy profile in figure 5.3c, which is not consistent with the concept of available potential energy.

We aim to define a new APE variable $\mathcal{A}$ that can be used in the time-varying domain. Progress can be made by considering the *total potential energy* $\mathcal{P} + \mathcal{S}$ that appears in (5.19). The decrease in $\mathcal{P}$ from figure 5.3a to 5.3c is matched exactly by an increase in $\mathcal{S}$. In terms of the total potential energy, states (a) and (c) are therefore equivalent background states. This motivates subdividing the potential energy into

$$\mathcal{P} + \mathcal{S} = \mathcal{A} + \mathcal{B}. \tag{5.22}$$

We expect $\mathcal{A} = 0$ for states (a), (c), and (d) in figure 5.3. In particular for state (d) this means that any change in $\mathcal{P} + \mathcal{S}$ due to a vertical shift of the domain is captured by the background potential energy $\mathcal{B}$. We therefore construct the background profile $b_*(z)$ over the domain $\overline{z_1} < z < \overline{z_2}$, such that

$$Z_*(0,t) = \overline{z_1}(t), \qquad Z_*(L_z,t) = \overline{z_2}(t), \qquad b_*(\overline{z_1},t) = 0, \qquad b_*(\overline{z_2},t) = L_z. \tag{5.23}$$

This ensures that any change in $\mathcal{P}$ due to a shift in the mean height of the lower isopycnal $\overline{z_1}$ leads to a corresponding change in $\mathcal{P}_B$. Accounting also for the corresponding change in $\mathcal{S}$ leads to the following definitions for background and available potential energy:

$$\mathcal{B} = \langle -Ri_0 b z_* \rangle + \frac{Ri_0}{2}\overline{z_2}^2, \tag{5.24}$$

$$\mathcal{A} = \langle -Ri_0 b\,(z - z_*) \rangle + \frac{Ri_0}{2}\left(\overline{z_2^2} - \overline{z_2}^2\right). \tag{5.25}$$

Note that for a closed system with fixed, insulated boundaries, these definitions recover the Winters et al. (1995) form for BPE and APE up to a constant in the BPE. Since $\overline{z_2^2} - \overline{z_2}^2 = \overline{z_1^2} - \overline{z_1}^2$, we find that the additional terms exactly match those arising from the volume-integrated local APE in (5.14). The strong agreement between $\mathcal{A}$ and E_A gives us hope that in flows where $\mathcal{A}$ is not well defined, E_A can provide an accurate measure of available potential energy.

Evolution equations for these quantities can be readily obtained through multiplying the buoyancy evolution equation (5.3) by z_* and taking volume averages. An analogous derivation as that leading to (5.19), as shown in appendix A.2.2, results in

$$\frac{d\mathcal{B}}{dt} = \mathcal{M} + \mathcal{D}_p - \mathcal{F}_d, \tag{5.26}$$

where $\mathcal{M}$ is the irreversible mixing rate defined in (5.10). Subtracting (5.26) from (5.19) also gives an evolution equation for our new APE variable as

$$\frac{d\mathcal{A}}{dt} = -\mathcal{J} - \mathcal{M}. \tag{5.27}$$

We therefore recover the simple evolution equation for APE in a closed system, where the irreversible mixing rate $\mathcal{M}$ may also be identified with a destruction of APE (e.g. Peltier and Caulfield 2003).

5.3 Numerical simulations

We apply the extended APE framework developed in §5.2.3 to two sets of direct numerical simulations. All of these simulations are performed using DIABLO, which uses a third-order Runge–Kutta scheme for time stepping and a pseudo-spectral method for calculating spatial derivatives (Taylor 2008). The software also implements dealiasing of nonlinear terms through a 2/3 rule. One set of simulations (from chapter 3, now denoted set F) adds forcing terms to (5.2) and (5.3) to produce a flow in a statistically steady state, whereas the other simulations (from chapter 4, and now in set U) solve the equations unforced as an initial value problem. In all of the simulations, the bulk Richardson number Ri_0 and Prandtl number Pr are both set to one.

The first set of simulations are those used in our previous study on mixing in forced stratified turbulence in chapter 3. We refer to the simulations H, R and P in that chapter by F1, F2, and F3 respectively, and repeat some of their key parameters in table 5.1. Simulation F1 is forced by randomly phased large-scale vortical modes, and importantly features no direct forcing of the buoyancy field. The evolution equations (5.26) and (5.27) for $\mathcal{B}$ and $\mathcal{A}$ still therefore hold. On the other hand, simulations F2 and F3 are forced by large-scale internal gravity waves that include a buoyancy forcing component. The buoyancy forcing can act as a source or sink of potential energy, modifying the

Table 5.1 Overview of the various numerical simulations.

Simulation	F1	F2	F3	U1	U2	U3	U4
Reynolds number (Re)	10 000	10 000	10 000	8000	8000	5000	5000
Domain size ($L_x \times L_y \times L_z$)	$2\pi \times 2\pi \times 2\pi$			$8\pi \times \pi/2 \times 2\pi$			
Resolution	$1024 \times 1024 \times 1024$			$4096 \times 256 \times 1024$			
Initial condition	IGW spectrum			Shear and wave			
Forcing	Vortical	Waves	Waves	Unforced			

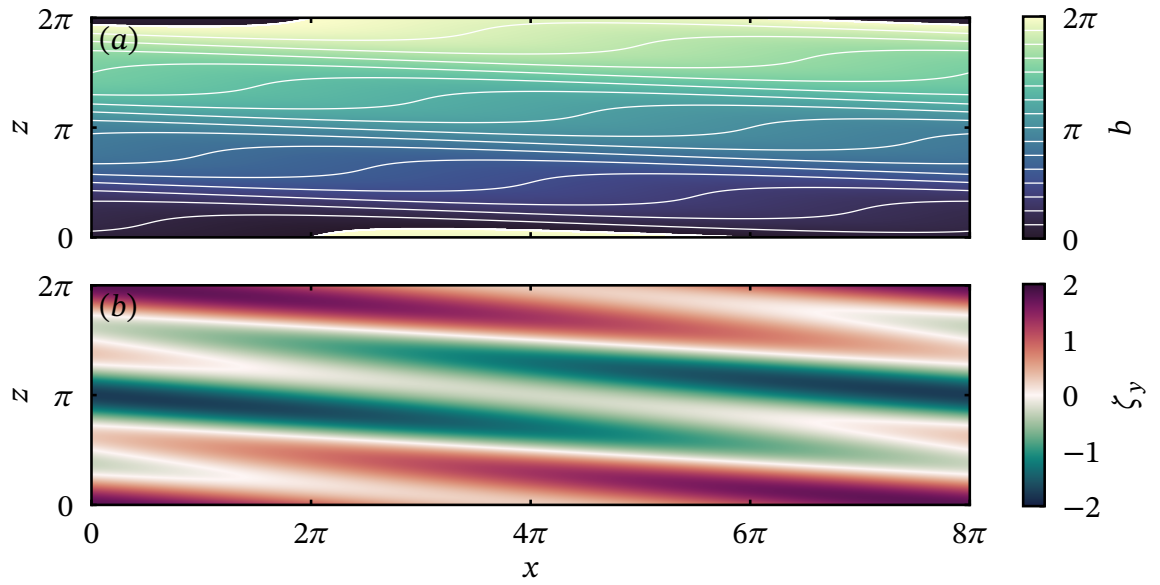

Fig. 5.4 The initial condition of simulation U4, where $s = 0.75$. (a) Contours and colour map of the total buoyancy field $b = z + \theta \bmod 2\pi$. (b) Colour map of the spanwise vorticity $\zeta_y = \dfrac{\partial u}{\partial z} - \dfrac{\partial w}{\partial x}$.

evolution equations. However if we are primarily concerned with diapycnal mixing, it remains useful to calculate the irreversible mixing rate $\mathcal{M}$ in these cases.

The second set of simulations, from chapter 4, investigate the interaction of a sinusoidal vertical shear flow and a plane internal gravity wave. The initial velocity and buoyancy fields are given by $\boldsymbol{u} = (\sin z)\,\hat{\boldsymbol{x}} + \boldsymbol{u}'$ and $\theta = \theta'$ respectively, where

$$\theta' = \frac{s}{m}\cos(kx + mz), \qquad \boldsymbol{u}' = \frac{s}{\sqrt{k^2 + m^2}}\sin(kx + mz)\left(1, 0, -\frac{k}{m}\right). \tag{5.28}$$

As before, we express the initial amplitude of the internal wave through its steepness s and choose the wave vector $\boldsymbol{k} = (k, l, m) = (1/4, 0, 3)$ based on the typical aspect ratios of waves observed in the thermocline by Alford and Pinkel (2000). Small-amplitude noise is added to the initial velocity field to allow the development of three-dimensional motion from the two-dimensional initial condition. Simulations U1 and U3 use an initial wave steepness of $s = 1$, with $s = 0.5$ for simulation U2 and $s = 0.75$ for simulation U4. As an example, the initial buoyancy and spanwise vorticity fields for U4 are shown in figure 5.4. Note that by taking $b = z + \theta \bmod 2\pi$ in figure 5.4a, we have effectively defined isopycnal boundaries at $b = 0$ and $b = 2\pi$.

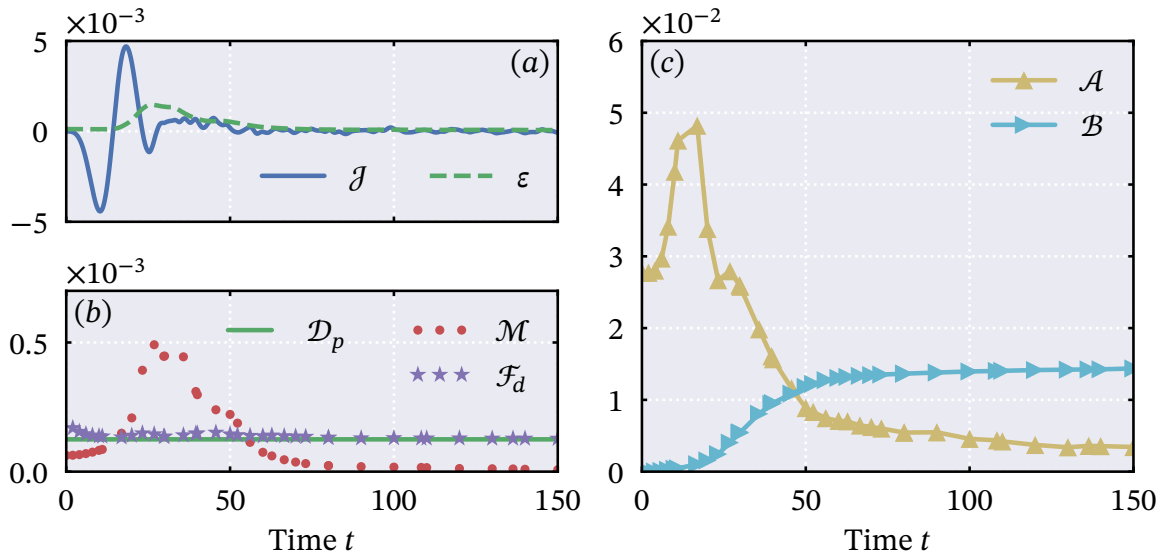

Fig. 5.5 Energy budgets for simulation U1. (*a*) Time series of the mean buoyancy flux and viscous dissipation rate; (*b*) time series of the BPE budget terms; (*c*) time series of available and background potential energies defined in (5.24) and (5.25). The time series for $\mathcal{B}$ is shifted by $-\mathcal{B}(0)$ for clarity. Terms denoted by symbols are computed from full flow output files, and so have lower time resolution than $\mathcal{J}$ and ε, which are computed 'on-the-fly'.

5.4 Results

5.4.1 Energy budgets

We now investigate the evolution of background and available potential energy in the various simulations, and consider how terms in the energy budgets (5.26) and (5.27) relate to the flow dynamics. Figure 5.5 plots a range of time series associated with the unforced simulation U1. The kinetic energy budget terms $\mathcal{J}$ and ε, defined in (5.18), are shown in figure 5.5a, and the BPE budget terms from (5.26) are shown in figure 5.5b. Time series of $\mathcal{A}$ and $\mathcal{B}$ are finally shown in figure 5.5c. Up to time $t \approx 20$, the energetics are dominated by large, reversible changes through the buoyancy flux. The initial increase in $\mathcal{A}$ seen in figure 5.5c is almost entirely returned to the kinetic energy through wave-mean flow interactions. During this time, there is little mixing and any changes in $\mathcal{B}$ are small. A wave breaking event follows, producing an intermittent burst of turbulent activity that coincides with high values of the diapycnal mixing rate $\mathcal{M}$ and the KE dissipation rate ε. For $30 < t < 50$, this mixing coincides with positive values of the mean buoyancy flux, leading to a fast drop in $\mathcal{A}$. The flow relaminarizes at late

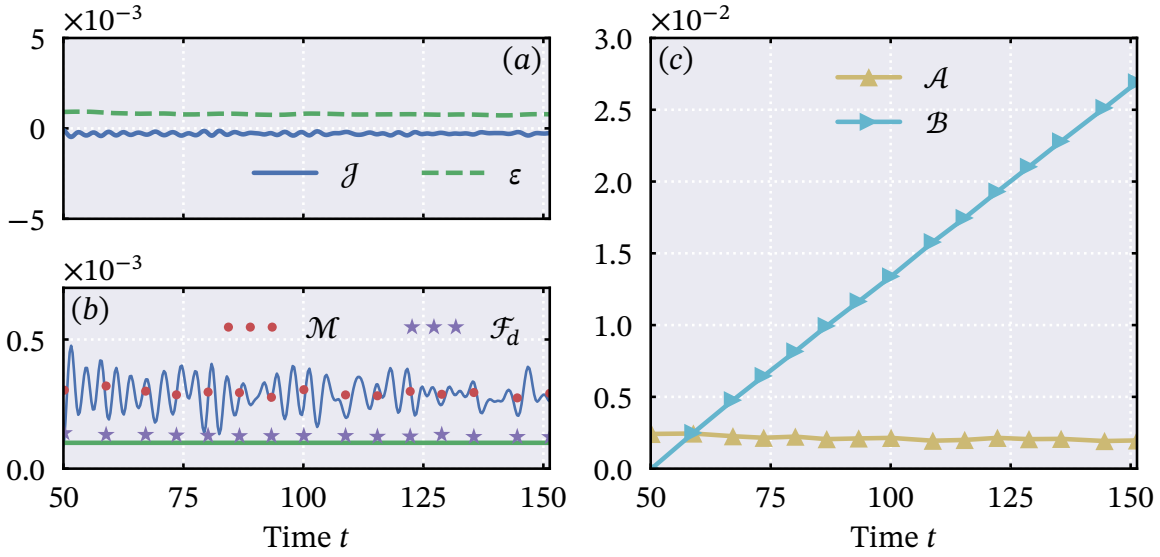

Fig. 5.6 Potential energy budgets for the late-time statistically steady state achieved in simulation F1. Subplots are as in figure 5.5, with $-\mathcal{J}$ additionally plotted on panel (b).

times, with all quantities tending to constant values and small fluctuations persisting in the APE and buoyancy flux.

The increase in $\mathcal{B}$ over the duration of the simulation is well described by the total diapycnal mixing associated with the breaking event. Indeed the other non-negligible terms in the budget (5.26) are close to being equal, as shown in both figures 5.5 and 5.6. The diffusive boundary term $\mathcal{F}_d$ primarily acts to cancel out any increase in $\mathcal{B}$ due to the conversion of internal energy to potential energy through $\mathcal{D}_p$. This cancellation is exact when the boundary has no lateral variation, and arises since the system is forced to maintain a constant mean buoyancy gradient through the periodicity of θ.

Figure 5.6 repeats the analysis of figure 5.5 for the forced simulation F1. We only consider the statistically steady period achieved at late times in this flow. Unlike in the unforced simulation, the mean buoyancy flux remains negative throughout as shown in figure 5.6a, providing a source of APE from the kinetic energy. Figure 5.6b furthermore shows that the buoyancy flux is on average in balance with the mixing rate, leading to an approximately constant value of $\mathcal{A}$, as shown in figure 5.6c. The constant mixing rate also predictably leads to a linear increase in the background potential energy.

5.4.2 Visualising mixing with local APE

We can further investigate the local processes that lead to the global results above by analysing the distribution of local APE throughout the domain. Figure 5.7 plots snap-

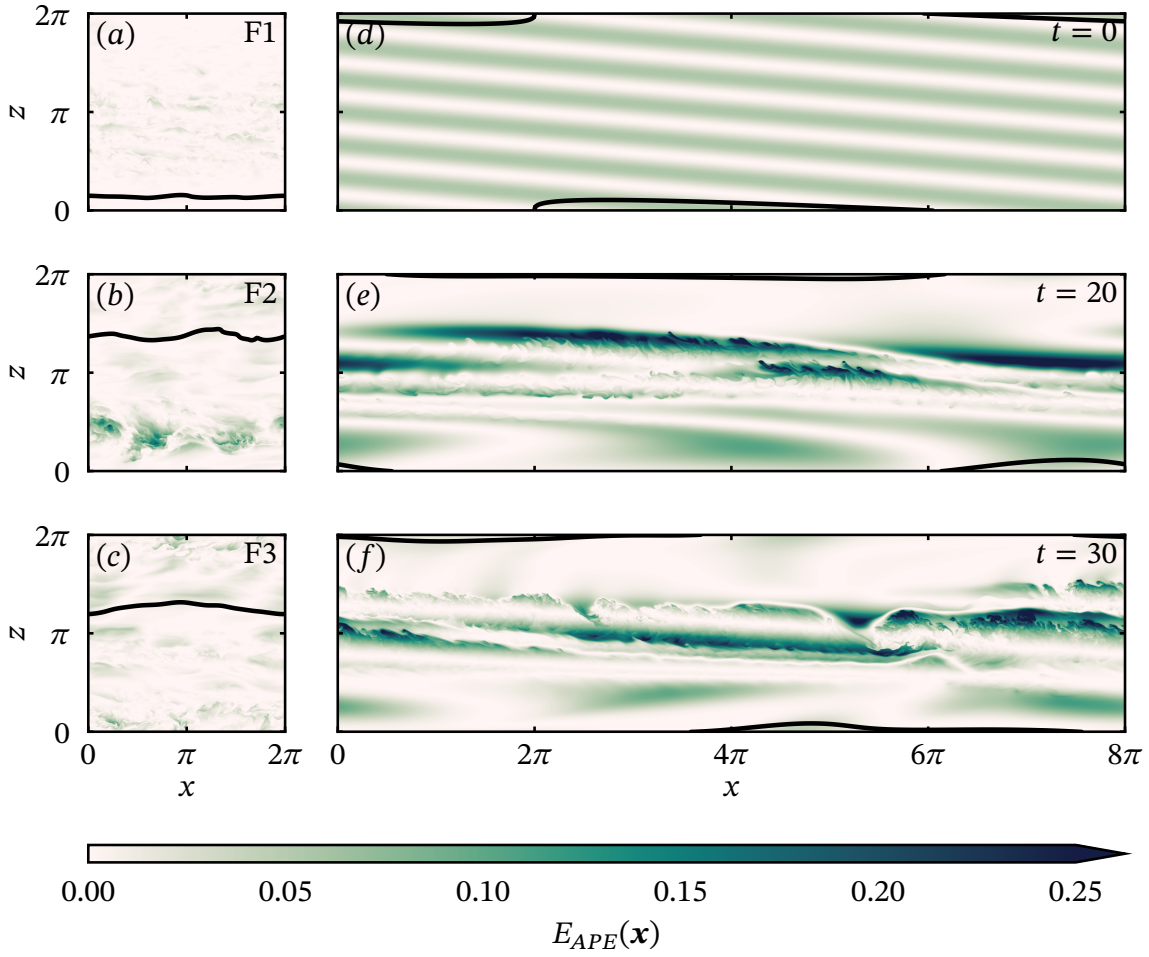

Fig. 5.7 Vertical plane snapshots of E_{APE} as defined in (5.11) for simulations performed in chapters 3 and 4. Solid lines in each case denote the isopycnal boundary z_1 from which the APE is calculated. Snapshots from the forced simulations of chapter 3 are each taken at time $t \approx 150$ with runs F1, F2, F3 shown in (a), (b), (c) respectively. Panels (d)-(f) display the evolution of E_{APE} in simulation U1 of chapter 4 from the initial condition to the peak in mixing at time $t = 30$.

shots of $E_{APE}(\boldsymbol{x}, t)$ from simulations F1-F3 and from simulation U1 at various times. Since the turbulence arising in each simulation is patchy and inhomogeneous, we are able to choose appropriate isopycnal boundaries for each simulation and hence calculate the surface potential energy $\mathcal{S}$. These isopycnal boundaries are shown in figure 5.7 as solid black lines.

Data from the forced simulations of set F are presented in figures 5.7a-c. Each snapshot of E_{APE} is taken at time $t \approx 150$, when the turbulence is in a statistically steady state. Figure 5.7a highlights low local APE values throughout the domain of simulation F1. Increased E_{APE} occurs only at small scales and in regions with high turbulent dissipation rates (not shown). In this sense, APE is primarily associated here with the distortion of the buoyancy field by turbulence, and not with internal waves. By contrast, figures 5.7b and 5.7c show patches of high local APE throughout the domain at a range of scales. This is consistent with associating mixing with intermittent, large-scale overturns and convectively-driven turbulence, as discussed in chapter 3.

The development of local APE during the unforced simulation U1 is presented in figures 5.7d-f. The distribution of E_{APE} in the initial condition is shown in figure 5.7d, and is entirely associated with the internal gravity wave described by (5.28). At early times, the wave is refracted by the shear flow, leading to a distortion of the banded structure in the local APE field. By time $t = 20$, E_{APE} preferentially accumulates in the upper half of the domain while maintaining some signal of the wave structure, as shown in figure 5.7e. The large values of E_{APE} lead to locally unstable buoyancy profiles, and the development of convective instabilities. The associated convection converts APE to kinetic energy through the buoyancy flux, and also promotes the emergence of small scale structures seen in figure 5.7e. Later, at $t = 30$, the flow becomes more complex with the development of shear-driven turbulent billow structures. These structures, seen prominently on the right of figure 5.7f, span regions of both high and low E_{APE}. Although the volume-averaged mixing rate peaks near this time, the banded structure of E_{APE} leads to strong local variation in local mixing rates within the turbulent patches. Mixing is high where turbulence and APE coexist, and it cannot occur where there is no APE to remove.

5.4.3 Estimating mixing with χ

In the limit of small buoyancy perturbations from the uniform, imposed buoyancy gradient, available potential energy can be approximated by

$$\tilde{\mathcal{A}} = \frac{Ri_0}{2} \left\langle \theta^2 \right\rangle. \tag{5.29}$$

This quantity satisfies the simple evolution equation

$$\frac{d\tilde{\mathcal{A}}}{dt} = -\mathcal{J} - \chi, \tag{5.30}$$

where χ is the rate of destruction of buoyancy variance, i.e. the dissipation rate defined by

$$\chi = \frac{Ri_0}{RePr} \left\langle |\boldsymbol{\nabla}\theta|^2 \right\rangle = \frac{Ri_0}{RePr} \left\langle |\boldsymbol{\nabla} b|^2 - 1 \right\rangle. \tag{5.31}$$

Comparing the definitions (5.10) and (5.31), we see that χ precisely takes the form of the irreversible mixing rate $\mathcal{M}$ only for the specific case where the sorted background buoyancy profile b_* exactly matches the imposed uniform stratification. Recall that this imposed constant stratification has a dimensionless buoyancy gradient equal to one by construction. In our simulations, local deviations in the buoyancy field are not always small and we should treat the above approximation with caution. For example, during the convective phase ($20 < t < 30$) of simulation U1 there are sizeable regions of the domain with statically unstable buoyancy gradients. The peak mixing in this case occurs where the (horizontal) mean buoyancy is in a layered state, with 'layers' of relatively low stratification separated by 'interfaces' of relatively high stratification compared to the imposed constant buoyancy gradient. Such layered states are observed to arise naturally in turbulent stratified flows, for a wide variety of dynamical reasons (Caulfield 2021).

Nevertheless the dissipation rate χ is significantly more straightforward to quantify than the true mixing rate $\mathcal{M}$, and so it is useful to investigate how well it can actually approximate the mixing. The accuracy of χ for estimating mixing is also important in the context of ocean microstructure measurements, where small-scale gradients are measured directly but there is no way to obtain the relevant reference profile b_*. In figures 5.8a-c, we therefore plot the time series of both χ and $\mathcal{M}$ for each of our simulations. By inspection, the two quantities appear to match up very well, with the symbols marking the mixing rate overlapping the lines plotting the time series of χ. To quantify how well χ approximates $\mathcal{M}$, we plot the time series of their ratio in figures 5.8d-f. Throughout the forced simulations, and for the early times of the unforced simulations, χ remains

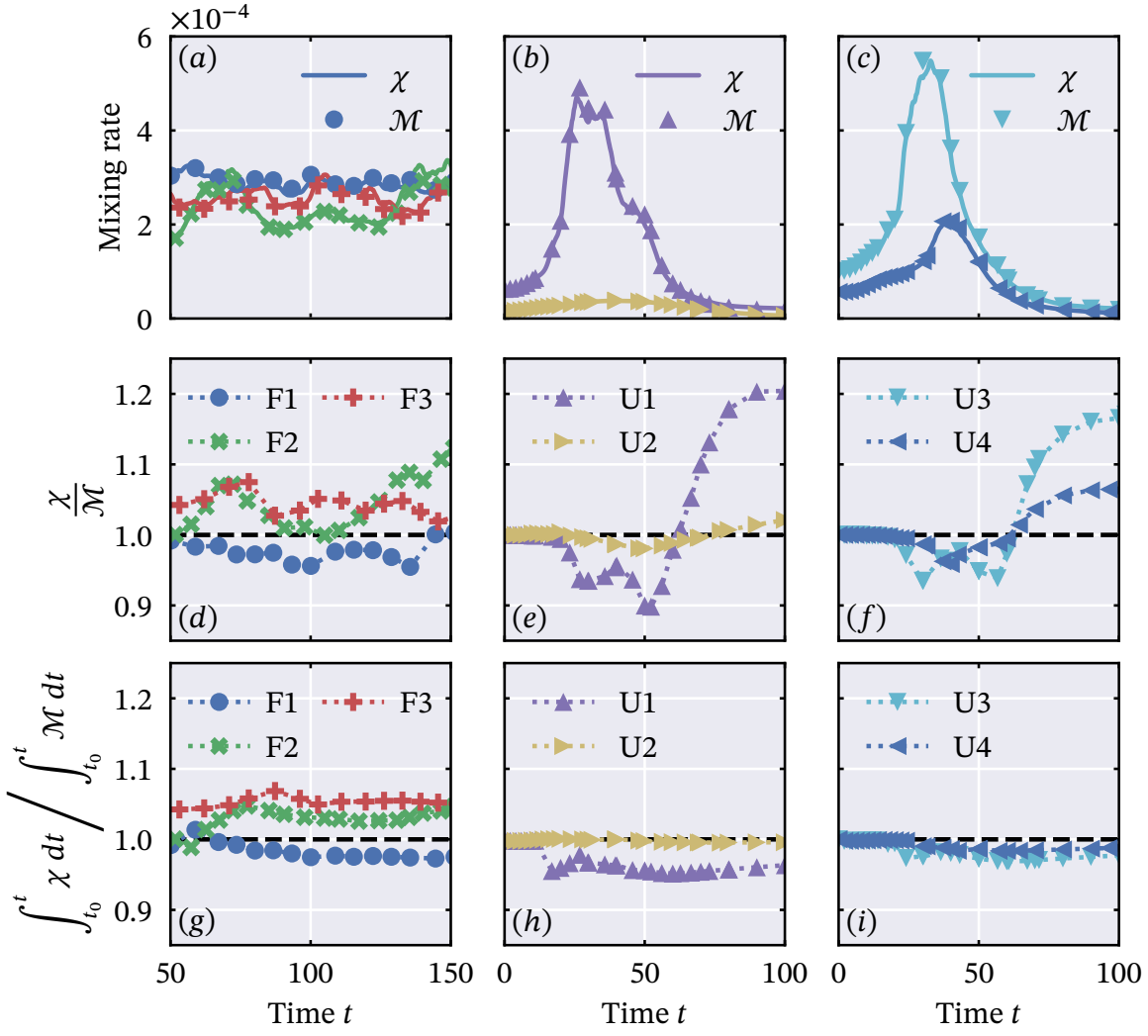

Fig. 5.8 A time series comparison of the irreversible mixing rate $\mathcal{M}$ and the dissipation rate χ for each simulation in table 5.1. (a)-(c) plot the time series of $\mathcal{M}$ and χ; (d)-(f) plot the time series of $\chi/\mathcal{M}$ to highlight the fractional difference between the two; (g)-(i) plot the time series of the ratio of the time-integrated quantities.

within 10% of the true mixing rate. At late times in simulations U1 and U3 the difference increases up to 20%, but at this stage the flow is relaminarizing and $\mathcal{M}$ and χ are both small. Indeed we show that this discrepancy is unimportant for quantifying the total mixing achieved over the course of the simulations in figures 5.8g-i, where we plot the ratio of time-integrated χ and $\mathcal{M}$. The time integral of $\mathcal{M}$ is equal to the increase in background potential energy due to diapycnal mixing, and we see that using χ to estimate this quantity results in at most a 5% error in the total BPE change (corresponding to the final values of the cumulative ratio plotted in figures 5.8g-i).

In the unforced simulations, χ consistently provides a slight underestimate of the diapycnal mixing rate. This suggests that regions of intense turbulent mixing, associated with high values of $|\boldsymbol{\nabla} b|$, preferentially sample regions where $\partial Z_*/\partial b > 1$. These regions are in turn associated with the reference buoyancy profile b_* having a locally *weaker* stratification than the mean. In simulations F2 and F3, where forcing is applied in the form of internal gravity waves, the opposite is true and χ provides a slight overestimate of $\mathcal{M}$. However it is not true that intense mixing occurs only in regions of strong or weak local stratification in each flow. In all of the forced simulations for example, the standard deviation of $\partial Z_*/\partial b$ rises from the range 0.1-0.15 at time $t = 50$ up to 0.25-0.3 at $t = 150$, suggesting that as mixing persists throughout the simulations, the background profile is modified. The fractional error between χ and $\mathcal{M}$ seen in figure 5.8d does not show this increasing trend, suggesting that some local overestimates of $\mathcal{M}$ (where $\partial Z_*/\partial b < 1$) cancel with some local underestimates (where $\partial Z_*/\partial b > 1$) in the global average. Similarly, the standard deviation of $\partial Z_*/\partial b$ reaches values in the range 0.15-0.2 for simulations U1 and U3 when $t > 30$, approximately double the fractional error during the period of peak mixing.

5.4.4 The effect of mean flow dissipation

In the unforced simulations of set U, the majority of the kinetic energy is associated with the initial mean shear profile $\overline{u} = \sin z$. At late times in these scenarios, the flow begins to relaminarize and the kinetic energy dissipation rate ε is dominated by the laminar diffusion of the mean shear. Mixing efficiency is however often calculated using the *turbulent* kinetic energy dissipation rate, that we quantify here as

$$\varepsilon' = \frac{1}{Re}\left\langle \frac{\partial u_i'}{\partial x_j}\frac{\partial u_i'}{\partial x_j}\right\rangle, \tag{5.32}$$

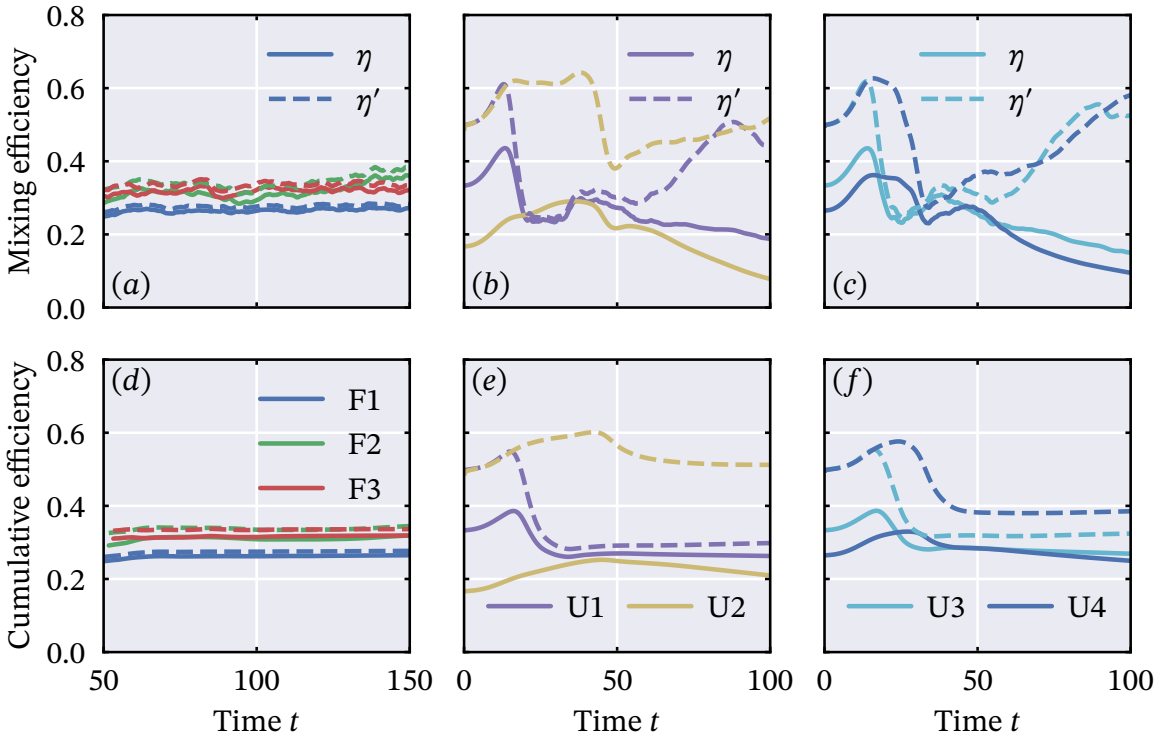

Fig. 5.9 Time series of (a)-(c) instantaneous and (d)-(f) cumulative mixing efficiency, calculated with and without the mean flow dissipation, as defined in (5.33) and (5.34) respectively.

where $\boldsymbol{u}' = \boldsymbol{u} - \overline{\boldsymbol{u}}$ is the velocity field perturbation from the horizontal average. Figure 5.9 compares time series of the following definitions of mixing efficiency calculated using either the turbulent dissipation rate ε' or the total rate ε

$$\eta = \frac{\chi}{\chi + \varepsilon}, \qquad \eta' = \frac{\chi}{\chi + \varepsilon'}. \tag{5.33}$$

We use χ rather than $\mathcal{M}$ in our definition of efficiency, since we have seen that the difference between them is small in the previous section, and our records of χ have better resolution in time. Large discrepancies between η and η' are observed when the average TKE dissipation rate ε' is small compared to the dissipation rate of the mean flow $\bar{\varepsilon} = \langle |\partial \overline{\boldsymbol{u}}/\partial z|^2 \rangle / Re$. In simulation U2, wave breaking occurs at $t \approx 50$ and consists of small, strongly localised overturns that dissipate relatively quickly. Consequentially ε' remains smaller than $\bar{\varepsilon}$ for the entire duration, leading to large differences between the efficiencies in figure 5.9b. η' takes much larger values than η in all of the unforced simulations at early and late times, with η' close to its initial value of 0.5. This value corresponds to the diffusion associated with the plane wave form of (5.28) and is a con-

sequence of the choice $Pr = 1$, that is molecular diffusion of buoyancy occurs at the same rate as the diffusion of momentum. At larger values of Pr, diffusion of the wave would result in a far lower value of η'.

In figure 5.9d-f we also plot associated cumulative mixing efficiencies, defined here in terms of appropriate integrals of χ and ε (or ε'):

$$\eta_c = \frac{\int_{t_0}^{t} \chi(t')\,\mathrm{d}t'}{\int_{t_0}^{t} \chi(t') + \varepsilon(t')\,\mathrm{d}t'}, \qquad \eta_c{}' = \frac{\int_{t_0}^{t} \chi(t')\,\mathrm{d}t'}{\int_{t_0}^{t} \chi(t') + \varepsilon'(t')\,\mathrm{d}t'}, \tag{5.34}$$

where $t_0 = 50$ for the forced cases, and $t_0 = 0$ for the unforced cases. The time integrals represent the energy changes associated with the cumulative effects of χ and ε. Figures 5.9e and 5.9f show that the diffusion of the mean shear flow has a significant impact on the total cumulative efficiency in the unforced simulations. In oceanographic flows, we expect molecular diffusion to be negligible compared to the turbulent dissipation rate for the vast majority of the internal wave spectrum. This result therefore highlights the challenge of using direct numerical simulations, where Re is inevitably limited by computational resources, to investigate ocean mixing processes.

5.5 Discussion and conclusions

In this study, we have highlighted how the APE framework of Winters et al. (1995) should be generalised in the triply-periodic system often used in numerical simulations of stratified turbulent flows. In these systems it is important to constrain the buoyancy field, inferred from the periodic perturbation θ, to lie in a prescribed range. We can then construct an accurate background buoyancy profile b_* that is consistent with the periodic nature of the system. However, setting limits on the buoyancy values effectively means that the shape of the domain can change in time. In the case where the limiting buoyancy value has a non-overturning isopycnal surface, we find that this introduces an extra potential energy term $\mathcal{S}$ as defined in (5.21). Appropriate definitions of available and background potential energy can then be obtained by accounting for this additional term as in (5.24) and (5.25).

Constructing the correct background profile is also vital for accurately calculating the local APE density E_{APE} defined by Scotti and White (2014). This quantity can then provide useful information for identifying mechanisms by which mixing can occur. When integrated over the domain, the local APE also recovers all of the additional terms in our new global APE variable $\mathcal{A}$. Furthermore, the local APE can even be quantified

in scenarios where our global APE is not well defined. So long as the background profile b_* is identified, both $E_A \equiv \langle E_{APE} \rangle$ and the irreversible mixing rate $\mathcal{M}$ can be calculated. The evolution of E_A is then entirely determined by the mixing rate and the buoyancy flux, with zero contribution from boundary fluxes. We can therefore calculate the exact rate of diapycnal mixing in more energetic stratified flows that use periodic domains, such as those considered by de Bruyn Kops and Riley (2019) and Portwood et al. (2019). This technique for calculating APE could also be applied to *unstably* stratified periodic systems, where $Ri_0 < 0$, used to study bulk properties of convection (e.g. Lohse and Toschi 2003). In traditional Rayleigh–Bénard convection, Gayen et al. (2013) find that irreversible mixing is largely confined to thermal boundary layers. It would therefore be interesting to investigate whether the theoretical prediction of $\eta \to 0.5$ at high Ra holds for the periodic convection setup, where such boundary layers are absent.

In observational oceanography, turbulent mixing can be estimated through the use of fast-response thermistors to measure small-scale temperature gradients. The primary aim in this context is to estimate a diapycnal diffusivity, defined in our dimensionless formulation as

$$K_d = \frac{Ri_0}{RePr} \left\langle \left(\left. \frac{\partial Z_*}{\partial b} \right|_{b(\boldsymbol{x},t)} \right)^2 |\boldsymbol{\nabla} b|^2 \right\rangle = \frac{Ri_0}{RePr} \left\langle \frac{|\boldsymbol{\nabla} b|^2}{\left(\left. \partial b_*/\partial z \right|_{z_*(\boldsymbol{x},t)} \right)^2} \right\rangle. \tag{5.35}$$

Since the reference profile b_* cannot be obtained in the ocean, a large-scale average is taken of the buoyancy (or temperature) gradient. The estimate often attributed to Osborn and Cox (1972) is then used such that

$$K_d \approx \frac{Ri_0}{RePr} \frac{\left\langle |\boldsymbol{\nabla} \theta|^2 \right\rangle}{\langle \partial b/\partial z \rangle^2} = \chi. \tag{5.36}$$

Note that the internal energy conversion rate $\mathcal{D}_p$ is neglected here, since it is assumed to be much smaller than χ in a turbulent flow. In dimensional form it is common to see (5.36) written as $K_d = \chi/N^2$, but in our non-dimensionalization the mean buoyancy gradient in the denominator is prescribed to be equal to one. The approximation made in estimating K_d in (5.36) is the same approximation used in §5.4.3 to estimate the mixing rate $\mathcal{M}$ with χ. Precisely, we approximate the reference buoyancy gradient $\partial b_*/\partial z$ by the imposed mean stratification. We test this approximation in the context of diapycnal diffusivity in figure 5.10 by plotting the time series of $(\chi + \mathcal{D}_p)/K_d$. The fractional error between the estimate $\chi + \mathcal{D}_p$ and the true diffusivity remains within one standard deviation of $\partial Z_*/\partial b$ for every simulation. Figures 5.10b and 5.10c show

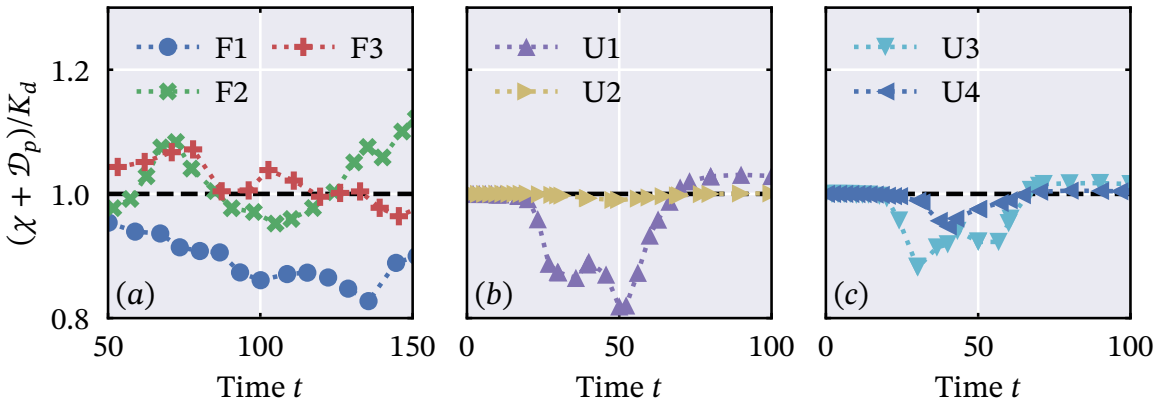

Fig. 5.10 A time series comparison of the diapycnal diffusivity K_d and the approximation of $\chi + \mathcal{D}_p$. The ratio of the two is plotted in an analogous fashion to figures 5.8d-f.

that $\chi + \mathcal{D}_p$ underestimates the diffusivity at the time of most intense mixing in the unforced simulations. This reaffirms the conclusion drawn from figures 5.8e and 5.8f that the turbulent mixing in this flow preferentially samples regions of relatively weak local stratification. Salehipour and Peltier (2015) find a similar underestimation of K_d in turbulent flows developing from Kelvin–Helmholtz instability in a stratified shear layer. An investigation to identify in which flows (5.36) provides an over/underestimate of the diffusivity would be valuable for understanding the variability associated with the approximation.

We include the internal energy conversion rate $\mathcal{D}_p$ in our estimate in figure 5.10 since it is not always negligible in the simulations. Furthermore Gregg et al. (2018) remark that $\mathcal{D}_p$ should be included when applying mixing results to the strongly stratified pycnocline where mixing is localised and intermittent. In the periodic setup studied here, the boundary flux $\mathcal{F}_d$ counteracts $\mathcal{D}_p$ in the BPE energy budget (5.26) to maintain the constant mean stratification. Indeed in a state of statistically steady *homogeneous* stratified turbulence, $\mathcal{F}_d$ must cancel both $\mathcal{D}_p$ and $\mathcal{M}$ to ensure a constant value of $\mathcal{B}$ through (5.26). When quantifying diffusivity in this system, it is therefore important to include the contribution from $\mathcal{D}_p$ and to compute $\mathcal{M} + \mathcal{D}_p$ directly, instead of relying on changes in BPE. In many observational studies focused on mixing in turbulent patches (where $\mathcal{D}_p$ is negligible), practical difficulties in obtaining an accurate value of χ result in far larger implied levels of uncertainty than those apparent in in figure 5.10 (see for example Waterhouse et al. 2014). In this sense our results show that (5.36) provides a good estimate of the diapycnal diffusivity in the stratified flows considered.

Due to the aforementioned difficulties involved in accurately resolving small-scale temperature gradients, shear probes are used more frequently than thermistors to infer

mixing rates in the ocean. Further assumptions are however needed to obtain mixing estimates from such velocity gradient measurements. On top of the Osborn and Cox (1972) model, the buoyancy variance destruction rate may be approximated by $\chi \simeq -\mathcal{J} = \Gamma\varepsilon$, where the turbulent flux coefficient Γ is taken to be a constant, usually 0.2 in practice after Osborn (1980), under a set of assumptions that the turbulent flow is, for example quasi-steady. The turbulent flux coefficient is related to the mixing efficiency defined in (5.33) through

$$\Gamma = \frac{\eta}{1-\eta}. \tag{5.37}$$

Many experimental and numerical studies have shown variation in the mixing efficiency across a range of stratified flows, as reviewed by Ivey et al. (2008) and Caulfield (2021). This has motivated a body of work to investigate the functional dependence of η on various dimensionless parameters, including the Richardson number, buoyancy Reynolds number $Re_b = \varepsilon/\nu N^2$, and turbulent Froude number $Fr = \varepsilon/N\mathcal{K}$. Despite this concerted effort to provide insight into how η varies, there is no clear physical explanation as to why $\Gamma = 0.2$ is a sensible assumption or why it appears to provide diffusivity estimates in line with those from tracer release experiments (Ledwell et al. 2000). In figure 5.9 we highlight examples where laminar diffusion of a shear flow can strongly impact the calculated values of η. Although not relevant for high Reynolds number flows found in the ocean, it is important to acknowledge the effect of this diffusion in idealised numerical studies that discuss mixing efficiency in the context of ocean mixing. This is most relevant for flows where turbulence is transient and localised, such as those arising from instabilities in stratified shear layers.

In particular, for the energetic framework presented here to be truly applicable to real oceanographic flows, there are at least three open issues which need to be addressed. First, it is not at all clear what the effect of more realistic Reynolds numbers, or indeed realistically higher values of $Pr = O(10-1000)$ will have on the various mixing properties and energetic pathways discussed here. Second, it is still an open question of some controversy whether $\Gamma \approx 0.2$, or equivalently $\eta \approx 1/6$, is actually 'typical' of quasi-steady mixing processes, or whether Γ actually depends on parameters of the flow. Portwood et al. (2019) recently demonstrated the emergence of $\Gamma = 0.2$ in sheared DNS that was controlled by construction to be quasi-steady. It is at least plausible that the higher values of efficiency observed for the flows discussed here are artefacts of the inherent transience of these flows. Of course, mixing events in the ocean are likely to be highly spatio-temporally intermittent, not least because of the key role played by 'breaking' internal waves, as argued by MacKinnon et al. (2017) and modelled here, so the relevance of quasi-steady sustained stratified turbulence to the real ocean is not immedi-

ately obvious. Thirdly, complications associated with layered states, either due to hydrodynamic mechanisms associated with turbulence (Caulfield 2021) or associated with double-diffusive convection (Schmitt 1994) are clearly of interest. The energetic framework presented here is nevertheless well-suited to address these three open issues, or indeed other challenges of real relevance to the quantification and parameterization of mixing in realistic stratified flows.

Chapter 6

A perspective on stratified mixing

6.1 Thesis summary

Throughout this dissertation, we have explored the complex interaction between internal waves, mean vertical shear, and turbulence in a collection of stratified flow simulations. Motivated to understand the processes by which diapycnal mixing occurs in the ocean interior, we have chosen not to focus on a single, canonical flow problem to act as a model for turbulence in the ocean. In the context of a downscale transfer of energy from internal waves, there are many plausible physical mechanisms by which turbulence can be generated in the stratified ocean. We have therefore investigated a range of stratified flows, with various interpretations of the primary large-scale effects of internal waves and shear. We summarise below the key findings from these studies.

In chapter 2, we studied the development of Kelvin–Helmholtz instability in a stratified shear layer. Using two-dimensional direct numerical simulations, we focused on the nonlinear development of the instability as the minimum Richardson number Ri_m of the flow approaches the 'marginal' value of 1/4 from below. Steady inviscid parallel shear flows must be linearly stable if $Ri_m > 1/4$ by the theorem of Miles (1961) and Howard (1961). In its application to strongly-sheared oceanographic flows by Thorpe and Liu (2009) and Smyth and Moum (2013), this theoretical result has been assumed to imply the growth or decay of turbulence for values of the gradient Richardson number Ri_g below or above 1/4 respectively.

As a first investigation of how nonlinear dynamics are affected by a change in Ri_m near such marginal values, we performed simulations with a range of Ri_m up to 0.245 at finite Reynolds number. Since the growth rate of the linear Kelvin–Helmholtz instability decreases with increasing Ri_m, laminar diffusion of the shear flow suppressed the growth of the instability at higher values of Ri_m. By actively forcing the flow to counter

this diffusion of the base shear flow, we were able to quantify the maximum energy attained by the nonlinear perturbations arising from the linear instability. The maximum energy decreased linearly to a small but somewhat surprisingly non-zero value as $Ri_m \to 1/4$, as shown in figure 2.3a. This trend applied both when the base shear flow was steady and when it was forced to accelerate.

At Richardson numbers close to 1/4, the familiar billow structures associated with Kelvin–Helmholtz instability become very thin, as if squashed by the stable stratification. Together with a very slow growth to saturation, this suggests that such nonlinear states become difficult to access when Ri_m is close to (but still less than) 1/4. This is at least superficially consistent with the recent study of Portwood et al. (2019), who find a 'marginal' steady state of sheared, stratified turbulence at $Ri_g \approx 0.16$, significantly below the classical value of 1/4. There however remain several open questions related to stratified shear flows, not least concerning the applicability of the concept of 'self-organised criticality' (Salehipour et al. 2018; Smyth et al. 2019).

The vast majority of the ocean cannot of course be treated as a statistically steady state of shear-driven stratified turbulence. The study of chapter 2 did not address the question of how energy is supplied to the shear flow. Away from boundaries, it is commonly accepted that the internal gravity wave field plays a key role in the supply of energy to turbulence in the ocean. Velocity shear in internal waves varies significantly in space and time, suggesting that a more general consideration of internal wave breaking is necessary to investigate turbulent mixing relevant to the ocean interior.

Scales at which waves break and transfer energy nonlinearly to turbulence are associated with an energy spectrum of $E(m) \sim N^2 m^{-3}$ (Gargett et al. 1981). This spectrum is consistent with the self-similar regime of 'strongly stratified turbulence' proposed by Billant and Chomaz (2001), although most simulations aimed at reproducing that regime (e.g. Maffioli et al. 2016) supplied energy to the large-scales through the forcing of vortical modes, rather than internal waves. In chapter 3, we therefore compared the flows arising from forcing vortical modes with those arising from forcing internal waves, with a particular focus on their mixing properties.

In each case, turbulence was spatially inhomogeneous, with the horizontal average of the TKE dissipation rate varying over orders of magnitude in the vertical. By fixing the rate of energy input from each type of forcing, we obtained flows where the turbulence (characterised by the perturbations from the horizontal mean) was maintained in a statistically steady state. Slow changes in the mean shear, as also seen in previous studies, did not appear to impact the turbulence significantly.

From the statistically steady states, we found that the forcing of internal gravity waves led to a higher turbulent flux coefficient $\Gamma = \chi/\varepsilon$ than the forcing of vortical modes. Inspection of the buoyancy field suggested that this was related to larger buoyancy overturns in the wave-forced cases, and hence a more 'convective' mixing mechanism. Using horizontal averages, we showed that χ and ε were extremely well-correlated throughout the domains of each flow. Even though Γ took different values depending on the forcing applied, within each simulation Γ (calculated from horizontal averages) was shown to be independent of an appropriately calculated turbulent Froude number $Fr = \varepsilon/N\mathcal{K}$, consistent with the low Fr results of Maffioli et al. (2016). In the vortically-forced simulation, a trend of $\Gamma \sim Fr^{-1}$ appeared to emerge at $Fr = O(0.1)$, consistent with the scalings of Garanaik and Venayagamoorthy (2019). However their link between Fr and the Elisson and Ozmidov length scales L_E and L_O was not found to apply to our data. Given the prevalence of field observations showing $L_E \sim L_O$ (e.g. Moum 1996), further research is warranted in understanding how Γ, Fr, and L_E/L_O may be related when $L_E/L_O = O(1)$.

We also investigated the pointwise correlations between χ and ε in the statistically steady state. A positive correlation was still observed in the pointwise calculations, albeit with a far wider spread. Perhaps understandably, the earlier trends for Γ and Fr were not seen in the pointwise calculations. The Γ-Fr scalings, as with most parameterizations, rely on comparing statistical properties of the flow (such as mean dissipation rates and mean buoyancy frequency) and should not be expected to hold locally.

Similarities between the simulations extended to the energy spectra. In all cases, we found a horizontal wavenumber spectrum of $E \sim k^{-5/3}$, but the vertical wavenumber spectrum produced no obvious consistent scaling. By using wavelets to sample heights conditionally depending on the local buoyancy Reynolds number $Re_b = \varepsilon/\nu N^2$, we identified two scaling regimes in the vertical wavenumber spectrum. For $Re_b > 10$, we obtained a spectral scaling most like $E \sim m^{-5/3}$, consistent with an inertial range of near-isotropic turbulence. By contrast when $Re_b < 1$ a clear $E \sim m^{-3}$ spectrum emerged. The association of the m^{-3} scaling with low Re_b suggests an interpretation where near-isotropic patches of (high Re_b) turbulence intermittently appear on a background field of nonlinear buoyancy-dominated motions (characterised by low Re_b).

As highlighted in §1.3, high values of Re_b naturally lead to high values of diapycnal diffusivity. Understanding how intense turbulent patches may be produced from an internal wavefield, and what their characteristic mixing properties are, is therefore vital for quantifying diapycnal mixing in the ocean interior. Motivated by the observation of turbulent patches in the internal wave-dominated thermocline by Alford and Pinkel

(2000), we subsequently performed further simulations of a single, breaking internal gravity wave in chapter 4.

In the observations, spatially varying large-scale vertical shear (likely associated with a near-inertial wave) and large-amplitude internal waves were both significant in locations where turbulence was generated. We therefore decided to investigate the flow arising from the superposition of an internal gravity wave and a sinusoidal shear flow. Despite a lack of scale separation between the shear and the wave, we found that linear ray tracing theory was useful in describing how the internal wave broke. Similar to wave breaking at a critical level in a slowly varying mean flow, the internal wave was refracted by the shear, focusing its energy towards certain regions of the flow. In these regions, the wave became locally unstable to both convective and shear instabilities.

The convective instabilities appeared first, forming streamwise-aligned rolls, and introducing small scale plume structures to the flow. These structures however achieved relatively little mixing compared to the billow-like vortices that developed later through local shear instabilities. The size of the billows, relative to the wave-induced shear layers that they developed from, was consistent with the fastest growing wavelengths of Kelvin–Helmholtz instability. Although the mean buoyancy field had been strongly distorted by the wave, the mixing efficiency of the subsequent turbulence $\eta \approx 0.24$ was similar to that found developing from Kelvin–Helmholtz instability in stratified shear layers at $Pr = 1$ (e.g. in Salehipour et al. 2015). Unlike in turbulent flows driven by mean shear, where the mean flow is blunted by the turbulence, the mean flow in our case was accelerated where the turbulence was generated. Development of the mean flow was primarily determined by the wave-mean flow interaction, which appeared to dominate energy transfers between the turbulence and the mean flow.

These simulations from chapter 4 provided an intriguing perspective on how the nonlinear interaction between a near-inertial wave and an internal gravity wave may lead to turbulent mixing. The internal wave broke down through a convective instability, but did not lead to the high mixing efficiencies seen in the simulations of chapter 3. There remain many interesting questions about the mixing processes arising in this flow, some of which we will revisit in §6.2.

Finally, in chapter 5, we tackled the problem of quantifying available potential energy (APE) in our simulations. We showed that direct application of the existing Winters et al. (1995) framework could produce inconsistent results for the triply-periodic domains used in chapters 3 and 4. This is why in previous chapters we had used $\mathcal{P} \approx \langle\theta^2\rangle/2$ to approximate APE and χ to approximate diapycnal mixing. By considering a control

volume bounded by surfaces of constant buoyancy, we devised a method for accurately calculating APE and diapycnal mixing in stratified, periodic domains in chapter 5.

This method was found to be consistent with the local APE density of Scotti and White (2014), which we then applied to further analyse our earlier simulations. Snapshots of local APE provided further evidence that the wave-forced simulations of chapter 3 exhibited more large-scale, convective mixing processes than the vortically-forced flows. The local APE snapshots also highlighted how local mixing was affected by the distortion of the buoyancy field in the wave breaking simulations of chapter 4. Despite strong local effects in this case, we found that χ had proved to be a good approximation for the global mixing rate in all of our flows, with a maximum error of about 10%.

With our new framework, we were also newly able to calculate an accurate diapycnal diffusivity, which we compared to the approximation of χ/N_0^2 from Osborn and Cox (1972). We found that for shear-driven turbulence this approximation typically resulted in an underestimate of the diffusivity of about 10%, consistent with the results of Salehipour and Peltier (2015). This error is however smaller than those associated with most microstructure measurements, and the approximation does not rely on the empirical prescription of a parameter (unlike the Osborn (1980) model and Γ). In this sense, for the flows we have considered, the Osborn and Cox (1972) model appeared to provide a reliable estimate of irreversible, diapycnal mixing.

Throughout this thesis we have explored various aspects of mixing relevant to the breaking of oceanic internal waves, and offered answers to some important questions on this topic. However many more questions remain unanswered. It is unsurprising that we have not revealed some grand, unifying theory for open ocean mixing through internal wave-driven stratified turbulence. A quick search on Web of Science for example provides over 4000 results for 'stratified turbulence', highlighting a history of incremental gains (and occasional leaps) towards a better understanding of small-scale geophysical flows. It would be clichéd to say that there is still much to learn about ocean mixing, so rather than leave it there, let us now discuss some outstanding open questions. Given what we have learned from this thesis, we are hopeful that the answers to these questions may provide us with further insight into the processes and dynamics at the heart of mixing in the ocean.

6.2 An outlook on the future

The simulations of chapter 4, aimed at resembling the nonlinear interaction of a near-inertial wave and an internal gravity wave, provide a useful starting point for future questions. In these flows, we identified Kelvin–Helmholtz instability (KHI) as the mechanism producing the billow structures that achieve most of the mixing. Theoretical and numerical studies of KHI often focus on its development on a stratified interface or in a uniform stratification, but our simulations suggest other buoyancy profiles may be relevant for modelling turbulent mixing from breaking internal waves.

In our simulations, even as it became unstable, the internal wave appeared to maintain its structure, at least in terms of the phase difference between the velocity and buoyancy fields. This may partly explain why ray tracing was able to capture the early vertical propagation of the wave reasonably well. Since the velocity field and buoyancy field are out of phase, the minimum Richardson number Ri_m of an internal wave is not typically found at the locations of maximum shear or maximum stratification. Indeed, given the polarization relations of an internal gravity wave, the flow must become locally statically unstable for Ri_m to drop below 1/4.

This motivates looking at a simple system where the flow is unstable to both shear and convective instabilities despite a mean stable stratification. We could imagine the flow being that arising as a wave approaches a critical level, similar to that considered by Winters and Riley (1992). The wave would then be represented by

$$u' = \frac{s}{m}\sin(mz), \qquad \theta' = \frac{s}{m}\cos(mz). \tag{6.1}$$

This flow is linearly stable by the Miles–Howard criterion if $s < m$, so shear instabilities will only be possible if the buoyancy field is also statically unstable somewhere. The flow is reminiscent of the 'stratified Kolmogorov flow' studied by Balmforth and Young (2002), where KHI-like billows emerged from an imposed sinusoidal shear flow. That study could provide a useful benchmark to compare to when identifying the role of local convection on the development of structures from shear instability.

Although such a setup would provide a simple system to investigate the development of local convection and shear instabilities, the development of nonlinear structures would be constrained by the periodic boundaries. We could instead introduce local convection to the well-studied $u(z) = \tanh z$ shear layer with an appropriate buoyancy profile. By comparing the turbulence from such a system to previous studies of stratified shear layers, we might be able to identify the key parameters that best describe mixing in transient shear-driven flows for arbitrary mean buoyancy profiles. Given our

earlier result showing comparable mixing efficiency between our wave breaking simulation and the KHI study of Salehipour et al. (2015), there is at least hope that a general parameterization can be found for such flows.

As mentioned above, we used vertical shear to emulate a slowly-propagating near-inertial wave. This however omits a key aspect of the structure of a near-inertial wave: the rotation of the velocity vector. The horizontal velocity of an inertial oscillation with frequency $\omega = f$ and vertical wavenumber m is given by

$$u' = U_0 \cos(mz \mp ft), \qquad v' = \pm U_0 \sin(mz \mp ft). \tag{6.2}$$

For sufficiently small f, this can be approximated by a steady, but non-parallel, shear flow where the velocity vector rotates around the z-axis with height. The orientation of this depth-dependent rotation determines whether phase propagation is upward or downward. Near-inertial waves are often cited as important sources of mixing due to strong vertical shears that they develop (see e.g. Alford et al. 2016), but the presence of significant velocity swirl is rarely considered in fundamental studies of mixing triggered through shear instabilities.

The classical stability theory for parallel shear flows cannot apply in this case, and it is possible that nonlinear structures such as billows could be significantly altered by the presence of an additional spanwise flow. As might be expected in flows with this type of rotational symmetry, Lelong and Dunkerton (1998) found a near-isotropic development of disturbances in simulations of shear-unstable near-inertial waves. Fritts et al. (2013) also found that a rotational shear flow inhibited the growth of streamwise-aligned convective rolls, and modified the growth of shear-driven billows in their simulations of finescale shear and a large amplitude internal wave. Further study of the flow described by (6.2) and its breakdown in a uniform stratification might provide much needed insight for the nature of mixing achieved by near-inertial waves.

An elephant in the room throughout the studies in this thesis has been the Prandtl number $Pr = \nu/\kappa$, the ratio of the molecular diffusivities of momentum and buoyancy. We have set $Pr = 1$ in all of the simulations we have performed, whereas its value in the ocean is $O(10-100)$ depending on the scalar determining the density stratification. For KHI, most relevant to the results of chapters 2 and 4, previous studies by Smyth et al. (2001) and Salehipour et al. (2015) have highlighted a trend for the mixing efficiency η to decrease monotonically with increasing Pr. In forced stratified turbulence, the scalings proposed by Maffioli et al. (2016) rely on a high Péclet number assumption $Pe = RePr \gg 1$, supposedly implying Pr independence for mixing in energetic flows. However Gregg et al. (2018) cite a private communication from S. M. de Bruyn Kops

detailing a similar negative correlation between η and Pr. The mechanism by which a change in Pr affects mixing in highly turbulent flows is still unclear and warrants further investigation. Any changes in mixing efficiency at high Pr is particularly important for quantifying mixing in salt-stratified regions of the ocean, where microstructure observations rely on the Osborn (1980) method.

Maintaining a stratified turbulent flow through large-scale forcing would be useful for a study into Pr dependence since comprehensive statistics can be obtained of the downscale energy transfers. However, as we have shown in chapter 3, the choice of forcing can itself affect the mixing efficiency. Any such study aimed at resolving the multi-parameter dependence of mixing efficiency (in statistically steady flows) should therefore use a simple, consistent forcing scheme. The work of Maffioli et al. (2016) marks significant progress towards an understanding of these flows, but there remain unresolved questions about the role of Pr and the interdependence of the turbulent Froude number $Fr = \varepsilon/N\mathcal{K}$ and the buoyancy Reynolds number $Re_b = \varepsilon/\nu N^2$.

Mixing in such simulations should be calculated precisely using the APE framework of chapter 5. In an ideal scenario, where the flow is truly statistically stationary, the turbulent buoyancy flux $\mathcal{J}$, the buoyancy variance destruction rate χ, and the diapycnal mixing rate $\mathcal{M}$ would all be equivalent. However, even in flows where the turbulence is considered steady, slow changes to the background buoyancy profile can lead to variations between these quantities. This will be particularly important for quantifying mixing in flows where the buoyancy field becomes layered.

Finally, we note that there remains somewhat of a disconnect between studies of forced stratified turbulence and the downscale transfer of energy through the internal wave spectrum. In forcing an isotropic collection of internal gravity waves, we provided an alternative method of large-scale energy injection, but this should not be considered 'typical' of the ocean interior. It is still not entirely clear which mechanisms are responsible for the majority of internal wave dissipation in the open ocean. A combined effort spanning observations, numerical simulations, and theory is likely required to connect the spectral descriptions with the physical mechanisms involved. Given the vast increase in computational power in the last 20 years, it may perhaps be useful to revisit a direct simulation of the internal wave field as performed by Winters and D'Asaro (1997) and Furue (2003). An increase in the range of scales accessible to such computations may be able to shed new light on the nature of energy transfers to turbulent scales in the ocean.

References

Alford, M. H., MacKinnon, J. A., Simmons, H. L., and Nash, J. D. (2016), "Near-Inertial Internal Gravity Waves in the Ocean", *Annu. Rev. Mar. Sci.* 8: 95–123.

Alford, M. H. and Pinkel, R. (2000), "Observations of Overturning in the Thermocline: The Context of Ocean Mixing", *J. Phys. Oceanogr.* 30 (5): 805–32.

Almalkie, S. and de Bruyn Kops, S. M. (2012), "Kinetic energy dynamics in forced, homogeneous, and axisymmetric stably stratified turbulence", *J. Turbul.* 13: N29.

Andrews, D. G. (1981), "A note on potential energy density in a stratified compressible fluid", *J. Fluid Mech.* 107: 227–36.

Armi, L. (1978), "Some Evidence for Boundary Mixing in the Deep Ocean", *J. Geophys. Res. Oceans*, 83 (C4): 1971–9.

Arthur, R. S., Venayagamoorthy, S. K., Koseff, J. R., and Fringer, O. B. (2017), "How we compute N matters to estimates of mixing in stratified flows", *J. Fluid Mech.* 831: R2.

Augier, P., Billant, P., and Chomaz, J.-M. (2015), "Stratified turbulence forced with columnar dipoles: numerical study", *J. Fluid Mech.* 769: 403–43.

Baker, M. A. and Gibson, C. H. (1987), "Sampling Turbulence in the Stratified Ocean: Statistical Consequences of Strong Intermittency", *J. Phys. Oceanogr.* 17 (10): 1817–36.

Balmforth, N. J. and Young, Y.-N. (2002), "Stratified Kolmogorov flow", *J. Fluid Mech.* 450: 131–67.

Bewley, T. R. (2010), *Numerical Renaissance: Simulation, Optimization, and Control* (Renaissance Press).

Billant, P. and Chomaz, J.-M. (2000*a*), "Experimental evidence for a new instability of a vertical columnar vortex pair in a strongly stratified fluid", *J. Fluid Mech.* 418: 167–88.

Billant, P. and Chomaz, J.-M. (2000*b*), "Theoretical analysis of the zigzag instability of a vertical columnar vortex pair in a strongly stratified fluid", *J. Fluid Mech.* 419: 29–63.

Billant, P. and Chomaz, J.-M. (2001), "Self-similarity of strongly stratified inviscid flows", *Phys. Fluids*, 13 (6): 1645–51.

Bluteau, C. E., Jones, N. L., and Ivey, G. N. (2013), "Turbulent mixing efficiency at an energetic ocean site", *J. Geophys. Res. Oceans*, 118 (9): 4662–72.

Booker, J. R. and Bretherton, F. P. (1967), "The critical layer for internal gravity waves in a shear flow", *J. Fluid Mech.* 27 (3): 513–39.

Bretherton, F. P. (1966), "The propagation of groups of internal gravity waves in a shear flow", *Q. J. R. Meteorol. Soc.* 92 (394): 466–80.

Brethouwer, G., Billant, P., Lindborg, E., and Chomaz, J.-M. (2007), "Scaling analysis and simulation of strongly stratified turbulent flows", *J. Fluid Mech.* 585: 343–68.

Broutman, D., Macaskill, C., McIntyre, M. E., and Rottman, J. W. (1997), "On Doppler-spreading models of internal waves", *Geophys. Res. Lett.* 24 (22): 2813–6.

Bühler, O. (2014), *Waves and Mean Flows* (2nd edn., Cambridge: Cambridge University Press), 360 pp.

Bühler, O. and McIntyre, M. E. (2005), "Wave capture and wave–vortex duality", *J. Fluid Mech.* 534: 67–95.

Caulfield, C. P. and Peltier, W. R. (2000), "The anatomy of the mixing transition in homogeneous and stratified free shear layers", *J. Fluid Mech.* 413: 1–47.

Caulfield, C. (2021), "Layering, Instabilities, and Mixing in Turbulent Stratified Flows", *Annu. Rev. Fluid Mech.* 53: 113–45.

Cessi, P. (2019), "The Global Overturning Circulation", *Annu. Rev. Mar. Sci.* 11: 249–70.

Cimoli, L., Caulfield, C.-c. P., Johnson, H. L., Marshall, D. P., Mashayek, A., Naveira Garabato, A. C., and Vic, C. (2019), "Sensitivity of Deep Ocean Mixing to Local Internal Tide Breaking and Mixing Efficiency", *Geophys. Res. Lett.* 46 (24): 14622–33.

Corcos, G. M. and Sherman, F. S. (1976), "Vorticity concentration and the dynamics of unstable free shear layers", *J. Fluid Mech.* 73 (2): 241–64.

Dauxois, T., Joubaud, S., Odier, P., and Venaille, A. (2018), "Instabilities of Internal Gravity Wave Beams", *Annu. Rev. Fluid Mech.* 50: 131–56.

Davidson, P. A. (2013), *Turbulence in Rotating, Stratified and Electrically Conducting Fluids* (Cambridge, United Kingdom: Cambridge University Press), 681 pp.

Davies Wykes, M. S., Hughes, G. O., and Dalziel, S. B. (2015), "On the meaning of mixing efficiency for buoyancy-driven mixing in stratified turbulent flows", *J. Fluid Mech.* 781: 261–75.

De Bruyn Kops, S. M. and Riley, J. J. (2019), "The effects of stable stratification on the decay of initially isotropic homogeneous turbulence", *J. Fluid Mech.* 860: 787–821.

De Lavergne, C., Madec, G., Le Sommer, J., Nurser, A. J. G., and Naveira Garabato, A. C. (2015), "The Impact of a Variable Mixing Efficiency on the Abyssal Overturning", *J. Phys. Oceanogr.* 46 (2): 663–81.

Dillon, T. M. (1982), "Vertical overturns: A comparison of Thorpe and Ozmidov length scales", *J. Geophs. Res.: Oceans*, 87 (C12): 9601–13.

Drazin, P. G. (1977), "On the instability of an internal gravity wave", *Proc. R. Soc. Lond. A.* 356: 411–32.

Drazin, P. G. and Reid, W. H. (2004), *Hydrodynamic Stability* (2nd ed, Cambridge: Cambridge University Press), 605 pp.

Eakins, B. W. and Sharman, G. F. (2010), *Volumes of the World's Oceans from ETOPO1*.

Eckermann, S. D. (1999), "Isentropic advection by gravity waves: Quasi-universal M^{-3} vertical wavenumber spectra near the onset of instability", *Geophys. Res. Lett.* 26 (2): 201–4.

Falder, M., White, N. J., and Caulfield, C. P. (2016), "Seismic Imaging of Rapid Onset of Stratified Turbulence in the South Atlantic Ocean", *J. Phys. Oceanogr.* 46 (4): 1023–44.

Fernando, H. J. S. (1991), "Turbulent Mixing in Stratified Fluids", *Annu. Rev. Fluid Mech.* 23: 455–93.

Ferrari, R. and Wunsch, C. (2009), "Ocean Circulation Kinetic Energy: Reservoirs, Sources, and Sinks", *Annu. Rev. Fluid Mech.* 41: 253–82.

Fitzgerald, J. G. and Farrell, B. F. (2018), "Statistical state dynamics of vertically sheared horizontal flows in two-dimensional stratified turbulence", *J. Fluid Mech.* 854: 544–90.

Fritts, D. C. and Wang, L. (2013), "Gravity Wave–Fine Structure Interactions. Part II: Energy Dissipation Evolutions, Statistics, and Implications", *J. Atmos. Sci.* 70 (12): 3735–55.

Fritts, D. C., Wang, L., Werne, J., Lund, T., and Wan, K. (2009*a*), "Gravity Wave Instability Dynamics at High Reynolds Numbers. Part I: Wave Field Evolution at Large Amplitudes and High Frequencies", *J. Atmos. Sci.* 66 (5): 1126–48.

Fritts, D. C., Wang, L., Werne, J., Lund, T., and Wan, K. (2009*b*), "Gravity Wave Instability Dynamics at High Reynolds Numbers. Part II: Turbulence Evolution, Structure, and Anisotropy", *J. Atmos. Sci.* 66 (5): 1149–71.

Fritts, D. C., Wang, L., and Werne, J. A. (2013), "Gravity Wave–Fine Structure Interactions. Part I: Influences of Fine Structure Form and Orientation on Flow Evolution and Instability", *J. Atmos. Sci.* 70 (12): 3710–34.

Furue, R. (2003), "Energy Transfer within the Small-Scale Oceanic Internal Wave Spectrum", *J. Phys. Oceanogr.* 33 (1): 267–82.

Garanaik, A. and Venayagamoorthy, S. K. (2019), "On the inference of the state of turbulence and mixing efficiency in stably stratified flows", *J. Fluid Mech.* 867: 323–33.

Garaud, P. (2018), "Double-Diffusive Convection at Low Prandtl Number", *Annu. Rev. Fluid Mech.* 50: 275–98.

Gargett, A. E., Hendricks, P. J., Sanford, T. B., Osborn, T. R., and Williams, A. J. (1981), "A Composite Spectrum of Vertical Shear in the Upper Ocean", *J. Phys. Oceanogr.* 11 (9): 1258–71.

Garrett, C. and Kunze, E. (2007), "Internal Tide Generation in the Deep Ocean", *Annu. Rev. Fluid Mech.* 39: 57–87.

Garrett, C. and Munk, W. (1972), "Space-Time scales of internal waves", *Geophys. Fluid Dyn.* 3 (3): 225–64.

Gayen, B., Hughes, G. O., and Griffiths, R. W. (2013), "Completing the Mechanical Energy Pathways in Turbulent Rayleigh-Bénard Convection", *Phys. Rev. Lett.* 111 (12): 124301.

Gibson, C. H. (1986), "Internal waves, fossil turbulence, and composite ocean microstructure spectra", *J. Fluid Mech.* 168: 89–117.

Goldstein, S. (1931), "On the Stability of Superposed Streams of Fluids of Different Densities", *Proc. R. Soc. Lond. A.* 132 (820): 524–48.

Gregg, M. C. (1989), "Scaling turbulent dissipation in the thermocline", *J. Geophys. Res. Oceans*, 94 (C7): 9686–98.

Gregg, M., D'Asaro, E., Riley, J., and Kunze, E. (2018), "Mixing Efficiency in the Ocean", *Annu. Rev. Mar. Sci.* 10: 443–73.

Gregg, M. C., Winkel, D. P., and Sanford, T. B. (1993), "Varieties of Fully Resolved Spectra of Vertical Shear", *J. Phys. Oceanogr.* 23 (1): 124–41.

Hazel, P. (1972), "Numerical studies of the stability of inviscid parallel shear flows", *J. Fluid Mech.* 51 (1): 39–61.

Holliday, D. and McIntyre, M. E. (1981), "On potential energy density in an incompressible, stratified fluid", *J. Fluid Mech.* 107: 221–5.

Holmboe, J. (1962), "On the behavior of symmetric waves in stratified shear layers", *Geophys. Nor.* 24: 67–113.

Howard, L. N. (1961), "Note on a paper of John W. Miles", *J. Fluid Mech.* 10 (4): 509–12.

Howland, C. J., Taylor, J. R., and Caulfield, C. P. (2018), "Testing linear marginal stability in stratified shear layers", *J. Fluid Mech.* 839: R4.

Howland, C. J., Taylor, J. R., and Caulfield, C. P. (2020), "Mixing in forced stratified turbulence and its dependence on large-scale forcing", *J. Fluid Mech.* 898: A7.

Hughes, G. O., Hogg, A. M. C., and Griffiths, R. W. (2009), "Available Potential Energy and Irreversible Mixing in the Meridional Overturning Circulation", *J. Phys. Oceanogr.* 39 (12): 3130–46.

Ijichi, T. and Hibiya, T. (2018), "Observed Variations in Turbulent Mixing Efficiency in the Deep Ocean", *J. Phys. Oceanogr.* 48 (8): 1815–30.

Ijichi, T., Laurent, L. S., Polzin, K. L., and Toole, J. M. (2020), "How Variable Is Mixing Efficiency in the Abyss?", *Geophys. Res. Lett.* 47 (7): e2019GL086813.

Ivey, G. N. and Imberger, J. (1991), "On the Nature of Turbulence in a Stratified Fluid. Part I: The Energetics of Mixing", *J. Phys. Oceanogr.* 21 (5): 650–8.

Ivey, G. N., Winters, K. B., and Koseff, J. R. (2008), "Density Stratification, Turbulence, but How Much Mixing?", *Annu. Rev. Fluid Mech.* 40: 169–84.

Ivey, G. N., Bluteau, C. E., and Jones, N. L. (2018), "Quantifying Diapycnal Mixing in an Energetic Ocean", *J. Geophs. Res.: Oceans*, 123: 346–57.

Kaminski, A. K., Caulfield, C. P., and Taylor, J. R. (2014), "Transient growth in strongly stratified shear layers", *J. Fluid Mech.* 758: R4.

Kaminski, A. K., Caulfield, C. P., and Taylor, J. R. (2017), "Nonlinear evolution of linear optimal perturbations of strongly stratified shear layers", *J. Fluid Mech.* 825: 213–44.

Kaminski, A. K. and Smyth, W. D. (2019), "Stratified shear instability in a field of pre-existing turbulence", *J. Fluid Mech.* 862: 639–58.

Klaassen, G. P. and Peltier, W. R. (1985), "Evolution of Finite Amplitude Kelvin–Helmholtz Billows in Two Spatial Dimensions", *J. Atmospheric Sci.* 42 (12): 1321–39.

Klostermeyer, J. (1991), "Two- and three-dimensional parametric instabilities in finite-amplitude internal gravity waves", *Geophys. Astrophys. Fluid Dyn.* 61 (1-4): 1–25.

Klymak, J. M. and Legg, S. M. (2010), "A simple mixing scheme for models that resolve breaking internal waves", *Ocean Model.* 33 (3): 224–34.

Koop, C. G. and McGee, B. (1986), "Measurements of internal gravity waves in a continuously stratified shear flow", *J. Fluid Mech.* 172: 453–80.

Koudella, C. R. and Staquet, C. (2006), "Instability mechanisms of a two-dimensional progressive internal gravity wave", *J. Fluid Mech.* 548: 165–96.

Kunze, E. (2018), "A Unified Model Spectrum for Anisotropic Stratified and Isotropic Turbulence in the Ocean and Atmosphere", *J. Phys. Oceanogr.* 49 (2): 385–407.

Lamb, K. G. (2014), "Internal Wave Breaking and Dissipation Mechanisms on the Continental Slope/Shelf", *Annu. Rev. Fluid Mech.* 46: 231–54.

Laval, J.-P., McWilliams, J. C., and Dubrulle, B. (2003), "Forced stratified turbulence: Successive transitions with Reynolds number", *Phys. Rev. E* 68 (3): 036308.

Ledwell, J. R., Montgomery, E. T., Polzin, K. L., Laurent, L. C. S., Schmitt, R. W., and Toole, J. M. (2000), "Evidence for enhanced mixing over rough topography in the abyssal ocean", *Nature*, 403 (6766): 179–82.

Legg, S. (2021), "Mixing by Oceanic Lee Waves", *Annu. Rev. Fluid Mech.* 53: 173–201.

Lelong, M.-P. and Dunkerton, T. J. (1998), "Inertia–Gravity Wave Breaking in Three Dimensions. Part I: Convectively Stable Waves", *J. Atmos. Sci.* 55 (15): 2473–88.

Lindborg, E. (2006), "The energy cascade in a strongly stratified fluid", *J. Fluid Mech.* 550: 207–42.

Linden, P. F. (1979), "Mixing in stratified fluids", *Geophys. Astrophys. Fluid Dyn.* 13 (1): 3–23.

Lohse, D. and Toschi, F. (2003), "Ultimate State of Thermal Convection", *Phys. Rev. Lett.* 90 (3): 034502.

Lombard, P. N. and Riley, J. J. (1996), "Instability and breakdown of internal gravity waves. I. Linear stability analysis", *Phys. Fluids*, 8 (12): 3271–87.

Lorenz, E. N. (1955), "Available Potential Energy and the Maintenance of the General Circulation", *Tellus*, 7 (2): 157–67.

MacKinnon, J. A., Zhao, Z., Whalen, C. B., Waterhouse, A. F., Trossman, D. S., Sun, O. M., St. Laurent, L. C., Simmons, H. L., Polzin, K., Pinkel, R., et al. (2017), "Climate Process Team on Internal Wave–Driven Ocean Mixing", *Bull. Amer. Meteor. Soc.* 98 (11): 2429–54.

Maffioli, A., Brethouwer, G., and Lindborg, E. (2016), "Mixing efficiency in stratified turbulence", *J. Fluid Mech.* 794: R3.

Maffioli, A. and Davidson, P. A. (2016), "Dynamics of stratified turbulence decaying from a high buoyancy Reynolds number", *J. Fluid Mech.* 786: 210–33.

Maffioli, A. (2017), "Vertical spectra of stratified turbulence at large horizontal scales", *Phys. Rev. Fluids*, 2 (10): 104802.

Marshall, J. and Speer, K. (2012), "Closure of the meridional overturning circulation through Southern Ocean upwelling", *Nat. Geosci.* 5 (3): 171–80.

Mashayek, A., Caulfield, C. P., and Peltier, W. R. (2013), "Time-dependent, non-monotonic mixing in stratified turbulent shear flows: implications for oceanographic estimates of buoyancy flux", *J. Fluid Mech.* 736: 570–93.

Mashayek, A. and Peltier, W. R. (2012*a*), "The 'zoo' of secondary instabilities precursory to stratified shear flow transition. Part 1 Shear aligned convection, pairing, and braid instabilities", *J. Fluid Mech.* 708: 5–44.

Mashayek, A. and Peltier, W. R. (2012*b*), "The 'zoo' of secondary instabilities precursory to stratified shear flow transition. Part 2 The influence of stratification", *J. Fluid Mech.* 708: 45–70.

Mashayek, A. and Peltier, W. R. (2013), "Shear-induced mixing in geophysical flows: does the route to turbulence matter to its efficiency?", *J. Fluid Mech.* 725: 216–61.

Mashayek, A., Salehipour, H., Bouffard, D., Caulfield, C. P., Ferrari, R., Nikurashin, M., Peltier, W. R., and Smyth, W. D. (2017), "Efficiency of turbulent mixing in the abyssal ocean circulation", *Geophys. Res. Lett.* 44 (12): 1–11.

Mater, B. D. and Venayagamoorthy, S. K. (2014), "The quest for an unambiguous parameterization of mixing efficiency in stably stratified geophysical flows", *Geophys. Res. Lett.* 41 (13): 4646–53.

McDougall, T. J. (1987), "Thermobaricity, cabbeling, and water-mass conversion", *J. Geophys. Res. Oceans*, 92 (C5): 5448–64.

Mied, R. P. (1976), "The occurrence of parametric instabilities in finite-amplitude internal gravity waves", *J. Fluid Mech.* 78 (4): 763–84.

Miles, J. W. (1961), "On the stability of heterogeneous shear flows", *J. Fluid Mech.* 10 (4): 496–508.

Monismith, S. G., Koseff, J. R., and White, B. L. (2018), "Mixing Efficiency in the Presence of Stratification: When Is It Constant?", *Geophys. Res. Lett.* 45 (11): 5627–34.

Moum, J. N. (1996), "Energy-containing scales of turbulence in the ocean thermocline", *J. Geophs. Res.: Oceans*, 101 (C6): 14095–109.

Moum, J. N., Farmer, D. M., Smyth, W. D., Armi, L., and Vagle, S. (2003), "Structure and Generation of Turbulence at Interfaces Strained by Internal Solitary Waves Propagating Shoreward over the Continental Shelf", *J. Phys. Oceanogr.* 33 (10): 2093–112.

Moum, J. N. and Nash, J. D. (2009), "Mixing Measurements on an Equatorial Ocean Mooring", *J. Atmos. Oceanic Technol.* 26 (2): 317–36.

Müller, P., Holloway, G., Henyey, F., and Pomphrey, N. (1986), "Nonlinear interactions among internal gravity waves", *Rev. Geophys.* 24 (3): 493–536.

Munk, W. (1981), "Internal Waves and Small-Scale Processes", in B. A. Warren and C. Wunsch (eds.), *Evolution of Physical Oceanography* (Cambridge, MA: MIT Press), 264–91.

Munk, W. and Wunsch, C. (1998), "Abyssal recipes II: energetics of tidal and wind mixing", *Deep-Sea Res. Pt. I* 45 (12): 1977–2010.

Munk, W. H. (1966), "Abyssal recipes", *Deep Sea Res. Oceanogr. Abstr.* 13 (4): 707–30.

Nazarenko, S. (2011), *Wave Turbulence* (Lecture Notes in Physics, 825; Heidelberg: Springer), 279 pp.

Orszag, S. A. and Patterson, G. S. (1972), "Numerical Simulation of Three-Dimensional Homogeneous Isotropic Turbulence", *Phys. Rev. Lett.* 28 (2): 76–9.

Osborn, T. R. (1980), "Estimates of the Local Rate of Vertical Diffusion from Dissipation Measurements", *J. Phys. Oceanogr.* 10 (1): 83–9.

Osborn, T. R. and Cox, C. S. (1972), "Oceanic fine structure", *Geophys. Fluid Dyn.* 3 (4): 321–45.

Parker, J. P., Caulfield, C. P., and Kerswell, R. R. (2019), "Kelvin–Helmholtz billows above Richardson number 1/4", *J. Fluid Mech.* 879: R1.

Peltier, W. R. and Caulfield, C. P. (2003), "Mixing Efficiency in Stratified Shear Flows", *Annu. Rev. Fluid Mech.* 35: 135–67.

Phillips, O. M. (1966), *The Dynamics of the Upper Ocean* (Cambridge: Cambridge University Press).

Plumb, R. A. (1977), "The Interaction of Two Internal Waves with the Mean Flow: Implications for the Theory of the Quasi-Biennial Oscillation", *J. Atmos. Sci.* 34 (12): 1847–58.

Polzin, K. L. and Lvov, Y. V. (2011), "Toward Regional Characterizations of the Oceanic Internal Wavefield", *Rev. Geophys.* 49 (4).

Pope, S. B. (2000), *Turbulent Flows* (Cambridge University Press).

Portwood, G. D., de Bruyn Kops, S. M., and Caulfield, C. P. (2019), "Asymptotic Dynamics of High Dynamic Range Stratified Turbulence", *Phys. Rev. Lett.* 122 (19): 194504.

Portwood, G. D., de Bruyn Kops, S. M., Taylor, J. R., Salehipour, H., and Caulfield, C. P. (2016), "Robust identification of dynamically distinct regions in stratified turbulence", *J. Fluid Mech.* 807: R2.

Radko, T. (2013), *Double-Diffusive Convection* (Cambridge: Cambridge University Press), 342 pp.

Riley, J. J. and de Bruyn Kops, S. M. (2003), "Dynamics of turbulence strongly influenced by buoyancy", *Phys. Fluids*, 15 (7): 2047–59.

Riley, J. J. and Lelong, M.-P. (2000), "Fluid Motions in the Presence of Strong Stable Stratification", *Annu. Rev. Fluid Mech.* 32: 613–57.

Riley, J. J. and Lindborg, E. (2008), "Stratified Turbulence: A Possible Interpretation of Some Geophysical Turbulence Measurements", *J. Atmos. Sci.* 65 (7): 2416–24.

Riley, J. J., Metcalfe, R. W., and Weissman, M. A. (1981), "Direct numerical simulations of homogeneous turbulence in density-stratified fluids", *AIP Conference Proceedings*, 76: 79–112.

Rippeth, T. P., Lincoln, B. J., Kennedy, H. A., Palmer, M. R., Sharples, J., and Williams, C. A. J. (2014), "Impact of vertical mixing on sea surface pCO_2 in temperate seasonally stratified shelf seas", *J. Geophys. Res. Oceans*, 119 (6): 3868–82.

Rohr, J. J., Itsweire, E. C., Helland, K. N., and Van Atta, C. W. (1988), "Growth and decay of turbulence in a stably stratified shear flow", *J. Fluid Mech.* 195: 77–111.

Roullet, G. and Klein, P. (2009), "Available potential energy diagnosis in a direct numerical simulation of rotating stratified turbulence", *J. Fluid Mech.* 624: 45–55.

Salehipour, H., Peltier, W. R., and Mashayek, A. (2015), "Turbulent diapycnal mixing in stratified shear flows: the influence of Prandtl number on mixing efficiency and transition at high Reynolds number", *J. Fluid Mech.* 773: 178–223.

Salehipour, H., Caulfield, C. P., and Peltier, W. R. (2016), "Turbulent mixing due to the Holmboe wave instability at high Reynolds number", *J. Fluid Mech.* 803: 591–621.

Salehipour, H. and Peltier, W. R. (2015), "Diapycnal diffusivity, turbulent Prandtl number and mixing efficiency in Boussinesq stratified turbulence", *J. Fluid Mech.* 775: 464–500.

Salehipour, H., Peltier, W. R., and Caulfield, C. P. (2018), "Self-organized criticality of turbulence in strongly stratified mixing layers", *J. Fluid Mech.* 856: 228–56.

Sarkar, S. and Scotti, A. (2017), "From Topographic Internal Gravity Waves to Turbulence", *Annu. Rev. Fluid Mech.* 49: 195–220.

Schmitt, R. W. (1994), "Double Diffusion in Oceanography", *Annu. Rev. Fluid Mech.* 26: 255–85.

Scotti, A. and White, B. (2014), "Diagnosing mixing in stratified turbulent flows with a locally defined available potential energy", *J. Fluid Mech.* 740: 114–35.

Shibley, N. C., Timmermans, M.-L., Carpenter, J. R., and Toole, J. M. (2017), "Spatial variability of the Arctic Ocean's double-diffusive staircase", *J. Geophys. Res. Oceans*, 122 (2): 980–94.

Shih, L. H., Koseff, J. R., Ivey, G. N., and Ferziger, J. H. (2005), "Parameterization of turbulent fluxes and scales using homogeneous sheared stably stratified turbulence simulations", *J. Fluid Mech.* 525: 193–214.

Smith, L. M. and Waleffe, F. (2002), "Generation of slow large scales in forced rotating stratified turbulence", *J. Fluid Mech.* 451: 145–68.

Smyth, W. D. and Moum, J. N. (2013), "Marginal instability and deep cycle turbulence in the eastern equatorial Pacific Ocean", *Geophys. Res. Lett.* 40 (23): 6181–5.

Smyth, W. D., Moum, J. N., and Caldwell, D. R. (2001), "The Efficiency of Mixing in Turbulent Patches: Inferences from Direct Simulations and Microstructure Observations", *J. Phys. Oceanogr.* 31 (8): 1969–92.

Smyth, W. D., Nash, J. D., and Moum, J. N. (2019), "Self-organized criticality in geophysical turbulence", *Sci. Rep.* 9 (1): 3747.

Smyth, W. D. and Peltier, W. R. (1990), "Three-dimensional primary instabilities of a stratified, dissipative, parallel flow", *Geophys. Astrophys. Fluid Dyn.* 52 (4): 249–61.

Smyth, W. D. and Moum, J. N. (2012), "Ocean mixing by Kelvin-Helmholtz instability", *Oceanography*, 25 (2): 140–9.

Spiegel, E. A. and Veronis, G. (1960), "On the Boussinesq Approximation for a Compressible Fluid.", *Astrophys. J.* 131: 442.

Staquet, C. and Godeferd, F. S. (1998), "Statistical modelling and direct numerical simulations of decaying stably stratified turbulence. Part 1. Flow energetics", *J. Fluid Mech.* 360: 295–340.

Sutherland, B. R. (2010), *Internal Gravity Waves* (Cambridge: Cambridge University Press), 377 pp.

Tailleux, R. (2009), "On the energetics of stratified turbulent mixing, irreversible thermodynamics, Boussinesq models and the ocean heat engine controversy", *J. Fluid Mech.* 638: 339–82.

Tailleux, R. (2013*a*), "Available Potential Energy and Exergy in Stratified Fluids", *Annu. Rev. Fluid Mech.* 45: 35–58.

Tailleux, R. (2013*b*), "Available potential energy density for a multicomponent Boussinesq fluid with arbitrary nonlinear equation of state", *J. Fluid Mech.* 735: 499–518.

Tailleux, R. (2018), "Local available energetics of multicomponent compressible stratified fluids", *J. Fluid Mech.* 842: R1.

Talley, L. (2013), "Closure of the Global Overturning Circulation Through the Indian, Pacific, and Southern Oceans: Schematics and Transports", *Oceanography*, 26 (1): 80–97.

Taylor, G. I. (1931), "Effect of Variation in Density on the Stability of Superposed Streams of Fluid", *Proc. R. Soc. Lond. A.* 132 (820): 499–523.

Taylor, J. R., de Bruyn Kops, S. M., Caulfield, C. P., and Linden, P. F. (2019), "Testing the Assumptions Underlying Ocean Mixing Methodologies Using Direct Numerical Simulations", *J. Phys. Oceanogr.* 49 (11): 2761–79.

Taylor, J. R. (2008), "Numerical simulations of the stratified oceanic bottom layer", PhD Thesis (University of California, San Diego).

Thorpe, S. A. (1973), "Experiments on instability and turbulence in a stratified shear flow", *J. Fluid Mech.* 61 (4): 731–51.

Thorpe, S. A. (2005), *The Turbulent Ocean* (Cambridge: Cambridge University Press), 439 pp.

Thorpe, S. A. (2018), "Models of energy loss from internal waves breaking in the ocean", *J. Fluid Mech.* 836: 72–116.

Thorpe, S. A. and Liu, Z. (2009), "Marginal Instability?", *J. Phys. Oceanogr.* 39 (9): 2373–81.

Thorpe, S. A., Smyth, W. D., and Li, L. (2013), "The effect of small viscosity and diffusivity on the marginal stability of stably stratified shear flows", *J. Fluid Mech.* 731: 461–76.

Torrence, C. and Compo, G. P. (1998), "A Practical Guide to Wavelet Analysis", *Bull. Amer. Meteor. Soc.* 79: 61–78.

Vallis, G. K. (2017), *Atmospheric and Oceanic Fluid Dynamics: Fundamentals and Large-Scale Circulation* (2nd edition, Cambridge: Cambridge University Press), 946 pp.

Van Haren, H. and Gostiaux, L. (2010), "A deep-ocean Kelvin-Helmholtz billow train", *Geophys. Res. Lett.* 37 (3): 1–5.

Villermaux, E. (2019), "Mixing Versus Stirring", *Annu. Rev. Fluid Mech.* 51: 245–73.

Waite, M. L. and Bartello, P. (2004), "Stratified turbulence dominated by vortical motion", *J. Fluid Mech.* 517: 281–308.

Waite, M. L. and Bartello, P. (2006), "Stratified turbulence generated by internal gravity waves", *J. Fluid Mech.* 546: 313–39.

Waterhouse, A. F., MacKinnon, J. A., Nash, J. D., Alford, M. H., Kunze, E., Simmons, H. L., Polzin, K. L., St. Laurent, L. C., Sun, O. M., Pinkel, R., et al. (2014), "Global Patterns of Diapycnal Mixing from Measurements of the Turbulent Dissipation Rate", *J. Phys. Oceanogr.* 44 (7): 1854–72.

Waterman, S., Naveira Garabato, A. C., and Polzin, K. L. (2012), "Internal Waves and Turbulence in the Antarctic Circumpolar Current", *J. Phys. Oceanogr.* 43 (2): 259–82.

Winters, K. B. and D'Asaro, E. A. (1994), "Three-dimensional wave instability near a critical level", *J. Fluid Mech.* 272: 255–84.

Winters, K. B. and Riley, J. J. (1992), "Instability of internal waves near a critical level", *Dynam. Atmos. Oceans*, 16 (3-4): 249–78.

Winters, K. B. and Barkan, R. (2013), "Available potential energy density for Boussinesq fluid flow", *J. Fluid Mech.* 714: 476–88.

Winters, K. B. and D'Asaro, E. A. (1996), "Diascalar flux and the rate of fluid mixing", *J. Fluid Mech.* 317: 179–93.

Winters, K. B. and D'Asaro, E. A. (1997), "Direct Simulation of Internal Wave Energy Transfer", *J. Phys. Oceanogr.* 27 (9): 1937–45.

Winters, K. B., Lombard, P. N., Riley, J. J., and D'Asaro, E. A. (1995), "Available potential energy and mixing in density-stratified fluids", *J. Fluid Mech.* 289: 115–28.

Woods, J. D. (1968), "Wave-induced shear instability in the summer thermocline", *J. Fluid Mech.* 32 (4): 791–800.

Wunsch, C. and Ferrari, R. (2004), "Vertical Mixing, Energy, and the General Circulation of the Oceans", *Annu. Rev. Fluid Mech.* 36: 281–314.

Zhou, Q. and Diamessis, P. J. (2019), "Large-scale characteristics of stratified wake turbulence at varying Reynolds number", *Phys. Rev. Fluids*, 4 (8): 084802.

Zhou, Q., Taylor, J. R., and Caulfield, C. P. (2017), "Self-similar mixing in stratified plane Couette flow for varying Prandtl number", *J. Fluid Mech.* 820: 86–120.

Appendix A

Further details on mixing and APE

A.1 Considering a more general boundary isopycnal

In (5.15), we assume that the boundary buoyancy contour can be parameterized by x and y. Now let us consider a more general isopycnal boundary that may overturn, where the surface of constant buoyancy is parameterized by arbitrary coordinates p and q. The implicit definition of the isopycnal surface $\boldsymbol{x}_1(p,q,t)$ is then given by

$$b(x_1(p,q,t), y_1(p,q,t), z_1(p,q,t), t) = b_0. \tag{A.1}$$

Considering the same volume integral as in (5.16), we apply the Reynolds Transport Theorem to obtain

$$\frac{d}{dt}\left(\int_V f \,\mathrm{d}V\right) = \int_V \frac{\partial f}{\partial t}\,\mathrm{d}V + \int_S \left(f|_{\boldsymbol{x}=\boldsymbol{x}_2} - f|_{\boldsymbol{x}=\boldsymbol{x}_1}\right)\frac{\partial \boldsymbol{x}_1}{\partial t}\cdot\boldsymbol{n}\,\mathrm{d}S. \tag{A.2}$$

S denotes the domain in (p,q) space that parameterizes the surface, $\boldsymbol{x}_1 = (x_1, y_1, z_1)$ is the location of the isopycnal surface in Cartesian coordinates, and the area element is given by

$$\boldsymbol{n}\,\mathrm{d}S = \left(\frac{\partial \boldsymbol{x}}{\partial p}\times\frac{\partial \boldsymbol{x}}{\partial q}\right)\mathrm{d}p\,\mathrm{d}q. \tag{A.3}$$

Note that for $p = x$ and $q = y$, this recovers the original Leibniz rule result of (5.16) since $\boldsymbol{x}_1 = (x, y, z_1(x,y,t))$ and

$$\boldsymbol{n}\,\mathrm{d}S = \frac{\boldsymbol{\nabla} b}{\partial b/\partial z}\,\mathrm{d}x\,\mathrm{d}y. \tag{A.4}$$

We know in general that the direction of the normal is that of the buoyancy gradient $\boldsymbol{\nabla} b$, but for the arbitrary form (A.3) the magnitude of $\boldsymbol{x}_p \times \boldsymbol{x}_q$ depends on the coordinates chosen. Since we wish to calculate the surface integral from simulation data, it is convenient to restrict ourselves to non-overturning isopycnals, where the magnitude of the area element can be straightforwardly obtained.

We can however manipulate (A.2) further by noting that $\boldsymbol{n} = \boldsymbol{\nabla} b/|\boldsymbol{\nabla} b|$, and defining the average over the surface S as

$$\overline{f}^{*} = \frac{1}{A_S} \int_S f \, \mathrm{d}S, \tag{A.5}$$

where A_S is the surface area of the isopycnal defined in (A.1). Applying this to (A.2) gives

$$\frac{d}{dt}\left(\int_V f \, \mathrm{d}V\right) = \int_V \frac{\partial f}{\partial t} \, \mathrm{d}V + \overline{[f]_{b=b_0}^{b=b_0+L_z} \frac{\partial \boldsymbol{x}_1}{\partial t} \cdot \frac{\boldsymbol{\nabla} b}{|\boldsymbol{\nabla} b|}}^{*} . \tag{A.6}$$

Substituting $f = -Ri_0 bz$ to find the extra term in the potential energy equation provides

$$\frac{d\mathcal{P}}{dt} = -Ri_0 \left\langle z \frac{\partial b}{\partial t} \right\rangle - Ri_0 \frac{A_S}{A} \overline{(b_0 + z_2) \frac{\partial \boldsymbol{x}_1}{\partial t} \cdot \frac{\boldsymbol{\nabla} b}{|\boldsymbol{\nabla} b|}}^{*} , \tag{A.7}$$

where A is the cross-sectional area of the domain in the x-y plane, and from Winters and D'Asaro (1996) we know that

$$\frac{A_S}{A} = \frac{\partial Z_*}{\partial b} \frac{\overline{|\boldsymbol{\nabla} b|^2}^{*}}{\overline{|\boldsymbol{\nabla} b|}^{*}}. \tag{A.8}$$

Although the last term in (A.7) can be expressed analytically, its computation is far more arduous than $-d\mathcal{S}/dt$, and it does not appear (thus far) to simplify to a similar form.

A.2 Derivation of the potential energy equations

A.2.1 Total potential energy

In this section, the control volume is bounded by the isopycnals $b = b_0$ (that defines z_1) and $b = b_0 + L_z$ (that defines z_2). Consider the time evolution of $\mathcal{P} = -Ri_0\langle bz\rangle$ by applying the Leibniz rule as in (5.16):

$$\frac{d\mathcal{P}}{dt} = -Ri_0\left\langle\frac{\partial(bz)}{\partial t}\right\rangle - \frac{Ri_0}{V}\int_A [bz]_{z=z_1}^{z_2}\frac{\partial z_1}{\partial t}\,\mathrm{d}A, \tag{A.9}$$

$$= -Ri_0\left\langle z\frac{\partial b}{\partial t}\right\rangle - \frac{Ri_0}{V}\int_A L_z(b_0+z_2)\frac{\partial z_2}{\partial t}\,\mathrm{d}A, \tag{A.10}$$

$$= -Ri_0\left\langle z\frac{\partial b}{\partial t}\right\rangle - Ri_0 b_0\frac{d\overline{z_2}}{dt} - Ri_0\frac{d}{dt}\left(\frac{\overline{z_2^2}}{2}\right). \tag{A.11}$$

Defining $\mathcal{S}$ as in (5.21), we move the last two terms in the above equation to the right hand side, and use the buoyancy evolution equation (5.3) to expand the first term as

$$\frac{d\mathcal{P}}{dt} + \frac{d\mathcal{S}}{dt} = -Ri_0\left\langle z\left(-\boldsymbol{u}\cdot\boldsymbol{\nabla}b + \frac{1}{RePr}\nabla^2 b\right)\right\rangle, \tag{A.12}$$

$$= Ri_0\left\langle\boldsymbol{\nabla}\cdot(zb\boldsymbol{u}) - wb - \frac{z}{RePr}\boldsymbol{\nabla}\cdot\boldsymbol{\nabla}b\right\rangle, \tag{A.13}$$

$$= Ri_0\langle\boldsymbol{\nabla}\cdot(zb\boldsymbol{u})\rangle - Ri_0\langle w\theta\rangle - Ri_0\langle wz\rangle - \frac{Ri_0}{RePr}\langle\boldsymbol{\nabla}\cdot(z\boldsymbol{\nabla}b) - \boldsymbol{\nabla}z\cdot\boldsymbol{\nabla}b\rangle, \tag{A.14}$$

$$= Ri_0\langle\boldsymbol{\nabla}\cdot(zb\boldsymbol{u})\rangle - \mathcal{J} - Ri_0\left\langle\boldsymbol{\nabla}\cdot\left(\frac{z^2}{2}\boldsymbol{u}\right)\right\rangle - \frac{Ri_0}{RePr}\langle\boldsymbol{\nabla}\cdot(z\boldsymbol{\nabla}b)\rangle + \mathcal{D}_p. \tag{A.15}$$

With the boundaries we have specified, the divergence theorem for an arbitrary vector field $\boldsymbol{f}(\boldsymbol{x},t)$ takes the form

$$\int_V \boldsymbol{\nabla}\cdot\boldsymbol{f}\,\mathrm{d}V = \int_A [\boldsymbol{f}]_{z=z_1}^{z_2}\cdot\frac{\boldsymbol{\nabla}b}{\partial b/\partial z}\,\mathrm{d}A, \tag{A.16}$$

where $\boldsymbol{\nabla}b/(\partial b/\partial z)$ is evaluated on the surface $z = z_1$ (and takes the same value on the surface $z = z_2$).

Applying the divergence theorem to each of the above terms then gives

$$\langle \boldsymbol{\nabla} \cdot (zb\boldsymbol{u}) \rangle = \frac{1}{V} \int_A [zb\boldsymbol{u}]_{z_1}^{z_2} \cdot \frac{\boldsymbol{\nabla} b}{\partial b/\partial z} \, \mathrm{d}A = \frac{1}{A} \int_A (b_0 + z_2) \left[\frac{\boldsymbol{u} \cdot \boldsymbol{\nabla} b}{\partial b/\partial z} \right]_{z_1} \mathrm{d}A, \tag{A.17}$$

$$\left\langle \boldsymbol{\nabla} \cdot \left(z^2 \boldsymbol{u}/2 \right) \right\rangle = \frac{1}{V} \int_A \left[\frac{z^2 \boldsymbol{u}}{2} \right]_{z_1}^{z_2} \cdot \frac{\boldsymbol{\nabla} b}{\partial b/\partial z} \, \mathrm{d}A = \frac{1}{A} \int_A \left(\frac{L_z}{2} + z_1 \right) \left[\frac{\boldsymbol{u} \cdot \boldsymbol{\nabla} b}{\partial b/\partial z} \right]_{z_1} \mathrm{d}A, \tag{A.18}$$

$$\langle \boldsymbol{\nabla} \cdot (z \boldsymbol{\nabla} b) \rangle = \frac{1}{V} \int_A [z \boldsymbol{\nabla} b]_{z_1}^{z_2} \cdot \frac{\boldsymbol{\nabla} b}{\partial b/\partial z} \, \mathrm{d}A = \frac{1}{A} \int_A \left[\frac{|\boldsymbol{\nabla} b|^2}{\partial b/\partial z} \right]_{z_1} \mathrm{d}A. \tag{A.19}$$

The potential energy evolution therefore simplifies to

$$\frac{d\mathcal{P}}{dt} + \frac{d\mathcal{S}}{dt} = -\mathcal{J} - \mathcal{F}_d + \mathcal{D}_p + \left(b_0 + \frac{L_z}{2} \right) \frac{1}{A} \int_A \left[\frac{\boldsymbol{u} \cdot \boldsymbol{\nabla} b}{\partial b/\partial z} \right]_{z_1} \mathrm{d}A. \tag{A.20}$$

We can show that this final integral is zero by considering the evolution of the volume-averaged buoyancy. Since $b = z + \theta$, we know that $\langle b \rangle = L_z/2 + \overline{z_1} + \langle \theta \rangle$. The mean buoyancy perturbation is coupled to the mean vertical velocity through the system

$$\frac{d\langle \theta \rangle}{dt} = \left\langle \frac{\partial \theta}{\partial t} \right\rangle = -\langle w \rangle, \qquad \frac{d\langle w \rangle}{dt} = \left\langle \frac{\partial w}{\partial t} \right\rangle = Ri_0 \langle \theta \rangle. \tag{A.21}$$

Importantly, if both $\langle \theta \rangle$ and $\langle w \rangle$ are initially zero, then they remain so forever. This is the scenario most commonly applied in studies using the periodic stratified setup, so we proceed taking $\langle \theta \rangle \equiv 0$. We therefore know that

$$\frac{d\langle b \rangle}{dt} = \frac{d\overline{z_1}}{dt}. \tag{A.22}$$

Applying the Leibniz rule of (5.16) to $\langle b \rangle$ instead gives

$$\frac{d\langle b \rangle}{dt} = \left\langle \frac{\partial b}{\partial t} \right\rangle + \frac{1}{V} \int_A [b]_{z_1}^{z_2} \frac{\partial z_1}{\partial t} \, \mathrm{d}A = \left\langle \frac{\partial b}{\partial t} \right\rangle + \frac{d\overline{z_1}}{dt}. \tag{A.23}$$

We can then deduce that the desired integral is zero as follows

$$0 = \left\langle \frac{\partial b}{\partial t} \right\rangle = \left\langle -\boldsymbol{\nabla} \cdot (b\boldsymbol{u}) + \frac{1}{RePr} \boldsymbol{\nabla} \cdot \boldsymbol{\nabla} b \right\rangle, \tag{A.24}$$

$$= -\frac{1}{V} \int_A [b\boldsymbol{u}]_{z_1}^{z_2} \cdot \frac{\boldsymbol{\nabla} b}{\partial b/\partial z} \, \mathrm{d}A + \frac{1}{VRePr} \int_A [\boldsymbol{\nabla} b]_{z_1}^{z_2} \cdot \frac{\boldsymbol{\nabla} b}{\partial b/\partial z} \, \mathrm{d}A, \tag{A.25}$$

$$= -\frac{1}{A} \int_A \left[\frac{\boldsymbol{u} \cdot \boldsymbol{\nabla} b}{\partial b/\partial z} \right]_{z_1} \mathrm{d}A, \tag{A.26}$$

where we have applied the divergence theorem and used that $\boldsymbol{\nabla} b|_{z_1} = \boldsymbol{\nabla} b|_{z_2}$.

A.2.2 Background potential energy

In this section, we set $b_0 = 0$ so the boundary surfaces z_1 and z_2 correspond to the isopycnals $b = 0$ and $b = L_z$. We begin by determining the time evolution of $\mathcal{P}_B = -Ri_0\langle bz_*\rangle$. Applying the Leibniz result of (5.16) to this quantity gives

$$\frac{d\mathcal{P}_B}{dt} = -Ri_0\left\langle\frac{\partial(bz_*)}{\partial t}\right\rangle - \frac{Ri_0}{V}\int_A [bz_*]_{z=z_1}^{z_2}\frac{\partial z_1}{\partial t}\,\mathrm{d}A, \tag{A.27}$$

$$= -Ri_0\left\langle z_*\frac{\partial b}{\partial t} + b\frac{\partial z_*}{\partial t}\right\rangle - \frac{Ri_0}{V}\int_A L_z\overline{z_2}\frac{\partial z_1}{\partial t}\,\mathrm{d}A, \tag{A.28}$$

$$= -Ri_0\left\langle z_*\frac{\partial b}{\partial t}\right\rangle - Ri_0\left\langle b\frac{\partial z_*}{\partial t}\right\rangle - Ri_0\overline{z_2}\frac{d\overline{z_2}}{dt}. \tag{A.29}$$

The second term in the line above is zero in the case of fixed, insulating, horizontal boundaries. We therefore consider the simple case of $\theta = -z_1(x, y, t)$ to investigate the contribution this term has in the case of time-dependent isopycnal boundaries. As in §5.2.1, this example has the linear sorted background profiles $Z_*(s, t) = s + \overline{z_1}$ and $b_*(s, t) = s - \overline{z_1}$, so

$$z_*(\boldsymbol{x}, t) = Z_*(b(\boldsymbol{x}, t), t) = b(\boldsymbol{x}, t) + \overline{z_1}(t) = z - z_1(x, y, t) + \overline{z_1}(t). \tag{A.30}$$

For this simple example we find that

$$\left\langle b\frac{\partial z_*}{\partial t}\right\rangle = 0, \tag{A.31}$$

and conclude that there is no additional contribution to this term when considering a moving boundary. We now consider the first term in (A.29), and use the buoyancy evolution equation (5.3) to obtain

$$\left\langle z_*\frac{\partial b}{\partial t}\right\rangle = \left\langle z_*\left(-\boldsymbol{u}\cdot\boldsymbol{\nabla} b + \frac{1}{RePr}\nabla^2 b\right)\right\rangle, \tag{A.32}$$

$$= \left\langle -\boldsymbol{u}\cdot z_*\boldsymbol{\nabla} b + \frac{1}{RePr}z_*\boldsymbol{\nabla}\cdot\boldsymbol{\nabla} b\right\rangle, \tag{A.33}$$

$$= \left\langle -\boldsymbol{\nabla}\cdot(\psi\boldsymbol{u}) + \frac{1}{RePr}\left(\boldsymbol{\nabla}\cdot(z_*\boldsymbol{\nabla} b) - \boldsymbol{\nabla} z_*\cdot\boldsymbol{\nabla} b\right)\right\rangle. \tag{A.34}$$

Here we have introduced the Casimir

$$\psi(b) = \int_0^b Z_*(s)\,\mathrm{d}s, \tag{A.35}$$

that satisfies $\boldsymbol{\nabla}\psi = z_*\boldsymbol{\nabla}b$. Since Z_* is the inverse of b_*, and we know $\langle b_*(z)\rangle = \langle b(\boldsymbol{x})\rangle$, we can furthermore deduce that

$$\psi(L_z) = \int_0^{L_z} Z_*(s)\,\mathrm{d}s = L_z\overline{z_2} - \int_{\overline{z_1}}^{\overline{z_2}} b_*(s)\mathrm{d}s = \frac{{L_z}^2}{2}. \tag{A.36}$$

We also note that $\boldsymbol{\nabla}z_* = (\partial Z_*/\partial b)\boldsymbol{\nabla}b$, and this can be applied to the final term in (A.34). Applying the divergence theorem (A.16) to the term involving the Casimir produces

$$\langle\boldsymbol{\nabla}\cdot(\psi\boldsymbol{u})\rangle = \frac{L_z}{2A}\int_A \left[\frac{\boldsymbol{u}\cdot\boldsymbol{\nabla}b}{\partial b/\partial z}\right]_{z=z_1} \mathrm{d}A = 0. \tag{A.37}$$

Only the diffusive terms remain, giving

$$-Ri_0\left\langle z_*\frac{\partial b}{\partial t}\right\rangle = \frac{-Ri_0}{RePr}\left(\frac{1}{A}\int_A\left[\frac{|\boldsymbol{\nabla}b|^2}{\partial b/\partial z}\right]_{z=z_1}\mathrm{d}A - \left\langle\frac{\partial Z_*}{\partial b}|\boldsymbol{\nabla}b|^2\right\rangle\right), \tag{A.38}$$

$$= -\mathcal{F}_d + \mathcal{M} + \mathcal{D}_p. \tag{A.39}$$

We now have

$$\frac{d\mathcal{P}_B}{dt} = \mathcal{M} + \mathcal{D}_p - \mathcal{F}_d - Ri_0\frac{d}{dt}\left(\frac{\overline{z_2}^2}{2}\right). \tag{A.40}$$

Defining $\mathcal{B} = \mathcal{P}_B + Ri_0\overline{z_2}^2/2$ as in (5.24), we finally arrive at the evolution equation

$$\frac{d\mathcal{B}}{dt} = \mathcal{M} + \mathcal{D}_p - \mathcal{F}_d. \tag{A.41}$$

A.3 Equivalence of various local APE definitions for an adiabatically sorted buoyancy profile

Tailleux (2013*b*) proposes the following APE density as work against buoyancy forces defined relative to an arbitrary z-dependent reference density profile $\rho_r(z,t)$:

$$\mathcal{E}_a(S_i,T,z,t) = \int_{z_r}^{z} \frac{g}{\rho_0}\left(\rho(S_i,T,z') - \rho_r(z',t)\right)\,\mathrm{d}z'. \tag{A.42}$$

Here the density field depends on a materially conserved temperature variable T as well as an arbitrary number of compositional variables S_i, and z_r is the level of neutral buoyancy satisfying $\rho(S_i,T,z_r) = \rho_r(z_r,t)$. The above expression generalises the 'potential energy density' of Andrews (1981) to an arbitrary nonlinear equation of state. Although (A.42) only applies under the Boussinesq approximation, this expression can be extended as in Tailleux (2018) to describe APE density for a *compressible* multicomponent fluid. The arbitrary reference profile can be useful for defining alternative measures of APE. For example if the uniform, mean gradient is taken as the reference buoyancy profile $b_r = z$, then (A.42) recovers the APE defined in (5.29).

In this study, we consider a Boussinesq fluid with a linear equation of state in one variable, and take the reference profile to be the adiabatically sorted buoyancy $b_r = b_*$. With these assumptions, and applying our non-dimensionalisation, (A.42) becomes

$$\mathcal{E}_a(\boldsymbol{x},t) = -Ri_0 \int_{z_*(\boldsymbol{x},t)}^{z} b(\boldsymbol{x},t) - b_*(z',t)\,\mathrm{d}z'. \tag{A.43}$$

This expression is exactly that used by Roullet and Klein (2009). Note that (A.43) can also be rearranged into the form

$$\mathcal{E}_a(\boldsymbol{x},t) = -Ri_0\left(z - z_*(\boldsymbol{x},t)\right)\left[b(\boldsymbol{x},t) - \frac{1}{z - z_*(\boldsymbol{x},t)}\int_{z_*(\boldsymbol{x},t)}^{z} b_*(z',t)\,\mathrm{d}z'\right], \tag{A.44}$$

the expression for APE density used by Winters and Barkan (2013).

We can further relate (A.43) to the definition of APE by Scotti and White (2014) (which itself is equivalent to the original definition of Holliday and McIntyre (1981) but with simpler notation). We rewrite (A.43) as

$$\mathcal{E}_a = -Ri_0 b(z - z_*) + Ri_0 \int_{z_*}^{z} b_*(z',t)\,\mathrm{d}z', \tag{A.45}$$

and make the substitution $z' = Z_*(s,t)$, where Z_* is the inverse map of the sorted buoyancy profile b_*. The integral part of (A.45) then becomes

$$\int_{z_*}^{z} b_*(z',t)\,\mathrm{d}z' = \int_{b}^{b_*} s\frac{\partial Z_*}{\partial s}\mathrm{d}s, \tag{A.46}$$

since $b_*(Z_*(s,t),t) = s$ and $b_*(z_*(\boldsymbol{x},t),t) = b_*(Z_*(b(\boldsymbol{x},t),t),t) = b(\boldsymbol{x},t)$. Integrating by parts then leads to

$$\int_{z_*}^{z} b_*(z',t)\,\mathrm{d}z' = [sZ_*(s,t)]_{s=b}^{s=b_*} - \int_{b}^{b_*} Z_*(s,t)\,\mathrm{d}s, \tag{A.47}$$

$$= b_*z - bz_* - \int_{b}^{b_*} Z_*(s,t)\,\mathrm{d}s. \tag{A.48}$$

Finally, we can substitute this expression into (A.45) to recover the form of Holliday and McIntyre (1981) and Scotti and White (2014):

$$\mathcal{E}_a = -Ri_0\left[bz - bz_* - b_*z + bz_* + \int_{b}^{b_*} Z_*(s,t)ds\right], \tag{A.49}$$

$$\Rightarrow \mathcal{E}_a = E_{APE} \equiv -Ri_0\int_{b_*}^{b} z - Z_*(s,t)\,\mathrm{d}s. \tag{A.50}$$